Modelling Novel Heat Exchangers for Aircraft Thermal Management

Evaldas Greiciunas

Submitted in accordance with the requirements for the degree of
Doctor of Philosophy

The University of Leeds

Centre for Doctoral Training in Fluid Dynamics
School of Computing
March 2019

Intellectual Property and Publication Statements

The candidate confirms that the work is his own, except where work which has formed part of jointly-authored publications has been included. The contribution of the candidate and the other authors work has been explicitly indicated herein. The candidate confirms that appropriate credit has been given within the thesis where reference has been made to the work of others.

The work presented in Chapter 4 resulted in the following publication:

Greiciunas, E., Borman, D. and Summers, J., 2017, July. Unsteady flow modelling in plate-fin heat exchanger channels. In *ASME 2017 Heat Transfer Summer Conference* (pp. V001T02A011-V001T02A011). American Society of Mechanical Engineers.

The work presented in Chapter 5 resulted in following journal articles:

Greiciunas, E., Borman, D. and Summers, J., 2018. A Novel HE Corrugation Modelling Approach Utilising Conjugate Heat Transfer Methodology. *International Conference on Computation Fluid Dynamics (ICCFD10).*

Greiciunas, E., Borman, D., Summers, J. and Smith, S.J., 2019. A multiscale conjugate heat transfer modelling approach for corrugated heat exchangers. *International Journal of Heat and Mass Transfer*, 139, pp.928-937.

I was responsible for the research work undertaken in this thesis and publications while Duncan Borman and Jon Summers are my thesis supervisors and contributed in editing of the manuscripts. Steve J. Smith is my industrial supervisor who provided insight into the field of aircraft thermal management.

Dedicated to my parents, Ona and Valdas

Acknowledgements

Firstly I would like to thank my academic supervisors Dr Duncan Borman and Dr Jon Summers who guided me and provided continuous support during the journey towards the PhD thesis. Without their expertise, experience and enthusiasm it would have been impossible to complete the project.

I would also like to extend my gratitude towards BAE Systems which partially funded the project and in particular Steve J. Smith, Richard Seed and other staff members within BAE Systems sites in Warton and Samlesbury. They enabled the activities relating to additive layer manufacturing and patenting of the novel heat transfer ideas. In addition, HS Marston Aerospace Limited deserves a special mention as it provided technical support and experimental test data of the current generation heat exchanger.

Finally, I would like to thank the management board of EPSRC Centre for Doctoral Training in Fluid Dynamics (Grant No. EP/L01615X/1) for believing in me four years ago and giving me a chance to work towards this thesis.

Abstract

This thesis focuses on proposing a novel heat management solution which could be applied in the next generation aircraft. The need for novel solutions in this sector arises primarily from the severe installation constrains and the increased use of electronics which in turn creates the need for more efficient cooling. The research is accomplished by focusing on numerical modelling of heat exchanger performance using computational fluid dynamics.

In Chapters 1-3 an overview of the topics relating to the project is provided. It was particularly focused on current heat exchangers used in industry and the recent advancements within the aircraft thermal management systems driving this project. Various additive layer manufacturing techniques are compared and the most suitable one for heat exchangers is identified. In addition, current analytical/empirical design methodology of heat exchangers is compared to existing numerical modelling work.

In Chapter 4 a two dimensional sinusoidal heat exchanger channel geometry was taken from a published numerical study. It was used to assess the impact of various numerical modelling assumptions at the highest computational resolution feasible. It was found that for the flows occurring in the transitional Reynolds number regime a particular care needs to be taken in numerical solution setup to predict flow and heat transfer accurately which is often not demonstrated in the literature.

In Chapter 5 a plate-fin heat exchanger with serrated corrugation was experimentally and numerically evaluated allowing to build a robust numerical modelling framework for heat exchangers. During the process a novel approach to model heat exchanger corrugation was proposed. It uses a slice of a heat exchanger core and models both hot and cold fluid streams separated by a solid. It enables simulating the cross-flow heat transfer effects directly and eliminates the need for analytical/empirical models still popular within industry. The data from this novel corrugation model was then used in the heat exchanger unit model and produced a better agreement with the experimental data than normally obtained in industry.

In Chapter 6 the research focused on applying additive layer manufacturing to heat exchangers. A series of novel heat transfer ideas were designed and manufactured of titanium using selective layer melting. The most

promising inter-layer heat exchanger corrugation was incorporated in a novel proof of concept heat exchanger design with manifold headers. It was then evaluated numerically and compared to a more conventional pin-fin heat exchanger. Overall, the novel heat exchanger design led to increased heat transfer with no penalty in flow resistance compared to the pin-fin heat exchanger. This novel design, whilst is a proof of concept heat exchanger, is a significant step in industry and opens the way for the next generation more efficient heat transfer solutions.

Nomenclature

A_c	Cross sectional area, $[m^2]$
A_s, A_h	Total heat transfer area, $[m^2]$
β	Surface area density, $[m^2/m^3]$ or global pressure gradient, $[Pa/m]$
C_p	Specific heat at constant pressure, $[J/(kgK)]$
Co	Courant Number
d_h	Hydraulic diameter, $[m]$
δ	Fin thickness, $[m]$
ϵ	Heat Exchanger Effectiveness or Turbulence dissipation, $[s]$ or fin spacing ratio
f_c	core friction factor
$f_{fanning}$	Fanning friction factor
f	Frequency, $[Hz]$ or Forschheimer friction factor
G	Mass flow velocity, $\dot{m}/A_c$, $[kg/(m^2s)]$
γ	Corrugation spacing ratio
h	Convective film coefficient $[W/(m^2K)]$
h_f	Head pressure loss, $[m]$
η_0, η_f	Effectiveness of secondary heat transfer surfaces
j	Colburn Factor
K_c	Entrance loss coefficient
K_e	Exit loss coefficient
k	Turbulent kinetic energy, $[J/kg]$ or thermal conductivity of a material, $[W/(mK)]$
L, l	Length or fin length, $[m]$
$LMTD$	Log Mean Temperature Difference, $[K]$
M	Mach Number
$\dot{m}$	Mass flow, $[kg/s]$
μ	Dynamic viscosity, $[Pa \cdot s]$
N_{st}	Stanton number
Nu	Nusselt number
ν	Kinematic viscosity, $[m^2/s]$
P	Perimeter, $[m]$ or fluid pressure, $[Pa]$
Pr	Prandtl number
Re	Reynolds number
ρ	Density, $[kg/m^3]$
Q or $\dot{Q}$	Heat transferred, $[W]$
$Q_{balance}$	Heat balance between the heat exchanger streams
Q_{hot}	Heat emitted by the hot side of the heat exchanger, $[W]$
Q_{cold}	Heat absorbed by the cold side of the heat exchanger, $[W]$
ϕ	Flow area to face area ratio or standard deviation
T	Temperature, $[K]$
U	Overall heat transfer coefficient $[W/(m^2K)]$
u_m	Mean fluid velocity, $[m/s]$
V_s	Flow volume, $[m^3]$
v	Specific volume V/m, $[m^3/kg]$
v_m	Mean specific volume $(1/2(v_e - v_i))$
ω	Specific turbulence dissipation $1/\epsilon$

Abbreviations

ALM	Additive Layer Manufacturing
ASHRAE	American Society of Heating, Refrigeration, and Air
ASME	American Society of Mechanical Engineers
BC	bleed cabin
BE	Bleed electronics
C	compressor
CAD	Computer Aided Design
CAU	cold air unit
CYC	cyclone device
CFD	Computational Fluid Dynamics
CTAI	Cowl Thermal Anti-Ice
DNS	Direct Numerical Simulation
EA	Exergy Analysis
EC	exhaust cabin
ECS	Environmental Control System
EE	exhaust electronics
EGM	Entropy Generation Optimisation
ERS	secondary exhaust ram
FDM	Fused Deposition Modelling
FVM	Finite Volume Method
HE	Heat Exchanger(s)
HX	Heat Exchanger
HXP	primary heat exchanger
HXS	secondary heat exchanger
IR	Infra Red
LOM	Laminated Object Manufacturing
LPWE	low pressure water extractor
M	Motor
MC	mixer cabin
ME	mixer electronics
MEA	More Electric Aircraft
NTU	Number of Transfer Units
P	Hydraulic Pump
PIV	Particle Image Velocimetry
RANS	Reynolds Averaged Navier Stokes
RAT	Ram Air Turbine
SB	supply bleed
SG	Started Generator
SLM	Selective Laser Melting
SLS	Selective Laser Sintering
SRS	secondary ram supply
T	turbine
TE	Thermoeconomics
TMS	Thermal Management System
XFR	TRANS/Rectifier

Contents

List of Figures

List of Tables

Chapter 1

Introduction

Contents

1.1 Project Outline

Various thermal duties within aeroplanes are handled by Aircraft Thermal Management Systems (TMS) and Heat Exchangers (HE) play a crucial role in reliable and efficient operation of these systems. The need for novel approaches to improve heat transfer performance of them comes from multiple areas of interest. Firstly, current aircraft TMS face an increased thermal stress during the operational cycle caused by various upgrades such as installation of more powerful or additional electronics [1]. This in turn requires either additional research into the capability of an existing TMS or a more efficient heat transfer solution. Second trend is the replacement of the compressed bleed air powered systems in new aeroplanes by electrical generators and independent electrically driven systems. It is overall a more efficient method of carrying out different TMS tasks [2, 3], however, it requires additional power generation (e.g. a factor of 2 for Boeing 767 versus 787 Dreamliner [4]) which requires additional cooling [2]. Third area is the improvement of stealth (low observability) characteristics accomplished by managing the external thermal profile of the aircraft by reconfiguring the arrangement of heat management systems or by using active approaches [4].

A HE is a device which enables transfer of energy between multiple fluid streams separated by a solid or between a solid and a fluid stream in thermal contact, provided

that there is a significant temperature difference between them [5]. Often HE are classed by their compactness which is particularly important for the aviation industry. It is described as a ratio of the heat transfer area to the overall HE core flow volume and is achieved by reducing size of various heat transfer surfaces [6]. This leads to reduction of the overall HE unit size which enables reducing installation space and material requirements. Alternatively, enhancement in heat transfer performance is accomplished by promoting boundary layer separation (mixing) using different secondary heat transfer surfaces (fins) or turbulators, such as coiled wire inserts. However, whilst they help to enhance heat transfer, fins can also lead to large frictional losses [5, 6, 7], especially with increasing flow rates. This feature of the field yields a huge variety of surface configurations available in order to balance between heat rejection versus friction losses, making the HE design process challenging.

The project assesses the conventional CFD methodology and develops a robust novel method for accurate numerical analysis of HE. The developed methodology and knowledge is then utilised to create a novel platular HE which allows to minimise the inherent negative aspects of current generation HE. The novel HE design is then realised by introducing Additive Layer Manufacturing (ALM) technology called Selective Laser Melting (SLM) [8]. The technique relies on a computer controlled laser which melts powder in successive layers and enables to construct previously impossible and/or impractical geometries for HE to enhance heat transfer. The concept design is then analysed using CFD and evaluated against a conventional HE unit design.

1.2 Aircraft Thermal Management Systems

Modern aircraft are subjected to various heat sources which are managed using TMS to ensure their reliable operation. The main heat sources arise from: kinetic heating (skin friction), solar radiation (mainly subject for military aircraft), cabin pressurising and conditioning, airframe system heat loads (wing de-icing, hydraulics and etc.) and avionics heating [1, 2, 4]. A conventional air cycle TMS uses bleed air from the compressor stage of a jet engine as a energy source (Figure 1.1a) which is then conditioned by HE for various on-board tasks.

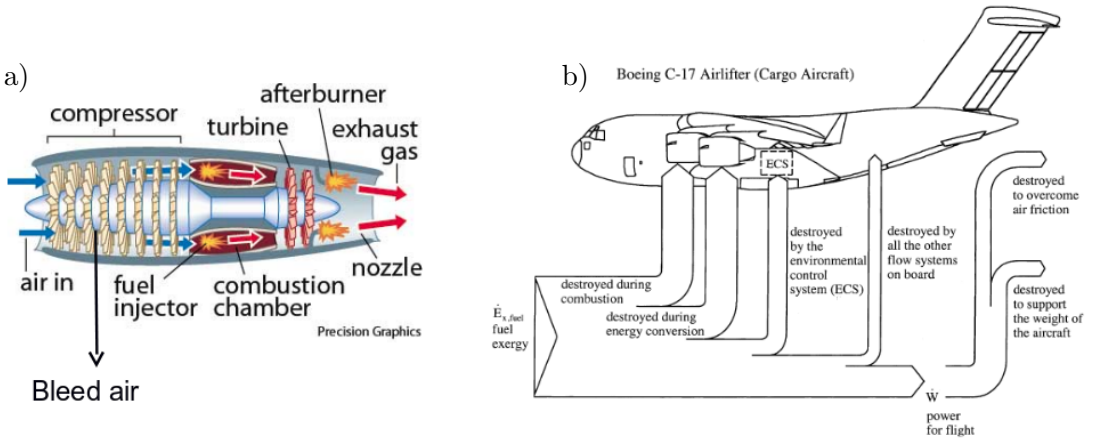

Figure 1.1: a) Turbojet Engine schematics on the left [9] with b) Fuel exergy diagram highlighting the importance of efficient TMS [10].

Figure 1.1b illustrates the effect TMS has on the overall efficiency and fuel consumption of an aircraft which could reach $\approx 65\%$ in cruise conditions [10] (Boeing C-17). An example part of the TMS is given in Figure 1.2 where flow path of conditioned air to the cabin is shown for a military aircraft in order to explain the working principle and complexity of such systems. The air flow in the Figure 1.2 system is firstly extracted from the engine at the Supply Bleed (SB) position and its moisture is reduced using a cyclone device. The bleed air is then cooled by the Primary Heat Exchanger (HXP) using ram air (cold air from the atmosphere) before the entering compressor stage of the Cold Air Unit (CAU). Compressed air is then further cooled down using a Secondary Ram Air Source (SRS) at the Secondary Heat Exchanger (HXS). Then the flow is expanded using the turbine and is mixed with the hot bleed air at a Mixer (ME) to achieve a required flow temperature. Part of the air is then exhausted into the cabin to cool the Electronics (EE) whilst from the rest of the flow the residual moisture is extracted using the Low Pressure Water Extractor (LPWE). The flow again is mixed with bleed air at the station MC and supplied to the cabin. Such system is known as a two-wheel bootstrap cycle ECS - a widespread solution because of its self regulating features for various conditions [11, 12].

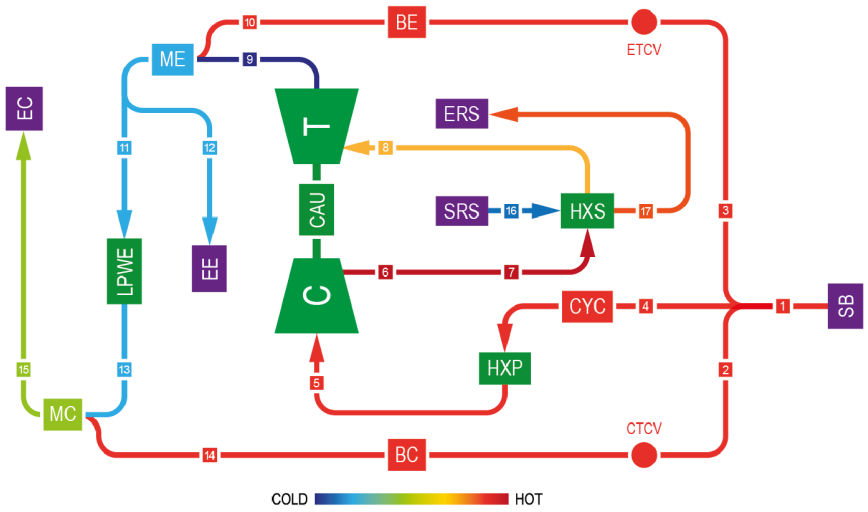

Figure 1.2: Air ECS schematics of an in service military fast-jet. Arrows indicate the flow direction and colour - temperature [11].

SB - supply bleed	CYC - cyclone device
HXP - primary heat exchanger	C - compressor
HXS - secondary heat exchanger	SRS - secondary ram supply
ERS - secondary exhaust ram	T - turbine
CAU - cold air unit	BE - Bleed electronics
ME - mixer electronics	LPWE - low pressure water extractor
EE - exhaust electronics	MC - mixer cabin
BC - bleed cabin	EC - exhaust cabin

Table 1.1: Air ECS nomenclature.

Fuel is an alternative heat sink used to absorb the heat [13] and whilst it is a much more efficient heat absorption source its use is mainly limited to oil cooling within different aircraft systems. The main limitation of it comes from variable fuel flow rate to the engine which depends on the operating conditions and the overall reduction in fuel volume during the flight. This is turn could result in an abrupt increase of the fuel temperature affecting the engine performance [4]. To improve the ram/bleed air systems the TMS of some modern aircrafts use liquid cooling in parts of the system as vapour cycle systems are compact and up to 5 times more efficient in terms of the coefficient of performance. However, their use is limited due to the added weight and a narrow operating temperature range of refrigerants. Cooling with dielectric fluids has also been used for avionics which are conventionally cooled by air due to the flight safety [4].

Continuous design aim of a TMS is to minimise the cooling system size and the bleed air requirement. It is driven by inefficiency of the current systems where the

ratio between engine power consumed to the heat load cooled is approximately 10:1 [4]. The problems become more pronounced for high performance military aircrafts where the density of avionics causes the weight to increase not only in terms of the electronics itself, but also by the supply network. This in turn requires bigger ram air inlets and HE which create drag and higher usage of bleed air leading to reduced efficiency of an aircraft [4].

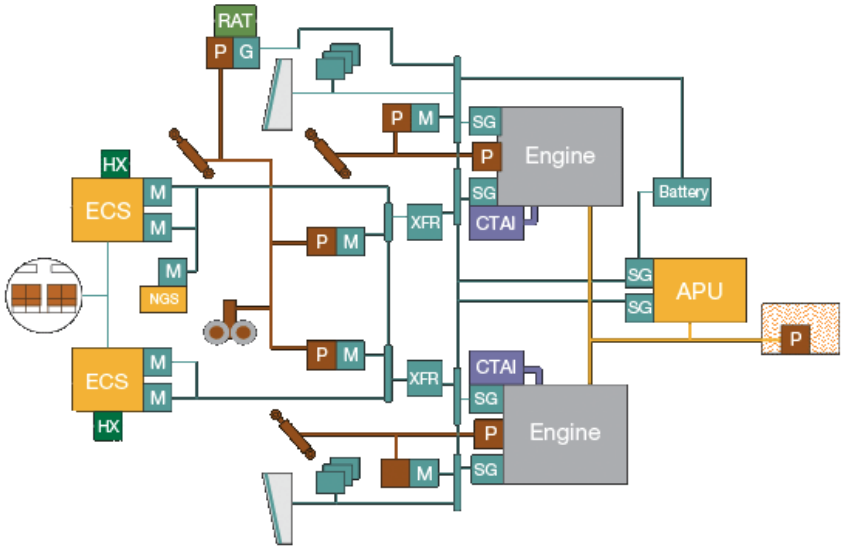

Figure 1.3: No bleed air TMS architecture schematic of the Boeing 787 [14].

HX - Heat Exchanger	CTAI - Cowl Thermal Anti-Ice
XFR - TRANS/Rectifier	— Electrical
SG - Started Generator	— Hydraulic
RAT - Ram Air Turbine	— Pneumatics
P - Hydraulic Pump	— Fuel
M - Motor	— Ram air

Table 1.2: No bleed TMS nomenclature.

Thus, researchers have been developing TMS in which the bleed air is almost completely eliminated to reduce complexity, cost and weight of the new systems. The design framework is known as More Electric Aircraft (MEA), initially considered in the defence industry in the early 1990's [15, 16]. Interestingly, both TMS types have been used in aeroplanes during the WWII [17]. However, the electrically driven concept was forgotten due to initially higher compactness of the bleed air systems. The switch back to the electrical systems has become feasible recently due to advances in power electronics [17]. In the no-bleed systems the energy source (compressed air) is replaced

with the electrical power generators connected to the plane engines and storage capacity (batteries) making different components modular. Systems designed under this framework replace the bleed air used for pneumatics and hydraulics by electrical actuation. This in turn makes the aircraft more reliable as a failure of a single component will have little/no effect on other systems. The benefits of eliminating engine bleed are further pronounced in modern jet engines where the negative efficiency effects of bleed air extraction are higher due to greater compression ratios [4]. The most known civil example of this design framework is Boeing 787 [2] (Figure 1.3) where the bleed air has almost been eliminated apart from the engine cowl de-icing. Other systems use electrical generators and hydraulic pumps connected to the engine or are powered by electrical motors. Electrical compressors are used for the systems which require compressed air (such as ECS) or in case of wing anti-icing - heating mats are employed. This allows to save the ducting space and weight (up to 8" diameter pipes can be used in commercial aircrafts [4]). However, no bleed air TMS also requires a new approach for aircraft cooling, arising from the increased use of electrical equipment [2].

1.3 Heat Exchangers and Aviation

1.3.1 Main Types of Heat Exchangers

There are various traditional HE types, some of the most popular include shell and tube, tube-fin, plate and plate-fin. The shell and tube is one of the most well known types of HE (Figure 1.4a). However, it is difficult to manufacture it sufficiently compact for an application in aerospace [7]. A more compact alternative is the tube-fin HE (Figure 1.4b) with the variety of tube and fin configurations available depending on an application with the examples detailed in [18, 19, 20, 21]. It is utilised in aerospace industry [21] because of the high pressure containment capability [5, 7].

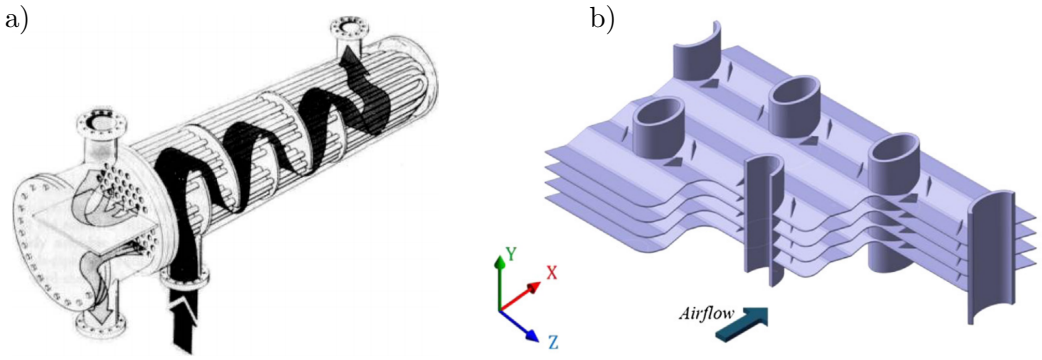

Figure 1.4: Examples of a) Shell and tube HE [22] and b) Tube-fin HE [18].

Plate HE consist of layers of thin metal plates separating the two flows (Figure 1.5a). They are normally used for compact liquid-liquid heat transfer and offer good thermal efficiency, but clean fluid streams are required to prevent blockages of the HE [5]. Again, a variety of plate corrugations are used depending on the manufacturer and application [7].

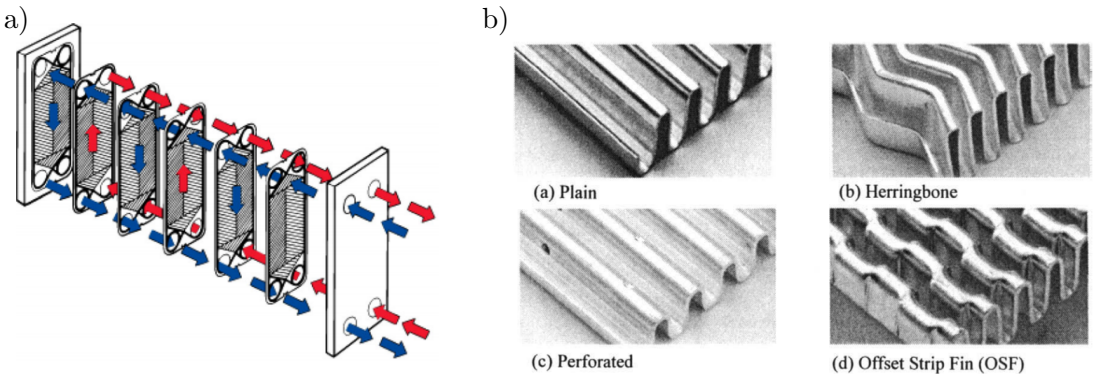

Figure 1.5: a) Platular HE example with the flow schematics [23]. b) Types plate-fin HE secondary heat transfer surfaces (corrugation). [7].

Plate-fin HE are cross-flow HE where secondary surfaces (fins) are installed between the flat plates separating the two flows. Alternatively, flat tubes can be incorporated between the fins for condensing/evaporating applications. These HE are used widely in the aerospace and automotive industries due to their reliability, compactness and operation with low temperature difference between the fluid streams. It can be applied for liquid-liquid, gas-liquid or gas-gas heat transfer with some of the most popular secondary surfaces illustrated in Figure 1.5b [5, 7].

1.3.2 Summary of Heat Exchanger Modelling

HE design can be accomplished using three main methods: experiments, analytical and numerical calculations. One of the key books focusing on compact HE design was published by Kays and London (1964) [6]. It describes the required experimental setup to evaluate different HE corrugation and the analytical $NTU - \epsilon$ modelling method which is still popular in the HE industry. A more recent summary of the field was completed by Hesselgreaves (2001) [7] which also includes some of the modern manufacturing methods. An extensive summary of the analytical heat transfer theory and alternative NTU-P, LMTD and other analytical HE modelling methods are also provided by Shah and Sekulic [24] and Rohsenow et al. [5]. The analytical models above require the HE corrugation data obtained prior either experimentally or analytically and allows one to quickly estimate HE performance for a specific application.

However, these methods fail to take into account more complex fluid flow effects such as flow inside the HE headers.

Modelling of the heat transfer network is another approach utilised in aerospace. It is typically based on exergy (available work) analysis and can be used to evaluate the overall performance of complicated systems such as aircraft TMS [10, 25]. Examples include Vargas and Bejan [10] who used exergy methods to optimise performance of the HE as part of a larger system. Another application is shown by Leo and Perez-Grande [25] where component cost per unit of exergy is used to analyse the aircraft performance during different operational regimes.

The emerging trend is to model HE with Computational Fluid Dynamics (CFD) because it allows to obtain a detailed prediction of flow and heat transfer inside the HE and to evaluate complicated geometries without the need for physical testing. A recent review of HE CFD studies was completed by Bhutta et al. [26] in which over 50 different studies are examined covering a broad range of HE types and show emerging popularity of the numerical methods. Analysis of relevant compact HE, such as plate-fin HE, was found to be undertaken in two steps. Firstly, a detailed flow and heat transfer analysis through a small representative section of HE corrugation is undertaken. The results of it are then extrapolated to a simplified model of the complete HE unit. These models use the same $NTU - \epsilon$ [6] relations implemented as a source term to the energy equation to provide with the simplified heat transfer prediction. The flow inside the HE core is simplified using porous media models, applied as source terms to flow momentum equation. This two step approach is necessary due to the high number of flow elements present (high HE compactness). The simplified modelling is often coupled with a conventional CFD analysis to study phenomena affecting the HE performance as a part of a system. Good examples are the studies of inefficient HE headers which cause maldistribution at the inlet section to the HE core [27, 28, 29]. It is a common HE problem occurring due to the employed manufacturing methods and restricted HE installation volume.

1.4 Aims and Objectives

Project Aims

1. To develop experimentally validated CFD modelling approaches for compact HE.

2. To identify the opportunities for improving performance (weight, space and heat transfer) of HE using validated CFD in combination with ALM.

Objectives to meet aim 1:

1. Identify the potential areas of novel research and different modelling approaches for current HE using the literature review (Chapters 1- 3).

2. Highlight challenges and limitations in detailed flow and heat transfer predictions at a range of Reynolds numbers through a selected HE corrugation. This was accomplished by the two dimensional CFD sinusoidal channel simulations using OpenFOAM and ANSYS Fluent (Chapter 4).

3. Experimentally test a compact HE to obtain a comprehensive dataset for validation of the CFD analysis. The work was completed with the expertise from an industrial partner (Chapter 5).

4. Compare and assess validity of different simplified modelling assumptions using CFD by modelling the full HE unit and the experimental data acquired for validation (Chapter 5).

Objectives to meet aim 2:

1. Produce and evaluate a series of novel HE concepts that exploit ALM. The concepts were modelled using HE knowledge obtained prior in the project (Chapter 6).

2. Evaluate the novel proof of concept HE performance aimed to reduce inherent inefficiencies of current HE by utilising prior developed CFD methodology (Chapter 6).

Chapter 2

Heat Exchanger Design

Contents

2.1 Introduction

In this section a comprehensive overview of the HE field is provided. Current HE are discussed, showing typical heat transfer surfaces and traditional HE manufacturing

methods employed. The main ALM techniques are summarised next discussing the suitability of each method for heat transfer applications. Finally, traditional methods used to design HE are presented, including analytical and network heat transfer modelling together with standard and novel experimental procedures.

2.2 Traditional Heat Exchangers

2.2.1 HE Classification

There is a large number of HE types available and HE compactness is often used as one of the measures to classify them (Figure 2.1). It is described by surface density [7]:

$$\beta = \frac{A_s}{V_s}, \left[\frac{m^2}{m^3}\right] \tag{2.1}$$

where A_s - total heat transfer area $[m^2]$, V_s - flow volume $[m^3]$. Another important characteristic for the HE compactness is the hydraulic diameter d_h of a HE core [6]:

$$d_h = \frac{4A_c}{P} = \frac{4A_cL}{A_s}, [m] \tag{2.2}$$

where A_c - cross-sectional area of the flow passage $[m^2]$, L - length of the channel $[m]$, P - perimeter $[m]$.

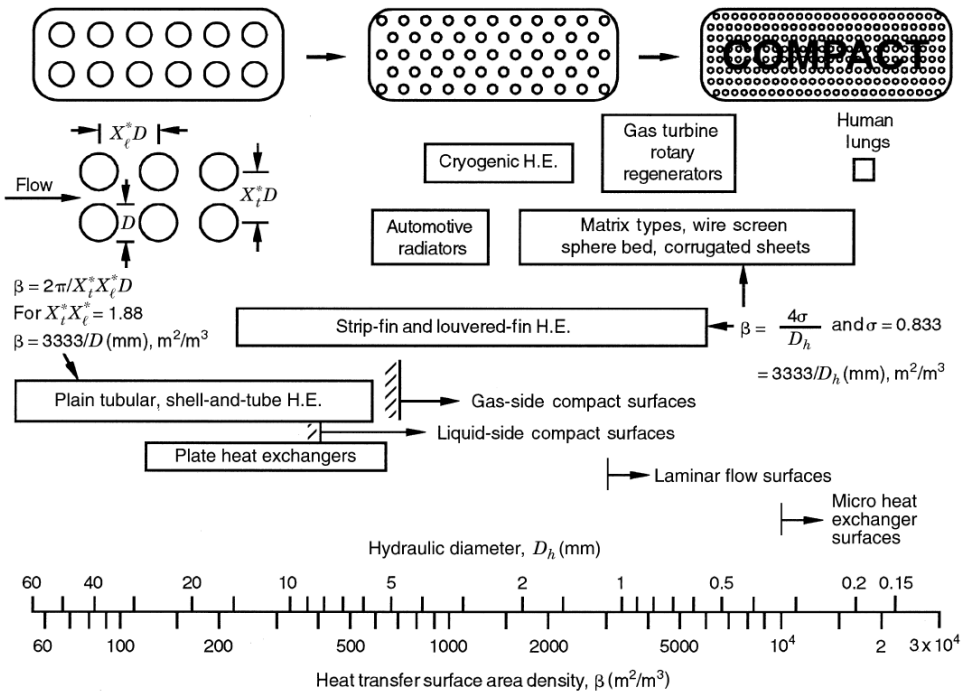

Figure 2.1: Main HE classification based on heat transfer surface density and hydraulic diameter [30].

Threshold value for a HE to be classed as compact varies depending on the fluids used. To achieve compactness of a gaseous HE, surface density should be at $\beta \gtrsim 700$ m^2/m^3 with the hydraulic diameter reduced to $d_h \lesssim 5$ mm. A liquid/two phase HE requires both a lower surface area density ($\beta \gtrsim 400$ m^2/m^3) and a higher hydraulic diameter of $d_h \lesssim 8$ mm due to better heat transfer properties of liquids. Next level of compactness is specified as laminar HE with $\beta \gtrsim 3000$ m^2/m^3. At this stage the flows always remain in laminar regime, because of the low hydraulic diameter and the resulting low Reynolds number defined as [31]:

$$Re = \frac{\rho u_m d_h}{\mu} \tag{2.3}$$

where u_m - mean flow velocity $[m/s]$, ρ - fluid density $[kg/m^3]$ and μ - shear viscosity of the fluid $[Pa{\cdot}s]$. Further compactness level is classed at a microchannel level $\beta \gtrsim 10000$ m^2/m^3 [5]. HE can also be classified using various other factors such as orientation of the flows (parallel, counter or cross) which allows to estimate the overall efficiency of the HE. Another method is classification by construction (Figure 2.2) with most of these HE are used in aerospace and are discussed further in the following sections.

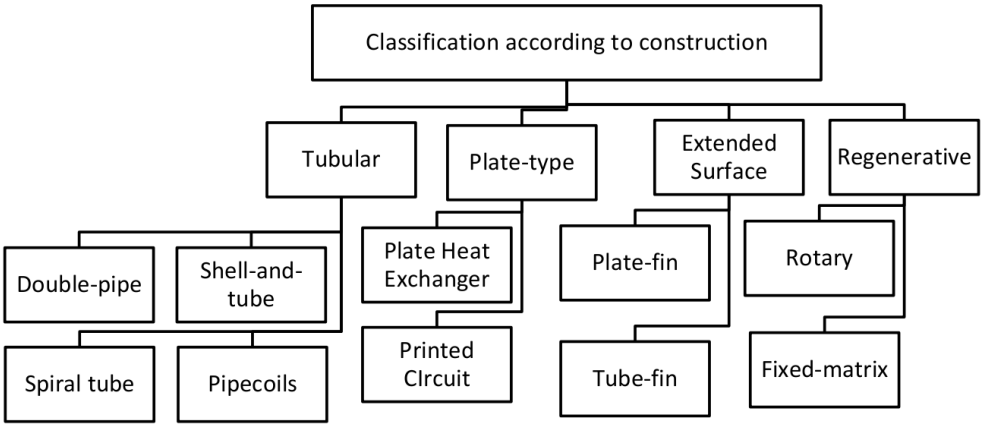

Figure 2.2: Main HE classification based on the construction/geometry features according to [5, 7, 32].

2.2.2 Shell and Tube HE

Shell and tube HE are one of the most commonly used HE in industry. A disassembled view of a simple single pass shell and tube HE is presented in Figure 2.3. In these HE one flow is passed through a number of small diameter tubes whilst the next fluid flows

through the shell side. There is a variety of alternative tube configurations available such as U-tube or straight flow arrangement whilst the flow inside the tubes is often perturbed using fins [24]. Flow though the shell side is disturbed using baffles, typically the semi-circular ones (Figure 2.3). Helical baffle design is a modern approach aimed to enhance heat transfer with minimised pressure losses (Figure 2.4) [33] with more arrangements available in Rohsenow et al. [5].

Figure 2.3: Shell and tube heat exchanger example with semi-circular baffles [34].

Shell and tube HE are normally used for liquid-liquid or liquid-steam heat transfer and have multiple advantages causing their popularity. These HE can be designed to be at a vast range of sizes and operated at various conditions (even in vacuum or high pressure applications) and be manufactured to enable access for cleaning (Figure 2.3) [34]. In addition, shell and tube HE can be made of a variety of materials including both metal and non-metal (e.g. glass, graphite), allowing the HE to be used in harsh environments such as nuclear plants, chemical and process industry [35]. The main disadvantage of the shell and tube HE, however, is the low surface area density ranging between 50 m^2/m^3 to 100 m^2/m^3 [5, 7], limiting their use for applications with highly constrained installation space available.

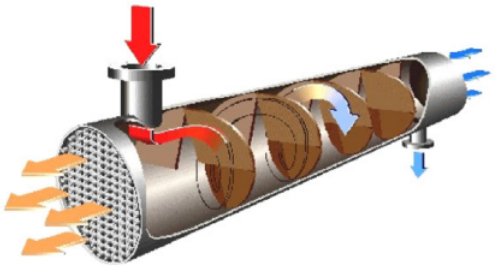

Figure 2.4: Shell and tube heat exchanger model with helical baffles [33].

2.2.3 Plate Heat Exchangers

These HE can be arranged in both cross-flow and counter-flow orientations and are often used as compact alternatives to the shell and tube HE. Plate HE consist of layers of thin metal plates separating the two flows with a variety of corrugations available (Figure 2.5) [7, 36]. They are typically used for compact liquid-liquid heat transfer

and offer good thermal efficiency. However, the surface area compactness requires clean fluid streams to prevent blockages [5], arising from the small hydraulic diameter ($d_h \lesssim 10\ mm$). Plate-and-frame HE is a highly modifiable version of the plate HE. It uses gaskets between the thin plates together with movable end covers which provide a flexibility to adapt for changing cooling requirements (Figure 1.5a).

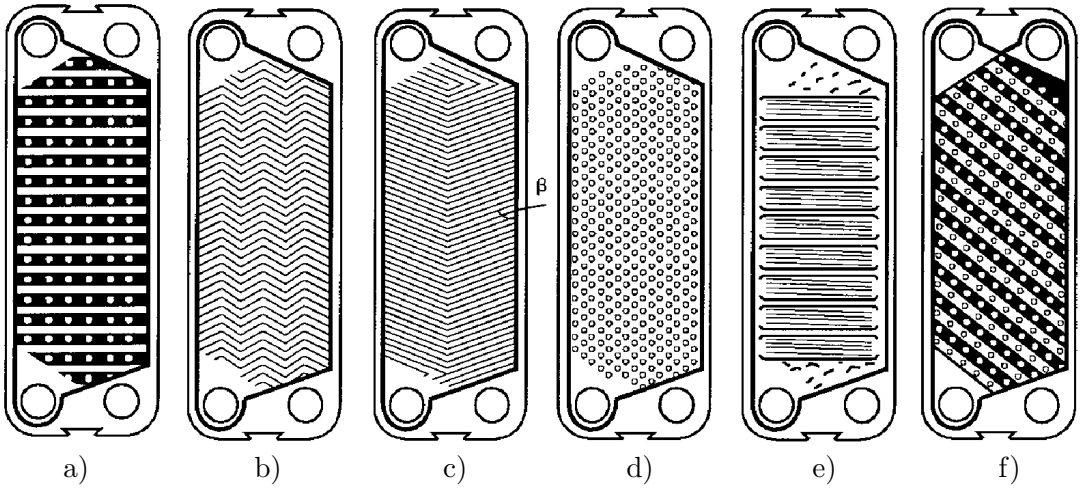

Figure 2.5: Different plate patterns: a) washboard, b) zigzag, c) herringbone, d) protrusions and depressions, e) washboard with secondary corrugation f) oblique washboard [36].

Welded plate HE (Figure 2.6) are also widely available and are used for more demanding duties including high pressure, corrosive applications [5, 7] and are extensively studied in the literature. A particular focus of research was the alignment angles of different plate HE corrugations with the goal to find the most effective solution (least amount of pressure drop versus increase in heat transfer).

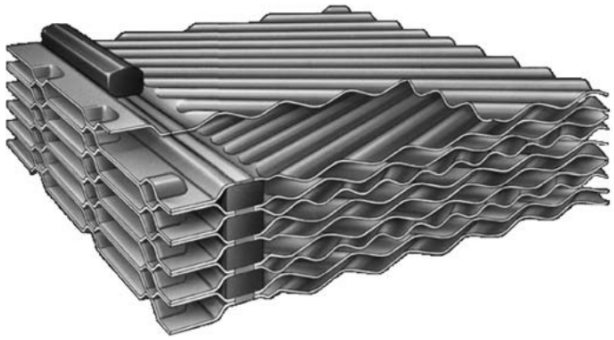

Figure 2.6: Welded washboard platular HE example [24].

2.2.4 Plate-fin Heat Exchangers

Plate-fin HE (Figure 2.7) are designed for cross-flow applications and are constructed using secondary surfaces (fins) between the flat plates which separate flows with the standard corrugation shapes shown before in Figure 1.5b. Schematic of a single plate-fin HE layer is shown in Figure 2.7a. Such HE unit is built by alternating the layers in cross-flow to form a HE core (Figure 2.7b). It is a labour intensive process, completed using a template rig and manual labour. The HE core is then cured using vacuum brazing to create a bond between the individual pieces. The technique allows the plate-fin HE to be made of nickel, stainless steel or inconel depending on an application [7]. This type of HE was primarily developed for aerospace in 1940's to be used in aircraft thermal management, however, currently it is used in various applications. Corrugation between the two parallel plates in the plate-fin HE (Figure 2.7) is beneficial for multiple reasons. Firstly, the fins disturb the fluid streams, providing improved heat transfer

a) b)

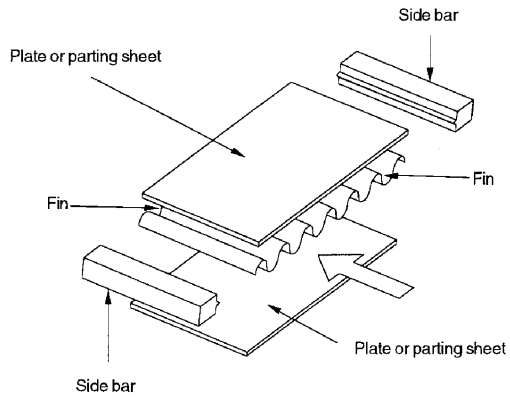

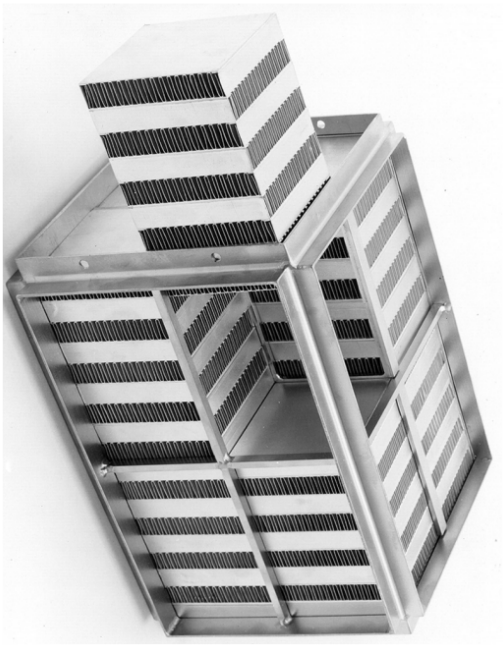

Figure 2.7: a) Single layer structure of a plate-fin HE core [24]. b) Example plate-fin HE core [37].

performance. Secondly, the fins enable a low d_h of HE which enhances the heat transfer coefficient through high HE compactness and enables it to be used for both gas-liquid or gas-gas applications. Thirdly, corrugation also aids structural integrity of the HE unit [7]. Plate-fin HE allows multistreaming capability (up to 12 streams reported in [7]) and high area density with $d_h = 1$ or 2 mm making it more efficient even at low ΔT. Plate-fin HE structure is also used in a hybrid configuration with flat tubes in condensers/evaporators, particularly in automotive industry. In these HE tubes are

used to carry the refrigerant in one of the two layouts: either headered (Figure 2.8a) or serpentine patterns (Figure 2.8b) [5, 7, 38].

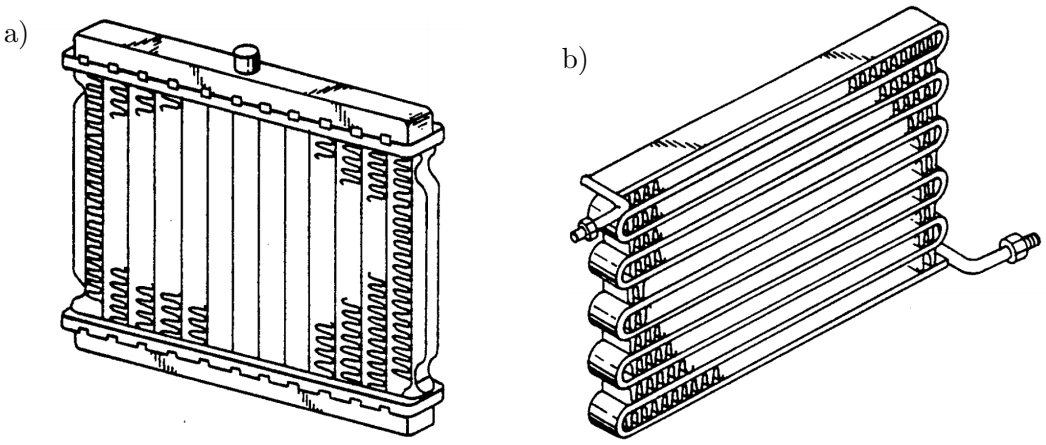

Figure 2.8: Plate-fin/tubular condenser/evaporator layouts. a) Headered flow pathway for the refrigerant, b) Serpentine flow pattern [39].

Phase change surface enhancement is undertaken for more demanding applications and requires a different approach depending if the fluid is evaporating or condensing. The purpose of secondary boiling surfaces is to promote formation of the steam. This is accomplished by preventing too rapid removal of liquid and gas mixture from the HE during vaporisation. However, for condensing applications the secondary surfaces are designed to ensure efficient drainage of the condensate, thus, a thick thermal boundary layer would not inhibit the heat transfer (Figure 2.9) [7].

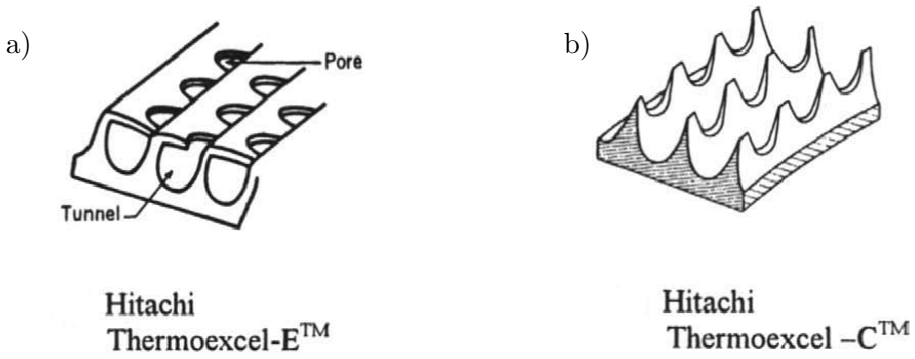

Figure 2.9: Enhanced a) evaporator and b) condenser surfaces for HE [7].

2.2.5 Tube-fin HE

This type of HE is used mainly for gas to liquid flows and has historically been popular for air cooling in locomotives, steam condensers. The outer flow is typically gaseous and either individual or flat fins are used to enhance heat transfer (Figure 2.10). The

individual fins are more commonly used in large assemblies whilst platular fins are a more cost effective solution [7]. A variety of platular fins were developed (such as louvred or wavy) to match a certain heat transfer requirement. However, the main

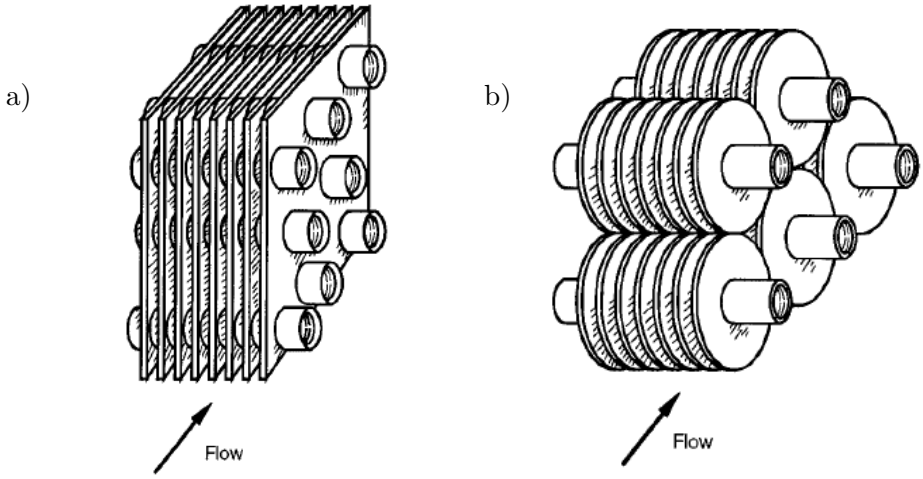

Figure 2.10: a) Flat finned tube-fin HE and b) Individually finned tube schematics [24].

issue associated with the platular fins is the design for extreme conditions which can cause expansion of the fins onto the tubes resulting in material stresses. Circular, rectangular or elliptical tubing is used for the tubular side [24] with various internal structures possible (Figure 2.11). The main advantage of the tube-fin HE is high pressure containment on the tubular side compared to the other HE. However, tube-fin HE are typically of lower compactness compared to plate-fin HE with the commercially available units reaching the compactness levels of only $\beta \approx 3300\ m^2/m^3$ [5, 7].

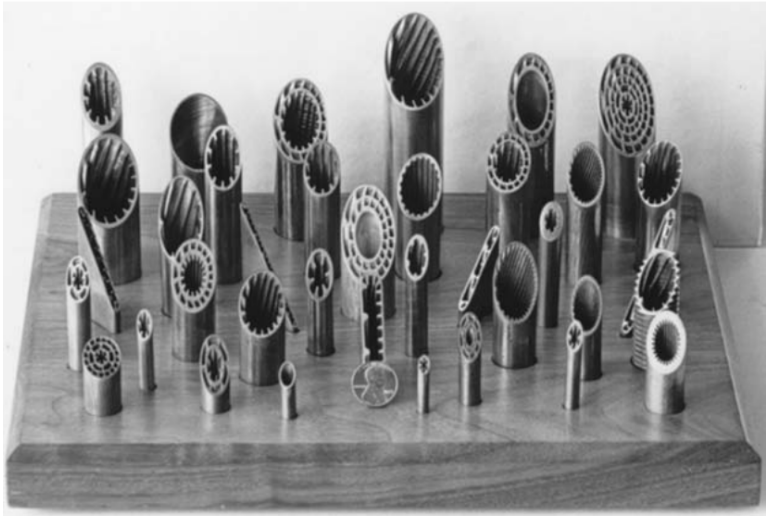

Figure 2.11: Various tubular heat transfer surfaces [24].

2.2.6 Printed Circuit HE (PCHE)

PCHE are formed by diffusion bonding a stack of plates with fluid passages manufactured by photochemically etching the flow channels [7] (Figure 2.12). This process results in the heat transfer channels having a depth ranging from 0.1 to 2.1 mm. The individual plates are then diffusion bonded to form a HE core to which the headers are attached. The process allows the HE unit to be manufactured using a range of materials such as steel, copper, aluminium, nickel and others enabling various applications. Different etching patterns can also be used to form cross, counter, or multi-fluid flow pass configurations. Another big advantage of this HE type is a very high pressure containment together with good anti-corrosion properties which led to popularity of this HE in offshore oil platforms. The main drawback of these HE is that due to the small hydraulic diameter the flow resistance can become excessive, limiting the application range [24].

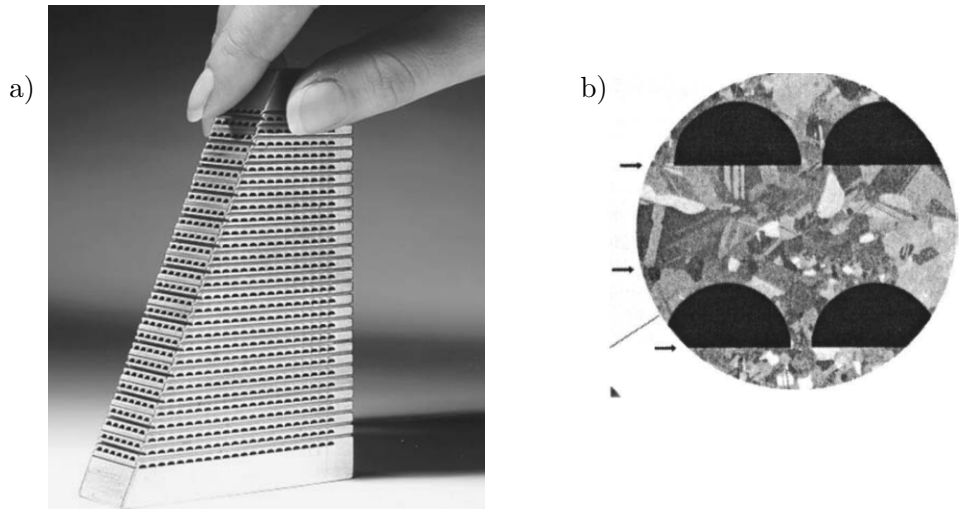

Figure 2.12: a) PCHE core section [24] and b) zoomed in view of the PCHE channel [7].

2.2.7 Integrated Heat Management Techniques

This type of heat transfer management is relatively new and arose due to the increased need for cooling, particularly in aerospace, requiring a more integrated approach [2]. A potential technology is to use foams which can be incorporated into the structure of the aircraft to minimise the space constraints (Figure 2.13). High performance graphite foams have been developed by Klett et al. [40] as they have several times higher specific thermal conductivity (thermal conductivity divided by specific gravity) than metallic substitutes. Alternatively, experimental studies were conducted by Kim

et al. [41] (2000) and by De Schampheleire et al. [42] (2013) proposing aluminium based foams for the heat transfer.

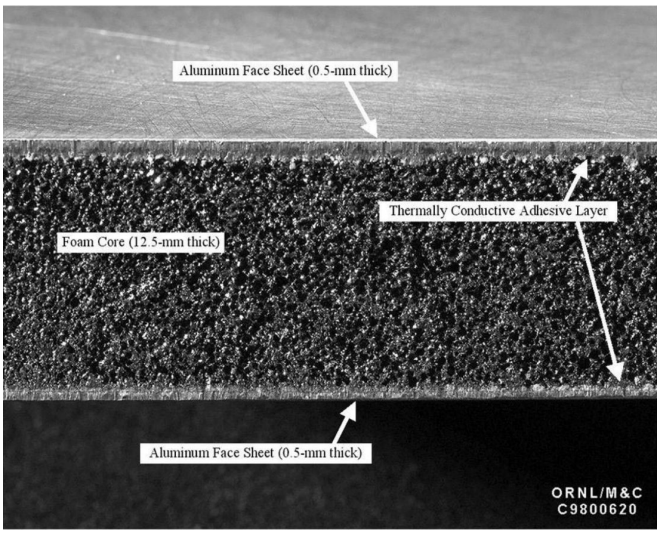

Figure 2.13: Graphite foam incorparated between aluminium plates [40].

Another idea is to utilise the air around the aircraft as a coolant for heat management (Figure 2.14)[43]. This has been implemented for the CL-600 Challenger (small passenger aircraft) [44] where a layer of HE fins is used between the outer and inner sections of the skin of the aircraft. The fluid movement is then promoted using fans. The main disadvantage of this system is that at the increasing altitude the heat capacity decreases [45] due to lower air density. Also, it would not work at supersonic speeds due to the heat induced by skin friction [46].

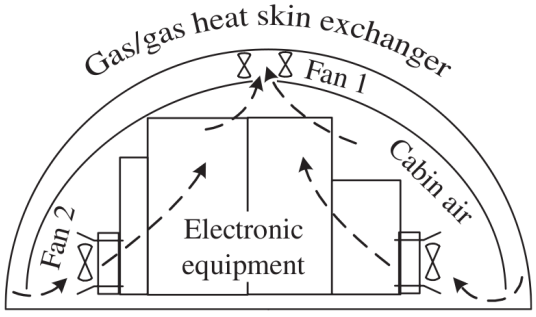

Figure 2.14: Aircraft skin heat transfer schematics [43].

2.3 Additive Layer Manufacturing and HE

Additive Layer Manufacturing (ALM) is a process during which a part is produced by incrementally adding solid material to form a desired part and is fundamentally different from traditional manufacturing where a part is formed using various material removal processes [47]. ALM has been developing rapidly due to its superiority to the traditional processes for many applications by allowing greater design freedom, shorter design and manufacture cycles. In addition, production of a part using multiple materials is enabled with ALM together with the overall saving in price arising from reduced labour, fixtures, tooling and energy requirements [48].

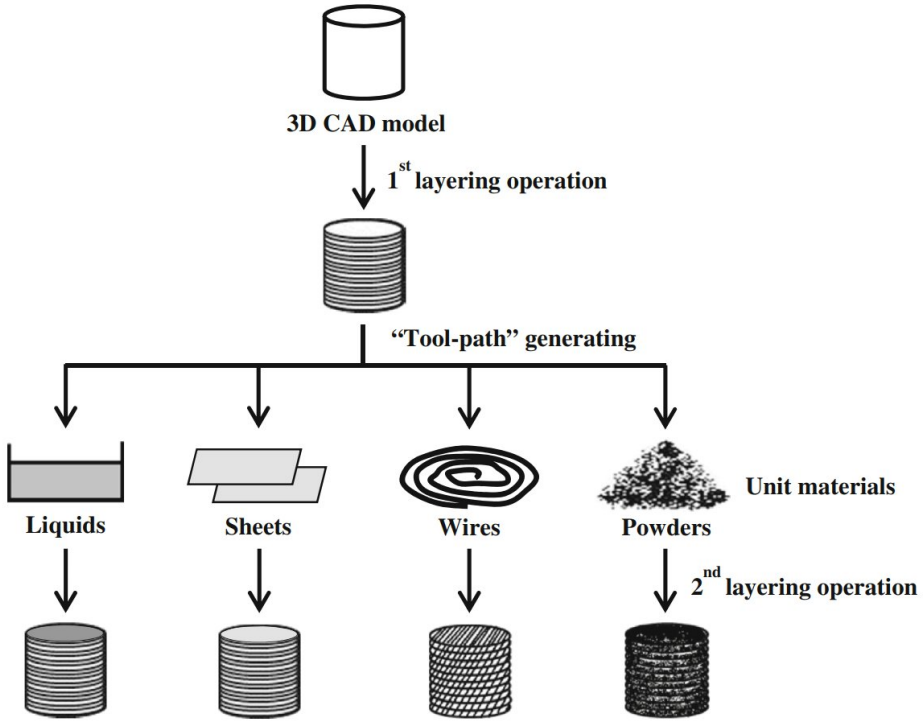

Figure 2.15: Additive layer manufacturing design schematic [49].

A typical ALM process is briefly explained in Figure 2.15. It starts from building a CAD model of a required part which is then sliced into layers using specialised software. Then one of the four types of the ALM machines is selected based on the design requirement in which a part is built in successive layers with Figure 2.16 showing a variety of manufacturing processes developed to date.

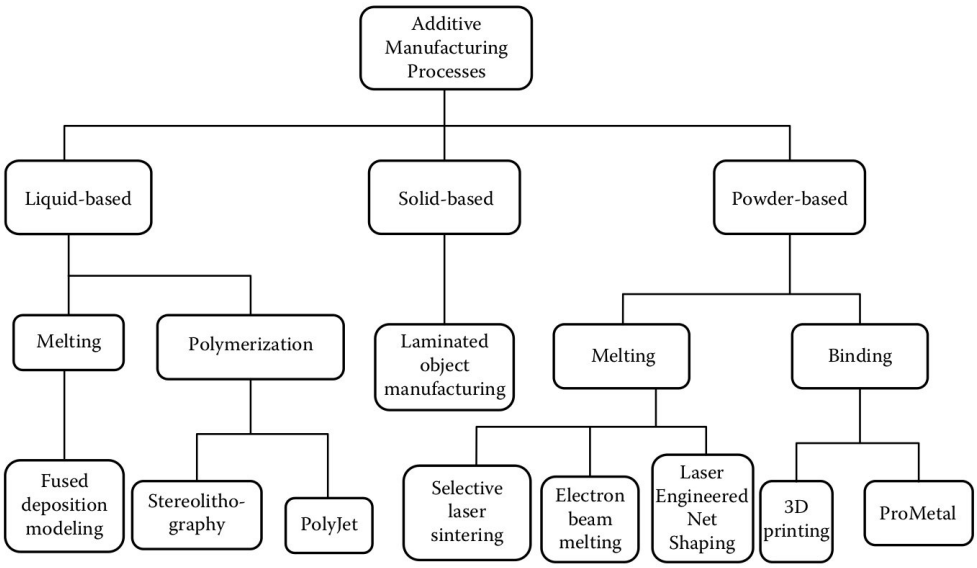

Figure 2.16: Different types of additive layer manufacturing techniques [48, 50].

2.3.1 Stereolithography

Stereolithography is one of the first popular ALM methods with patents found in 1980's [51]. The process works by curing the photosensitive resin to a polymer using a laser with Figure 2.17 providing a schematic of the process.

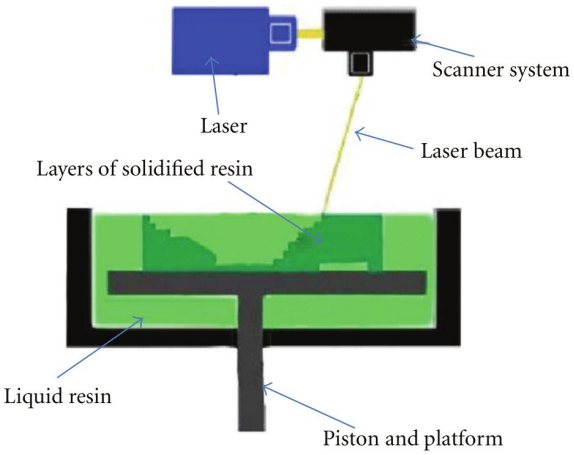

Figure 2.17: Stereolithography process [52].

A part is built in layers which vary in height based on the design requirements, curing the resin at specified locations. At the end of the print the build volume is drained of the resin which can then be reused [50, 53, 54]. Common manufacturing errors of

the technique are over-curing of the resin and height control during the layering steps. Initially, the technique was limited to demonstrational models, however, introduction of microstereolithography allowed ultra-dense structures for electronics substrates and expanded the applications to consumer, medical and defence electronics [48].

2.3.2 Fused Deposition Modelling

Fused deposition modelling (FDM) method [55] is one of the most widely used ALM processes. An array of materials including plastics, wax and even metals and ceramics (the latter two require binders) can be used for manufacture [47]. The process is illustrated in Figure 2.18 and works by extruding solid material (typically packed in reels) which is melted at the nozzle just above the melting temperature. The deposited material then solidifies instantaneously and adheres to the previous layers. However, the process causes two inherent disadvantages: seam line between the layers and need for support material. Thus, to aid manufacturing the support material is printed from a different nozzle and use an easy to remove material in more advanced FDM machines [56].

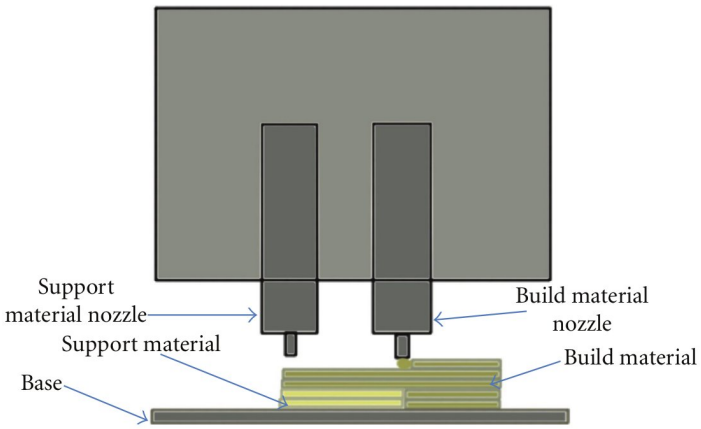

Figure 2.18: Fused deposition modelling schematic [52].

2.3.3 Laminated Object Manufacturing

Laminar Object Manufacturing (LOM) [57] combines the existing traditional stacked plate technique found in current HE and the ALM. The method works by cutting layers of a complex part from a sheet/roll of pre-manufactured material using a laser [48]. The completed part is then either brazed or utilises adhesives to form a part [58]. The method is cheap, fast and allows manufacture using a variety of materials including metals, plastics and even composites [48, 52, 59] and was observed to be used for HE

manufacture in industry. However, the process has two main disadvantages limiting its use: firstly, large amount of material produced [48, 60]. Secondly, the method results in low surface quality arising from vertical stacking of the structure, unacceptable for many industrial applications [61].

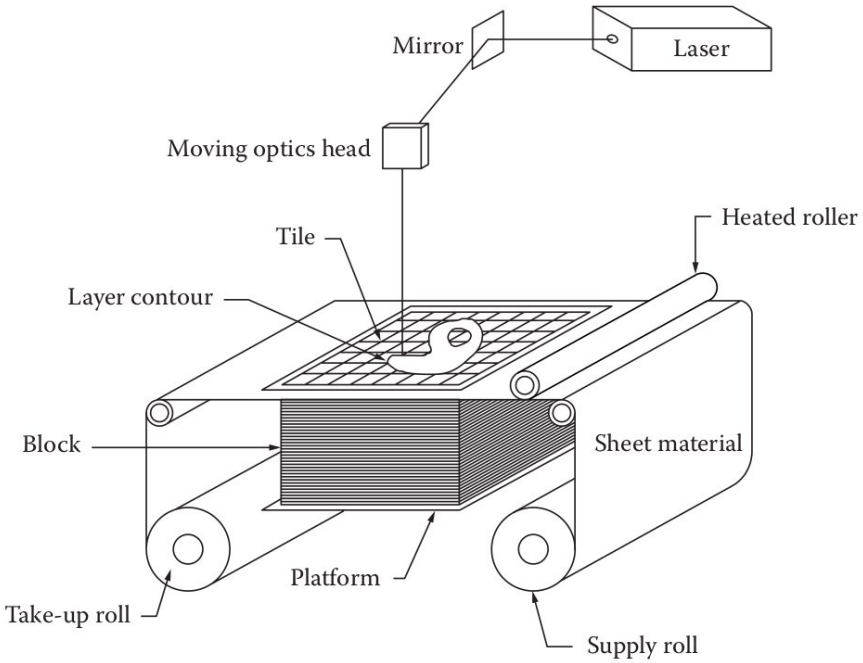

Figure 2.19: Laminar object manufacturing schematic [58].

2.3.4 Wire-Feed Metal Additive Layer Manufacturing

Technology, originating in 1925 [62] progressed only relatively recently, driven by the advances in power electronics, is reminiscent of FDM which is commonly used for manufacturing with polymers. In this method metal is extruded from a wire feeder which is then melted at selected locations, allowing to gradually form a part in layers (Figure 2.20). The melting process requires a heat source which is obtained through either a welding arc, laser or electron beam [63]. The technology has also been developed for a variety of materials, such as steel [64], nickel [65] and titanium [66, 67]. Compared to powder based metal ALM it has higher production speeds and minimises the material wastage. However, constant high heat input into the part also needs to taken into account which otherwise can lead to significant distortion and residual stresses in the structure [68, 69].

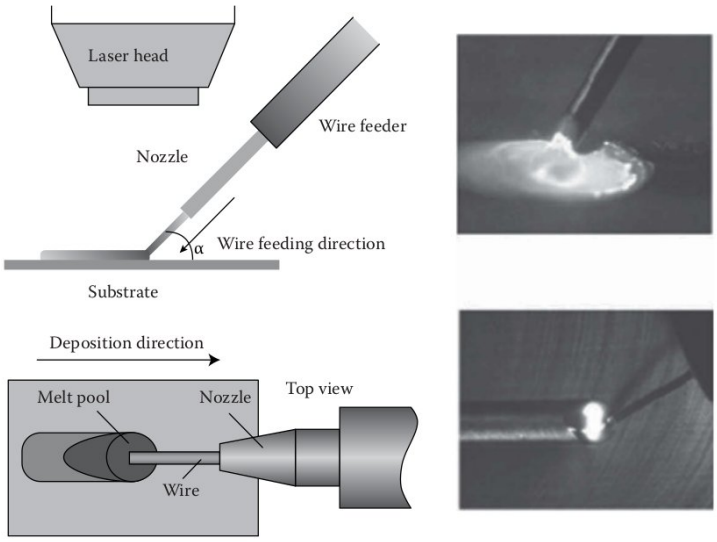

Figure 2.20: Wire feed ALM process schematic utilising a laser for constructing part layers [68, 69].

2.3.5 Metal Powder Additive Layer Manufacturing

A powder based metal ALM system consists of a laser, powder dispensing apparatus and a computer control system. Additions such as inert gas environment or powder bed preheating are also possible if required [70, 71, 72]. The process (Figure 2.21) works by firstly depositing material on a base using a blade, knife or a roller which is then selectively fused by a laser. Loose powder remains in a container serving as a support for the subsequent layers of a part until it is manufactured completely [73] and can be reused for future builds.

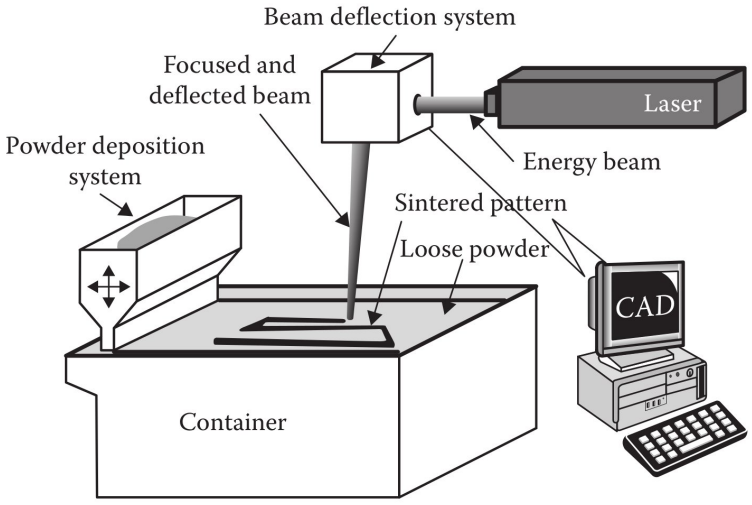

Figure 2.21: Powder based ALM process schematic [73, 74].

These machines have many variables, some of which include: powder size & density, pulse frequency, laser power, scan size & speed, scan spacing, making the manufacturing process highly customisable [75]. Selective Laser Sintering (SLS) is one of the powder-based ALM techniques in which a part is manufactured by either liquid-phase or solid-phase sintering [76].

Solid-phase sintering powders contain both, metal and binder material (polymer). Only the binder material surrounding the metal is fused during the laser irradiation stage which then solidifies during cool down [77]. This results in a highly porous part which requires further thermal treatment to increase sintering level [78] and to remove binder material [74]. The process is called debinding and works by increasing the density of a part by either filling the gaps with metallic or polymeric material [79, 80] or by hot isostatic pressing [81].

Liquid state sintering is a process where both single and two component powders are used. In the of case a single component powder a laser melts only exterior of the granules to make them adhere [76, 82]. Liquid sintering of two component powders is completed by fully melting the material with a lower melting point and uses it as a binder, shown schematically in Figure 2.22. It is a particularly useful for producing ceramic-metal hybrids called cermets [74]. However, both processes still require post-treatment if less porous parts are desired [78].

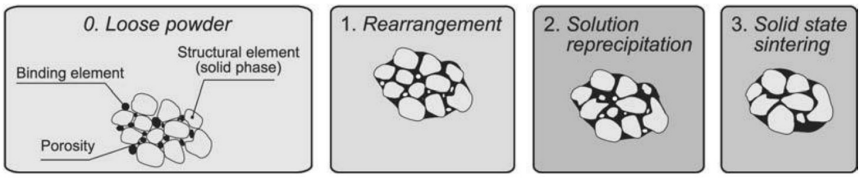

Figure 2.22: Stages of two material liquid phase sintering [74].

Selective Laser Melting (SLM) is a similar process to SLS in which the powder granules are fully melted to form a part [78, 83]. Compared to the other powder techniques it results in almost 100% dense part and avoids expensive and long post-treatment [78]. High residual stresses caused during powder melting is the main issue with the process. They can be detrimental to the structural integrity of a part and need to be reduced by either heating a manufactured part or a base plate of a SLM apparatus [84, 85]. However, SLM parts can be manufactured using relevant to HE materials such as: aluminium [86], titanium [87], stainless steel [88] and nickel alloys [89]. In addition, thin material layers (50 μm [90]) can be produced enabling manufacture at

the relevant lenghtscales to the HE. This allowed clearly identifying the method as the most suitable for novel heat transfer solutions.

2.4 Traditional Methods to Predict HE Performance

2.4.1 HE Modelling Methods

Traditional approaches for designing HE are presented with particular focus on compact HE which are the most common within aerospace. For a long time development of HE was limited to experimental studies and analytical calculations, including compact HE which are in the interest of this project. Kays and London [6] were pioneers in the field and summarised both experimental and analytical compact HE design methodology in the 1960's with more recent summaries of the subject available in [5, 7, 24]. However, accuracy of the analytical methodology is limited and it can only be used with confidence for simple geometries. It can also be beneficial as an initial guess of HE performance which then needs to be confirmed by experimental work. Modelling HE as a part of heat transfer network is another approach undertaken during the design of complex systems where a system view is taken instead. Such modelling is based around exergy (available work) and allows analysing complicated systems such as aircraft TMS [10, 25].

2.4.1.1 HE Design Process

Typical HE design objective is minimal pressure drop achieved with maximum heat transfer. HE design flow chart (Figure 2.23) illustrates complexity of the process and was constructed from the review of [5, 6, 7]. First point in the design cycle is to obtain accurate initial data from heat transfer network analysis. This enables an engineer to select a HE type which has a big impact on the size and price of the final HE unit and is often selected based on experience. Once the HE type is chosen, software employing analytical methodology selects appropriate secondary heat transfer surfaces (corrugation) and produces an initial guess of the HE core. It is then equipped with the connecting features for each flow (headers, bypass valves) and experimentally tested to check whether the required performance is achieved. In case it is not - the design cycle is then reiterated to select a more capable HE for a specific application.

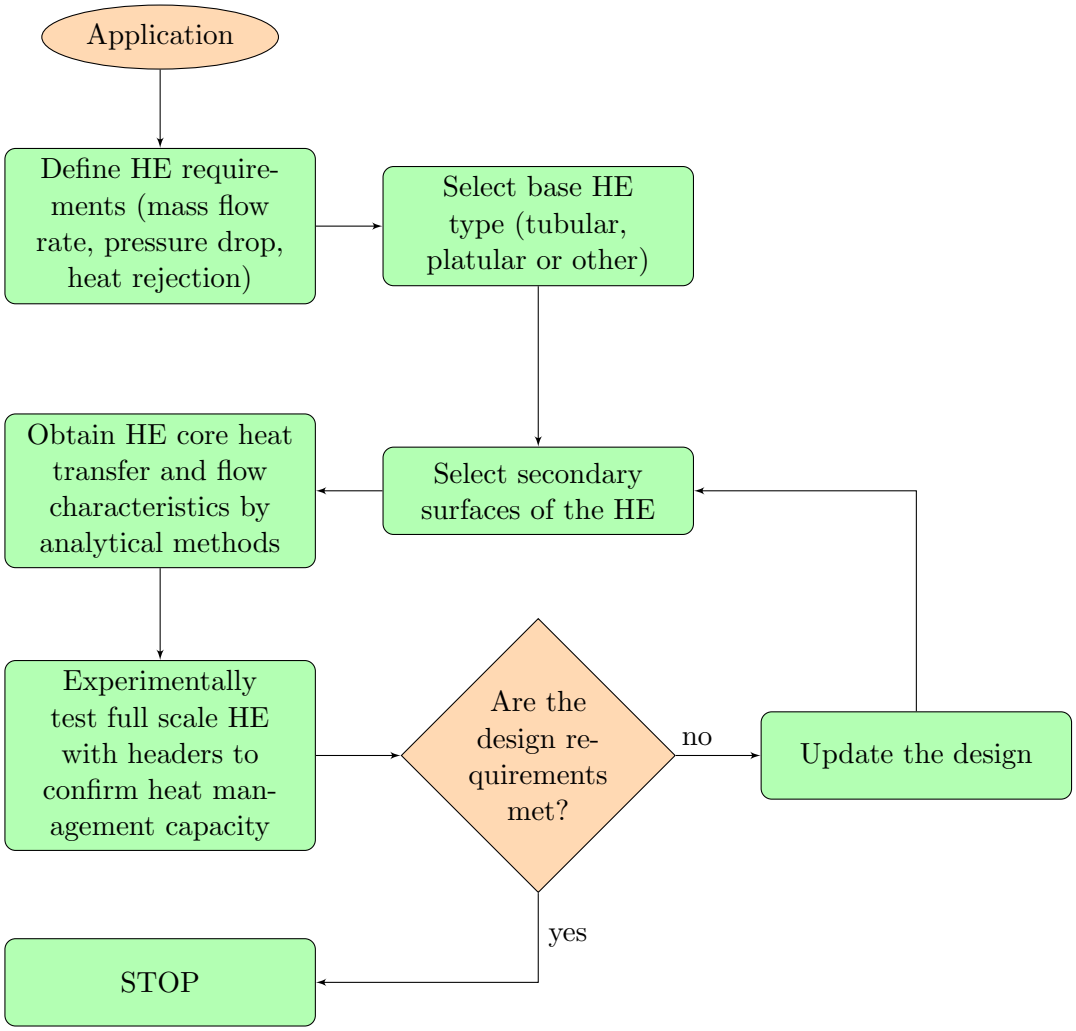

Figure 2.23: Typical HE design workflow.

2.4.2 Experimental Techniques

2.4.2.1 HE Corrugation

An important step of HE design is selecting the HE corrugation which enhances heat transfer. However, whilst for simple geometries analytical solutions can be found [91, 92], the majority of geometries require either numerical or experimental testing to evaluate their performance. Schematic of an experimental setup for compact HE corrugations is provided in Figure 2.24. It is based on research in 1950's [93, 94], summarised by Kays and London [6]. In this setup the standard procedure was to use rectangular HE test cores in cross-flow ($\approx 210 \times 250\ mm$). The test HE cores contained HE corrugation of interest on the primary flow side (air) and performance of it was measured against a range of flow rates. Uniform flow inlet to the test HE core provided using the rectangular ducting. The air flow rate was measured using orifice plates according to the ASME standards prior to the inlet to HE core with the

temperature measured with thermocouples at the same location. In order to provide accurate downstream air temperature the measurements were taken at 27 locations throughout the cross-sectional area of the duct.

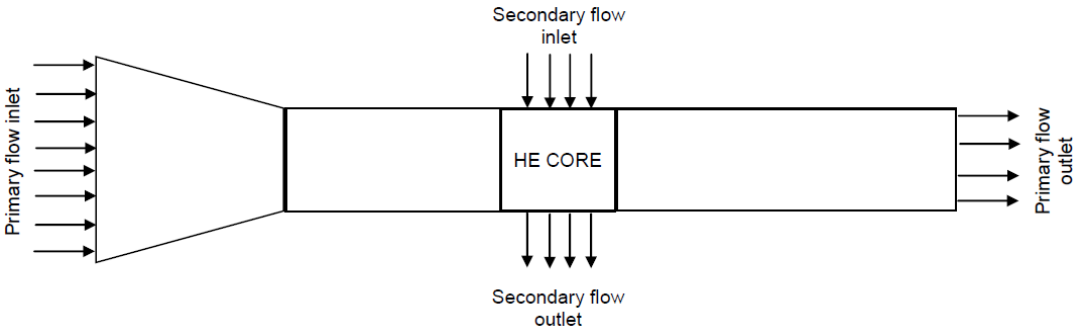

Figure 2.24: Schematic experimental test setup for evaluating HE corrugation.

Slightly superheated steam was supplied to provide with the constant heat transfer condition for the secondary flow. Both, steam and the condensate were measured separately allowing to calculate heat balance of the test:

$$Q_{balance} = \frac{Q_{cold}}{Q_{hot}}. \tag{2.4}$$

A ratio of 1 would mean an ideal heat transfer scenario, however, in practice some heat loss to the environment is inevitable, such as ±3% imbalance reported by Kays and London [6]. Setup given in [6] also provides with ±5% accuracy for other derived non-dimensional flow and heat factors which can then be used in the analytical heat transfer theory (Section 2.4.3) for estimating size of HE.

2.4.2.2 HE Unit Experiments

HE unit experimental analysis is the next step and whilst the experimental setup remains similar to Figure 2.24, the research found concentrated on studying the HE header effects (Figure 2.25a). They are often designed inefficient, due to the limited HE installation volume and manufacturing constrains. This leads to high levels of maldistribution produced by such designs resulting in under-utilised HE core regions. A common solution found was introduction of a baffle into an inlet HE header [27, 29, 95, 96, 97] (Figure 2.25b). Such baffle has smaller diameter holes where most of the flow is suspected in a non-baffled design - effectively blocking the flow through that area. Larger diameter holes are drilled in the corners of a header, distributing the flow more evenly. It is an acceptable solution, however, it also creates an additional

blockage inside HE as it requires higher pumping power which can be critical for a certain application.

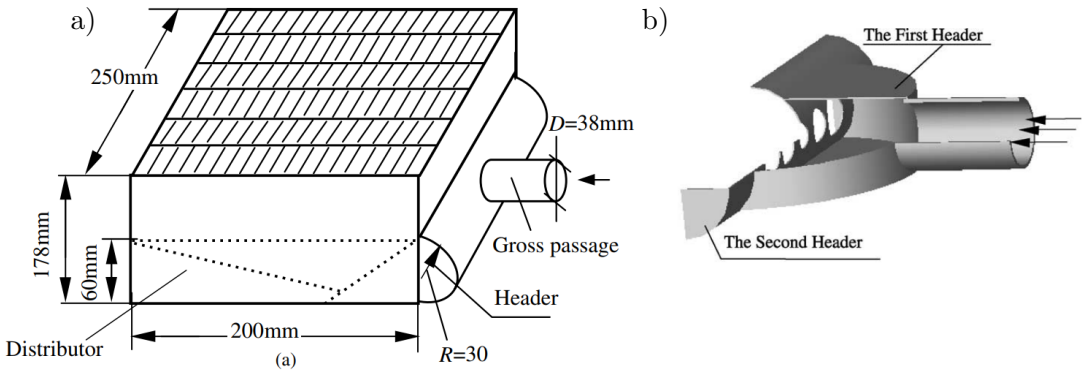

Figure 2.25: a) Plate-fin HE core example with the header [95] and b) Two stage baffled HE header to reduce maldistribution by [95].

2.4.2.3 Effects of HE Fouling

HE fouling is a critical parameter defining longevity of a certain HE and is another important area of experimental testing and should be considered during the HE design. Main negative impacts of fouling are: reduced heat transfer and increased pumping/fan power requirement whilst for stationary applications, such as air conditioning, dust accumulation acts as a bacterial spreading source [98, 99, 100]. Majority of the studies concentrated on the air-side (environment) HE fouling where it is difficult to control the quality of the fluid stream. Studies by Ahn et al. [98], Breuker and Braun [101] and Krafthefer and Bonne [102] reported fouling influence after a substantial HE performance in the field. In case of Ahn et al. [98], evaporators in operation were evaluated for 7 years and up to 44% increase in flow resistance with 10-15% reduction in cooling capacity were found. Krafter and Bonne [102] investigated fouling of a ground source heat pump coils in operation and found that over the period of 5-7 years the requirement for pumping power was doubled together with 18% efficiency reduction of the heat pump. Breuker and Baum [101] investigated various rooftop HE and found up to 56% blockage of the HE core inlet area which resulted in 11% decrease in cooling capacity and 18% decrease in the overall efficiency.

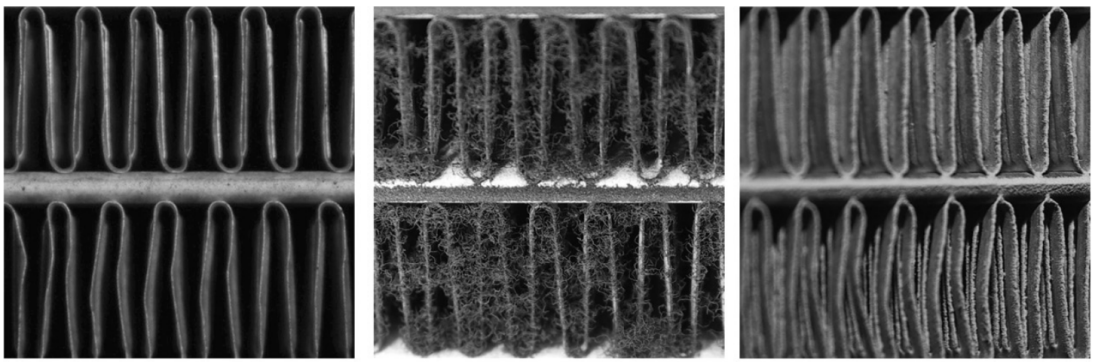

Clean HE | HE Fouled with 135g ASHRAE Test Dust | HE Fouled with 500g Arizona Road Test Dust

Figure 2.26: Frontal view of plate-fin HE before and after fouling experiments [103].

A range of studies were also conducted under laboratory conditions (Figure 2.26). Typical materials in testing for use were dust such as ASHRAE standard dust [103, 104] or saw dust [105]. Studies by Bell and Groll [103], Lakinnen et al. [104] and Pak et al. [106] found up to 200% increase in flow resistance with detrimental effect to heat transfer between 8-18% based on the HE configuration. Bell and Groll [103] also compared two types of standard dust (Figure 2.26). This study showed that whilst ASHRAE dust fouling resulted in higher pressure drop the heat transfer reduction was found larger with the Arizona road dust highlighting application related longevity specifics. In addition, the Bell and Groll [103] study concluded that the passages with smaller channel width than 2 *mm* were prone to blocking, indicating size limits of the HE fins exposed to the environment.

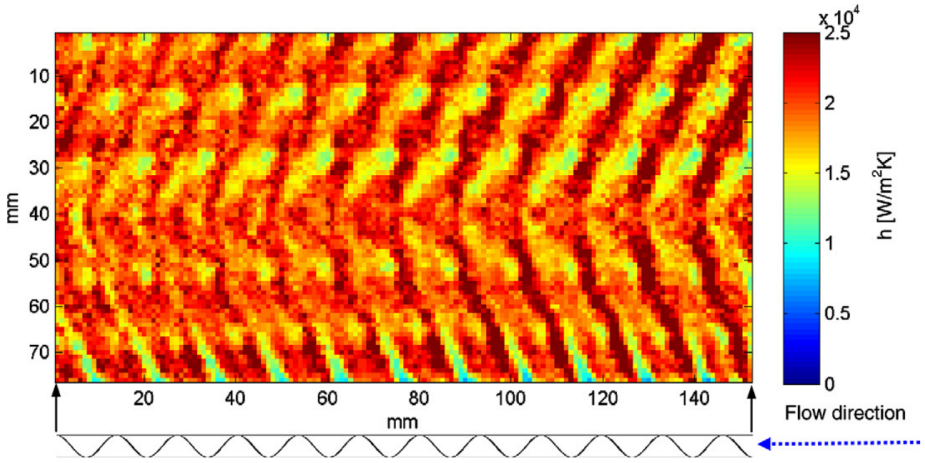

Figure 2.27: Heat transfer coefficient plot across the corrugated plate acquired using thermal imaging [107].

2.4.2.4 Advances in Experimental Analysis

Increased use of Particle Image Velocimetry (PIV) and thermal imaging cameras was observed in recent journal articles with the results of both often used in conjunction

with CFD simulations. Thermal imaging was found to have been used in a range of applications, including early 2000's studies of standard HE such as tube-fin [108, 109]. More recently it has been applied to compact surfaces such as heat pipe cooling of micro electronics [110] or HE with aluminium porous foam corrugation [42]. Freund and Kabelac [107] published a comprehensive article on thermal imaging (Figure 2.27) where various compact platular HE were tested and compared to CFD analysis, stating the importance of CFD for better understanding of heat transfer distribution inside HE.

PIV approach uses particles injected into the flow which are tagged and photographed at close time intervals. Movement of them allows determining local velocity vectors. The process is repeated a number of times until a clear time-average can be obtained [35, 111] (Figure 2.28). The technique has also been applied to a range of studies including the analysis of the before shown (Figure 2.25) HE header [96] to inform about the stagnant flow regions (Figure 2.28a). It was also applied in tube-fin HE studies (Figure 2.28b) [112, 113] and in a recent study of microchannels, often encountered in the plate-fin HE (Figure 2.28c) [114].

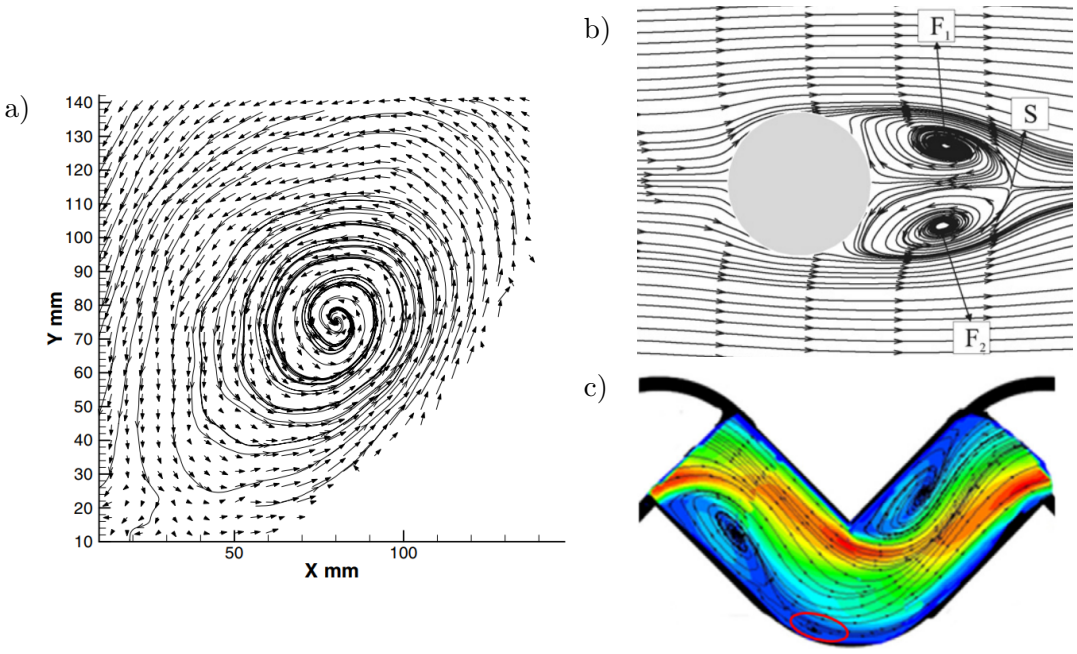

Figure 2.28: PIV examples: of a) Maldistribution in the HE header [96], b) Flow past the tube-fin corrugation [112] and c) Flow visualisation in a microchannel [114].

2.4.3 Analytical HE Core Modelling

Analytical predictions historically have been the only tool available for estimating the HE size. Theory for compact HE was firstly summarised by Kays and London [6] and later updated in books such as Rohsenow et al. [5] and Shah and Sekulic [24]. A

number of models were proposed ($\epsilon - NTU$, $P - NTU$, $LMTD$) [5, 6, 24] to predict pressure drop and heat transfer of the HE core, main quantities of interest. They all require analytical/empirical relations and here the $\epsilon - NTU$ methodology from Kays and London [6] is presented.

Firstly, pressure drop modelling across the HE core is presented. In most of the traditional HE cores (headers excluded) flow resistance is mostly notable for gases where due to the lower density flow resistance is often increased whilst for liquids it becomes more notable at higher flow rates. There are four main variables to consider in most of the HE applications: flow entrance, core friction, flow acceleration and flow exit. Taking into account the main effects a relationship for pressure drop can be derived:

$$\frac{\Delta P}{P_1} = \frac{G^2}{2}\frac{v_1}{P_1}\left[\underbrace{\left(K_c + 1 - \sigma^2\right)}_{\text{entrance effect}} + \underbrace{2\left(\frac{v_2}{v_1} - 1\right)}_{\text{flow acceleration}} + \underbrace{f_c\frac{A}{A_c}\frac{\nu_m}{v_1}}_{\text{core friction}} - \underbrace{\left(1 - \sigma^2 - K_e\right)\frac{v_2}{v_1}}_{\text{exit effect}}\right] \quad (2.5)$$

where the quantities detoned with 1 and 2 relate to flow conditions at the inlet and outlet of the HE respectively and the constants are:

ΔP - core pressure drop	P - fluid pressure
G - mass flow velocity ($\dot{m}/A_c$)	K_c - entrance loss coefficient
σ - flow area to face area ratio	v - specific volume V/m
f_c - core friction factor	A - primary fluid side surface area
A_c - minimum cross-sectional flow area	K_e - exit loss coefficient
ν_i - specific volume at inlet	$\dot{m}$ - mass flow
ν_e - specific volume at outlet	ν_m - mean specific volume ($\frac{1}{2}(\nu_e - \nu_i)$)

The relation can be simplified based on the application specifics. HE core, inlet and outlet factors for different HE are either analytical or empirical and can be found in Kays and London [6].

Heat transfer estimation is based on three main ideas: similarity of heat transfer to electrical resistance, heat transfer effectiveness and the concept of Number of Transfer Units (NTU). Firstly, the heat transfer potential is formulated:

$$\frac{dQ}{dA} = U(t_h - t_c) \quad (2.6)$$

where dQ/dA is heat transfer per unit area $[W/m^2]$, introducing overall heat transfer coefficient U which has the units of $[W/(m^2K)]$ whilst subscripts h and c refer to the hot and cold side components. In order to estimate the overall heat transfer coefficient a number of factors need to be considered such as hot and cold HE side film convection components, wall conduction component. This allows Equations 2.7 & 2.8

to be developed:

$$\frac{1}{U_h} = \frac{1}{\eta_{o,h} h_h} + \frac{a}{(A_w/A_h)k} + \frac{1}{(A_c/A_h)\eta_{o,c} h_c} \tag{2.7}$$

and

$$\frac{1}{U_c} = \frac{1}{\eta_{o,c} h_c} + \frac{a}{(A_w/A_c)k} + \frac{1}{(A_c/A_h)\eta_{o,h} h_h} \tag{2.8}$$

where, η_o - efficiency of the fins, a - plate thickness, A_h - heat transfer area and A_w - average wall area $A_w = (A_c + A_h)/2$. The conservation of energy also means that $1/U_h = 1/U_c$. Convective film coefficients h for the case of plate-fin HE can be estimated using:

$$h = N_{st} C_p G \tag{2.9}$$

where the C_p - specific heat, and N_{st} - Stanton number characteristics taken from experimental/analytical correlations defined by:

$$N_{st} = \frac{Nu}{RePr} = \frac{h}{C_p G} \tag{2.10}$$

It is important to note that as in most of the cases the extended surfaces (fins) are used, the fin effectiveness (η_o) decreases and is proportional to:

$$\eta_o = 1 - \frac{A_f}{A}(1 - \eta_f) \tag{2.11}$$

where the fin effectiveness for thin surfaces (such as plate-fin HE) can be estimated by:

$$n_f = \frac{\tanh(ml)}{ml} \tag{2.12}$$

where

$$m = \sqrt{\frac{2h}{k\delta}} \tag{2.13}$$

where k - conduction coefficient of the solid, δ - fin thickness, l - fin length. To complete the heat transfer estimation, the most useful non-dimensional groupings are given, such as heat transfer effectiveness:

$$\epsilon = \frac{Q}{Q_{max}} = \frac{C_h(T_{h,in}T_{h,out})}{C_{min}(T_{h,in} - T_{c,in})} = \frac{C_c(T_{h,in}T_{h,out})}{C_{min}(T_{h,in} - T_{c,in})} \tag{2.14}$$

with

$$C_h = \dot{m}_h C_{ph} \tag{2.15}$$

$$C_c = \dot{m}_c C_{pc} \tag{2.16}$$

$$C_{min} = min|C_h, C_c|. \tag{2.17}$$

It can also be expressed as $Q = \epsilon Q_{max}$ and it measures the heat transfer achieved to the maximum heat transfer possible and varies depending on the type of HE and the heat capacity ratio $C_r = C_{min}/C_{max}$. The model is also incorporated into CFD codes such as Fluent [115]. The next useful quantities are the Number of Transfer Units (NTU):

$$NTU = \frac{AU}{C_{min}} \tag{2.18}$$

where A - heat transfer area and U - overall heat transfer coefficient. An the capacity ratio between the two streams

$$\frac{C_{min}}{C_{max}}. \tag{2.19}$$

Employing the above relationships a HE can be estimated for a specific application with the examples given in Kays and London [6]. It should be noted, that for many standard cases the effectiveness can be also expressed as a function of multiple parameters:

$$\epsilon = \Phi\left(NTU, \frac{C_{min}}{C_{max}}, \text{flow orientation}\right) \tag{2.20}$$

with the examples of developed analytical equations found in [6]. Overall, the $\epsilon - NTU$ method is a good initial indicator of the HE size and performance requirement during the design cycle. However, it requires numerical modelling (such as CFD) or experimental testing and optimisation parameters, so that a design could be finessed.

2.4.4 HE Network Modelling

Heat transfer network analysis is a particular branch of modelling where performance of an overall system such as aircraft ECS is considered. Although it is beyond the scope of the project it provides the user with initial conditions for HE design and is worth to be noted. It also helps to better understand complexity of the systems as they contribute considerably to the overall fuel consumption of an aircraft [10]. Analysis at the system level can be accomplished by Exergy Analysis (EA), Entropy Generation Minimisation (EGM) or Thermoeconomics (TE) [116, 117, 118, 119, 120] methods which can also be used in tandem to produce the best design. The EA method analyses mechanisms and system components responsible for the energy losses and the size of them. EGM can then be utilised to tune the system based on the global constrains whilst TE helps minimising building and operating costs associated with the system [10]. A good TE optimisation example was undertaken by Leo and Perez-Grande [25] where component cost per unit of exergy approach was undertaken allowing optimising the cabin conditioning for a range of aircraft operational regimes. Another optimisation study was undertaken by employing exergy methods by Vargas

and Bejan [10] in order to optimise performance of the system through optimising a particular HE which was a part of the ECS system.

2.5 Summary of the Chapter

This chapter provided a comprehensive review of current HE, novel HE manufacturing methods and explained traditional analytical and experimental HE modelling approaches. Traditional HE were presented highlighting limitations of each HE type and to show a variety of secondary heat transfer surfaces used to disrupt the flow in order to provide ideas for novel heat transfer solutions. Various ALM methods were summarised and SLM was identified as the most suitable technique for novel HE. Summary of the analytical $NTU - \epsilon$ HE design model was provided. The model allows a quick initial estimate of the HE size and performance for a specific application. However, it also relies on empirical/analytical data which can cause inaccuracies requiring the design to be validated and finessed by experimental work or numerical analysis.

Chapter 3

Heat Exchanger Modelling with Computational Fluid Dynamics

Contents

3.1 Introduction

More recently numerical approaches were employed to model flow and heat transfer inside the HE. They work by approximating solutions of partial differential equations

governing flow and heat transfer onto a set of discrete solution points, specified by a computational mesh. The numerical analysis allows evaluating complex geometries and minimises the need for expensive physical testing. Majority of numerical simulations are undertaken utilising one of the three methods: finite difference, finite volume and finite element which differ approach for approximating equations of interest. For industrial computational fluid dynamics problems, finite volume method is most commonly used (referred as Computational Fluid Dynamics, CFD). It was also used throughout the project due its efficiency and adaptability to complex geometries [121]. Simulations in this project are undertaken using two CFD software packages: commercial ANSYS Fluent and a widely used open-source alternative OpenFOAM. In this chapter an overview of the finite volume and solution methodology is provided with the relevant governing equations for the project. The full numerical solution procedure can be found in the technical manuals of ANSYS [115], source code and documentation of OpenFOAM [122] or in relevant fluid dynamics books such as Ferziger and Peric [123].

3.2 Governing Equations

Three governing equations are required for the HE analysis: continuity of mass, flow momentum (Navier-Stokes) and energy equations. They are also further simplified using incompressible flow assumption as the flows are below the Mach number $M < 0.3$ threshold [124]. Derivation of the equations provided can be found in many fluid dynamics books such as Chandrasekhar [125] and is not undertaken here. Using index notation and for a 3D Cartesian coordinate system, mass continuity for the incompressible flows reduces to:

$$\frac{\partial U_i}{\partial x_i} = 0. \tag{3.1}$$

For the incompressible fluid the momentum conservation equation is:

$$\rho\left(\frac{\partial U_i}{\partial t} + U_j\frac{\partial U_i}{\partial x_j}\right) = -\frac{\partial p}{\partial x_i} + \mu\left(\frac{\partial^2 U_i}{\partial x_j \partial x_j}\right) + \rho F_i. \tag{3.2}$$

The energy conservation, expressed in terms of T with the same assumptions becomes:

$$\rho\frac{\partial}{\partial t}(c_p T) + \rho u_j\frac{\partial}{\partial x_j}(c_p T) = \frac{\partial}{\partial x_j}(k\frac{\partial T}{\partial x_j}). \tag{3.3}$$

3.3 Turbulence Modelling

The equations above are capable of resolving numerous complex fluid dynamics problems numerically. However, the problem arises under turbulence where flow fluctua-

tions of various lengthscales appear. Equations in Section 3.2 are capable of resolving the fluid flow at all the different lenghtscales (known as Direct Numerical Simulation (DNS)) but this approach is computationally expensive. It is caused by the need of extremely fine computational grid capable of capturing flow fluctuations of all sizes. Thus, various turbulence modelling approaches were proposed to eliminate the need for resolving all the flow lengthscales such as Large Eddy Simulation (LES) or Reynolds Averaged Navier Stokes (RANS). Below, a widely used RANS approach for the fluid flow, used throughout the project, is explained. This method has been used for both steady-state [28] and transient problems [126] due to widespread use in industry and the significant computational cost saving compared to LES and DNS.

3.3.1 Reynolds-Averaged Navier-Stokes (RANS) Equations

The fundamental concept of RANS modelling is splitting of the flow components into the mean and fluctuating parts, which in terms of velocity is:

$$U_i = \bar{U}_i + U_i^{'} \tag{3.4}$$

where $\bar{U}_i$ denotes the mean velocity over a period of time t:

$$\bar{U}_i = \frac{1}{t}\int_t U dt \tag{3.5}$$

and U_i' - the fluctuating component of it. The timescale here is selected such that $\overline{U}_i \gg U_i^{'}$, thus that $U_i^{'} = 0$. Substituting the Equation 3.4 into the Equations 3.1 & 3.2 and assuming constant density and viscosity gives:

$$\frac{\partial}{\partial x_i}(\bar{U}_i + U_i^{'}) = 0 \tag{3.6}$$

$$\rho\left(\frac{\partial}{\partial t}(\bar{U}_i + U_i^{'}) + (\bar{U}_j + U_j^{'})\frac{\partial(\bar{U}_i + U_i^{'})}{\partial x_j}\right) = -\frac{\partial(\bar{p} + p')}{\partial x_i} + \mu\left(\frac{\partial^2(\bar{U}_i + U_i^{'})}{\partial x_j \partial x_j}\right) + \rho(\bar{F}_i + F_i^{'}) \tag{3.7}$$

Noticing that:

$$\frac{\partial\left((\bar{U}_i + U_i^{'})(\bar{U}_j + U_j^{'})\right)}{\partial x_j} = (\bar{U}_j + U_j^{'})\frac{\partial(\bar{U}_j + U_j^{'})}{\partial x_j} \tag{3.8}$$

and using the following averaging identities [127]:

$$\bar{\bar{A}} = \bar{A} \qquad \overline{A + B} = \bar{A} + \bar{B} \qquad \overline{AB} = \bar{A}\bar{B} \tag{3.9}$$

allows to establish the following form of continuity and momentum:

$$\frac{\partial \bar{U}_i}{\partial x_i} = 0 \tag{3.10}$$

$$\rho\left(\frac{\partial \bar{U}_i}{\partial t} + \frac{\partial \bar{U}_i \bar{U}_j}{\partial x_j}\right) = -\frac{\partial \bar{p}}{\partial x_i} + \mu\left(\frac{\partial^2 \bar{U}_i}{\partial x_j \partial x_j}\right) + +\rho\frac{\partial \overline{U_i' U_j'}}{\partial x_j}\rho + \bar{F}_i. \tag{3.11}$$

The important result from the Equation 3.11 is the $-\rho\overline{U_i' U_j'}$ term commonly know as the Reynolds stress term. It creates a closure problem which different RANS models (two of them provided below) attempt to resolve. The energy equation then becomes:

$$\rho\frac{\partial}{\partial t}\left(c_p \bar{T}\right) + \rho\bar{u_j}\frac{\partial}{\partial x_j}(c_p \bar{T}) = \frac{\partial}{\partial x_j}(k\frac{\partial \bar{T}}{\partial x_j}) \tag{3.12}$$

3.3.2 Bousinnesq Hypothesis

Bousinessq [128] was among the first to tackle the problem of the Reynolds stresses $-\rho\overline{U_i' U_j'}$ by introducing the following relation:

$$-\rho\overline{U_i' U_j'} = 2\mu_t S_{ij} - \frac{2}{3}k\rho\delta_{ij} \tag{3.13}$$

where S_{ij}:

$$S_{ij} = \frac{1}{2}\left(\frac{\partial \bar{U}_i}{x_j} + \frac{\partial \bar{U}_j}{x_i}\right) \tag{3.14}$$

and k is the turbulent kinetic energy:

$$k = \frac{1}{2}\left(\overline{U_i' U_i'}\right) = \frac{1}{2}\left(\bar{U}_x'^2 + \bar{U}_y'^2 + \bar{U}_z'^2\right) \tag{3.15}$$

The Equation 3.13 can be inserted into the Equation 3.11 eliminating the Reynolds stresses. This, however, creates two additional variables, μ_t and k. For simplistic problems, these can be estimated using Prandtl mixing theory [129] closing the system of equations. Alternatively, a number of models introducing additional equations for both terms have been proposed and two of the most notable ones ($k-\epsilon$ and $k-\omega$ SST) were used throughout the project and are presented in Sections 3.3.3 & 3.3.4.

3.3.3 $k-\epsilon$ Model

The first approximation is the popular $k-\epsilon$ turbulence model. It was summarised by Launder and Spalding [130] and uses two additional partial differential equations for the turbulent kinetic energy k:

$$\frac{\partial k}{\partial t} + \frac{\partial k\bar{U}_j}{\partial x_J} = \frac{1}{\rho}\frac{\partial}{\partial x_j}\left(\frac{\mu_t}{\sigma_k}\frac{\partial k}{\partial x_j}\right) + \frac{\mu_t}{\rho}\left(\frac{\partial \bar{U}_i}{\partial x_j} + \frac{\partial \bar{U}_j}{\partial x_i}\right)\frac{\partial \bar{U}_i}{\partial x_j} - \epsilon \tag{3.16}$$

and the turbulence dissipation ϵ:

$$\frac{\partial \epsilon}{\partial t} + \frac{\partial \epsilon \bar{U}_j}{\partial x_J} = \frac{1}{\rho}\frac{\partial}{\partial x_j}\left(\frac{\mu_t}{\sigma_\epsilon}\frac{\partial \epsilon}{\partial x_j}\right) + \frac{C_1 \mu_t}{\rho}\frac{\epsilon}{k}\left(\frac{\partial \bar{U}_i}{\partial x_j} + \frac{\partial \bar{U}_j}{\partial x_i}\right)\frac{\partial \bar{U}_i}{\partial x_j} - C_2\frac{\epsilon^2}{k} \tag{3.17}$$

The equations also allow the calculation of the turbulent viscosity μ_t in terms of the dissipation rate and the kinetic energy as [130]:

$$\mu_t = C_\mu \rho k^2/\epsilon \tag{3.18}$$

It should be noted that C_μ, C_1, C_2, σ_ϵ, σ_k are the model constants which can be found in [130] or the documentation of the CFD package of interest. The model described above is a commonly used high Reynolds number model with the original low-reynolds number model also available in [130]. However, whilst the $k-\epsilon$ models are robust general purpose turbulence models they struggle to predict flow for certain applications, such as wall bounded flows [127]. This led to the development of modified $k-\epsilon$ versions and the $k-\omega$ based models.

3.3.4 $k-\omega$ SST Model

This approximation, originally proposed by Menter [131] combines two models: the original $k-\epsilon$ model described afore and the $k-\omega$ introduced by Wilcox [132] where ω is specific turbulence dissipation $(1/\epsilon)$. Proposed model by Wilcox [132] predicts the near-wall flow accurately, but is sensitive away from the domain boundary. Thus, it was proposed to combine the two models using blending functions. Equations 3.19 & 3.20 show the updated $k-\omega$ SST model [133] implemented in OpenFOAM:

$$\frac{\partial \rho k}{\partial t} + \frac{\partial \rho \bar{U}_i k}{\partial x_i} = \widetilde{P}_k - \beta^* \rho k \omega + \frac{\partial}{\partial x_i}\left((\mu + \sigma_k \mu_t)\frac{\partial k}{\partial x_i}\right) \tag{3.19}$$

$$\frac{\partial \rho \omega}{\partial t} + \frac{\partial \rho \bar{U} \omega}{\partial x_i} = \alpha \rho S^2 - \beta \rho \omega^2 + \frac{\partial}{\partial x_i}\left((\mu + \sigma_\omega \mu_t)\frac{\partial \omega}{\partial x_i}\right) + 2(1-F_1)\rho \sigma_{w2}\frac{1}{\omega}\frac{\partial k}{\partial x_i}\frac{\partial \omega}{\partial x_i} \tag{3.20}$$

whilst the turbulent viscosity is computed by:

$$\nu_t = \frac{\alpha_1 k}{max(\alpha_1 \omega, SF_2)} \tag{3.21}$$

Here F_1 and F_2 are the blending functions whereas $\widetilde{P}_k$, β^*, S, β, σ_w, σ_{w2} are either constants or additional conditions of the model and full detail can be found in [133]. Two blending functions determine whether the model is switched to either $k-\epsilon$ ($F_1 = F_2 = 0$) away from the boundary or to $k-\omega$ SST ($F_1 = F_2 = 1$). Overall, this model was considered to be more versatile than most of the other RANS models [134].

3.4 Finite Volume Method

Finite Volume Method (FVM) is the numerical method of choice for the majority of industrial CFD applications. It arises from FVM versatility as it can be applied to any type of grid, making it suitable for a range of complex geometries [123]. The method applies a set of partial differential equations to the computational mesh (Figure 3.1) which splits the domain to a set of control volumes.

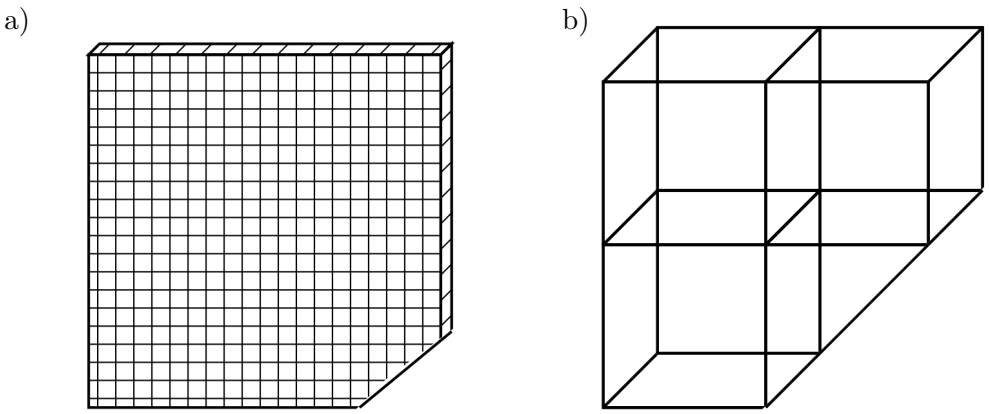

Figure 3.1: a) Computational mesh example and b) close up into the corner of the domain [127].

The equations themselves are transformed into the integral form for the solution. This is best illustrated by a generic scalar (ϕ) transport equation [127]:

$$\frac{\partial \rho\phi}{\partial t} + \frac{\partial \rho U_j \phi}{\partial x_j} - \frac{\partial}{\partial x_j}\left(\Gamma\left(\frac{\partial \phi}{\partial x_j}\right)\right) = 0 \tag{3.22}$$

with the diffusivity Γ. It can be converted into an integral form using the divergence theorem:

$$\frac{d}{dt}\int_V \rho\phi dV + \int_S \rho U_j \phi dn_j - \int_S \Gamma \frac{\partial \phi}{\partial x_j} dn_j = 0 \tag{3.23}$$

where n_j - outward surface normal integral, V - control volume and S - face area. The FVM works by applying the equations to each control volume (Figure 3.2). The cell centroid has a computational node where the variables are calculated and stored whilst interpolation is used for obtaining values at the control surface centre.

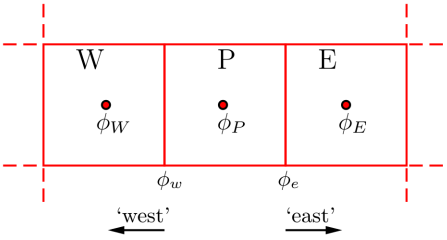

Figure 3.2: Several one-dimensional control volumes of the FVM mesh [127].

3.4.1 Discretisation Schemes

Equations such as Equation 3.23 need to be approximated. This is accomplished by selecting a suitable discretisation scheme for a certain application. Here one-dimensional forms of the discretisation schemes are presented for simplicity.

3.4.1.1 Transient term

The transient term in the simulations wherever it was required during the project was discretised using the implicit Euler formulation of first order accuracy (Equation 3.24). This was completed to save the computational power as the transient simulations required a small simulation timestep and is [123]:

$$\frac{d}{dt}\int_V \rho\phi dV = \rho V \frac{\phi^{n+1} - \phi^n}{\Delta t} \tag{3.24}$$

3.4.1.2 Advection Term

The advection term was dealt with in two accuracy levels during the CFD simulations in this thesis. The term itself, assuming the flow from west to east, can be discretised to:

$$\int_S \rho U_j \phi dn_j = \rho U_e \phi_e \Delta n_e \tag{3.25}$$

where Δn is the outward surface vector and subscript e denotes values of the components at the face location. The simplest way to approximate ϕ_e is to use the *upwind interpolation*. This, depending on the flow direction (Figure 3.2), selects the upstream value which for the flow west to east is [123]:

$$\phi_e = \phi_P \tag{3.26}$$

and for the flow east to west is:

$$\phi_e = \phi_E \tag{3.27}$$

The *upwind interpolation* scheme is a robust and stable discretisation approach, however, it is overly diffusive for some of the momentum equation terms requiring second order accuracy discretisation, such as *linear interpolation* [123]. At the point e this becomes (Figure 3.2):

$$\phi_e = \phi_E \lambda_e + \phi_P (1 - \lambda_e) \tag{3.28}$$

where the λ_e is the interpolator:

$$\lambda_e = \frac{x_e - x_P}{x_E - x_P} \tag{3.29}$$

Linear interpolation is the simplest and is widely used second order scheme, however, there are alternatives proposed of the same accuracy. Another popular choice is the *linear upwind* scheme which is also a second order accurate and takes into account two upstream flow values. This results in better convergence of the solution compared to the less stable *linear* scheme [123].

3.4.1.3 Diffusion Term

Regarding the diffusion term the same second order accuracy *linear interpolation* can be used. It uses linear profile assumption between the nodes P and E (Figure 3.2). This allows approximating the gradient to [123]:

$$\left(\frac{\partial \phi}{\partial x}\right)_e \approx \frac{\phi_E - \phi_P}{x_E - x_P}. \tag{3.30}$$

The diffusion term then becomes:

$$\int_S \Gamma \left(\frac{\partial \phi}{\partial x_j}\right)_e dn_j = \Gamma \frac{\phi_E - \phi_P}{x_E - x_P} \Delta n_e \tag{3.31}$$

3.4.2 Importance of the Mesh Resolution

A particular focus throughout the thesis is on the overall mesh resolution as it can be one of the major sources of the numerical solution errors. During mesh generation first cell thickness from a domain wall can be estimated using flat plate boundary layer theory for y^+ [135] which is:

$$y = \frac{y^+ \mu}{\rho u_*} \tag{3.32}$$

μ - kinematic viscosity and ρ - density at a certain temperature and u_* - friction velocity:

$$u_* = \sqrt{\frac{T_w}{\rho}} \tag{3.33}$$

with T_w - wall shear stress:

$$T_w = C_f \times \frac{1}{2} \rho U^2_{freestream} \tag{3.34}$$

where $U_{freestream}$ is the input velocity for a planned numerical calculation and C_f is a skin friction coefficient, calculated ($Re < 10^9$) using:

$$C_f = (2 \log(Re) - 0.65)^{-2.3}. \tag{3.35}$$

This methodology allows to evaluate the mesh resolution with increasing flow rates, bearing in mind that, the values of the y^+ should be kept as low as possible in order to obtain good quality results.

3.5 HE Design Workflow with CFD

The CFD is becoming increasingly used in designing HE, well shown by a recent literature review completed by Bhutta et al. [26], summarising and evaluating more than 50 recent HE CFD studies. The review also allowed developing a HE CFD design flowchart (Figure 3.3) which can be inserted into the historical HE design flow provided in Chapter 2 (Figure 2.23). Similar to traditional design methods, CFD modelling cycle is also accomplished in two steps. Firstly, a small HE section is selected to obtain the detailed flow and heat transfer data. This data is then used to form a simplified HE model containing both the HE core and the HE headers. The output of the simplified model can then be utilised in analysing the HE as part of a network as described in Section 2.4.4. Overall, the CFD approach has advantages of reducing the cost of HE development and allowing to design higher efficiency units. This is because CFD reduces the need for experimental testing to only validation of the numerical analysis methodology and provides more detailed information about the heat transfer inside HE.

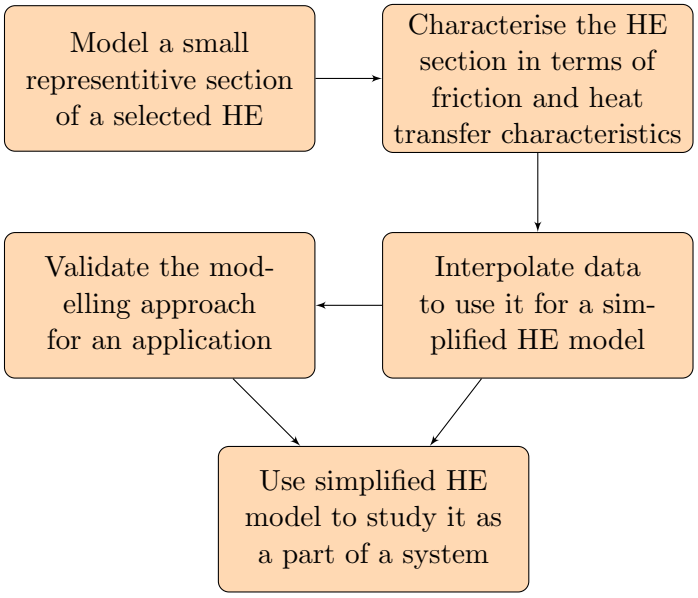

Figure 3.3: CFD modelling flow of a HE unit.

3.6 Numerical analysis of HE corrugation

Understanding detailed flow and heat transfer inside HE core is the first step of the CFD analysis cycle and it provides the essential input into the HE unit model. It is normally accomplished by modelling a section or a single channel of HE corrugation and applying various numerical boundary conditions such as symmetry or assuming the periodic domain to save computational cost. A particular exception is analysis

of non-compact HE, such as shell-and-tube (Figures 2.3 & 3.4) where performance of the complete single flow side of a HE has been evaluated using CFD [33, 136, 137]. The main trend observed in modelling plate HE was to consider up to a complete

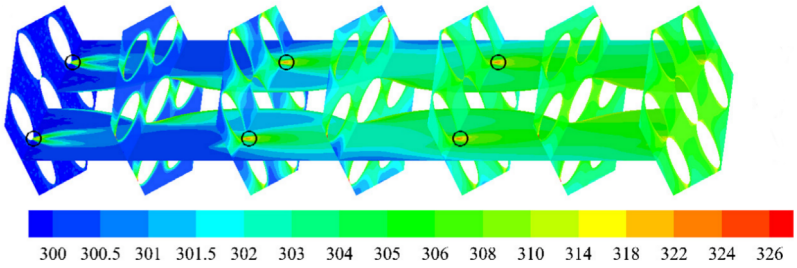

Figure 3.4: Shell side temperature distribution of the twisted oval tube shell HE [137].

single fluid layer of HE core between the two corrugated plates with examples in [138, 139, 140]. Significantly smaller corrugation sections were found to be utilised during the analysis of plate-fin and tube-fin HE. In the case of tube-fin HE sections and the plate-fin HE cores with louvred fins the corrugation would be modelled fully in the main streamwise direction (Figure 3.5) whereas the top and bottom of the domain would have a symmetry condition imposed. A particular interest was observed in studying the louvred fins of plate-fin HE which are often used in automotive for the cold side (ram air) flow [141, 142, 143] (Figure 3.5). These fins are efficient and low friction, however, the detailed geometry also makes the computational studies challenging. Also, a popular focus of recent research was to understand flow and heat transfer through serrated and wavy plate-fin HE fins (Figure 1.5b) [144, 145, 146]. Between all these studies certain similarities can be found and are discussed in the proceeding sections.

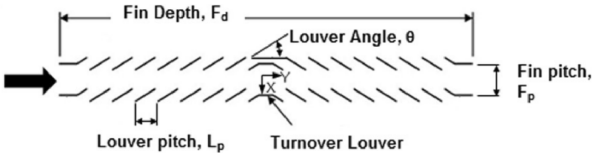

Figure 3.5: Louvred fin top view [141].

3.6.1 Periodic Domain Analysis

Periodic domain is an assumption, often used for resolving detailed flow and heat transfer in compact HE cores. It assumes periodicity of the geometry in the main stream-wise direction, allowing the numerical model to consider only a single period of HE corrugation. This numerical method for the HE was firstly introduced by Patankar et al. [147] with the equations given below for laminar flow. Considering the flow away

from an inlet to a HE core and the flow moving in the positive x direction, it follows that the pressure should be periodic:

$$p(x,y,z) - p(x+L,y,z) = p(x+L,y,z) - p(x+2L,y,z) = ... \tag{3.36}$$

Using the relationship in Equation 3.36 it is possible to define a global pressure gradient:

$$\beta = \frac{p(x,y,z) - p(x+L,y,z)}{L} \tag{3.37}$$

which allows to split the pressure term into two components:

$$p(x,y,z) = -\beta x_i + P(x,y,z) \tag{3.38}$$

here β is associated with the global mass flow and $P(x,y,z)$ - related to local motions. Considering periodicity the flow momentum equation (Equation 3.2) can be modified, assuming the periodic flow is in the x direction:

$$\rho\left(\frac{\partial U_i}{\partial t} + U_j\frac{\partial U_i}{\partial x_j}\right) = \beta x - \frac{\partial P}{\partial x_i} + \mu\left(\frac{\partial^2 U_i}{\partial x_j \partial x_j}\right) + \rho F_i \tag{3.39}$$

Original continuity of mass (Equation 3.1) and the modified momentum (Equation 3.39) equations then form a complete set of equations to resolve the flow field. Here β is the source pressure gradient with units of Pa/m and can be an assignable parameter to generate a certain Re number flow.

Defining temperature field for periodic flow is not as straightforward because the temperature distribution is independent of a streamwise coordinate. However, at the point where the flow is periodic the shapes of temperature contours become periodic as well. This allows the energy equation to be resolved using a chosen scaling [91] if constant temperature condition or heat flux was applied on heat transfer surfaces. Here the constant heat flux case is given. Using the condition on periodically repeating geometry it can be observed that [147]:

$$T(x+L,y) - T(x,y) = T(x+2L,y) - T(x+L,y) = ... \tag{3.40}$$

which is a similar observation to the pressure gradient scenario allowing to formulate:

$$\gamma = \frac{T(x+L,y) - T(x,y)}{L} = \frac{Q}{\dot{m}c_p L} \tag{3.41}$$

where Q heat flux (W), $\dot{m}$ - mass flow (kg/s) and c_p - constant pressure specific heat $(J/(kgK))$. Same as for the flow, the temperature field can be subdivided into the two components:

$$T(x,y,z) = \gamma x + \hat{T}(x,y,z) \tag{3.42}$$

where $\hat{T}$ is also periodic:

$$\hat{T}(x, y, z) = \hat{T}(x + L, y, z) = ... \tag{3.43}$$

The energy equation (Equation 3.3) then becomes [147]:

$$\rho \frac{\partial}{\partial t}\left(c_p \hat{T}\right) + u\gamma + \rho U_j \frac{\partial}{\partial x_j}(c_p \hat{T}) = \frac{\partial}{\partial x_j}(k \frac{\partial \hat{T}}{\partial x_j}). \tag{3.44}$$

However, this model has disadvantages. Taking into account physical behaviour of the flow down the pipe such as the original Reynolds experiment [31], it can be soon understood that steady-state simulations of periodic flows are only possible at the purely laminar regime. Appearance of unsteady flow also means that the flow and heat transfer will inevitably fluctuate, requiring more than one geometry period to study it. In addition, flow development inside HE corrugation at higher Reynolds numbers would have a bigger effect on the overall HE performance. This is not included in the proposed model above and would distort the predictions at higher Reynolds numbers.

However, the method is sufficient for parametric HE corrugation studies and has been widely used in the literature. A good example was produced by Patankar who used the model for the parametric study of staggered fins [148]. Zhang et al. [146] and Manglik et al. [144] simulated a broad range of sinusoidal HE corrugation in 2D and 3D respectively. Both studies treated the flow as steady-state and laminar limiting accuracy of their simulations as shown in Chapter 4. Another study by Metwally and Manglik [149] studied similar sinusoidal flow channel occurring between two parallel plates in a HE. Again, same flow assumptions were maintained within the Reynolds number range $10 \leq Re \leq 1000$, showing unawareness of the authors of the transitional flow regime occurring inside HE. Wang et al. [150] used the periodic assumption for both plain and serrated plate-fin HE corrugation, also ignoring the arising time-dependency of the flow. Rosaguti et al. [145] published the only sinusoidal geometry study acknowledging the transitional flow effects which can start at low Reynolds numbers and limited their calculation range to $Re = 200$.

3.6.2 Finite Length Channel Analysis

3.6.2.1 Tube-fin HE

Finite length computational domain provides more information about the heat transfer in the HE and is used for a variety of HE types. Tube-fin HE is a good example where small depth of the HE flow path, especially on the ram air side (Figure 3.6a) makes it computationally feasible. It enables modelling flow inlet/outlet effects whilst the

vertical/side boundaries of the computational domains are often closed using the symmetry condition. Bhuiyan et al. [151] (Figure 3.6a) studied different tube orientation patterns (staggered and in line) of the tube-fin HE using the CFD finding the staggered layout more efficient. A similar tube-fin HE was analysed with CFD by Sahin et al. [152] where a combination of elliptical tubes was used with different fin angles to find the optimum solution. Borrajo et al. [19] undertook one of the rare studies within tube-fin HE involving both single fluid and multi-fluid stream modelling. Second modelling approach involves a more complex conjugate heat transfer methodology where two flows are connected through a solid via boundary conditions. Solid material in this case is resolved employing heat conduction equation:

$$\rho C_p \frac{\partial(\rho T)}{\partial t} = \frac{\partial}{\partial x_j} \frac{\partial(kT)}{\partial x_j}. \tag{3.45}$$

Overall, Borrajo et al. [19] found that in terms of flow friction performance the two models performed similarly. However, heat transfer performance of the two models differed significantly, highlighting the need to consider the modelling assumptions carefully during the HE design cycle.

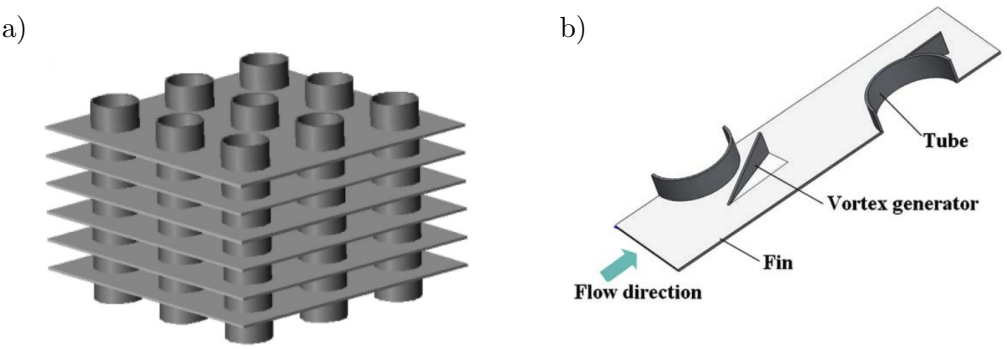

Figure 3.6: a) Example structure of the tube-fin HE geometry [151] b) Example tube-fin HE vortex generator [153].

A particular field of interest for the tube-fin HE has been introduction of various turbulators (Figure 3.6b). Their purpose is simple: to disturb the flow away from the inlet to the HE core. They increase mixing and eliminate the thick temperature gradient close to the solid, leading to increased heat transfer. This has been an interest for a few decades (for example, experimental study by Mitra et al. [154] in 1994). Recently, an increase in the numerical CFD studies attempting different shapes of the turbulators can also be observed, such as Lei et al. [153].

3.6.2.2 Platular HE

Platular HE were also modelled using finite channel length assumption (Figure 3.7). However, only the single fluid modelling was encountered in the literature between the two corrugated plates due to the increased computational domain compared to the tube-fin HE. Two studies on the subject were published by Kanaris et al. [138, 139]. The first study [138] focused on developing validated CFD methodology using the infra-red camera setup. The second study [139] combined the before validated CFD setup and developed a numerical design methodology. Tsai et al. [140] also developed similar methodology to Kanaris et al. [138, 139] but lacked computational power. This limited the mesh resolution and most likely led to 20% disagreement of numerics with experimental results in terms of the pressure drop.

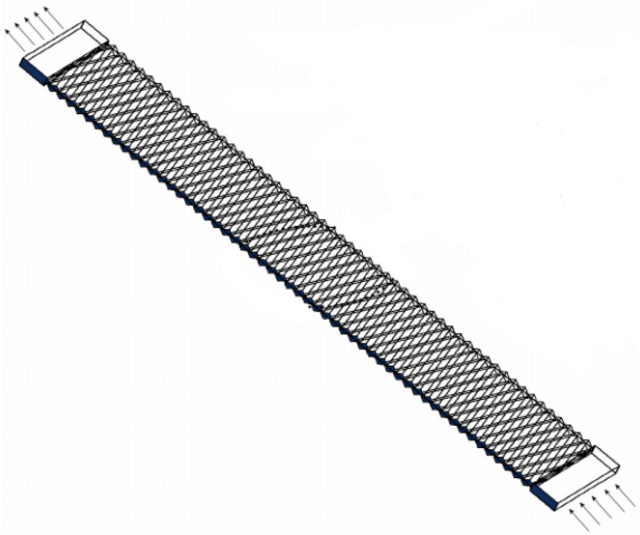

Figure 3.7: Finite length platular HE CFD domain example [139].

3.6.2.3 Plate-fin HE

Studies of plate-fin HE can be split into two parts. A number of the finite length channel studies analysed the louvred fins (Figure 3.8). Such corrugation is often used in the automotive applications for radiators or air conditioning systems. As the installation space is limited in automotive industry, thin HE are used with a single period of the fins on the ram-air side. This makes detailed HE corrugation simulations with the domain such as in Figure 3.8 feasible. Perrotin and Clodic [143] studied the louvred corrugation in both 2D and 3D and concluded that for accurate heat transfer prediction 3D calculations were necessary as the 2D estimate led to 83% heat transfer over-prediction. Ferrero et al. [141] carried out an optimisation study (Figure 3.8) using conjugate heat transfer formulation where various parameters were evaluated, complying to manufacturing constraints. An application of louvred fins to tube-fin

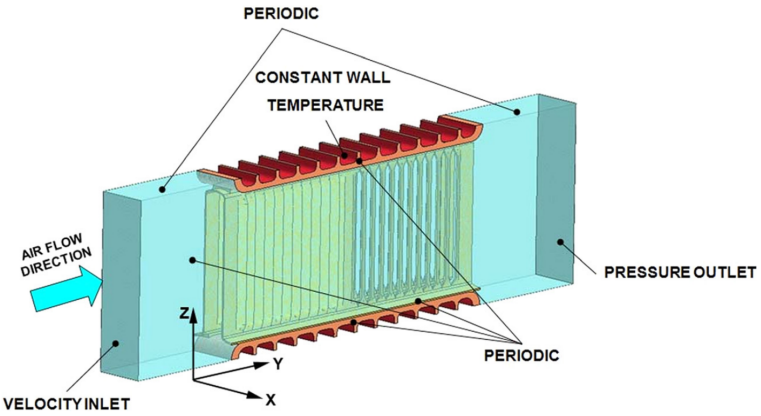

Figure 3.8: Louvred plate-fin corrugation HE CFD domain with conjugate heat transfer [141].

HE was also studied by Huisseune et al. [155]. Louvred features provided complex flow mixing between the fin layers and were compared to the straight fin model shown above (Figure 3.6a), suggesting potential for increased heat transfer performance.

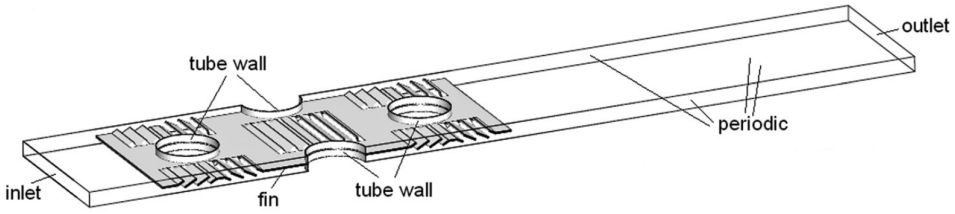

Figure 3.9: Louvred tube–fin corrugation HE CFD domain [155].

Studies of the long plate-fin HE corrugation channels were rarely found. Rao et al. [156] attempted modelling flow development of the straight plate-fin corrugation using a CFD code. However, usefulness of it is highly questionable - analytical and experimental solutions could be found for such geometry. In addition, predictions were obtained with simplified RANS $k - \epsilon$ model, which has numerous drawbacks for HE applications, shown in Chapter 4. More comprehensive studies using a finite length corrugation channel were completed by Dai et al. [114] and Zheng et al. [157] (Figure 3.10). Both studies evaluated long single tortuous channels with a semi circular cross-sectional area, differing from a standard rectangular plate-fin cross-section. Zheng et al. [157] study is, however, more valuable and expansive in terms of the CFD predictions whilst in Dai et al. [114] the use of CFD was limited to steady-state straight channel flows and paid attention on the experiments.

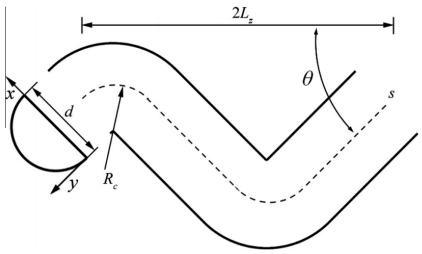

Figure 3.10: The computational domain schematic used by Zheng et al. [157].

3.6.3 Use of the Different Flow Modelling Assumptions

A significant variation in selecting different flow momentum modelling assumptions was found between the CFD studies analysing HE corrugation. One of the most popular assumptions found during the review was treating the flow as steady-state which was a reasonable assumption by Patankar et al. [147] in 1977, but is more questionable in the present day. Steady-state assumption was shown to break down at the Reynolds numbers in the order of several hundred (geometry dependent) both experimentally by Rush et al. [158] in 1999 and numerically by Hiramatsu et al. [159] already in the 1992 study and is further discussed in the Chapter 4.

It is also questionable whether with the onset of unsteady flow the laminar assumption is still valid. Recollecting the original Reynolds pipe flow study [31] it is evident that the flow in periodically repeating domain must turn unsteady and depending on the Reynolds number enter either transitional or turbulent regimes. However, usage of laminar equations can be seen in the unsteady flow studies up to $Re = 1200$ [143, 157], questioning accuracy of the results, especially at the higher Reynolds numbers. Some studies, though, considered using turbulence modelling assumptions to study the flow and heat transfer, namely the $k - \epsilon$ and its variations together with the $k - \omega$ SST. Although $k - \epsilon$ has been a standard choice for industrial applications for a long time, within the academic literature it was only used in two conditions: due to the restricted computational power [140] or for an optimisation study of straight plate-fin corrugation (Figure 2.6) [156] where no flow separation occurs due to the simplistic geometry. However, as concluded in many studies such as the recent PhD thesis by Woods [127], the $k - \epsilon$ model fails to accurately predict the flows where resolving boundary layer and flow separation is important. This severely limits the model for forced convection heat transfer applications such as HE. Instead, $k-\omega$ SST model was found to produce good agreement with experimental results. The same conclusion was found in a recent study by Bhuiyan et al. (2013) [151] where $k - \epsilon$ RNG, $k - \epsilon$ and $k - \omega$ SST models were used for a tube-fin HE. Kanaris et al. [138, 139] presented a good agreement of $k - \omega$ SST results (the only model tested) with experimental data for a platular HE.

All of the above indicate a superiority of the $k-\omega$ SST model in the transitional and turbulent flow regions and suggest that it is the best choice for resolving small scale HE flows.

3.6.4 Unsteady flow modelling

As mentioned afore in the chapter the trend in the literature is to study mostly low Reynolds number flows (Re of several hundred typically being a limit) through compact HE surfaces. It can be especially observed in the periodic flow studies [144, 145, 146]. This limit is questionable for low viscosity fluid applications such as air, a common working fluid in automotive and aerospace. In such applications flow past the HE corrugation often can be in the unsteady transitional/turbulent flow regime.

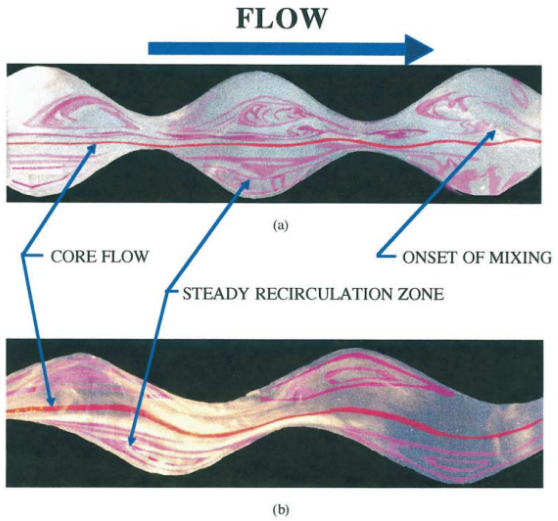

Figure 3.11: Unsteady flow at a) $Re = 468$ versus steady flow at b) $Re = 333$ obtained using the experimental die trace results [158].

Early computational effort to model unsteady flow was undertaken by Hiramatsu [159] past the serrated fins of a turbocharger intercooler. To validate simulations of this study experiments were completed and showed a good agreement with simulations. A recent modelling study was completed by Zheng et al. [157] of the flow through tortuous channels having a semi-circular cross section. In both of the studies [157, 159] the unsteady behaviour and its importance is clearly shown and stressed. However, both studies used laminar flow assumption which led to the rather chaotic results produced by Zheng et al. [157].

These claims are further supported by Rush et al. [158] who carried out experiments using sinusoidal channel sections (Figure 3.11) and observed that the unsteady regime onsets at around the Reynolds number in the order of a few hundred. In Rush et al. [158] it was also claimed that the unsteady regime increased fluid mixing and heat

transfer in the channel. Similar observations were also expressed in the experimental study by Nishimura et al. [160] where also a set of different sinusoidal geometries were tested. Overall, the evidence provided by a number of articles enables to conclude is that the unsteady flow regime is important. It should be taken into consideration and not resolving it is a potential source of error.

3.7 Numerical HE Unit Modelling

3.7.1 HE core modelling

CFD codes such as Ansys [115] and OpenFOAM use their implementations of models similar to the analytical $\epsilon - NTU$ [5] (Section 2.4.3) method to simplify the HE core of a HE unit model. This allows CFD methods assume that the HE core is a porous media block to reduce the computational cost and calculate the pressure drop and heat transfer based on the input values from HE corrugation simulations [115]. This modelling approach is implemented as a source term in the momentum equation in OpenFOAM simulations in Chapters 5 & 6 and can be accomplished in two ways. The first method is the Darcy-Forschheimer Law model. Darcy part of the model takes into account resistance caused by viscous forces and was firstly documented by Darcy in 1856 [161]. Ignoring the gravity effects for porous media and assuming it is isotropic, the Darcy's law could be written as [162, 163]:

$$\frac{\partial p}{\partial x_i} = -\frac{\mu}{K}\mathbf{u_f} \tag{3.46}$$

where ∇p - pressure gradient (Pa/m), μ - viscosity (Pas), $\mathbf{u_f}$ - stream-wise velocity (m/s), K - intrinsic permeability, $1/m^2$. At higher fluid velocities the inertia becomes important and was firstly investigated by Forschheimer [164] in 1901 where inclusion of the inertia was completed via kinetic energy of the fluid. Later work by in the area [165, 166, 167] established the commonly known relationship:

$$\frac{\partial p}{\partial x_i} = -\left(\frac{\mu}{K}u_i + \beta\rho u_i u_i\right) \tag{3.47}$$

where ρ - flow density (kg/m^3), β - inertial permeability coefficient $(1/m)$. In OpenFOAM the following implementation of the porosity model is:

$$S = -(\mu d + \frac{1}{2}f\rho\sqrt{u_i u_i})u_i = \frac{\partial p}{\partial x_i} \tag{3.48}$$

Similarity between the models is straightforward, however, it should be noted that Darcy coefficient is inverse to the commonly used one ($d = 1/K$, $[1/m^2]$) and for the inertial coefficient is $\beta = 0.5f$, $[1/m]$. For the HE modelling the viscous term was

set to $d = 0$ a value of f is selected in the three directions, following ANSYS [115] methodology. This is valid for HE as the flows are fast to enable forced convection heat transfer and because the fluids for HE are typically of low viscosity, making viscous contribution minimal. Alternative way is to model porous media in OpenFOAM using the power law model:

$$S = \rho C_0 \sqrt{u_i u_i}^{(C_1-1)} u_i = \nabla p. \tag{3.49}$$

This model uses curve fitted flow resistance data where C_0 and C_1 are the two curve fitting constants. It applies flow resistance uni-directionally and selects pressure drop of a porous zone based on the mass flow coming into it. It is potentially more advantageous compared to the Darcy-Forschheimer implementation where user input is required if the flow rate changes. The performance of the two models is assessed in Chapters 5 & 6.

Effectiveness model is implemented in the porous media HE core to simplify heat transfer. In OpenFOAM it is accomplished by adding the source term into the energy equation in the form of:

$$Q_t = \epsilon(\phi, \dot{m}_2)(T_2 - T_1)\phi c_p \tag{3.50}$$

where:

Q_t - total heat source
$\epsilon(\phi, \dot{m}_2)$ - effectiveness table
ϕ - net mass flux into HE [kg/s]
$\dot{m}_2$ - secondary mass flow [kg/s]
T_1 - primary inlet temperature [K]
T_2 - secondary inlet temperature [K]
c_p - specific heat capacity [J/kg/K]

The heat transfer distribution inside the HE is resolved by:

$$Q_c = \frac{V_c|U_c|(T_c - T_{ref})}{\sum(V_c|U_c|(T_c - T_{ref}))} \tag{3.51}$$

where:

Q_c - source for cell
V_c - volume of the cell $[m^3]$
U_c - local cell velocity $[m/s]$
T_c - local call temperature $[K]$
T_{ref} - min or max(T) in cell zone depending on the sign of Q_t $[K]$

The source term works by using the effectiveness table values provided prior to the simulation by the user. It prescribes a certain amount of heat transferred in a HE core section based on a mass flow coming into it and leads to a lower computational expense.

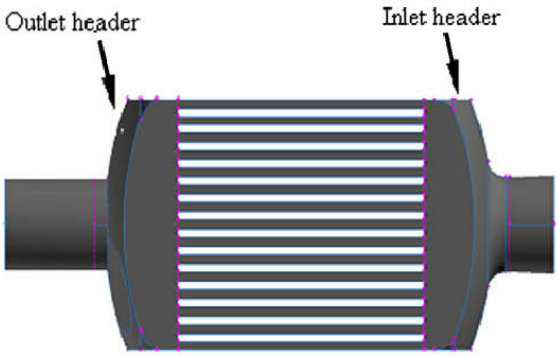

Figure 3.12: CFD modelling example of a HE unit [28].

3.7.1.1 Applications of the HE Unit Modelling

Examples of applications involving the two-stage HE simulation process are described in this section. An automotive application was studied by Carluccio et al. [168] using a plate-fin type HE where the full CFD design cycle of was undertaken. Firstly, detailed flow analysis of a few corrugation channel periods for both fluids was evaluated to obtain friction and heat transfer data. This data was then extrapolated for the porous media HE core approach. Ismail et al. [28] studied a similar plate-fin HE problem (Figure 3.12). Serrated and wavy fins were modelled first in detail and the results were then applied to a simplified HE unit model. In this case, porous media HE core was split into a number of layers of a single HE fluid side and good agreement was reported to the experimental in house data. This is questionable as the $k-\epsilon$ model was used to analyse a rather disruptive fin geometry and $k-\epsilon$ model is not equipped for such applications. Hayes et al. [169] applied the two stage methodology to a platular HE and validated the predictions using experimental data, showing applicability of the methodology beyond plate-fin HE.

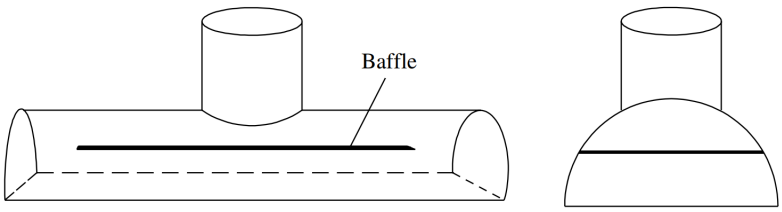

Figure 3.13: Plate-fin HE header with a proposed baffle location [96].

3.7.1.2 Numerical Analysis of the Heat Exchanger Headers

Design of the HE headers separately from the HE unit was found to be another area of interest. The importance of efficient HE headers is signified by the Lalot et al. [170] study where the flow maldistribution resulted in up to 25% loss of efficiency for cross-flow HE. In industry, inefficient HE headers are often caused by a limited installation volume. Besides Lalot et al. [170], maldistribution inside HE headers was also studied by Zhang et al. [27] and Wen et al. [96, 97]. All the studies suggested similar solutions: Lalot et a. [170] suggested an uniformly perforated grid whilst Zhang et al. [27] and Wen et al. [96, 97] introduced baffles (Figures 3.13 & 3.14) inside the HE header. This allows to redistribute the flow coming into the HE, but adds a pressure drop penalty as it is an additional blockage. It should also be noted that in computational studies above only the HE headers were modelled and inlet to the HE core was treated as a pressure outlet to reduce the computational cost.

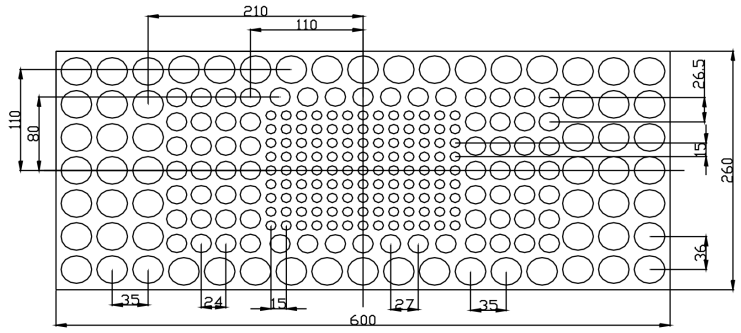

Figure 3.14: A complex baffle design proposed by Wen et al. [96].

3.8 Summary of the Chapter

Historically HE design was limited to analytical or experimental methods, summarised in books such as Kays and London [6] or Rohsenow et al. [5]. At around 1980's computing power has increased and allowed researchers to utilise numerical simulation tools. Whilst numerics require greater performing computer hardware it also provides the designer with more insight and potential for HE optimisation compared to the traditional analytical and experimental methods. One of the early developments was the periodic heat transfer model proposed by Patankar et al. [147]. It allowed evaluating a variety of heat transfer surfaces computationally cheaply and enabled implementing the obtained data into existing analytical HE models such as $NTU - \epsilon$ [6]. Analytical modelling methods are also implemented in the CFD codes such as ANSYS Fluent

[115], enabling to model a full size HE unit as a part of heat transfer system. In such implementation flow and heat transfer inside a HE core are simplified using porous media and heat transfer effectiveness models, allowing to study the overall HE unit performance. Current trend is to study a bigger section of HE corrugation (e.g. a full length single channel of HE corrugation layer) which provides with more information than the periodic computational domain [114, 157]. In addition, it was identified experimentally and numerically that at around the Reynolds number of several hundred unsteady flow onsets inside HE core. It enhances flow mixing and heat transfer and disqualifies the periodic flow assumption. However, in this regime a very limited number of studies have been found and the appropriate modelling techniques are unclear, thus, are thoroughly assessed in the next thesis chapter.

Chapter 4

Flow and Heat Transfer Modelling of a Single HE Corrugation Channel

Contents

4.1 Introduction

This chapter assesses the impact of various numerical assumptions on accurate flow and heat transfer analysis. This is undertaken as most of the literature studies were

found not to provide full details of the implemented numerical setup. To accomplish this a two-dimensional sinusoidal HE corrugation, taken from Zhang et al. [146], is analysed numerically. Two computational domains are evaluated for modelling HE corrugation. The first approach follows the guidelines of Zhang et al. [146] and models a single period of the sinusoidal channel, assuming periodic flow. This method was pioneered by Patankar et al. [147] in 1977 where it was applied to serrated HE fins. It is computationally cheap and enables to obtain flow and heat transfer estimates away from the HE core inlet. The second approach studies the sinusoidal HE corrugation by modelling a finite length channel containing several periods of HE fins. This method follows Zheng et al. [157] study where it is proposed to analyse the unsteady flow regime, occurring at $Re \approx 200$ in [157]. In this chapter, the HE corrugation is analysed within $5 \leq Re \leq 1000$ with the incompressible flow assumption. Laminar, $k-\omega$ SST and $k-\epsilon$ RANS modelling assumptions are compared across the Reynolds number range. In addition, the effect of different numerical discretisation schemes on the domain is evaluated and the commercial ANSYS Fluent with the open-source OpenFOAM CFD codes are compared.

4.2 Solution Independence Studies

4.2.1 Sinusoidal Channel Geometry

Sinusoidal HE corrugation was selected from a numerical study by Zhang et al. [146] where it was non-dimensionalised using the corrugation aspect ratio:

$$\gamma = \frac{2A}{L} \tag{4.1}$$

and the fin spacing ratio:

$$\epsilon = \frac{S}{2A} \tag{4.2}$$

where A - is amplitude of the sinusoidal function, L - period length and S - channel width. Schematic of the channel is shown in Figure 4.1a and to obtain geometries the lengthscale L was fixed to $L = 2\pi = 6.28$. In the subsequent sections the corrugation aspect ratio was kept to $\gamma = 1.0$ whilst two fin spacing ratios of $\epsilon = 0.25$ and $\epsilon = 0.375$ were used.

4.2.2 Periodic Domain Mesh Independence

Steady state calculations using ANSYS Fluent were carried out at $Re = 150$ (defined as $Re = (\rho u_m d_h)/\mu$ [5], with u_m - the mean flow velocity and the hydraulic diameter taken as $d_h = S$). Quadrilateral meshes were used with a coarse mesh visualisation in Figure 4.1b. Mesh resolution data is summarised in Table 4.1 with the relevant fluid

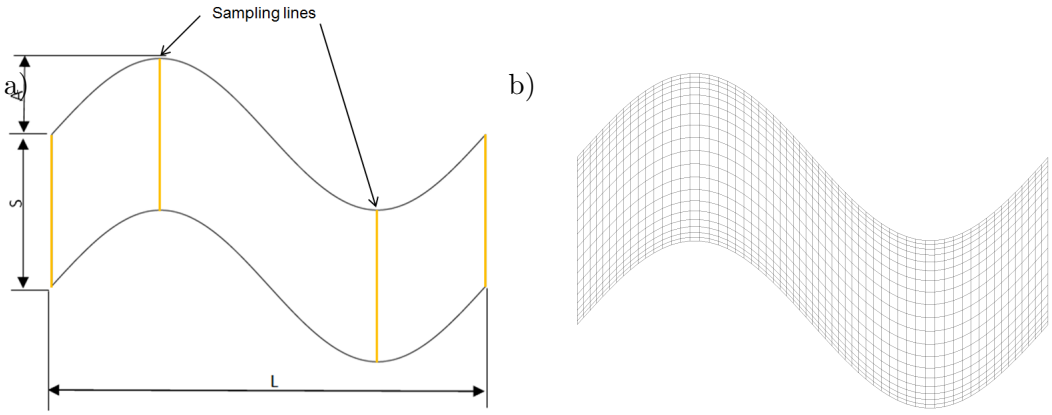

Figure 4.1: a) Coarse mesh visualisation. b) Data extraction lines at $x = 0, \pi/2, 3\pi/2, 2\pi$.

properties in Table 4.2. Inlet to the periodic channel was fixed to an average $T = 300$ K and a constant wall temperature boundary condition of $T_w = 350$ K was applied.

Mesh	Vertical divisions	Horizontal divisions
Coarse	20	60
Medium	60	180
Fine	100	260

Table 4.1: Resolutions of the mesh used of periodic geometry independence study.

	Air	units
Density	1.25	kg/m^3
Air Viscosity	1.7894×10^{-5}	$Pa \cdot s$
Conductivity	0.0242	$W/(mK)$
Specific Heat (C_p)	1000.6	$J/(kgK)$

Table 4.2: Constant properties of air used in the study [146].

Flow and heat transfer was modelled using laminar model and discretisation schemes in Table 4.14. Solutions were analysed at the four sampling lines of $x = 0, \pi/2, 3\pi/2, 2\pi$ (Figure 4.1b). Pressure and velocity magnitude data was used to evaluate the three meshes (Figure 4.2). It should be noted that here the pressure data are the local fluctuations rather than the global pressure gradient driving the flow as described in [147]. Results between the medium and the fine meshes agree well whilst the coarse mesh failed to accurately predict both velocity and pressure. Interestingly, twice higher grid resolution was required to achieve solution independence compared to Zhang et al. [146] and it is not completely understood why. However, Zhang et al. [146] paper does not provide complete detail about the numerical methodology implemented. This includes computing precision (the study was published in 2004) and discretisation schemes used which meant it was not possible to ensure that both studies were identical.

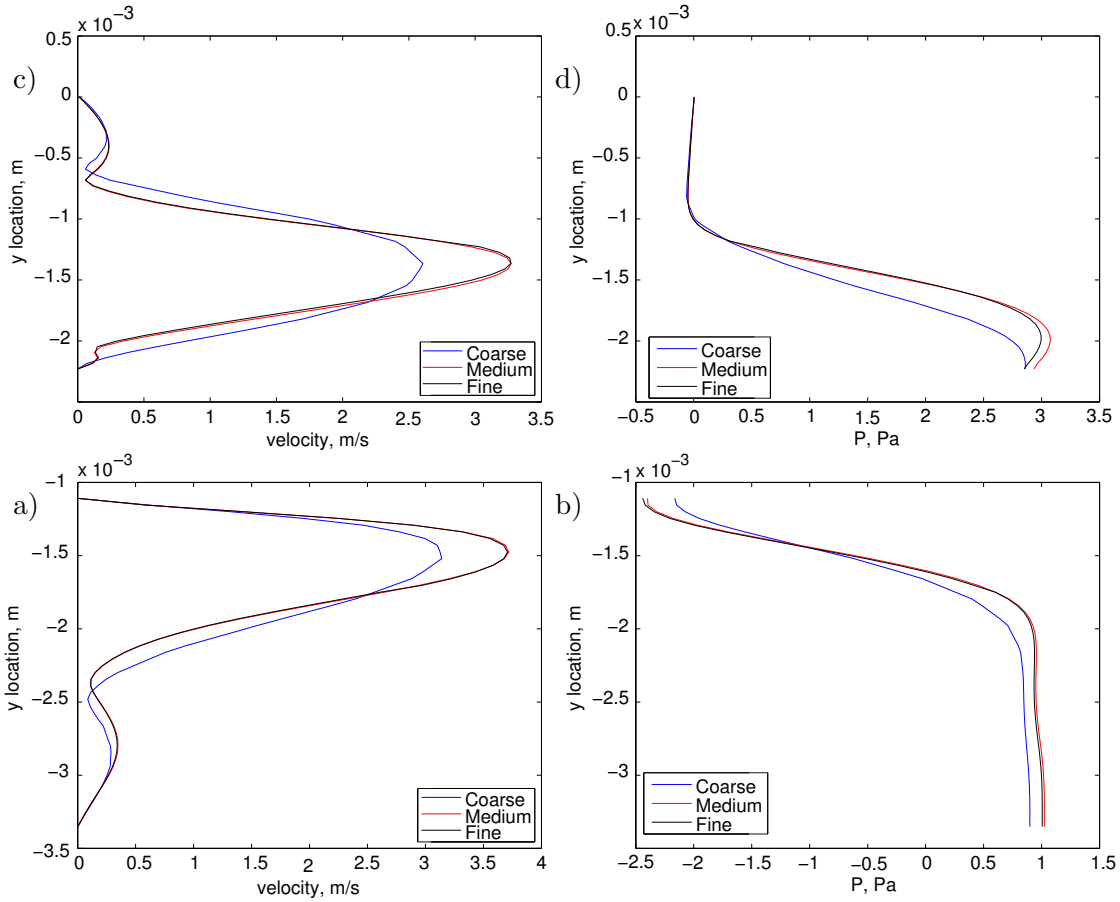

Figure 4.2: y location, $[m]$ vs: a) velocity magnitude at $x = 0$, b) pressure at $x = 0$, c) velocity magnitude at $x = (3/2)\pi$, d) pressure at $x = (3/2)\pi$.

Despite this, the numerical solution theory described in [146] is the same to the one implemented in ANSYS Fluent (based on Patankar et al. [147]). Thus, both studies should produce comparable results and only depend on smaller numerical solution details of [146]. Another way was also undertaken to compare the meshes uses the fanning friction ($f_{fanning}$) and Colburn (j) factors to compare the overall sinusoidal channel performance. Following the methodology in Zhang et al. [146] the fanning friction factor was defined as

$$f_{fanning} = \left(-\frac{dp}{dx}\right)\left(\frac{d_h}{2\rho u_m^2}\right) \tag{4.3}$$

where dp/dx - global pressure gradient (Pa/m), d_h - hydraulic diameter (m) here defined as $d_h = S$, ρ - fluid density (kg/m^3), u_m - mean velocity (m/s). Colburn factor was defined as

$$j = \frac{Nu}{RePr^{1/3}} \tag{4.4}$$

where the Nusselt number is

$$Nu = \frac{\dot{m}c_p(T_o - T_i)d_h}{kA_h(LMTD)} \tag{4.5}$$

here $\dot{m}$ - mass flow (kg/s), c_p - specific heat $(J/(kgK))$, T_i and T_o - mean temperature at the inlet and outlet respectively (K), k - thermal conductivity $(W/(mK))$, A_h - heat transfer area (m^2). The log mean temperature difference is

$$LMTD = \frac{(T_w - T_o) - (T_w - T_i)}{\ln[(T_w - T_o)/(T_w - T_i)]}. \tag{4.6}$$

To obtain A_h for the Nusselt number calculation, an arbitrary dimension of 1 was chosen in the third dimension. The data is summarised in Table 4.3 and shows that both fanning and Colburn factors agree well between the medium and fine meshes. This allows to conclude that the flow and heat transfer were resolved accurately at medium mesh resolution, enabling its use for further predictions.

Mesh	Fanning friction factor	Colburn factor
Coarse	0.126	0.094
Medium	0.146	0.087
Fine	0.143	0.084

Table 4.3: Fanning friction factors f and Colburn factors j for the three meshes.

4.2.3 Finite Length Channel Solution Independence

The second approach uses a finite length sinusoidal HE channel to study flow and heat transfer. This was undertaken following the Zheng et al. [157] study to provide more information about the unsteady flow regime. In this study the computational domain consisted of six sinusoidal channel periods (Figure 4.3) coupled with inlet and outlet sections (both the length of the sinusoidal section). These additional sections were created to enable pre-development of the flow and to minimise flow reversal errors at the end of the domain. Same fluid properties were used (Table 4.2) with an inlet temperature of $T = 300\ K$ and a constant temperature heat transfer condition at the sinusoidal walls ($T_w = 350\ K$). Data was extracted using sampling lines (Figure 4.3) to study flow development and its impact on heat transfer performance at every channel period.

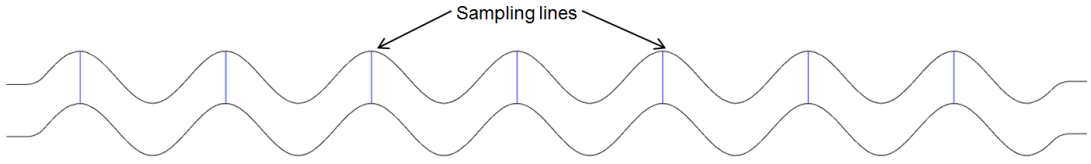

Figure 4.3: Data sampling lined for finite length channel domain ($\gamma = 0.375$, $\epsilon = 1.0$).

4.2.3.1 Effect of the Simulation Time-step

A strong unsteady flow behaviour was observed at $Re \geq 200$ during initial finite length channel analysis. Thus, the effect of the simulation time-step using laminar and $k-\omega$ SST models was assessed. The simulations were completed with ANSYS Fluent using the medium mesh resolution per sinusoidal corrugation period (60×180, Table 4.1). Figures 4.4 & 4.5 show the effect of the time-step on the predictions at $Re = 500$ using the laminar and $k-\omega$ SST models. Firstly, a steady-state solution was reached using

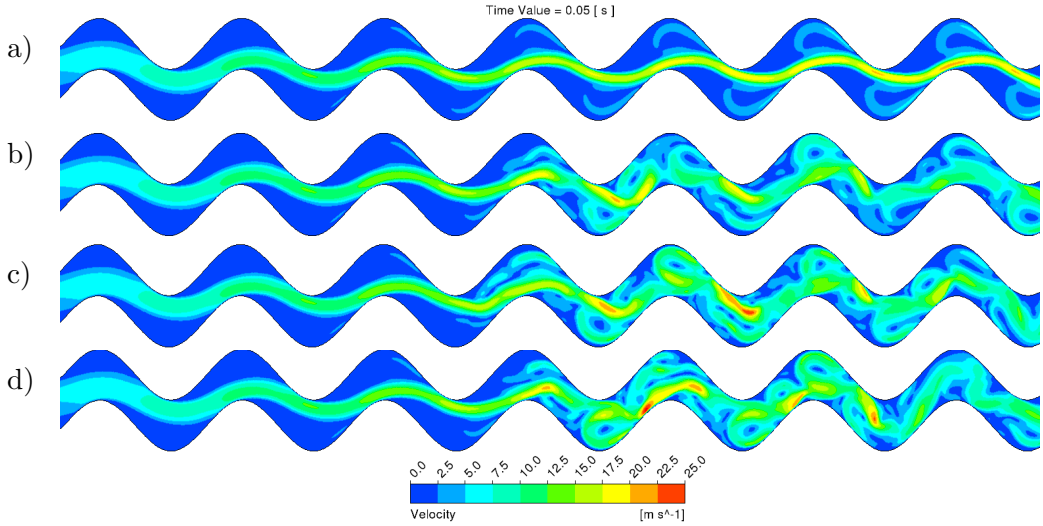

Figure 4.4: Instantaneous velocity magnitude at $t = 0.05\ s$ ($Re = 500$) with: a) $\Delta t = 1 \times 10^{-4}\ s$, b) $\Delta t = 1 \times 10^{-5}\ s$, c) $\Delta t = 1 \times 10^{-6}\ s$, d) $\Delta t = 1 \times 10^{-7}\ s$ using laminar flow model with ANSYS Fluent ($\gamma = 0.375$, $\epsilon = 1.0$).

$\Delta t = 1 \times 10^{-4}\ s$ with both flow models (Figures 4.4 & 4.5). These solutions were then used as initial conditions for simulations with decreased simulation time-steps. Reducing the time-step further to $\Delta t = 1 \times 10^{-5}\ s$ produced a clear unsteady solution, contrasting to the previous result. However, using time-steps of $\Delta t = 1 \times 10^{-6}\ s$ and $\Delta t = 1 \times 10^{-7}\ s$ led to closer solutions for both models, suggesting that time-step independence could be reached. In addition, Figures 4.4 and 4.5 highlight the differences between the two modelling assumptions. The laminar flow predictions resolved the flow to smaller scale vortices which in turn caused higher localised velocity magnitudes.

Thus, effects of the simulation time-step for both models were further analysed using the overall pressure drop and temperature change (Figures 4.6 & 4.7). However, laminar flow model predicted highly unstable flow which made it difficult to identify whether the time-step independence has been achieved (Figure 4.6) and to resolve it the results were time-averaged in Table 4.4. This enabled to conclude that the solutions became similar between $\Delta t = 1 \times 10^{-6}\ s$ and $\Delta t = 1 \times 10^{-7}\ s$. However, it still

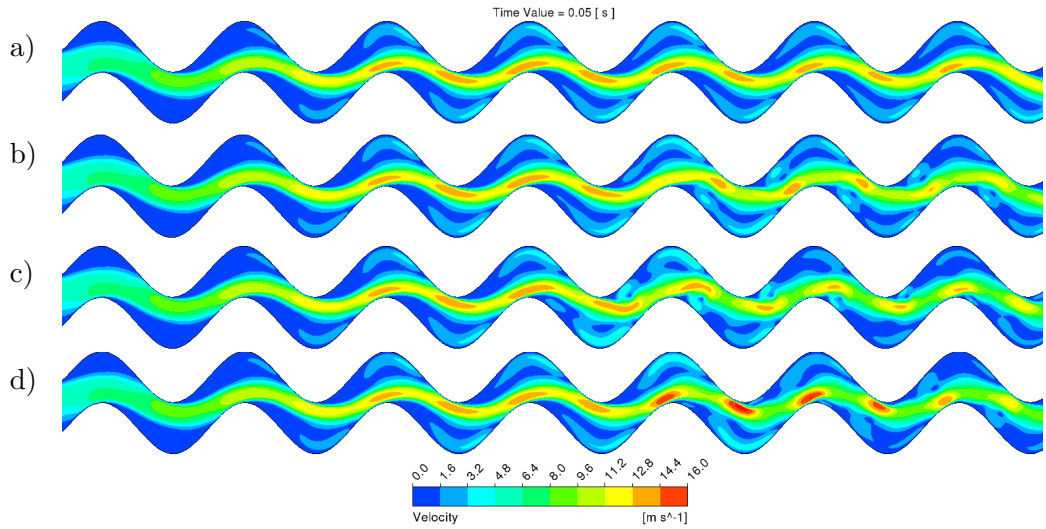

Figure 4.5: Instantaneous velocity magnitude at $t = 0.05$ ($Re = 500$) with: a) $\Delta t = 1 \times 10^{-4}$ s, b) $\Delta t = 1 \times 10^{-5}$ s, c) $\Delta t = 1 \times 10^{-6}$ s, d) $\Delta t = 1 \times 10^{-7}$ s, using $k - \omega$ SST flow model with ANSYS Fluent ($\gamma = 0.375$, $\epsilon = 1.0$).

remains questionable whether the laminar model is appropriate at Reynolds numbers which lead to highly unsteady flow. Furthermore, flow predictions with the laminar model took approximately twice the computational time to be resolved compared to the $k - \omega$ SST predictions, suggesting difficult numerical convergence.

	Laminar		$k - \omega$ SST	
Δt, s	ΔP, Pa	ΔT, K	ΔP, Pa	ΔT, K
1×10^{-4}	405	21.86	328	21.78
1×10^{-5}	388	20.63	308	21.25
1×10^{-6}	351	22.38	287	21.63
1×10^{-7}	354	22.09	297	21.63

Table 4.4: Time-averaged (throughout the simulation time) transient flow data using laminar and $k - \omega$ SST models at a range of solution time-steps.

Predictions with the $k - \omega$ SST model produced less chaotic results (Figure 4.7 and Table 4.4) and allow to conclude that time-step independence is reached at $\Delta t = 1 \times 10^{-6}$ s. However, results between laminar and $k - \omega$ SST models were found to differ in terms of the time-averaged pressure drop. The $k - \omega$ SST model predicted $\Delta P = 287$ Pa whilst with the laminar model the pressure drop was at $\Delta P = 351$ Pa (using $\Delta t = 1 \times 10^{-6}$ s). This discrepancy is assigned to incapability of the laminar flow model to predict the transitional flow regime. Interestingly, however, predictions of the temperature change (ΔT) through the channel were similar between the models, despite significantly different flow patterns.

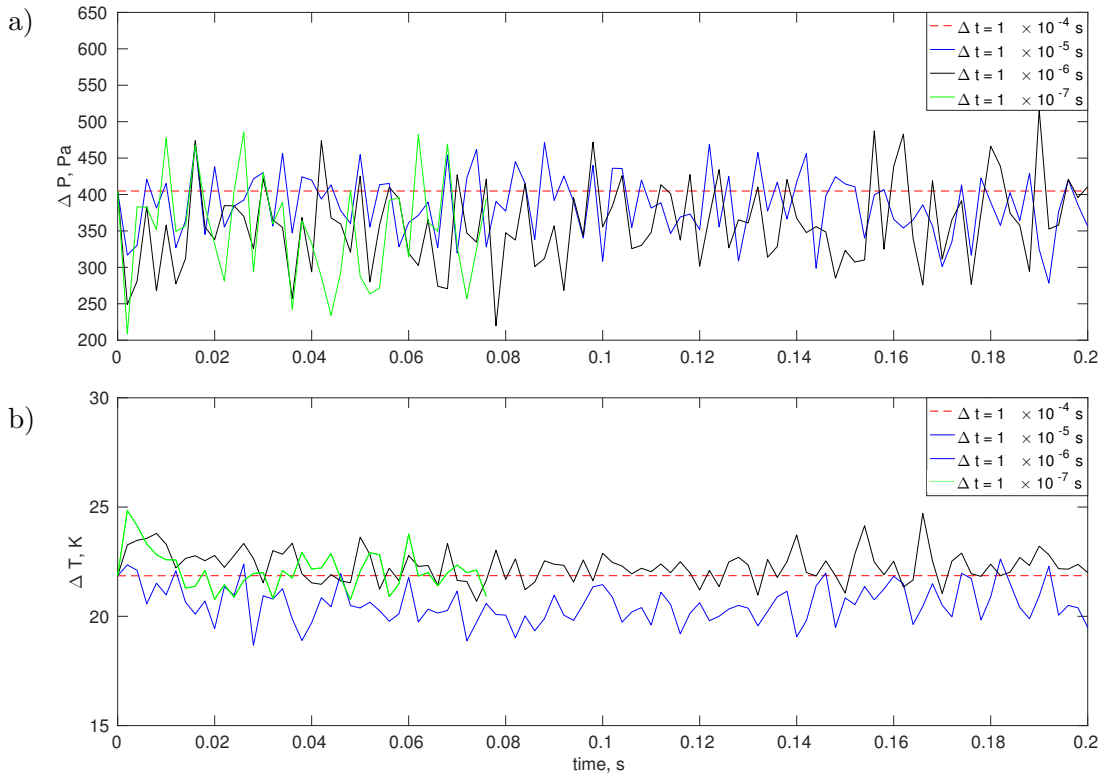

Figure 4.6: a) Pressure drop ΔP (Pa) and b) Temperature change ΔT, (K) through the sinusoidal channel at the range of solution time-steps using laminar flow momentum model with ANSYS Fluent ($\gamma = 0.375$, $\epsilon = 1.0$). Data was sampled at $f = 500$ Hz.

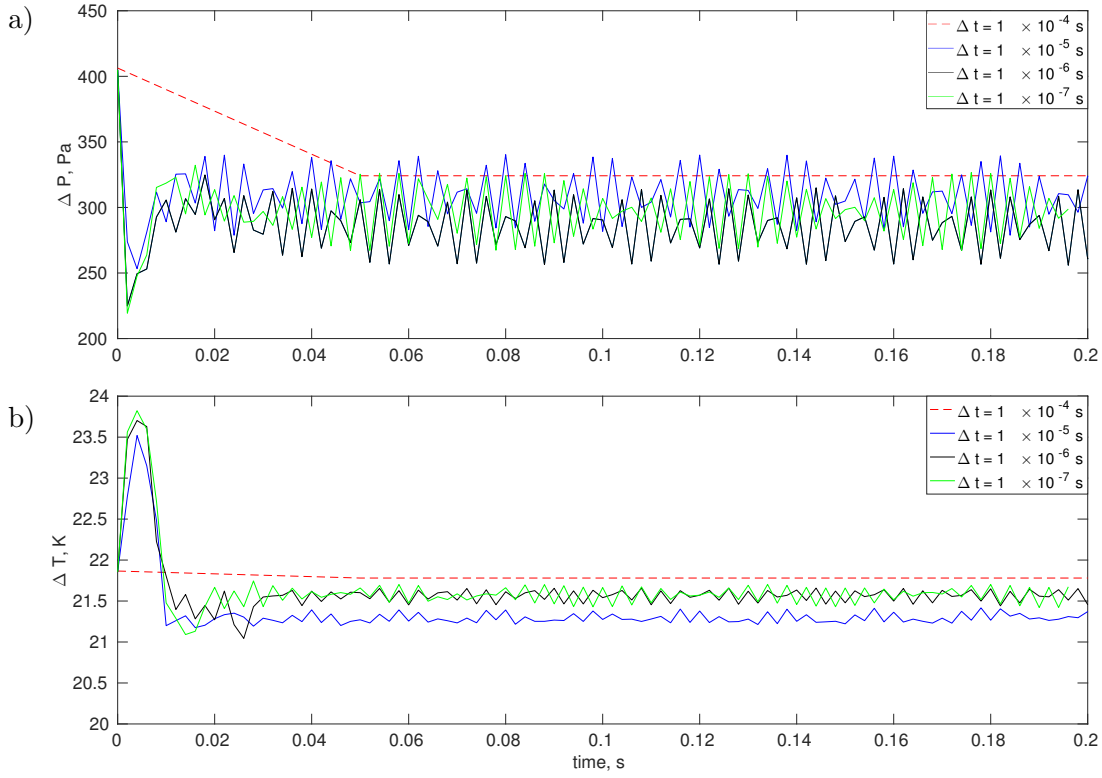

Figure 4.7: a) Pressure drop ΔP (Pa) and b) Temperature change ΔT, (K) through the sinusoidal channel at the range of solution time-steps using $k-\omega$ SST momentum model with ANSYS Fluent ($\gamma = 0.375$, $\epsilon = 1.0$). Data was sampled at $f = 500$ Hz.

4.2.3.2 Mesh Independence of the Finite Length Channel

The time-step independence predictions completed above used medium resolution mesh (60×180 every sinusoidal period). Further increasing the mesh resolution was computationally challenging, however, an attempt was made to ensure quality of the predictions. In addition, coarse mesh resolution was included to double check if the medium mesh resolution is still necessary for unsteady flow analysis. Results from the grid independence study are given in the Figure 4.8 with mesh resolutions summarised in Table 4.5.

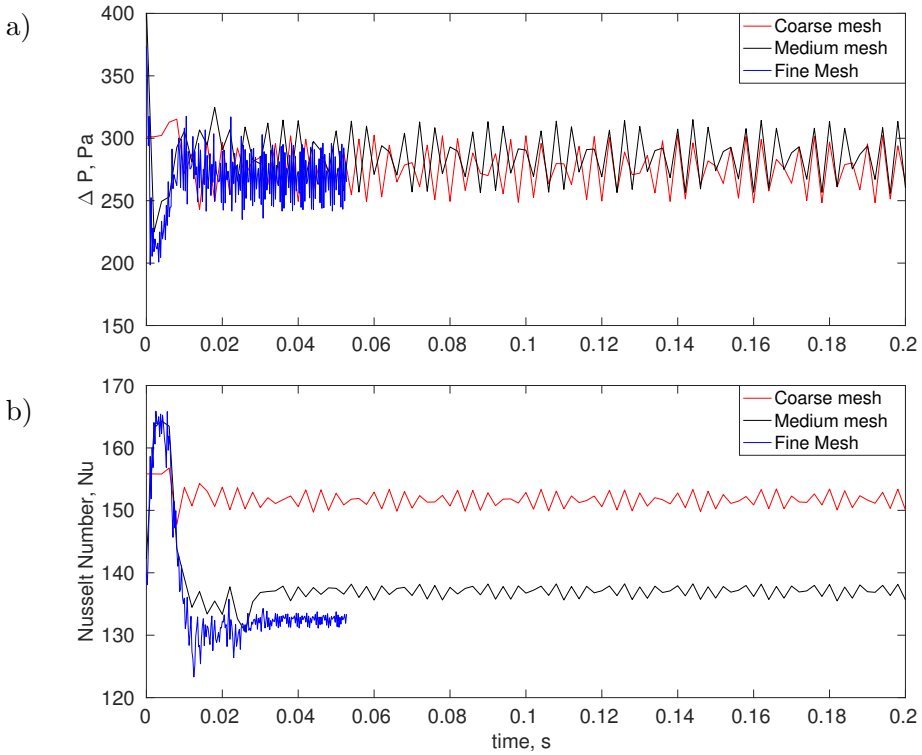

Figure 4.8: a) Pressure drop ΔP (Pa) and b) Nusselt number through a sinusoidal channel comparing the three (- coarse, - medium and - fine) meshes at $Re = 500$ and $k - \omega$ SST model with ANSYS Fluent ($\gamma = 0.375$, $\epsilon = 1.0$).

Mesh	Vertical divisions	Horizontal divisions
Coarse	31	90
Medium	61	180
Fine	121	360

Table 4.5: Transient mesh resolution per single sinusoidal channel period.

The simulation time-steps for each case were adapted from the medium mesh result ($\Delta t = 1 \times 10^{-6}$ s) to maintain the time-step independence. The data was acquired for coarse and medium meshes at sampling frequency of $f = 500$ Hz. For the fine mesh it was increased to $f = 1000$ Hz. Figure 4.8 shows that whilst the pressure

drop through the channel was resolved similarly between the three meshes, the heat transfer performance predictions slightly differed between the medium and fine grids. However, it took 5 days on 32 processors to produce the fine mesh results which was considered overly computationally expensive taking into account only marginal differences between the two grids (less than 10%). Thus, medium mesh was considered to be of a sufficient accuracy and was also proven to be more than 4 times faster.

4.2.4 Importance of the Discretisation Schemes

Selection of the discretisation schemes was also found to be critical in the transitional flow regime and it is not widely stressed in the literature. This was discovered during preliminary OpenFOAM simulations where low order accuracy schemes were used (Table 4.6). Whilst the results were reasonable in the laminar regime, this numerical setup almost fully damped the unsteady flow occurrence shown clearly afore. This is well shown by the contrasting velocity contours in Figure 4.9. The low order discretised domain resulted in much lower peak velocities (Figure 4.9a) compared to the higher order discretisation output (Figure 4.9b).

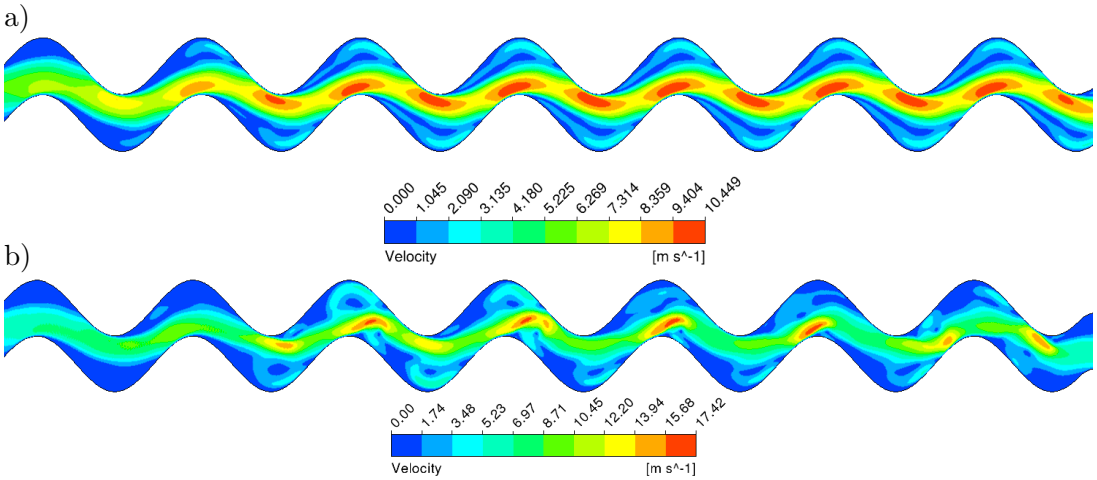

Figure 4.9: Velocity magnitude contours of OpenFOAM a) using first order momentum dominant discretisation (Table 4.6) and b) 0.006 s after the higher order discretisation (Table 4.14) was enabled, ($\gamma = 0.375$, $\epsilon = 1.0$) .

To assess the differences further, overall pressure drop through the channel was compared in Figure 4.10. An almost 50% lower pressure drop was predicted with the lower order discretisation. This limits the use of low accuracy discretised domain to steady state predictions. The result also questions accuracy of various CFD HE corrugation literature studies which do not acknowledge the unsteady flow whilst provide the predictions in the order of ($Re = \mathcal{O}(10^3)$).

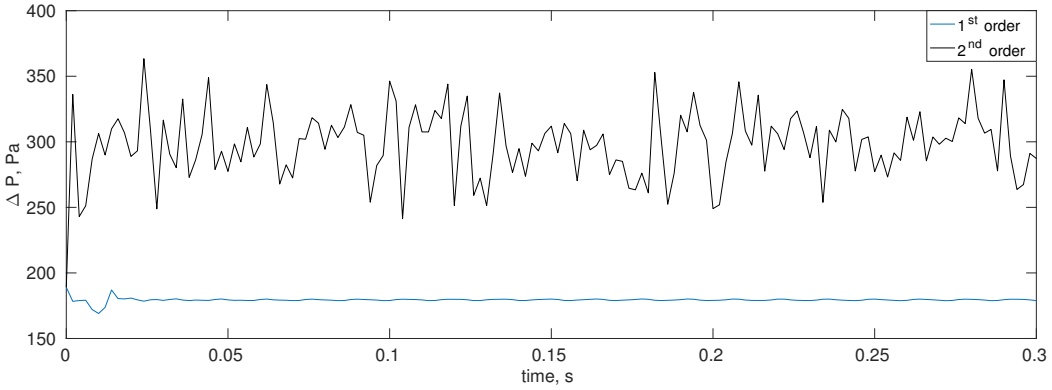

Figure 4.10: Pressure drop comparison between OpenFOAM predictions using low order (blue line) and higher order (black line) discretisation approaches. $Re = 500$, $\Delta t = 1 \times 10^{-6}$ s, data acquired at $f = 500$ Hz ($\gamma = 0.375$, $\epsilon = 1.0$).

Gradient	leastSquares
Pressure	leastSquares
Momentum	bounded Gauss upwind
Turbulent Kinetic Energy	bounded Gauss upwind
Specific Dissipation Rate	bounded Gauss upwind
Energy	bounded Gauss upwind
Transient	Euler

Table 4.6: First order accuracy dominant discretisation approach.

4.3 Steady-State Modelling Results

4.3.1 Periodic Domain Verification with the Literature

Periodic domain predictions were compared to the results of Zhang et al. [146] (Figure 4.11) using Fanning friction (Equation 4.3) and Colburn (Equation 4.4) factors. It should be noted that whilst both periodic flow and heat transfer were resolved with ANSYS Fluent, OpenFOAM predictions were limited to the flow predictions. This was done because the periodic heat transfer model from Patankar et al. [147] was not implemented in the open-source alternative. The results revealed that whilst the predictions between OpenFOAM and Fluent agree well, both solutions diverge from the literature study as the Reynolds numbers increase. A couple of potential reasons were identified. Firstly, Zhang et al [146] used a lower resolution grid than the current study (55×100 by Zhang et al. [146] to 60×180 here). The lack of resolution in the horizontal direction explains slightly different flow reattachment points shown in Figure 4.12. This in turn could cause a difference in the overall pressure gradient and heat transfer predicted.

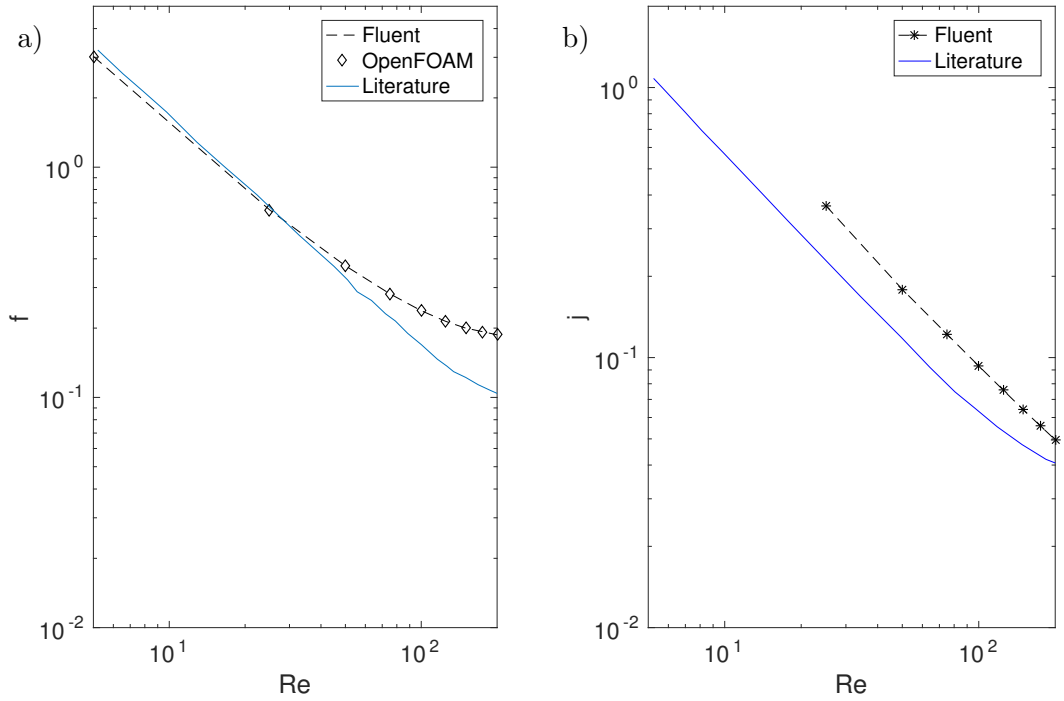

Figure 4.11: a) Fanning friction factor f and b) Colburn factor j predictions for a range of Reynolds numbers compared to Zhang et al. [146] ($\gamma = 0.25$, $\epsilon = 1.0$).

Secondly, Zhang et al. [146] study was published in 2004, thus, limited computational power and accuracy can be assumed. This could have resulted in their use of lower computing precision, examined with ANSYS Fluent (Table 4.7). In addition, this was checked using the coarse mesh resolution. However, the investigation revealed an opposite trend - decreasing mesh resolution increases the friction and colburn factors whilst change in computing precision made no difference. Thus, it was concluded that the differences were most likely due to other solution inaccuracies as Zhang et al. [146] did not acknowledge unsteady flow and showed steady-state results up to $Re = 300$. However, at $Re = 300$ a clear unsteady flow solution exists and is shown later in the chapter (Section 4.4). Because of the various potential reasons identified, the direct numerical match mesh to Zhang et al. [146] was not attempted further. A further visual comparison of predictions was undertaken using flow streamlines (Figures 4.12). No significant differences between the solutions were observed, however, current predictions are believed to be more reliable as they use a higher resolution grid. In addition, current predictions were verified using two different software packages producing identical results.

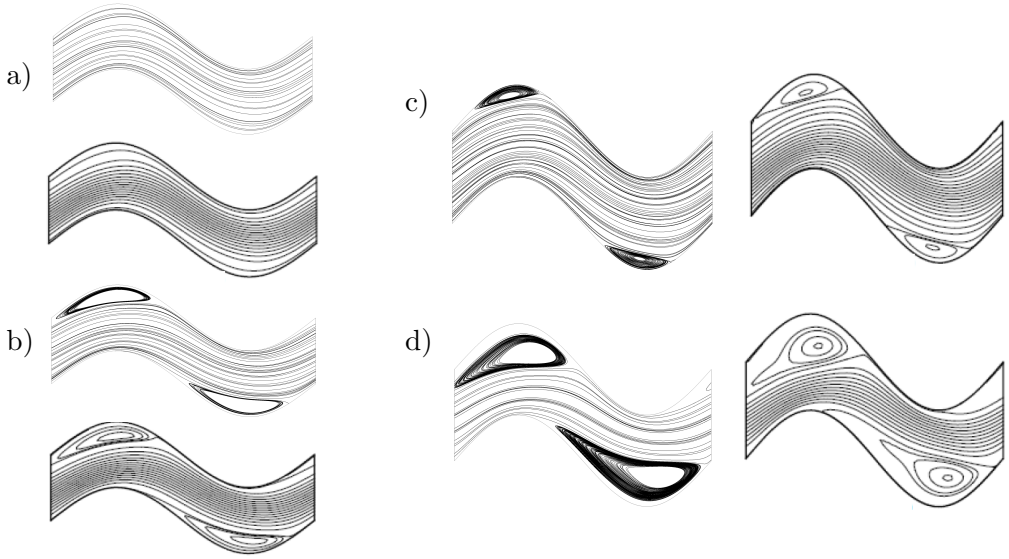

Figure 4.12: Streamline comparison with Zhang et al. [146]: Fluent predictions (top) to literature (below) at a) $Re = 50$ and b) $Re = 200$ ($\gamma = 0.25$, $\epsilon = 1.0$) and Fluent predictions (left) to literature (right) at c) $Re = 50$ and d) $Re = 200$ ($\gamma = 0.375$, $\epsilon = 1.0$).

	f at $Re = 50$	f at $Re = 175$	j at $Re = 50$	j at $Re = 175$
Literature, [146]	0.324	0.1221	0.118	0.047
Coarse mesh - SP	0.468	0.233	0.180	0.054
Coarse mesh - DP	0.468	0.233	0.180	0.054
Medium mesh - DP	0.433	0.214	0.179	0.056

Table 4.7: Fanning friction (f) and Colburn factor (j) data with $\gamma = 0.25$, $\epsilon = 1.0$ (SP - single and DP - double precision).

4.3.2 Steady-state Finite Length Channel Model Results

4.3.2.1 Comparison to the Periodic Domain

Firstly, simulations were completed in the steady-state regime ($5 \leq Re \leq 100$) to compare the periodic and finite length channel domains using ANSYS Fluent (Figures 4.13 & 4.14). Pressure drop comparison is undertaken in Figure 4.13a and shows that at low Reynolds numbers the pressure drop stabilises instantly inside the finite length channel. Only at $Re = 100$ the flow requires two sinusoidal periods to fully develop, but it did not affect the results significantly. However, it should be noted that in this case the flow development length was potentially made shorter due to the inclusion of the inlet section to the finite length domain. Pressure drop at each periodic sinusoidal unit of the finite channel also agreed reasonably well with the fully periodic simulations marked as dotted lines. This suggests suitability of the fully periodic model proposed by Patankar et al. [147] for the pressure drop predictions at low Reynolds number flows away from the inlet.

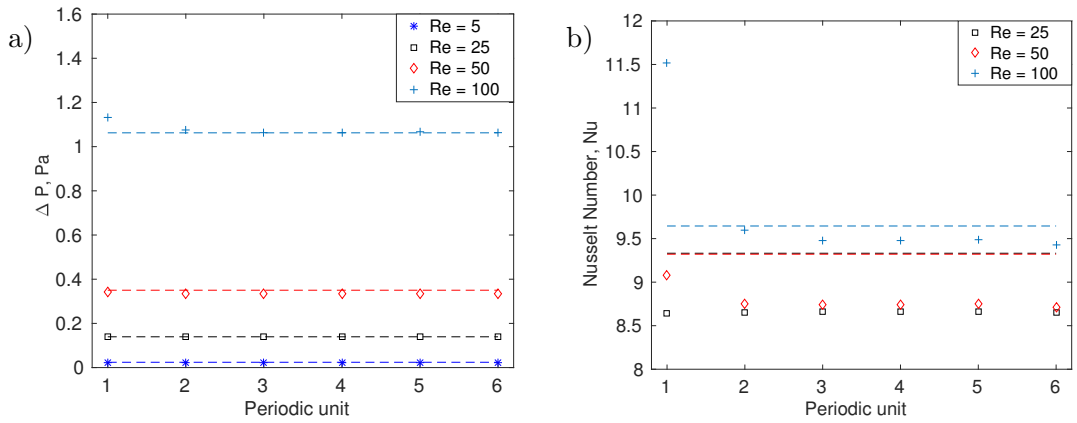

Figure 4.13: a) Pressure drop and b) Nusselt number through the periodic units. Points show data at each period of the channel whilst dotted lines (- -) represent data from fully periodic flow modelling ($\gamma = 0.375$, $\epsilon = 1.0$).

Figure 4.13 also shows a clear relation between the pressure drop and heat transfer. Stabilisation in ΔP leads to constant heat transfer through the channel periods whilst the Nusselt number is enhanced where the flow is developing. However, correlation between the periodic and finite channel domains was worse in terms of the heat transfer (Figure 4.13b). It was particularly inaccurate at the low Reynolds numbers ($Re = 25$ and $Re = 50$) with the predictions becoming only reasonably accurate at $Re = 100$. The discrepancies at low Reynolds numbers are suspected to be caused by the inlet temperature boundary scaling, required to estimate periodic heat transfer (Patankar et al. [147]). This locks inlet temperature to a certain average value and leads to practically identical Nusselt number predictions at $Re = 25$ and $Re = 50$ whilst Figure 4.14 provides further visual information. In the finite length channel the flow reaches uniform temperature right at the inlet due to low flow velocity at $Re = 25$ (Figure 4.14c) and $Re = 50$. However, in case of the periodic domain the prediction becomes distorted (Figure 4.14b). At $Re = 100$ this is not the case any more due to the increased flow velocity and a more accurate Nusselt number prediction is obtained (Figure 4.14b & 4.14d). However, due to the afore mentioned accuracy problems the use of periodic heat transfer estimates is severely limited in this project.

Re	u_{in}	τ_r, s	Δt, s	Iterations	Saving frequency, iterations
200	1.31	0.0763	2.5×10^{-6}	80000	800
300	1.97	0.0509	1.67×10^{-6}	122000	1200
400	2.62	0.0382	1.2×10^{-6}	167000	1600
500	3.27	0.0305	1×10^{-6}	200000	2000
1000	6.54	0.01525	0.5×10^{-6}	400000	4000

Table 4.8: Summary of simulation time-step scaling.

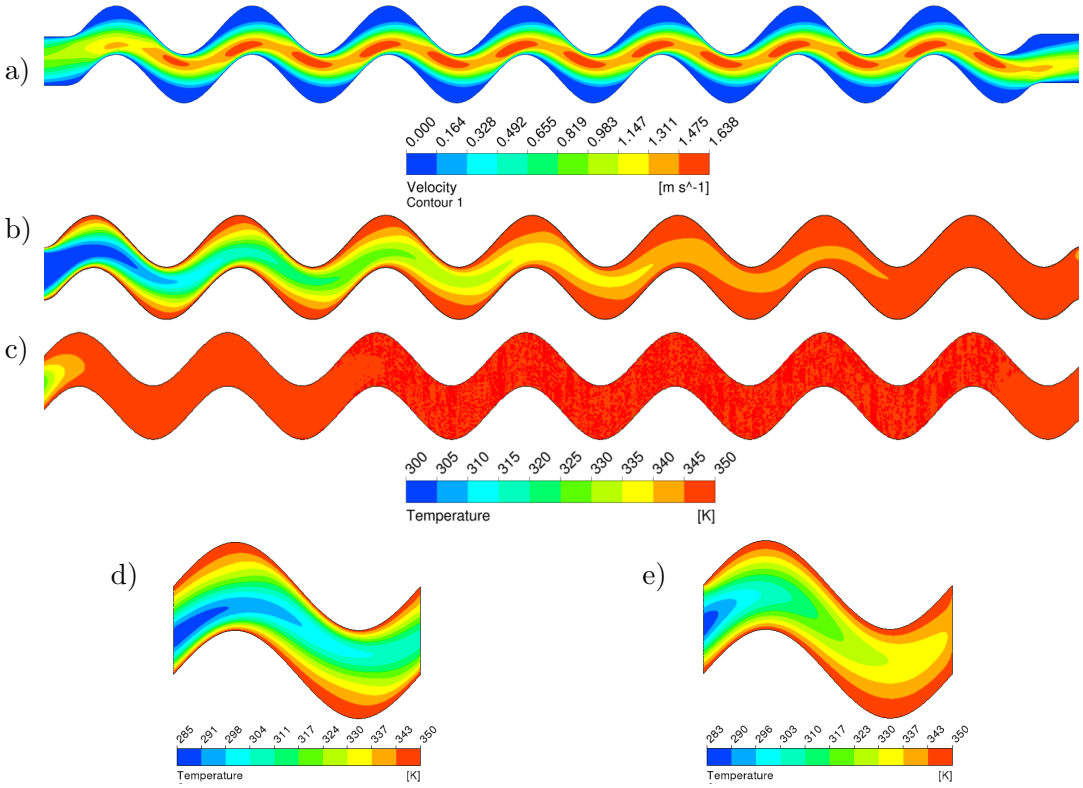

Figure 4.14: a) Velocity magnitude contours at $Re = 100$. Steady state temperature contours at b) $Re = 100$ c) $Re = 25$ with finite length model and d) $Re = 100$ e) $Re = 25$ with fully periodic prediction ($\gamma = 0.375$, $\epsilon = 1.0$).

4.4 Unsteady Flow Results

4.4.1 Onset of the Unsteady Flow

Unsteady flow and heat transfer onset is analysed in this section to understand the impact it has on the flow and heat transfer inside the sinusoidal channel. Additionally, it is compared to a steady-state simulation result obtained with a fully periodic model, a conventional way to predict such flows. Initial flow field for the transient simulation was a steady-state result, obtained using pseudo-transient solution stability feature of ANSYS Fluent. It allows the simulations at $Re \geq 200$ to arrive to a pseudo steady-state solution and was used for a periodic domain prediction in Figure 4.15. Time-steps for the transient simulations were scaled based on the time-step independence study (Section 4.2) where the domain with $u_{in} = 3.27\ m/s$ was time-step independent at $\Delta t = 1 \times 10^{-6}\ s$. Using the length of the channel in the flow-wise direction ($x = 0.1\ m$) an approximate time for the fluid to pass the domain was calculated: $\tau_r = 0.1m/3.27(m/s) = 0.0305\ s$. This allows non-dimensionalise the simulation time-step: $\tau_n = \Delta t/\tau_r = 1 \times 10^{-6}(s)/0.0305(s) = 3.28 \times 10^{-5}$. The relation $\Delta t = \tau_n \tau_r$ was then used to calculate the Δt for simulations at different Reynolds numbers (Table 4.8).

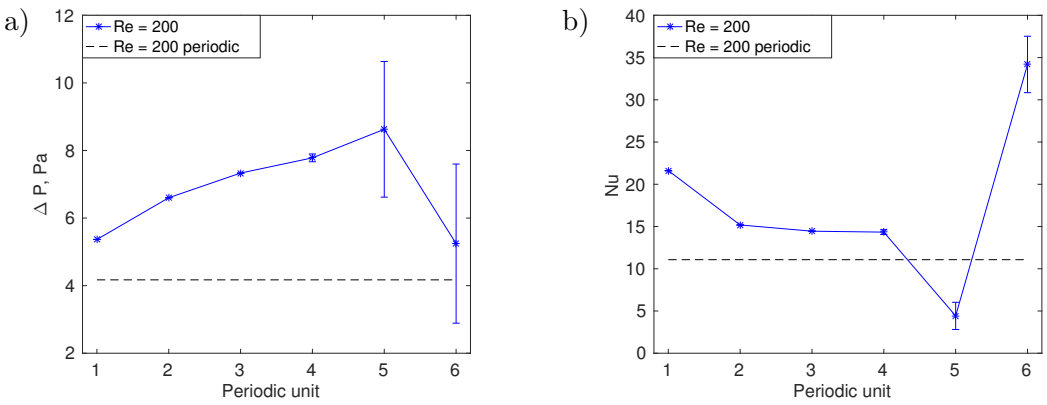

Figure 4.15: a) Pressure drop and b) Nusselt number through the periodic units. Modelled with $k-\omega$ SST assumption ($\gamma = 0.375$, $\epsilon = 1.0$). Dotted line shows the steady-state periodic prediction.

Figure 4.15 compares the finite channel predictions with the onset of the transitional flow to the fully periodic steady-state prediction. In addition, velocity and temperature contours of the finite length channel are given in Figure 4.16. It can be clearly seen, that the periodic domain fails to accurately predict both the pressure drop and there heat transfer where the transitional behaviour of the flow is clear, despite being a reasonable assumption at lower Reynolds numbers. The solution unsteadiness levels are displayed using error bars which show standard deviation at each finite channel period. The results also show that the highest pressure drop is measured at the HE corrugation period where the unsteady flow develops (Figure 4.15). This in turn leads to a drop in the Nusselt number and suggests that the unsteady flow onset creates an initial blockage in the channel. However, as the unsteady flow develops, a significant pressure drop reduction is then coupled with a sharp increase in Nusselt number. This signifies the importance of forced convection heat transfer (mixing) and agrees with observations in [158, 159] that the heat transfer increases in the transitional Reynolds regime.

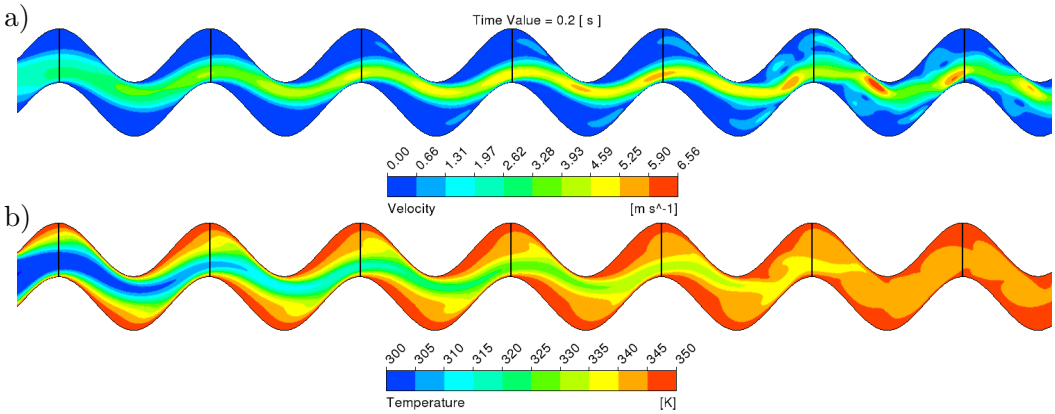

Figure 4.16: a) Velocity and b) Temperature contours at $Re = 200$. Modelled with $k-\omega$ SST assumption. ($\gamma = 0.375$, $\epsilon = 1.0$). Dotted line shows the steady-state periodic prediction.

4.4.2 Contrasting the Different Flow Models

Effects of the unsteady flow are further studied in Figures 4.17 - 4.19 using laminar, $k-\omega$ SST and $k-\epsilon$ momentum models at the $200 \leq Re \leq 500$. In terms of the trend-wise behaviour, results of the $k-\omega$ SST and laminar models (Figures 4.17 & 4.18) were similar. However, laminar model predicts greater levels of unsteady flow and earlier flow instability development in the computational domain. A sharp drop in the Nusselt number is observed at the instability onset which even enters the negative range inside the channel (laminar model only, Figure 4.18). Further investigation of the results revealed that at the corrugation period where the flow instability develops $T_{in} > T_{out}$, contrary to all the other channel periods where $T_{in} < T_{out}$ was found. The cause of it is thought to be a blockage in the flow at this location (identified by the peak in ΔP), relating to unsteady flow onset and resulting in a local heating up of the fluid. However, after this period the pressure drop reduces and the heat transfer is significantly enhanced by the unsteady flow. This again agrees with the experimental studies [159, 158] where it is noted that the transitional Reynolds number regime is beneficial for heat transfer.

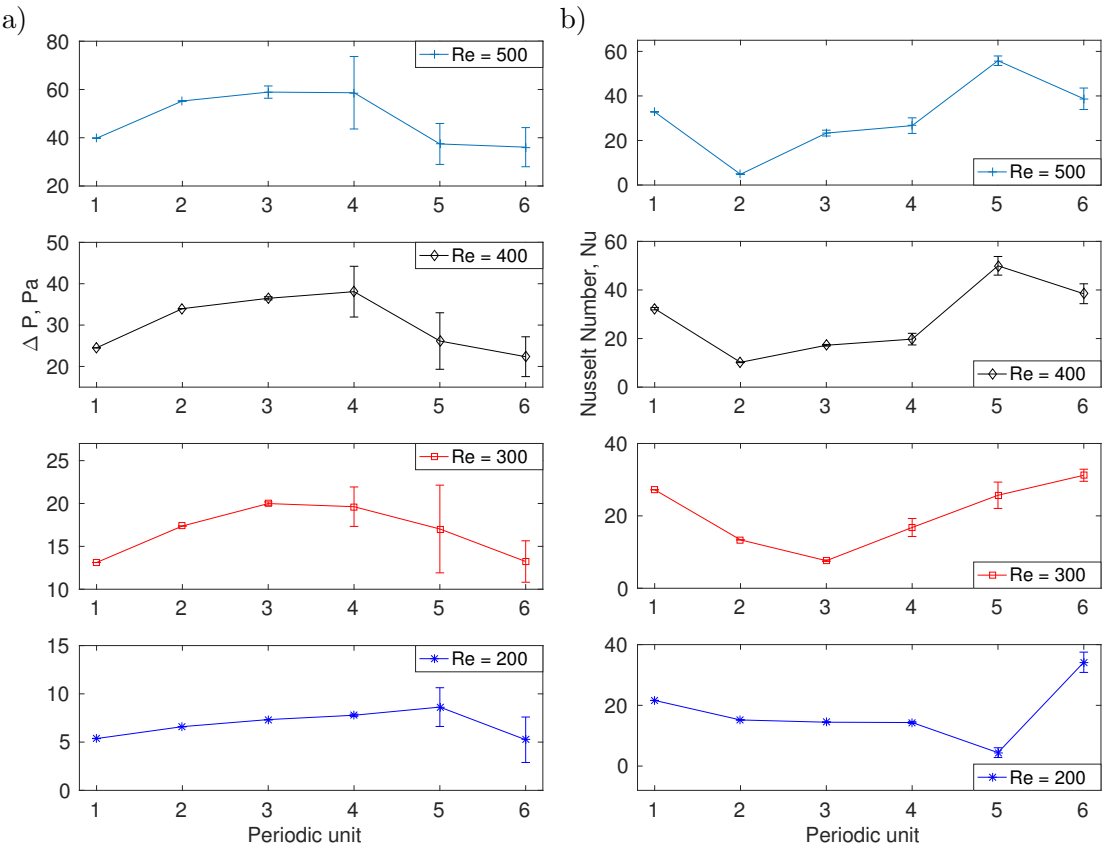

Figure 4.17: a) Pressure drop and b) Nusselt number through periodic units at various Reynolds numbers. Modelled with $k-\omega$ SST assumption. ($\gamma = 0.375$, $\epsilon = 1.0$).

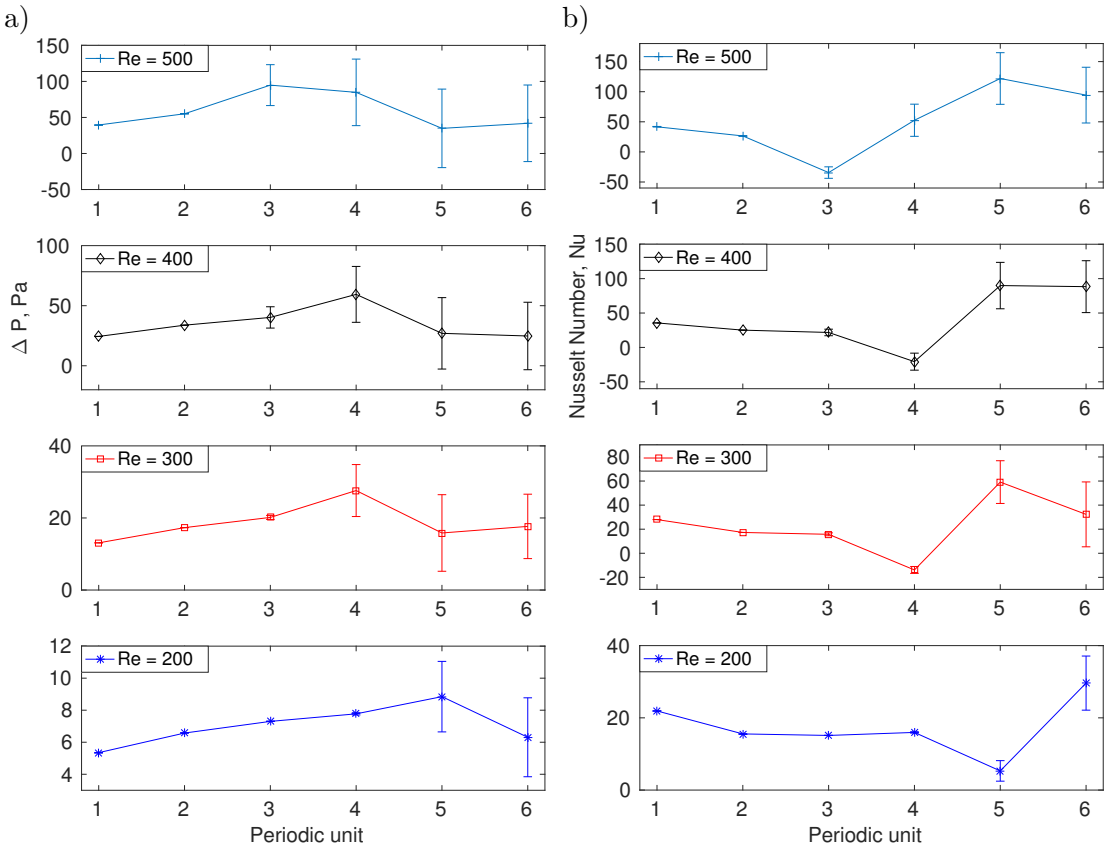

Figure 4.18: a) Pressure drop and b) Nusselt number through periodic units at various Reynolds numbers. Modelled with laminar assumption. ($\gamma = 0.375$, $\epsilon = 1.0$).

No unsteady flow was predicted by the $k - \epsilon$ model (Figure 4.19). This leads to completely different flow and heat transfer predictions compared to the laminar and $k - \omega$ SST models (Figure 4.17 & 4.18). It suggests inaccuracy of the $k - \epsilon$ model, especially for wall dominated flows. Such prediction was expected based on the previous experience and findings in the PhD thesis by Woods [127] where it was concluded to be an unsuitable model for the problems where accurately resolving the flow separation is important. It was nonetheless included in this study as the $k - \epsilon$ assumption is still encountered in the HE corrugation articles and in the HE industry. Figure 4.20 further illustrates the differences in the predictions of laminar, $k - \omega$ SST and $k - \epsilon$ models. The first two flow assumptions predict the unsteady flow despite resolving the instability level differently due to the different way in solving the momentum equation. The $k - \epsilon$ model completely fails to predict the unsteady flow and confirms its unsuitability for transitional Reynolds number regime.

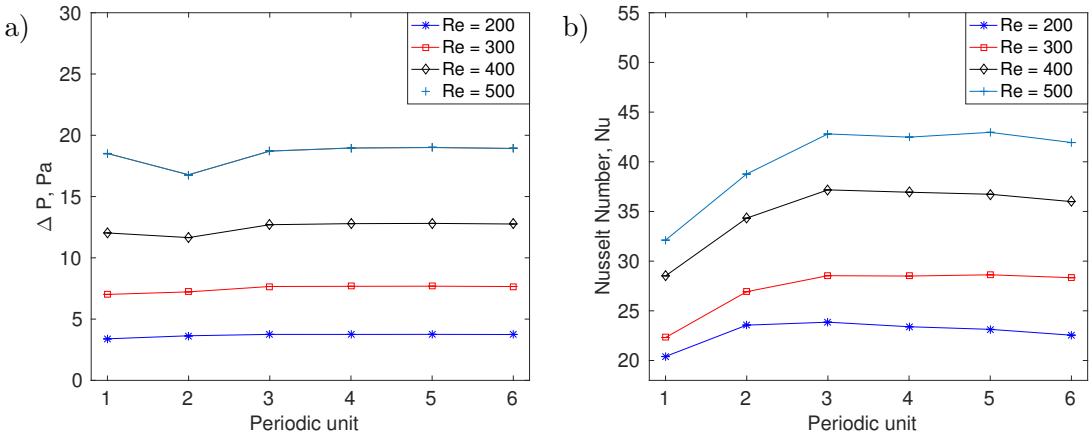

Figure 4.19: a) Pressure drop and b) Nusselt number through periodic units at various Reynolds numbers. Modelled with $k-\epsilon$ model. ($\gamma = 0.375$, $\epsilon = 1.0$).

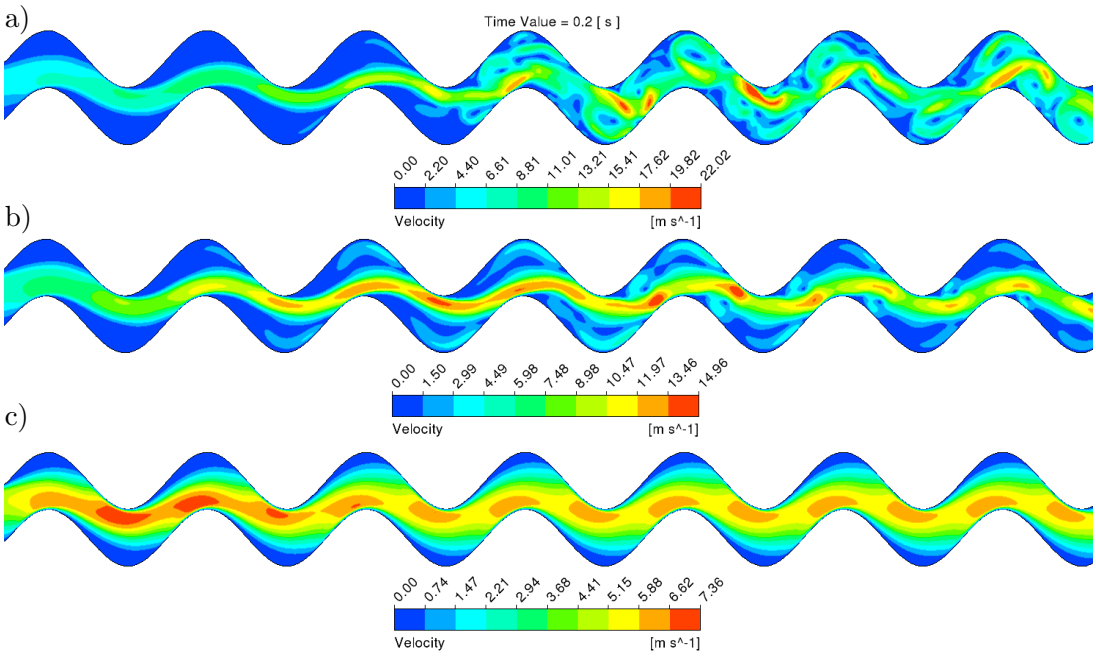

Figure 4.20: Velocity magnitude contours at $Re = 500$ using a) laminar b) $k-\omega$ SST and c) $k-\epsilon$ models. ($\gamma = 0.375$, $\epsilon = 1.0$).

4.4.2.1 Comparing the Overall Channel Performance

Overall channel performance was additionally compared at $5 \leq Re \leq 500$ using laminar, $k-\omega$ SST and $k-\epsilon$ models. Here the simulations were undertaken using ANSYS Fluent and the overall ΔP and Nusselt number were employed (Figure 4.21). The unsteady flow predictions ($Re \gtrsim 200$) were time-averaged and the flow instability levels were measured using standard deviation for the laminar and $k-\omega$ SST models (Table 4.9). In terms of the pressure drop (Figure 4.21a) the predictions started to differentiate between the three models at the unsteady flow onset ($Re \approx 200$). However, the $k-\epsilon$ model produced radically different results from the other two models.

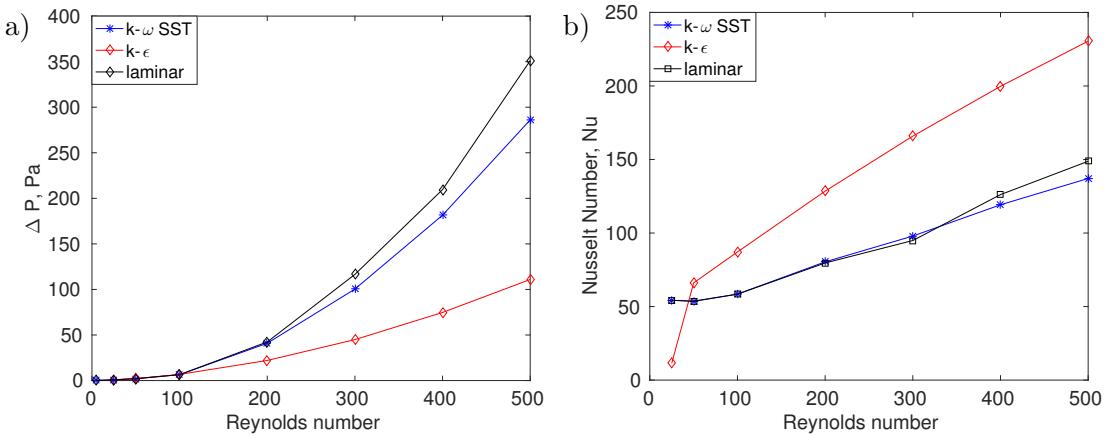

Figure 4.21: a) Pressure drop and b) Nusselt number through periodic units at various Reynolds numbers. Modelled with $k-\epsilon$ assumption. ($\gamma = 0.375$, $\epsilon = 1.0$).

It under-predicted the pressure drop and over-predicted the Nusselt number (around twice at $Re = 500$), questioning its accuracy again. Laminar model predicted higher pressure drop (up to 20%) and heat transfer (up to 10%) compared to the $k-\omega$ SST assumption. Nonetheless, both of these models show similar results overall, suggesting better quality of the predictions. Thus, it was concluded that $k-\omega$ SST model should be used for predictions in the unsteady flow regime. This was decided because the $k-\omega$ SST model is more suitable for predicting turbulent wall dominated flow than the laminar model. In addition, $k-\omega$ SST model produced similar results in the low Re range to the laminar model and converged faster. Thus, the $k-\omega$ SST model is a safer choice since it is not clear at which Reynolds number the flow turbulence onsets (laminar model fails to predict such flows efficiently).

Re	Laminar		$k-\omega$ SST	
	σ, ΔP, Pa	σ, Nu	σ, ΔP, Pa	σ, Nu
200	3.91	3.94	3.2	2.47
300	10.54	7.87	5.79	0.62
400	28.99	9.15	12.32	1.15
500	57.56	10.34	20.56	0.909

Table 4.9: Fluctuations in quantities using different models.

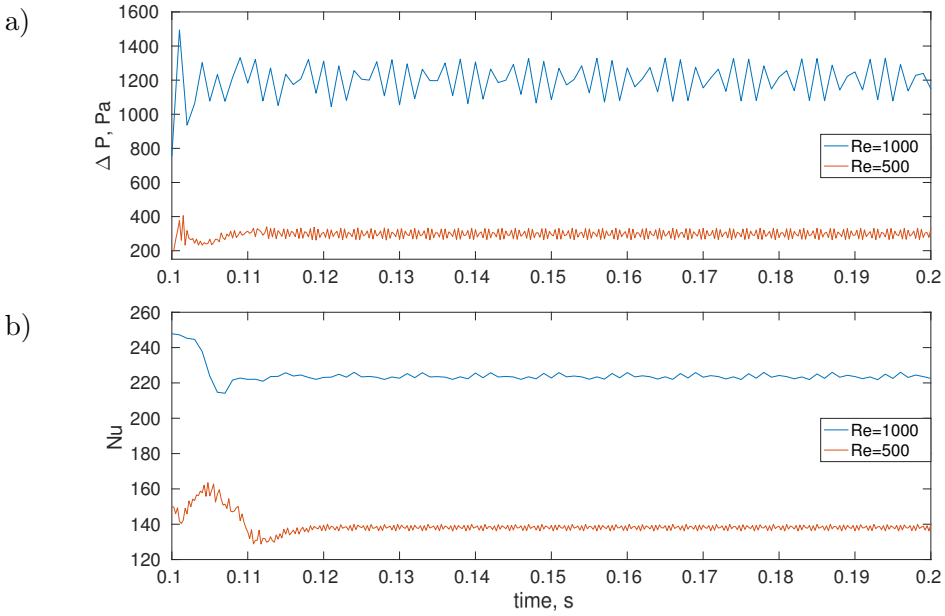

Figure 4.22: a) Pressure drop (ΔP) and b) Nusselt number through a finite length channel ($\gamma = 0.375$, $\epsilon = 1.0$).

4.4.3 Unsteady Flow at Higher Reynolds Numbers

Additional simulation was completed using the same numerical setup at $Re = 1000$ with $k-\omega$ SST model and ANSYS Fluent to check whether the flow instability persists (Figure 4.22). Both simulations were initialised using low order discretisation schemes (Table 4.6) to obtain a steady-state solution. The data was also time-averaged (Table 4.10) and revealed that the four times increased pressure drop resulted in only twice improved heat transfer performance in terms of the Nusselt number. The development

Re	ΔP, Pa	Nu	σ, Δp, Pa	σ, Nu
500	298	138	24.0	1.2
1000	1206	224	93.7	1.3

Table 4.10: Time averaged data of the two simulations.

of flow and heat transfer along the channel is further analysed in the Figure 4.23. The graphs show that at the $Re = 1000$ unsteady flow onsets a period earlier (period 3 at $Re = 1000$ versus period 4 at $Re = 500$) and much higher flow and heat transfer instability levels are observed. The unsteady flow then results in increased Nusselt number, improving heat transfer. However, increasing Reynolds number leads to higher pressure drop increase than the heat transfer enhancement, making this corrugation less efficient overall at higher flow rates.

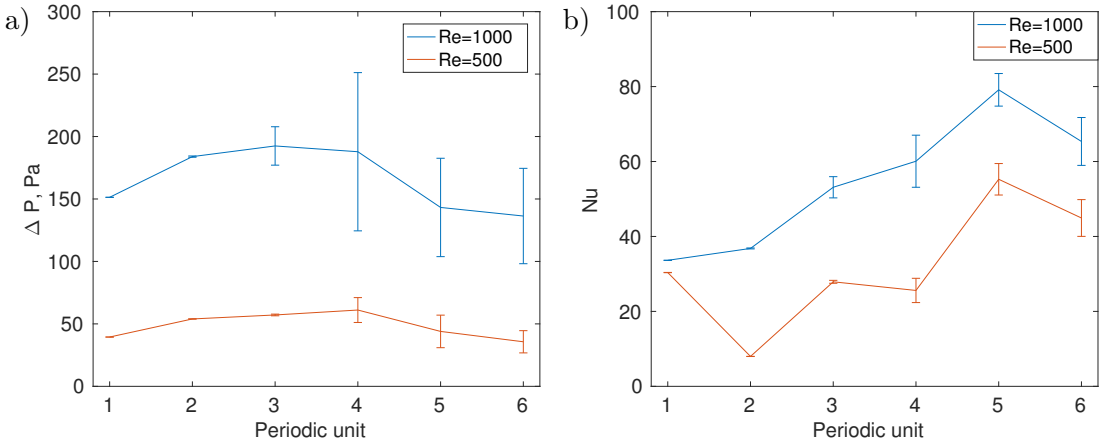

Figure 4.23: a) Pressure drop and b) Nusselt number through the finite length channel ($\gamma = 0.375$, $\epsilon = 1.0$).

4.5 Comparing OpenFOAM to ANSYS Fluent

4.5.1 Steady-state OpenFOAM Predictions

In this subsection suitability of the open-source OpenFOAM code is evaluated by comparing it against the commercial ANSYS Fluent. This was driven by two reasons: firstly, OpenFOAM is free which reduces the overall cost of calculations. Secondly, as OpenFOAM is open-source, it is easy to access and modify the code compared to ANSYS Fluent where it is harder to know the exact implementation of numerics. Firstly the steady-state simulation results are compared visually in Figures 4.24 & 4.25 where nearly identical performance can be observed. Overall performance of the channel models is then summarised in Table 4.11 and a good correlation between the two codes is found. The pressure drop agrees almost identically whilst the heat transfer is predicted only marginally different between OpenFOAM and ANSYS Fluent.

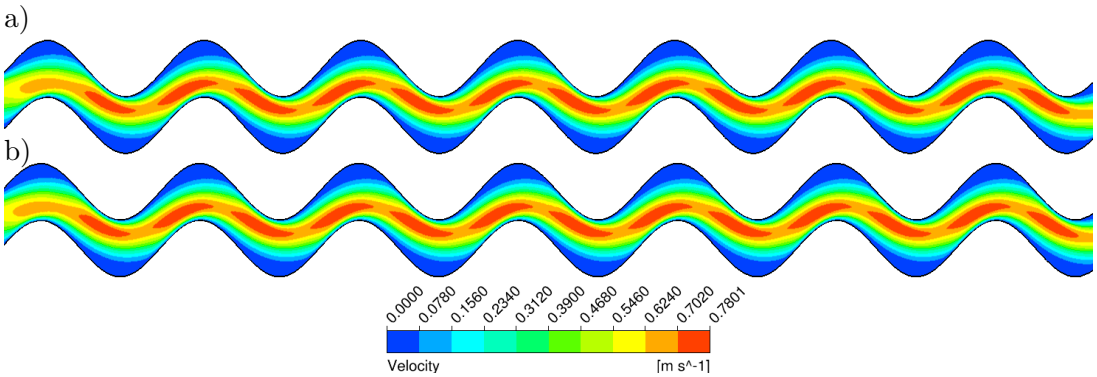

Figure 4.24: Velocity magnitude contours of a) OpenFOAM and b) Fluent predictions at $Re = 50$ ($\gamma = 0.375$, $\epsilon = 1.0$).

The small differences in the heat transfer predictions are thought to relate to the minor discrepancies in the numerical solution. This can include different implementation of the discretisation schemes (Table 4.14) or slightly different levels of solution convergence.

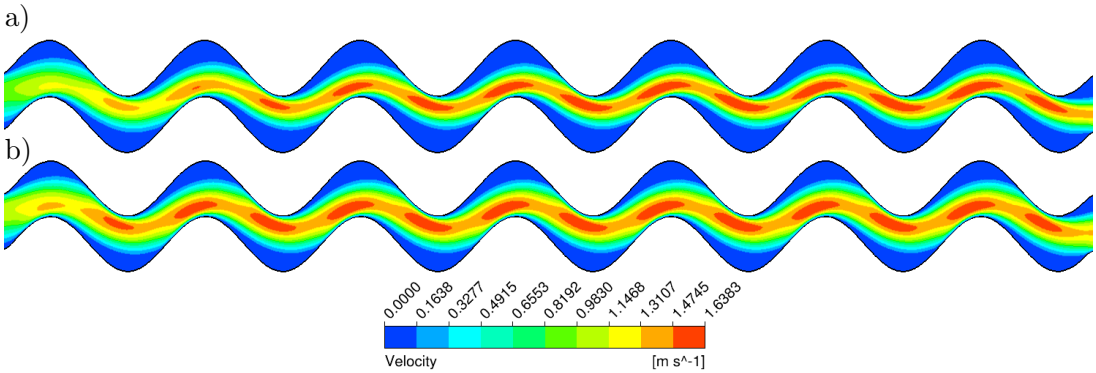

Figure 4.25: Velocity magnitude contours of a) OpenFOAM and b) Fluent predictions at $Re = 100$ ($\gamma = 0.375$, $\epsilon = 1.0$).

	ΔP		f		Nu		j	
Re	Fluent	OF	Fluent	OF	Fluent	OF	Fluent	OF
5	0.143	0.143	0.128	0.126	-	-	-	-
25	0.831	0.804	0.0296	0.0282	53	55	2.394	2.511
50	2.017	2.016	0.0172	0.0176	54	57	1.206	1.310
100	6.478	6.491	0.0138	0.0139	58	62	0.656	0.697

Table 4.11: Non-periodic steady state data of ANSYS Fluent and OpenFOAM.

	value	units	Fluent	OpenFOAM
U_x	3.27	m/s	×	×
U_y	0	m/s	×	×
Turbulence kinetic energy, k	0.04	m^2/s^2	×	×
Specific dissipation rate, ω	274.5	$1/s$	×	×
Temperature	350	K	$uniform$	$T = 350$ $walls$ $T = 300$ $rest$

Table 4.12: Initialisation parameters of both codes for unsteady flow predictions.

4.5.2 Unsteady Flow Predictions with OpenFOAM

Following the good agreement between OpenFOAM and ANSYS Fluent in the steady-state regime, the unsteady flow behaviour was compared next to further ensure that OpenFOAM is capable of resolving flows in the transitional Reynolds regime using the $k - \omega$ SST turbulence model. To accomplish it, pressure drop and Nusselt number across the finite channel was measured at $Re = 500$. Initialisation was completed using low order discretisation schemes in both codes (Table 4.6) together with other initial

conditions (Table 4.12). Transient flow solver was then run from $t = 0$ s to $t = 0.1$ s using $\Delta t = 1 \times 10^{-5}$ s, providing the closest possible initial steady-state solution (Figure 4.26).

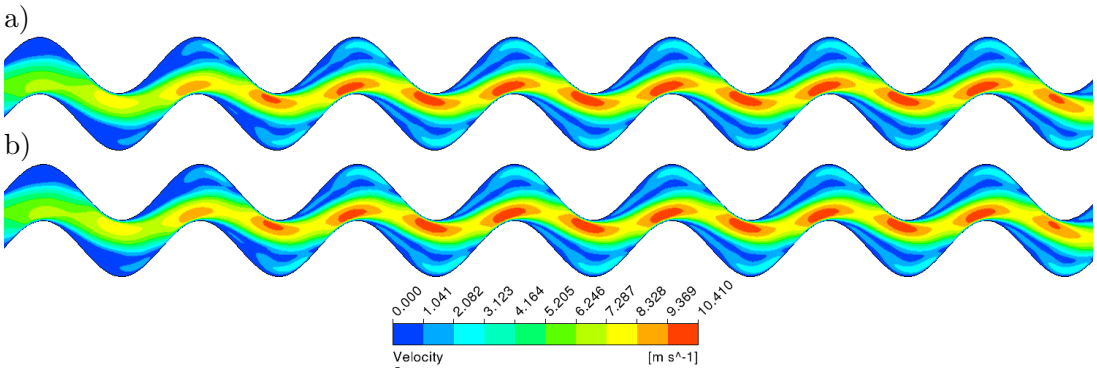

Figure 4.26: Velocity magnitude contours at the solution initialisation with a) OpenFOAM and b) Fluent predictions at $Re = 500$ and $t = 0.1$ s ($\gamma = 0.375$, $\epsilon = 1.0$).

However, the change to the higher order accuracy discretisation (Table 4.14) and decrease in the simulation time-step to $\Delta t = 1 \times 10^{-6}$ s yielded slightly different results between the two codes (Figure 4.27). OpenFOAM produced an overall more unsteady result (Figure 4.27), caused by small scale vortices being resolved slightly differently despite the identical mesh used (Figure 4.28). However, the time-averaged data (Table 4.13) shows results of significant similarity between the two codes. This allowed to conclude that the open-source OpenFOAM can be used for the HE applications of interest to the project.

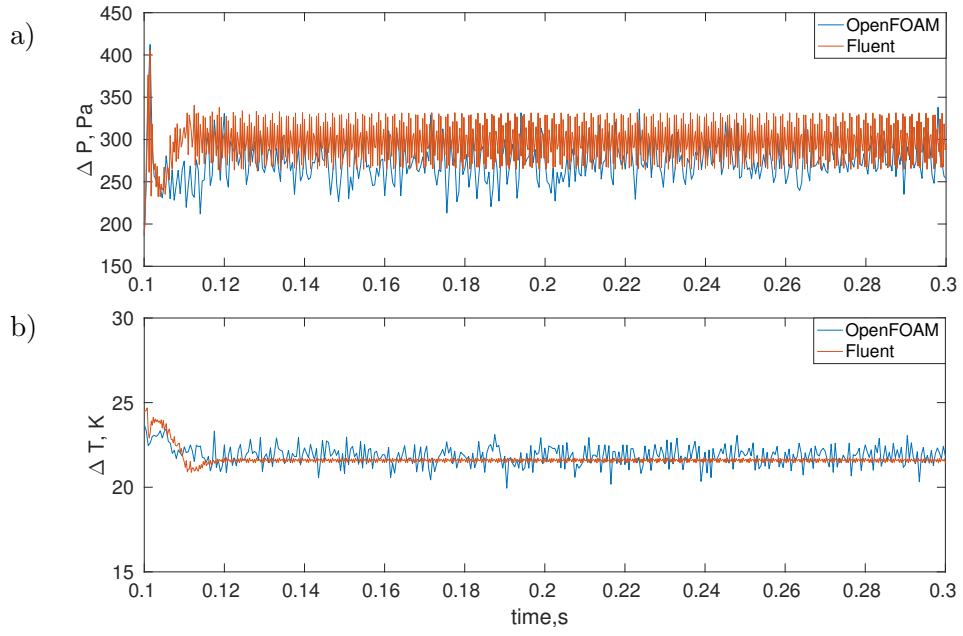

Figure 4.27: a) Pressure drop and b) Temperature change using Fluent ($f = 4000$ Hz) and OpenFOAM ($f = 2000$ Hz) at $Re = 500$ ($\gamma = 0.375$, $\epsilon = 1.0$).

	ΔP, Pa	ΔT, K	$\sigma\ \Delta P$, Pa	$\sigma\ \Delta T$, K
OpenFOAM	273	21.8	22.1	0.56
Fluent	298	21.6	24.0	0.11

Table 4.13: Time averaged OpenFOAM and Fluent prediction data.

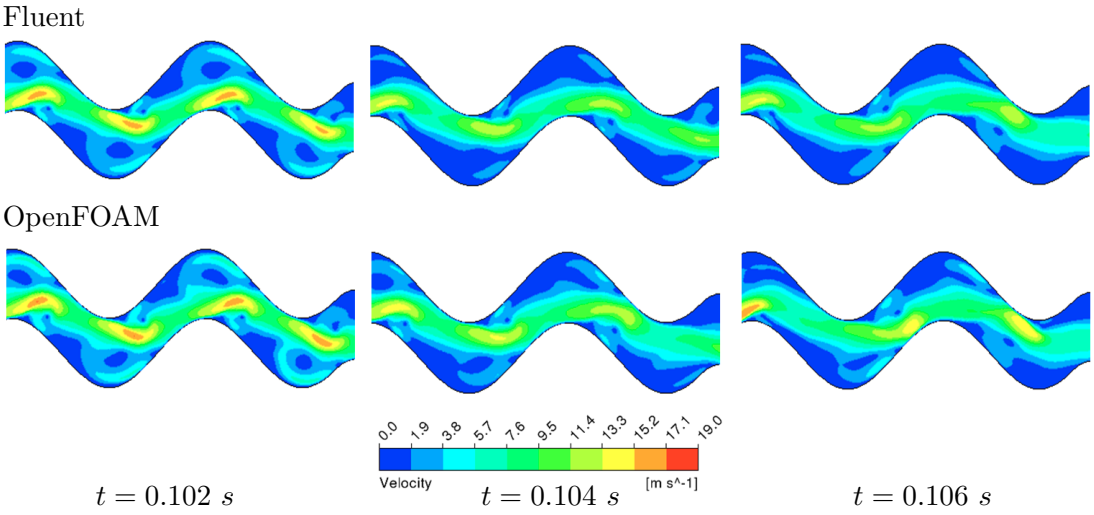

Figure 4.28: Velocity magnitude contours after the solution iniatialisation at the end of sinusoidal section, $Re = 500$ ($\gamma = 0.375$, $\epsilon = 1.0$).

	Fluent	OpenFoam
Gradient	Least Squares	leastSquares
Pressure	Second Order	leastSquares
Momentum	Second Order Upwind	bounded Gauss linear
Turbulent Kinetic Energy	First Order Upwind	bounded Gauss upwind
Specific Dissipation Rate	First Order Upwind	bounded Gauss upwind
Energy	Second Order Upwind	bounded Gauss linear
Transient	First Order Implicit	Euler

Table 4.14: Discretisation schemes after the initialisation for both codes.

4.5.3 Effects of the Low Order Discretisation

After identifying that the low order accuracy discretisation suppresses unsteady flow occurrence in the sinusoidal channel, a further study was undertaken at $25 \leq Re \leq 500$ to assess the influence its on both, the flow and the heat transfer performance. Thus, simulations using the two discretisation strategies (Table 4.6 vs 4.14) were run using the $k - \omega\ SST$ model in OpenFOAM. As seen in the Figure 4.29a, solutions with the higher order discretisation predicted significantly larger pressure drop across the channel. The difference between two approaches increased with Reynolds number (up to 30%) and was most likely caused by the failure of the low accuracy approach to predict the unsteady flow. However, the differences in domain discretisation were

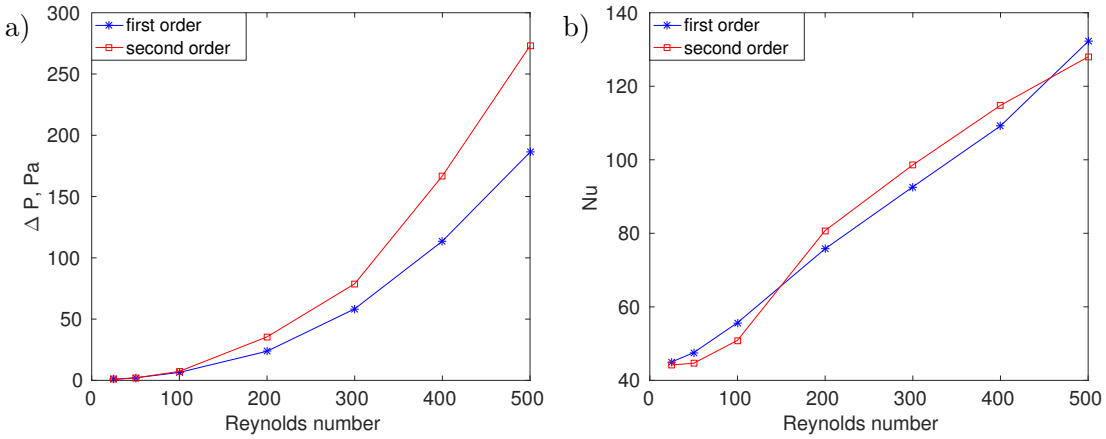

Figure 4.29: a) Pressure drop and b) Nusselt number through periodic units at various Reynolds numbers. Modelled with $k-\epsilon$ assumption. ($\gamma = 0.375$, $\epsilon = 1.0$).

found to have only a minor effect in heat transfer performance in terms of the Nusselt number (Figure 4.29b). Thus, the less accurate approach could be deemed acceptable for the situations where the simulation speed is prioritised over more accurate pressure drop prediction.

4.6 Summary of the Chapter

A two dimensional sinusoidal HE channel was used to assess different numerical modelling assumptions at $5 \leq Re \leq 1000$. Fully periodic and finite length channel computational domains were contrasted and fully periodic predictions were verified against a published study in a laminar flow regime. Compared to the finite length channel the periodic domain was found reasonable for pressure drop predictions in the steady-state laminar flow regime. However, the periodic domain had significant shortcomings for the heat transfer predictions which limited its use.

Laminar, $k-\omega$ SST and $k-\epsilon$ models were compared at $5 \leq Re \leq 500$ using a finite channel model. All the three models agreed well in steady-state laminar flow regime up to the onset of the unsteady flow ($Re \approx 200$). The $k-\epsilon$ model completely failed to predict the onset of the unsteady flow. It led to completely different solutions (e.g. up to 60% lower pressure drop) compared to both laminar and $k-\omega$ SST assumptions. A better agreement was found between the two latter models, however, the laminar model predicted higher pressure drop compared to the $k-\omega$ SST assumption (up to 20%). This was due to the higher levels of unsteady flow predicted by the laminar model. However, the heat transfer performance between the two models was found similar. It was concluded that using the $k-\omega$ SST is the right modelling approach in the transitional flow regime as it converged faster and is overall more suitable for highly unsteady wall-bounded flows, especially at higher Reynolds numbers.

Open-source CFD package OpenFOAM was compared to the commercial ANSYS Fluent. A good agreement was found between the two codes, confirming that OpenFOAM is suitable for HE despite the minor differences between the results of the two codes. OpenFOAM was also used to check sensitivity of the predictions to the numerical discretisation schemes. It was found that the low order domain approximation led to a lower pressure drop prediction (up to 30%) and omitted the unsteady regime. This, however, had only a minor influence over the Nusselt number predictions, enabling to conclude that the low accuracy discretisation approach could be used for certain applications where the computational cost is excessive.

Chapter 5

Heat Exchanger Modelling Validation

Contents

5.1 Introduction

In this chapter a plate-fin HE is selected in collaboration with an industrial partner to validate the developed CFD methodology. The HE unit experiments are completed using industrial equipment covering a broad range of Reynolds numbers to establish a

comprehensive dataset which is difficult to find in the literature. A range of HE corrugation computational domains are compared and their results are incorporated into the HE unit model. The HE unit is modelled by simplifying flow and heat transfer inside the HE core using porous media and heat transfer effectiveness models. CFD outputs are then compared to the experimental results in order to validate the numerical methodology.

5.2 Experimental Work

5.2.1 HE Unit

A compact plate-fin HE with serrated (off-set strip) corrugation (Figure 5.1a) which has an average hydraulic diameter of $d_h = 1.134\ mm$ was experimentally evaluated. Identical corrugation was used on both HE flow sides, arranged in cross-flow. The selected HE core has 10 cold (blue sections) and 9 hot (red sections) flow layers (Figure 5.1b) with individual HE core component geometry data in Table 5.1 and was manufactured using Aluminium 3003 alloy with its properties in Table 5.2. The assembled

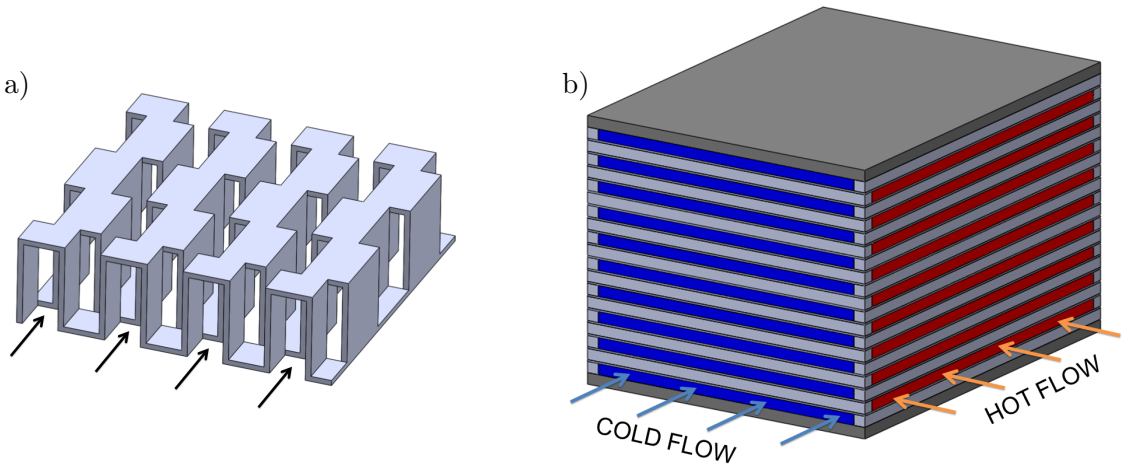

Figure 5.1: a) Schematic example of the serrated (off-set strip) corrugation and b) Schematic HE core model showing the flow directions.

HE is shown in Figure 5.2 with headers and bypass valves for both fluids (blocked with dummy valves during the experiments) and inlet/outlet ports of diameter $D = 17.62\ mm$ located on the fitting plate of the HE.

Part	Dimensions, (x, y, z, mm)
Top plate	$83.82 \times 64.77 \times 2.5$
Bottom plate	$83.82 \times 64.77 \times 2.5$
Partition sheet	$83.82 \times 64.77 \times 0.5$
Cold flow spacer	$83.82 \times 2.5 \times 2.5$
Hot flow spacer	$2.5 \times 64.77 \times 2.5$

Table 5.1: HE core geometry data prior to the vacuum brazing process. Empirical shrinkage coefficient of 0.958 should be used for post-brazing dimensions.

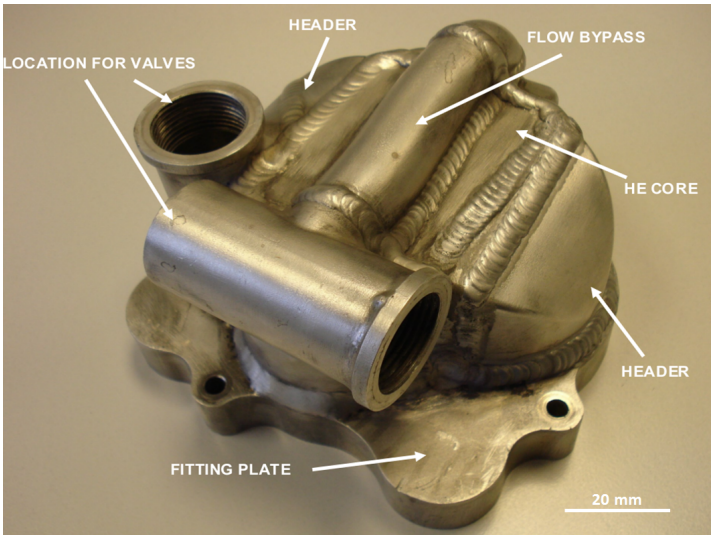

Figure 5.2: Assembled experimental HE unit with valves and headers. Inlet/outlet HE ports are located on the fitting plate.

Property	Quantity	Units
Density	2739	kg/m^3
Thermal Conductivity	168	$W/(mK)$
Specific Heat	910	$J/(kgK)$

Table 5.2: Properties of Aluminium 3003 used for plate-fin HE unit.

a) b)

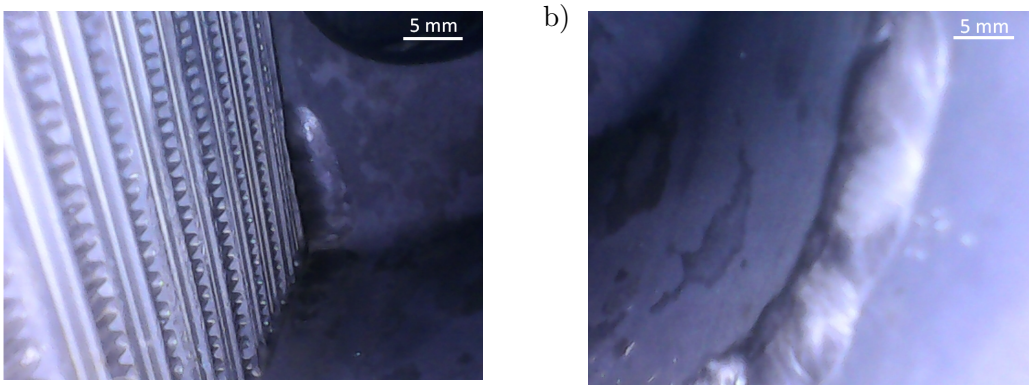

Figure 5.3: Flow blockages inside the cold flow outlet header: a) at the HE core b) at the outer walls of the header.

5.2.2 Inspection Inside the HE

A detailed visual investigation was completed inside the HE headers using a borescope. Design of the HE headers was found compromised in some areas by the thick welds (shown in Figures 5.2 & 5.5b) which occurred during the assembly process. The first defect was found at the cold flow outlet where part of the bottom HE core layer is blocked (Figure 5.3a). Additionally, thick welds were observed on the outer walls of the cold flow outlet header (Figure 5.3b). Similar flaws were also observed inside the

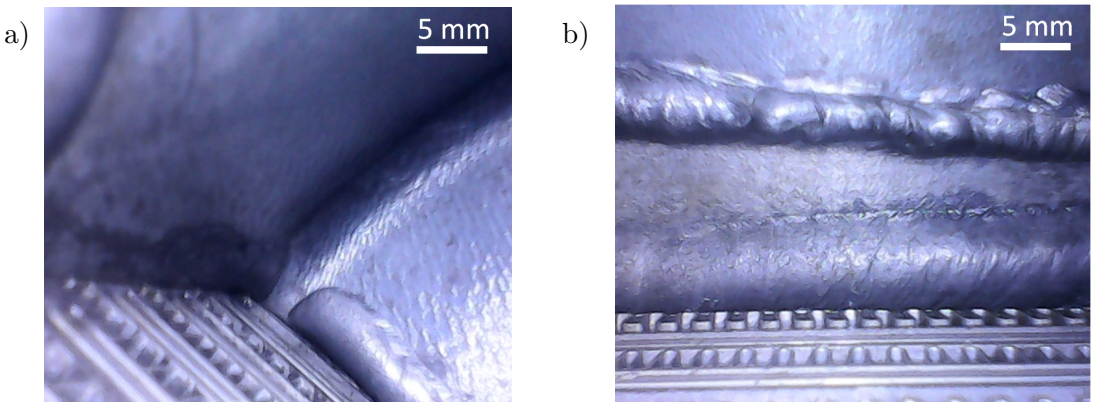

Figure 5.4: Flow blockages inside the hot flow headers at: a) inlet and b) outlet.

hot stream header (Figure 5.4). Welding flaws at the corners in all the HE headers were found to block multiple flow layers, an example is shown in Figure 5.5a. This was identified occurring at the meeting points of different welds, caused by prolonged HE unit exposure to heat (Figure 5.5b). It was considered the worst defect of the HE unit and the most important one to be aware of whilst validating the CFD predictions. It definitely affected the HE performance, estimated in the region of 2-10%, leading to a suspected increase in pressure drop and reduction in heat transfer.

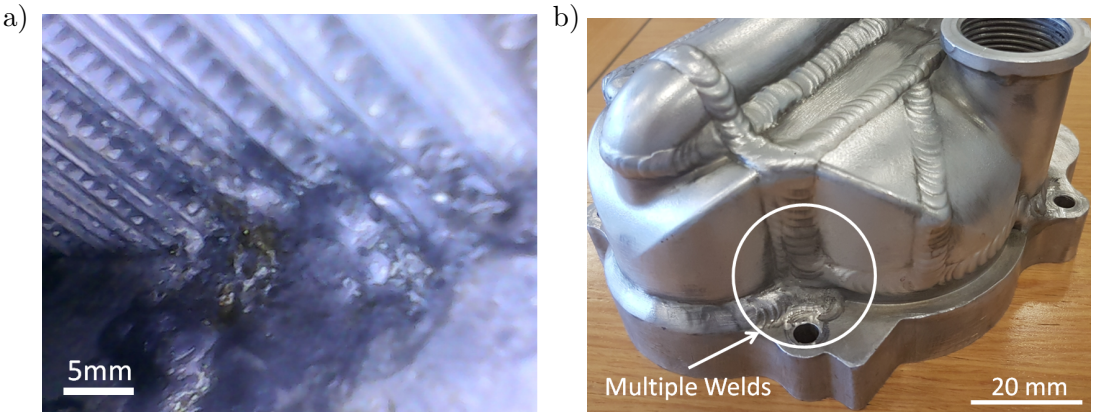

Figure 5.5: a) Multilayer blockage of the HE core layers, occurring at the meeting point of multiple welds. b) Outer HE view highlighting where the multiple welds meet.

5.2.3 Experimental Procedure

Comprehensive dataset was established using the experimental apparatus shown in Figure 5.7. Jet A1 fuel was used for the cold stream fluid and BP Turbo Oil 2380 was selected for the hot fluid side (Table 5.3). This selection provided contrasting fluid dynamics and heat transfer behaviour between the two fluid streams because approximately 5 times higher oil viscosity resulted in the hot side of the HE core remaining laminar. It also provided contrast in Prandtl numbers ($Pr = c_p\mu/(\rho k)$, a ratio between momentum and thermal diffusions) between the two fluids ($Pr_{oil} \approx 49$ and $Pr_{fuel} \approx 18$ during thermal performance testing). The experiments were split

	Cold flow, ΔT test	Hot flow, ΔT test	Cold flow, ΔP test	Units
ρ	781	926	743	ks/m^3
μ	0.0012	0.0031	6.1×10^{-4}	$Pa \cdot s$
C_p	2020	2111	-	$J/(kgK)$
Pr	18	49	-	-

Table 5.3: Properties of Fluids based on the measurements at the HE inlets during the experimental testing. ΔP and ΔT tests relate to isothermal pressure drop and thermal performance experiments respectively. Please note that both fluids are treated as Newtonian [171].

into two parts: pressure drop and thermal performance tests. HE unit flow resistance was established first using the cold fluid HE stream at isothermal conditions. Cold flow side rates were varied such that all three Reynolds regimes would occur inside the HE core: laminar, transitional and turbulent. Pressure drop was measured using SE labs pressure gauges 6.75" away from the inlet/outlet HE ports with Figure 5.6 showing the physical setup. Multiple flow rate meters (Table 5.4) were used during the experiments based on the test point planned (full list of the experimental points is in the Appendix (Tables A.1 to A.3)). Reliability of pressure drop experiments was established running each test point for 2 minutes in order to ensure steady-state was reached.

Thermal performance test measured the heat transferred between the two flow streams and was conducted by varying the cold stream flow rate whilst keeping the hot stream flow rate constant. A temperature difference of $\Delta T \approx 70\ K$ between the fluid stream inlets was maintained throughout the test to ensure a sufficient temperature gradient. The same flow rate meters (Table 5.4) were used together with thermocouples (tolerance of $T \pm 0.3\ K$) at the inlet and outlet ports to the HE unit. Heat loss to the environment was minimised by insulating the HE unit with calcium-magnesium silicate carbide sheets (Figure 5.8). To ensure reliability of the heat transfer data, each point was run up to 45 minutes in order to reach steady state and was repeated twice. However, pressure drop across the fluid streams was not measured during the thermal

performance test assuming that change in temperature would produce a negligible effect to the flow resistance characteristics of HE unit.

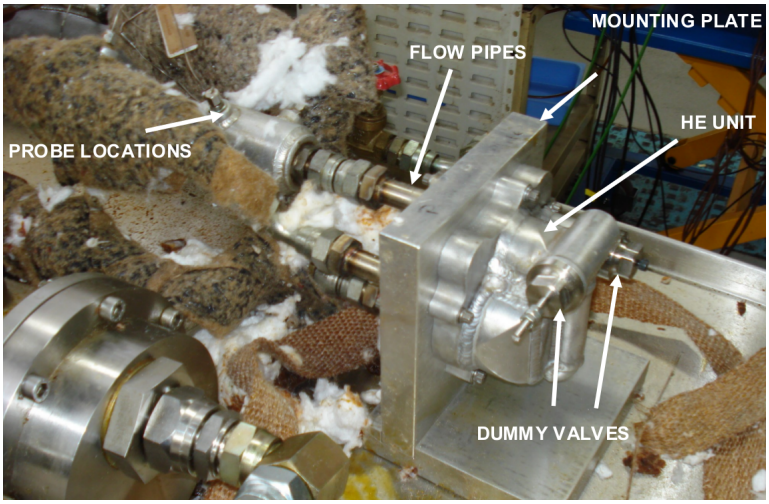

Figure 5.6: Uncovered HE unit after the experiments.

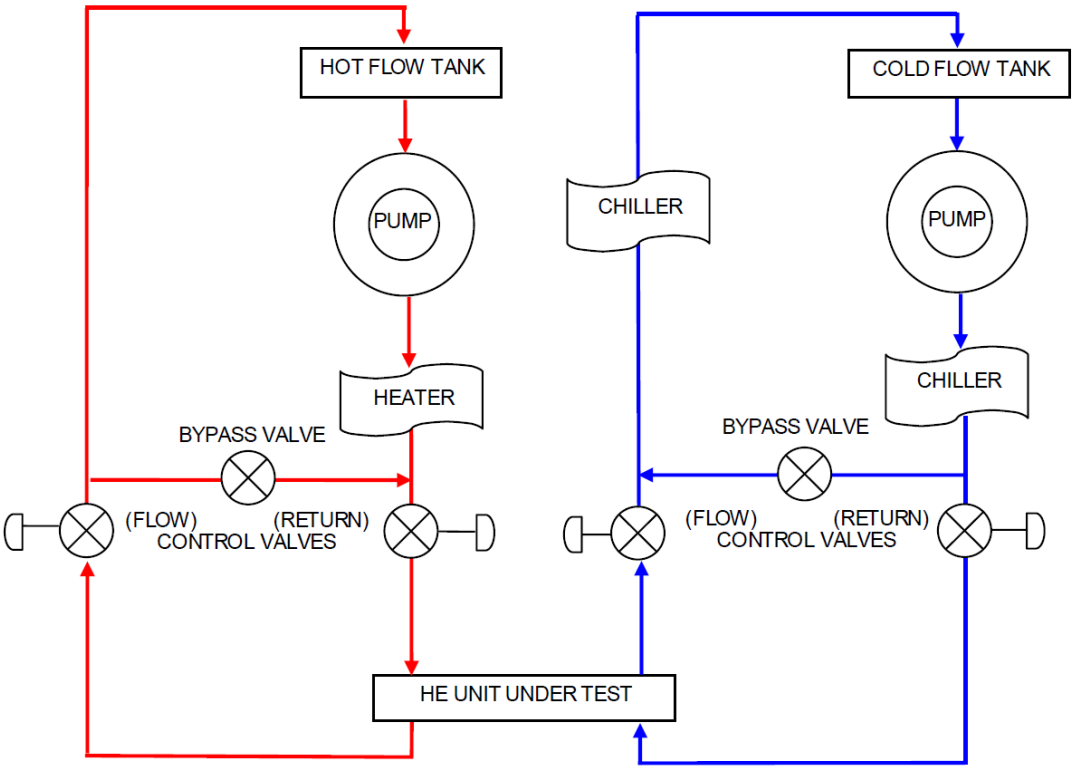

Figure 5.7: Schematic diagram of the test setup utilised to measure HE performance.

Figure 5.8: Insulated HE unit during the experiments.

Fluid	Manufacturer	Serial Number
Fuel	Nixon	2698501
Fuel	A.O.T	061135
Fuel	TheroFisher	6000545393-201
Oil	A.O.T	053096

Table 5.4: Data of the flow rate meters used.

5.2.4 Results and Discussion

Experimental HE data is given in Figures 5.9 - 5.11 where the results are plotted against the Reynolds number at the inlet to the cold HE stream. Pressure drop (Figure 5.9) increased non-linearly to $\approx$ 1.3 bar (relatively high for such compact unit), agreeing with general trends observed in the literature. However, it should be noted that in order to obtain a comprehensive data set, the HE was run beyond typical operation of such HE unit.

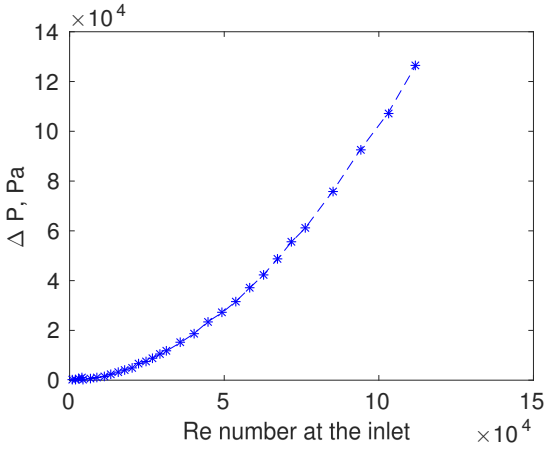

Figure 5.9: Experimental HE unit pressure drop versus Reynolds number at the cold flow inlet.

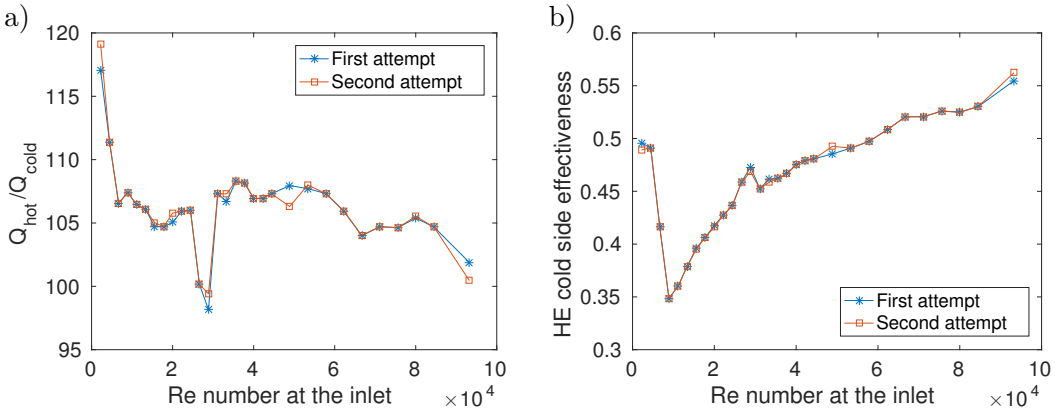

Figure 5.10: a) Heat balance of the system (%) at the cold inlet of the HE b) Heat exchanger cold side effectiveness versus Reynolds number at the inlet to the cold side of the HE.

Figure 5.10a presents an important quality measure of the thermal performance test - heat balance between the hot and cold fluid streams (Q_{hot}/Q_{cold}). The relationship indicates that at heat balance above 100% more heat is lost by the hot stream rather than gained by the cold stream. Such result is expected because although the HE unit was insulated during testing, heat loss to the environment and measurement inaccuracies are inevitable. This is thought to relate to accuracy of the experimental apparatus. At low flow rates the heat balance was the highest questioning quality of the results at the first two experimental points. In contrast, unusually low heat balance was calculated at the two test points around $Re_{inlet} \approx 20000 - 40000$ (Figure 5.10), even below 100%. This suggests that more heat was absorbed by the cold stream than lost by the hot stream which is unphysical and again questions the measurement accuracy at those two points. The rest of the thermal performance test points, however, appear to have a reasonable and repeatable heat balance, reinforcing quality of the data acquired.

Cold HE side heat transfer effectiveness (Equation 2.14), compares the amount of heat transferred in the HE to the maximum possible heat transfer at each experimental point and is given in Figure 5.10b. Again, the same two points ($Re_{inlet} \approx 20000 - 40000$) did not match the general trend and led to a spike in effectiveness reinforcing that the points were measured inaccurately. Two distinct heat transfer regimes can also be observed when analysing the effectiveness data. Firstly, at low Reynolds numbers high heat transfer effectiveness is measured which decreases until $Re_{inlet} \approx 10000$ and is thought to relate to conduction dominant heat transfer. From $Re_{inlet} \gtrapprox 10000$ dominance of forced convection increases which continuously improves the heat transfer performance of the HE, reinforcing the importance of mixing for efficient heat transfer.

Additional heat transfer performance data given in Figure 5.11a shows that increasing the cold HE side Reynolds number resulted in a heat transfer plateau. This

suggests that close to the maximum heat transfer was reached for this HE under the test conditions. Temperature change data in Figure 5.11b gives further supporting information on changing heat transfer mechanisms. An increase in flow rate of the cold stream led to a forced convection dominance and a small ΔT on the cold fluid side, despite higher heat transfer and HE effectiveness.

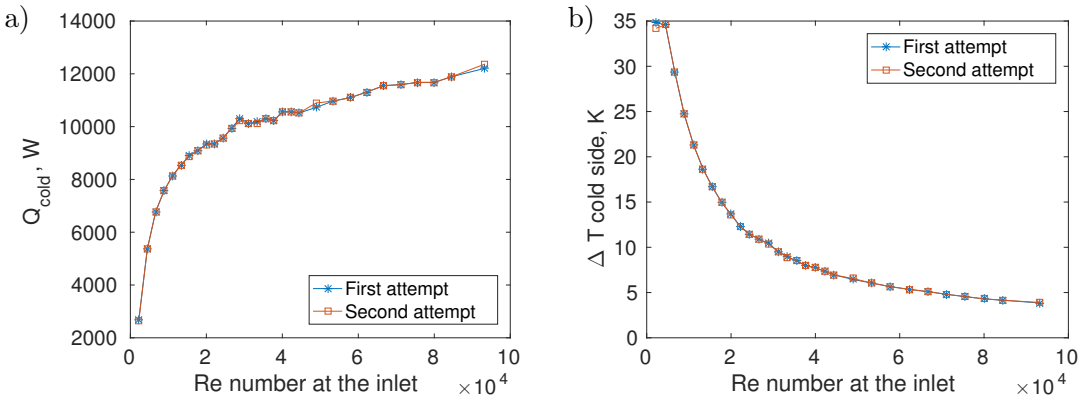

Figure 5.11: a) Heat absorbed by cold stream (W) and b)Temperature change for cold fluid (K) versus Reynolds number at the cold side inlet of the HE.

5.2.5 Conclusions of the Experimental Work

Aluminium plate-fin cross flow HE with serrated (offset strip) fins was experimentally evaluated. JET A1 fuel and BP Turbo Oil 2380 engine oil were used for the cold and hot flows respectively. Pressure drop was evaluated on the cold HE side and increased non-linearly to ≈ 1.3 bar, rather high for such compact HE unit. Thermal performance experiments highlighted that thermal losses to the surroundings still occur despite insulating the HE unit and were found more prominent at low Reynolds numbers. Increased flow rate of the cold stream led to forced convection dominance which in turn resulted in better HE effectiveness. Visual inspection of the HE after the experiments revealed that some of the pathways through the HE core were obstructed during manufacture. This could have affected the results, estimated in the range of $\approx 2-10\%$, by increasing pressure drop and decreasing heat transfer of the HE.

5.3 HE Unit CFD Modelling

5.3.1 Introduction

As outlined in Chapter 3 there are two methods to model HE. For a non-compact HE (e.g. shell and tube) or a small HE complete single fluid path can be modelled in full detail [172]. However, for the majority of HE a combination of detailed HE corrugation and simplified HE unit modelling should be undertaken [168]. The second

approach is used here for the experimentally evaluated HE unit (Figures 5.1 & 5.2). This approach was undertaken because the HE unit has 19 flow layers in total and high density flow elements (Figure 5.12), making the first approach infeasible. During the process a variety of HE corrugation and HE unit modelling approaches are evaluated which are then validated against experimental data in Section 5.5.

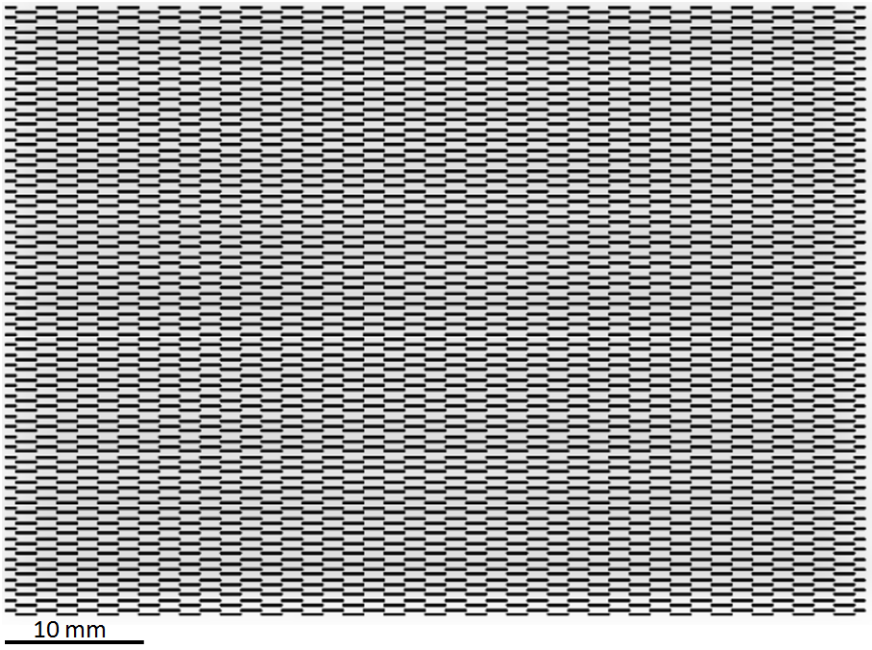

Figure 5.12: Slice through the single cold flow layer of the HE core.

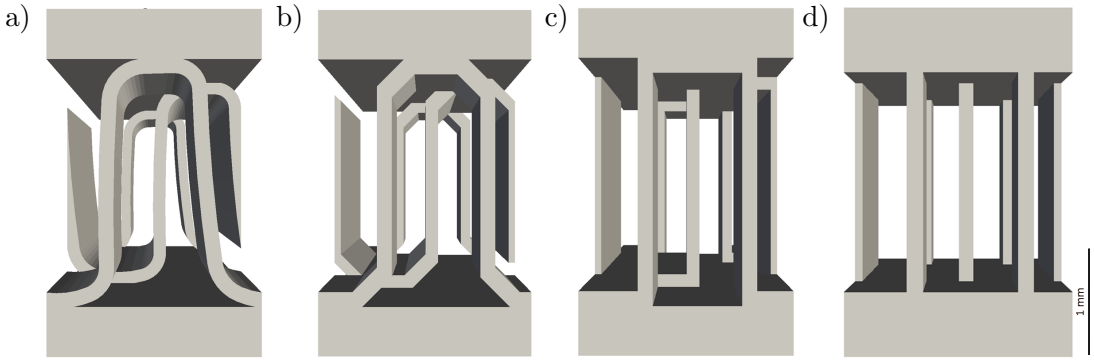

Figure 5.13: Plate-fin corrugation models: a) Original along with the b) Chamfered, c) Squared and d) Squared2 simplifications.

5.3.2 Simplifying the HE Corrugation

Firstly, the complex asymmetric serrated fin geometry (Figure 5.13a) was simplified in order to make the meshing process easier. It was completed using CFD with periodic flow assumption and the numerical setup from Chapter 4. Fluid properties for the predictions were taken from pressure drop experiments (Table 5.3). Three simplifications of the original design were created (Figure 5.13) and meshed using `snappyHexMesh`

application in OpenFOAM. The solution similarity was maintained by keeping the same mesh refinement limits and restraining the total mesh size to 80000 cells between the different simplifications. Mesh visualisations are shown in Figure 5.14, further illustrating similarity between the meshing domains. Overall flow pressure

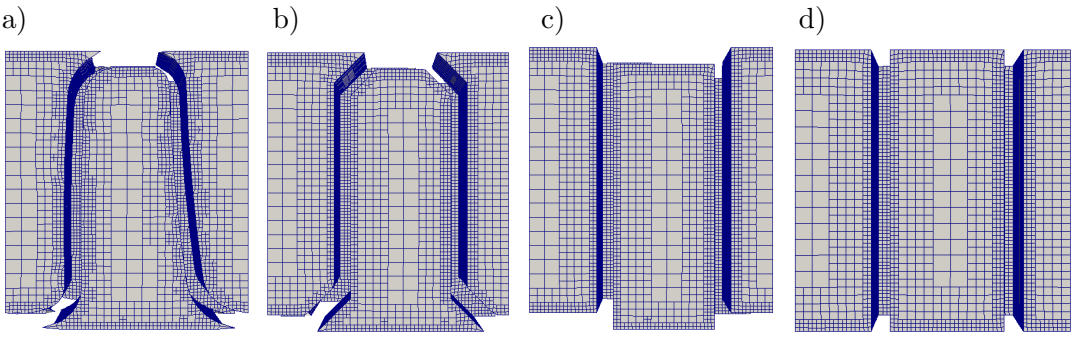

Figure 5.14: Plate-fin corrugation meshes of: a) Original along with the b) Chamfered, c) Squared and d) Squared2 simplifications.

gradient through HE corrugation was used to check if the domain simplifications altered the flow significantly from the original model predictions (Figure 5.15). Flow for $Re_{corrug} < 300$ converged using the steady state solver suggesting a fully laminar flow regime. However, flow predictions at Reynolds numbers higher than 300 required a transient solver to converge. A constant simulation timestep $\Delta t = 1 \times 10^{-6}$ s was used, taken from Chapter 4. Unsteady flow levels increased with the Reynolds number and are represented using standard deviation for flow fluctuations (Figure 5.15). At the low Reynolds numbers all models predicted similar pressure drop gradient. However, with increasing Reynolds number only the chamfered model remained in agreement with the original corrugation model. Thus, it was used for further simulations as it is an easier model to mesh accurately than the original corrugation model.

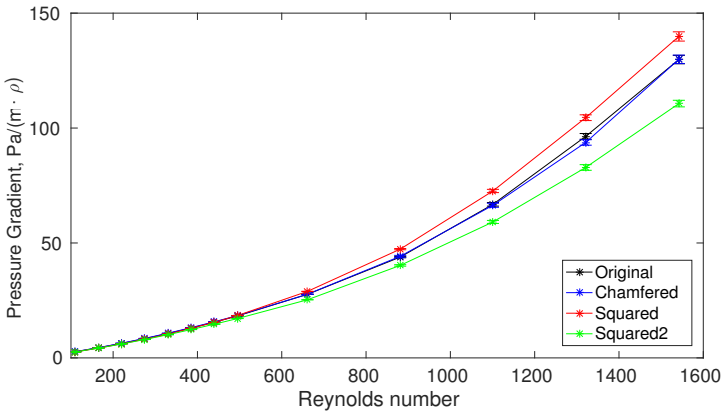

Figure 5.15: Overall pressure gradient results with error bars showing flow instability levels.

	Discretisation scheme
Gradient	Gauss linear
Pressure	Gauss linear corrected
Momentum	bounded Gauss (upwind/linearUpwind)
Turbulent kinetic energy	bounded Gauss upwind
Specific dissipation rate	bounded Gauss upwind
Energy	bounded Gauss (upwind/linearUpwind)
Transient	Euler

Table 5.5: Summary of discretisation schemes used for CFD simulations. Terms with a choice correspond to first and second order accuracy options.

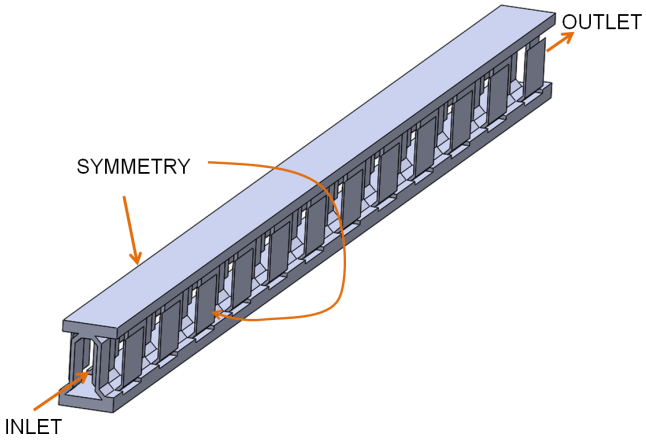

Figure 5.16: Serrated single channel corrugation model (50% cold flow side length, $\approx 40\ mm$) with the numerical boundary conditions used for meshing.

5.3.3 Single Channel Model

The first detailed HE corrugation model employed a finite length channel of the HE core layer, symmetric normal to the main flow direction. The mesh independence predictions used a 50% ($\approx 40\ mm$) length single channel of the cold side HE corrugation layer (Figure 5.16). Cold side HE layer was selected because the HE corrugation flow pathways on this HE side are longer and because the experimental pressure testing was completed on this side, making the validation easier. Constant cold fluid properties were used (Table 5.3) with discretisation schemes in Table 5.5. A constant temperature boundary was applied to the domain walls, following the methodology of recent studies [114, 157]. Temperature difference of 35 K was selected between the inlet and the walls of the domain (half of the experimental temperature difference between the two fluid streams, see Section 5.2.3). The setup then used `buoyantBoussinesqSimpleFoam` or `buoyantBoussinesqPimpleFoam` solvers for simulations (depending if the flow is considered steady-state or transient) with buoyancy effects disabled.

5.3.3.1 Single Channel Model Grid Independence

For the mesh independence study of the single channel model four meshes were generated (Table 5.6) with visualisations in Figure 5.17 and run at the thermal performance experimental point of $Re_{\text{corrug, cold}} = 146$ (assuming no maldistribution in the HE headers). The meshes were designed to resolve not only the boundary layer, but also to capture the heat transfer accurately across the domain, completed by increasing the overall mesh resolution. Domains were evaluated using the overall channel performance and the additional line data acquired along the middle of third and seventh corrugation periods (Figure 5.18).

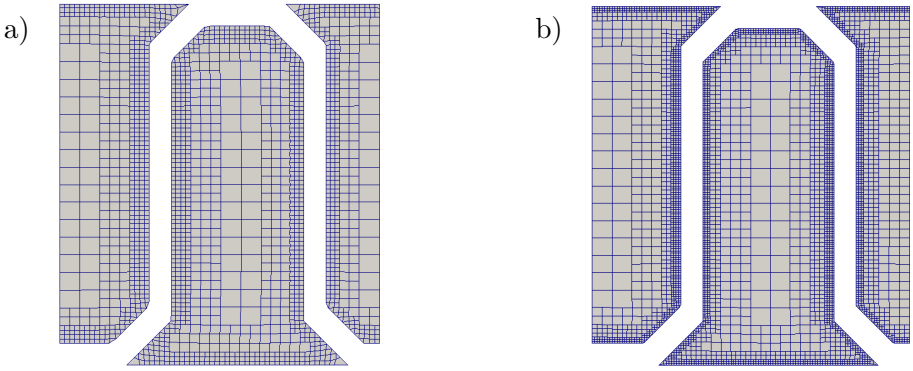

Figure 5.17: Visualisations of a) Coarse and b) Coarse 1 meshes at the inlet of the domain showing different boundary layer refinement levels.

Mesh	Mesh size, million	Boundary layer, $\times 10^{-5}$, m
Coarse	1.2	1.5
Coarse 1	2.9	0.8
Medium	8.7	0.8
Fine	18	0.8

Table 5.6: Data of the single channel model meshes.

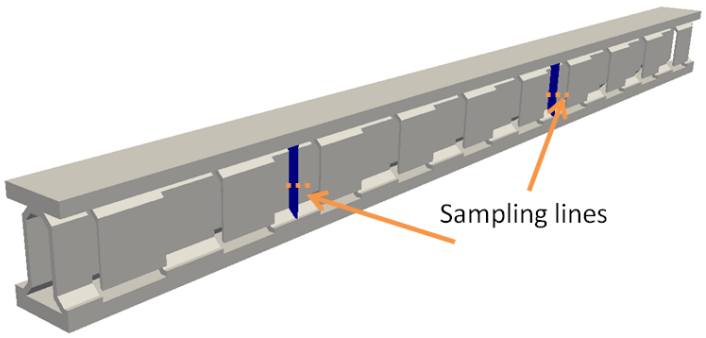

Figure 5.18: Serrated single channel corrugation model used for meshing with fluid sampling lines.

Firstly, visualisation of the domain is given at the medium mesh resolution (Figure 5.20) and shows asymmetric flow and heat transfer behaviour, expected due to the geometry of the HE corrugation used. Laminar flow model results from the different meshes are compared using pressure drop and temperature change in Table 5.7. Negligible differences in terms of the pressure drop predictions between medium and fine meshes were found whilst the temperature data differed more. Thus, to provide more information about the thermal performance the temperature line data was plotted in Figure 5.19. The data shows only a marginal difference between medium and fine meshes through the majority of the domain allowing to conclude that medium resolution is sufficient for accurate predictions.

Mesh	ΔP, Pa/ρ	% diff.	ΔT, K	% diff.
Coarse	0.5835	-	22.05	-
Coarse 1	0.6098	4.5	25.97	17.7
Medium	0.6423	5.3	27.04	4.1
Fine	0.6429	0.0001	28.69	6.1

Table 5.7: Overall single channel model data for different resolution meshes.

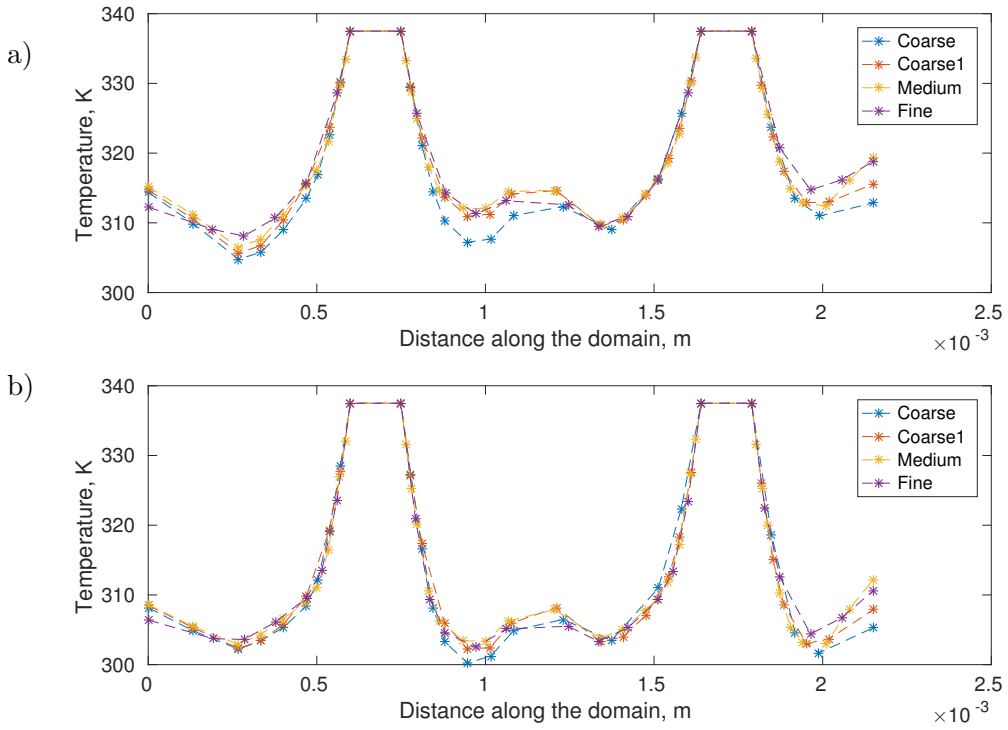

Figure 5.19: Temperature line data across the domain at a) third and b) seventh planes in the flow-wise direction with different mesh resolutions.

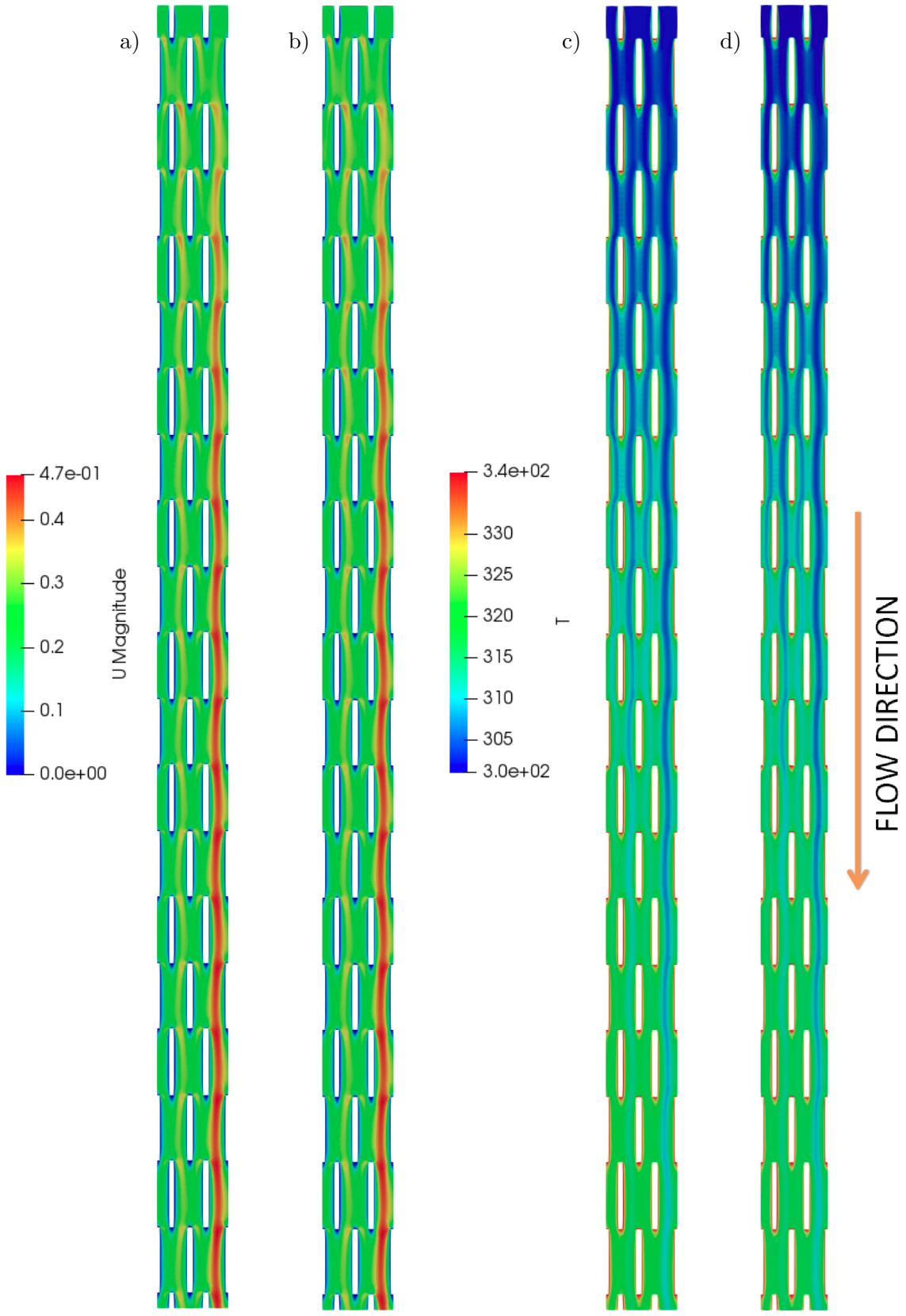

Figure 5.20: Visualisations of a) & b) Velocity magnitude and c) & d) Temperature contours with laminar and $k-\omega$ SST models respectively at medium mesh resolution.

5.3.3.2 Turbulence Modelling with the Single Channel Mesh Model

An unexpected numerical solution phenomenon was observed during $k-\omega$ SST model predictions for the mesh independence study. The simulation converged to steady state for the coarse mesh resolution, however, higher mesh resolutions required a transient solver to converge. Interestingly, the transient simulations led to a steady state solution (Figure 5.21) (despite the fact that the simulation time-step was controlled to $Co_{max} = u\Delta t/\Delta x = 0.5$ [173] which enables to capture unsteady flow), suggesting a numerical convergence problem. This also suggests that sufficiently fine boundary layer is required to capture this instability numerically.

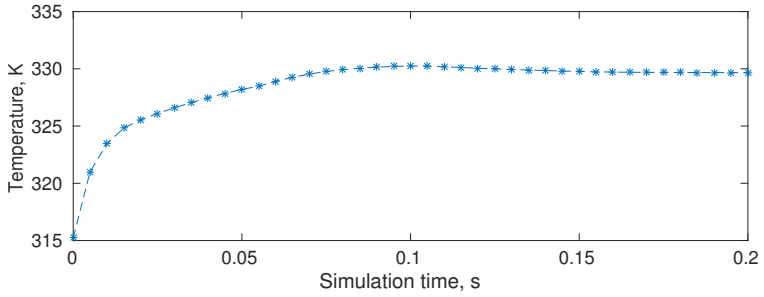

Figure 5.21: Mean temperature on plane 7 along the single column domain for the medium mesh using transient solver with $k-\omega$ SST model at $Re_{corrug} = 146$.

Table 5.8 compares final output of the transient $k-\omega$ SST prediction to the steady-state laminar result at the medium resolution. Negligible differences were found at $Re_{corrug} = 146$ between the two models which can also be visually observed in Figure 5.20. However, it was concluded to use laminar flow assumption for further single channel model calculations as the need of the transient solver for turbulent flow predictions significantly increased the computational time.

	laminar	$k-\omega$ SST	% difference
ΔP, Pa/ρ	0.642	0.638	0.6
ΔT, K	27.1	27.2	0.7

Table 5.8: Comparison of overall channel data between the two flow momentum assumptions.

5.3.3.3 Unsteady flow with Single Channel Model

Nonetheless, single channel domain predictions using the transient solver were also attempted at the thermal performance experimental point $Re_{\text{corrug}} = 1213$ using $k-\omega$ SST model. In this case a steady-state result was used obtained using low order discretisation schemes for a better flow field initialisation before switching back to the second order accuracy (Table 5.5). Maximum Courant number restriction was used to

limit the simulation time-steps and was varied from 4 to 0.5, saving data at 200 Hz frequency. The predictions ran for approximately a week using 128 Intel E5-2670 cores on ARC2 high performance computer at the University of Leeds and are summarised in Figure 5.22. Unsteady flow is predicted suggesting similar vortex shedding to Chapter

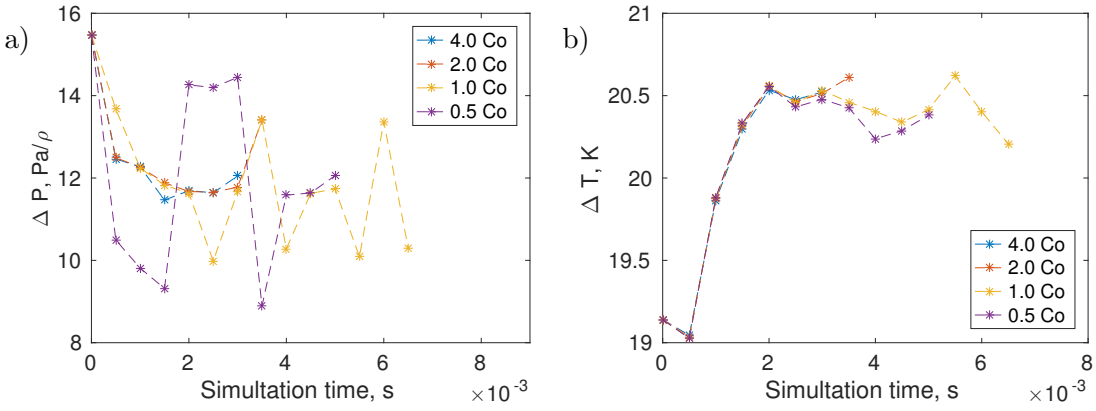

Figure 5.22: Single column domain results of a) ΔP, Pa/ρ and b) ΔT, K for medium resolution meshes at $Re = 1213$ using different Courant number restrictions.

4, however, the additional computational time of transient solutions proved to be excessive as the simulations did not progress significantly in simulation time. Thus, it was decided to limit the single channel domain computations to steady-state and laminar assumptions. This was considered to provide sufficiently accurate solutions as the laminar model proved to be a reasonable choice at low levels of unsteady flow (Chapter 4), shown to occur for this HE corrugation previously in this chapter (Section 5.3.2).

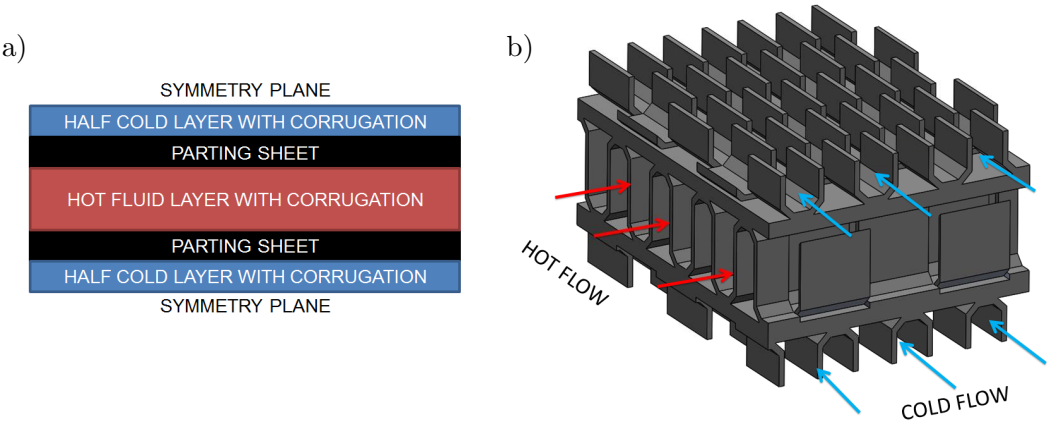

Figure 5.23: a) Schematic of the HE section domain b) HE section solid domain visualisation.

5.3.4 HE Section Model

A novel computational domain was formulated which utilises the conjugate heat transfer methodology (Figure 5.23a). The approach models a slice of the HE core containing both hot and cold fluid streams separated by a solid (parting sheets and fins between the fluids), termed as a HE section model in this document. A slice of $1/16^{th}$ of the HE core layer area (top view of Figure 5.1b) was used in mesh independence calculations to minimise the computational cost with the model schematic and visualisation of the solid domain provided in Figure 5.23b. Cold fluid layers were cut in half in order to create a representable symmetric model of the HE core as it has 10 cold and 9 hot flow layers. The approach allows to directly simulate the thermal interaction between the two fluid streams which is impossible using traditional methodology such as finite length channel or fully periodic models. For these predictions `chtMultiregionSimpleFoam` or `chtMultiregionFoam` OpenFOAM solvers had to be used which are capable of modelling multiple fluid and solid domains. In addition, the HE section model enables to apply the data acquired into the HE unit domain after simple extrapolation to the full HE core layer dimensions. This eliminates the necessity for analytical corrections from the literature such as Kays and London [6], needed for data acquired by the single channel model (Section 5.3.3). Constant fluid and solid properties from the experimental work (Table 5.2 and Table 5.3) and the discretisation schemes in Table 5.5 were used throughout all the simulations. Consequently, both fluids were also assumed to be Newtonian based on the information from widely available literature and manufacturer data-sheets, such as [171].

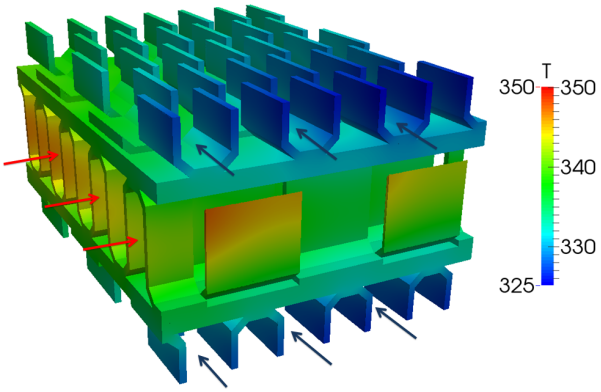

Figure 5.24: Visualisation of the solid domain using temperature contours at $Re_{\text{corrug, cold}} = 146$, $Re_{\text{corrug, hot}} = 35$ at medium mesh resolution.

5.3.4.1 HE Section Grid Independence

HE section computational domain was modelled using setup given in Section 5.3.4 using four meshes described in Table 5.9 at the thermal performance experimental

point of $Re_{\text{corrug, cold}} = 146$ and $Re_{\text{corrug, hot}} = 35$ (assuming no maldistribution in the HE headers). A different meshing approach compared to the single channel domain was undertaken as the boundary layer resolution was not altered which was considered sufficient. In addition, further near-wall resolution increase would have been computationally expensive because of the much larger domain than the single channel. Instead, the mesh was refined inside all the flow domains, critical for accurate heat and mass transfer predictions. Example outputs of the simulations at $Re_{\text{corrug, cold}} = 146$, $Re_{\text{corrug, hot}} = 35$ are shown in Figures 5.24 & 5.25.

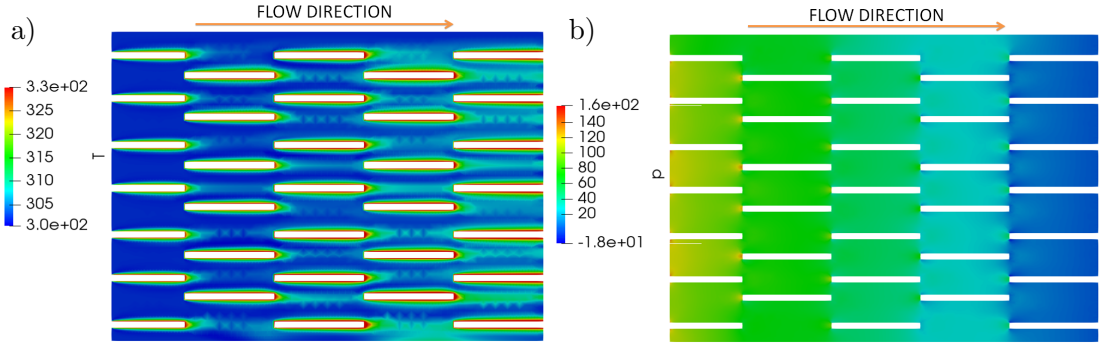

Figure 5.25: Visualisations through the middle of the top cold flow domain of a) Temperature and b) pressure contours at $Re_{\text{corrug, cold}} = 146$, $Re_{\text{corrug, hot}} = 35$ at medium mesh resolution. Flow direction is from left to right.

Mesh	Mesh size, million	Boundary layer, $\times 10^{-5}$, m
Coarse	6.5	1.5
Coarse 1	15.4	1.5
Medium	18.7	1.5
Fine	29.4	1.5

Table 5.9: HE section mesh data.

Data was sampled from all the fluid domains by using sampling lines in the main flow-wise direction in the locations shown in Figure 5.26. Additionally, the overall performance of each fluid domain was summarised in Table 5.10. It showed a similar trend as to the single column results as the pressure drop performance stabilised faster whilst the temperature change fluctuated slightly between the medium and fine meshes. Thus, temperature line data was analysed to provide with more information with an example in Figure 5.27 where the second line of the top cold fluid domain is presented. It showed that the additional mesh points of the fine mesh allowed capturing heat transfer away from the walls of the domain in more detail. However, overall the differences are reasonably minor and therefore medium mesh resolution was used for further simulations.

Flow Domain	ΔP, Pa	ΔT, K	% diff.	% diff.
Coarse, Cold	131.75	26.3	-	-
Coarse, Hot	119.51	20.0	-	-
Coarse 1, Cold	114.07	17.2	15.5%	52.9%
Coarse 1, Hot	99.03	17.2	20.7%	16.3%
Medium, Cold	113.01	17.3	0.9%	0.6%
Medium, Hot	97.8	17.2	1.3%	-
Fine, Cold	113.14	18.5	0.1%	6.5%
Fine, Hot	98.39	17.9	0.6%	3.9%

Table 5.10: Overall data for the HE section calculations.

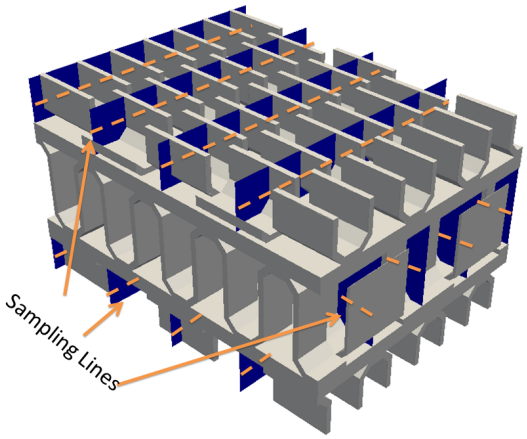

Figure 5.26: Visualisation of the sampling lines used to analyse the fluid domains.

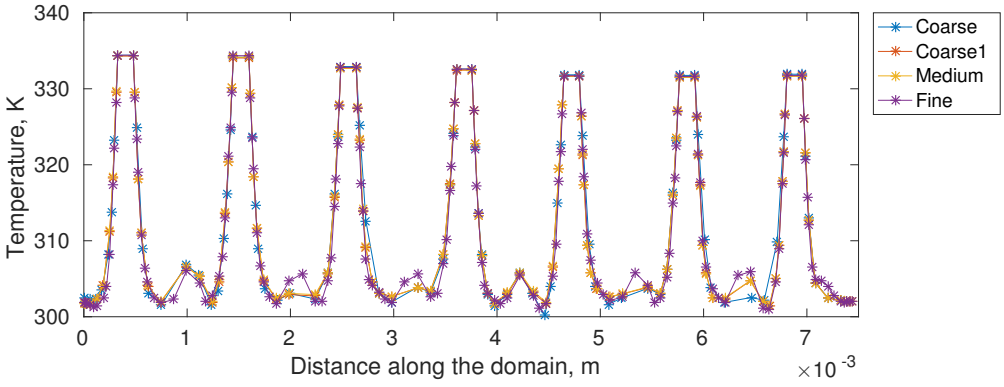

Figure 5.27: Temperature data through the second top cold fluid domain line at $Re_{\text{corrug, cold}} = 146$, $Re_{\text{corrug, hot}} = 35$ with various mesh resolutions.

5.3.4.2 HE Section Domain and Turbulent Flow Modelling

HE section model results in Table 5.11 compare the $k-\omega$ SST and laminar flow model predictions of the cold and hot flow domains using the same flow conditions. Interestingly, in the case of HE section model, the $k-\omega$ SST predictions did not require the transient solver and converged using a steady-state solver. This is thought

to relate to the lower resolution boundary layer, same to the coarse resolution of the single column model where the $k-\omega$ SST converged with a steady-state assumption. The predictions between the laminar and $k-\omega$ SST models also were almost identical (Table 5.11), showing no need to use a more complex model, at least at low Reynolds numbers.

	laminar		$k-\omega$ SST	
Flow Domain	ΔP, Pa	ΔT, K	ΔP, Pa	ΔT, K
Medium, Cold	113.01	17.3	113.1	17.3
Medium, Hot	97.8	17.2	97.8	17.2

Table 5.11: Overall data for the HE section calculations comparing laminar and $k-\omega$ SST model results.

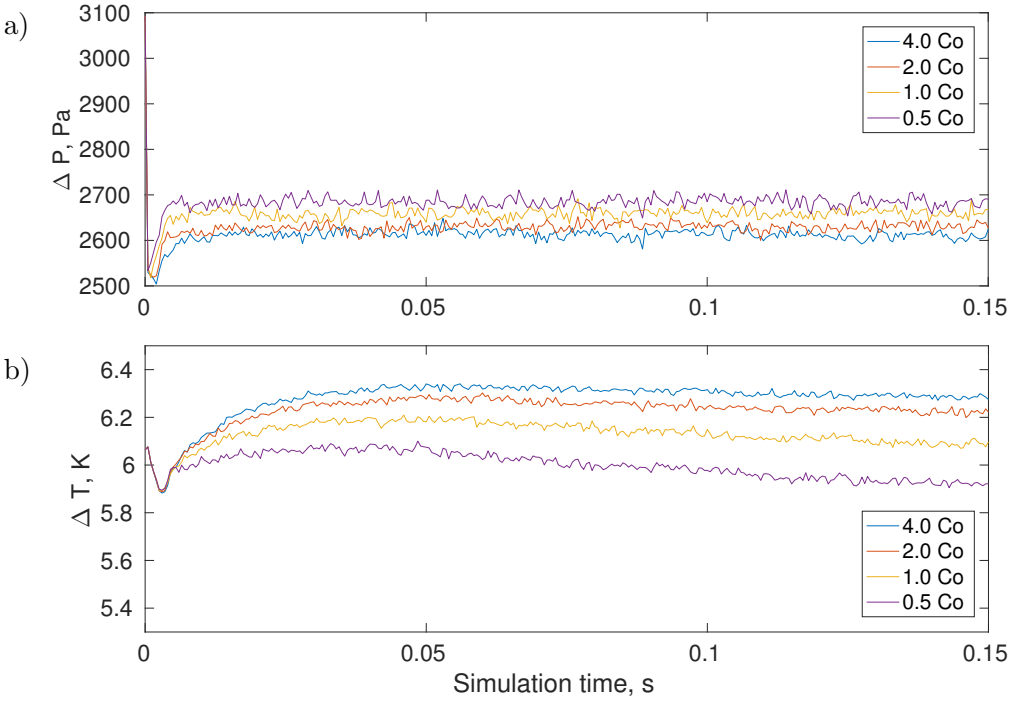

Figure 5.28: Overall a) pressure drop ΔP and b) temperature change ΔT predictions for the cold fluid at $Re_{corrug} = 1213$ with medium mesh resolution and varying the simulation time steps.

5.3.4.3 HE Section Time-step Independence

To test the unsteady flow occurrence with the HE Section model the medium grid was run at the thermal performance experimental point of $Re_{\text{corrug, cold}} = 1213$ and $Re_{\text{corrug, hot}} = 35$. To accommodate the increased cold flow rate it was simulated with the $k-\omega$ SST flow model whilst the hot flow used the laminar model. Flow fields were initialised using a steady solution obtained with low order dominant discretisation (Table 5.5). Then, a transient conjugate heat transfer solver was run at a range

of simulation time-steps, controlled by varying the maximum Courant number [173] ($Co_{max} = u\Delta t/\Delta x$) from 4 to 0.5. Data was saved at 200 Hz frequency and simulations were run up to 0.15 s due to storage and computing expense.

Figure 5.28 shows the overall pressure drop and temperature change through the cold flow side of the HE section model. In addition, the data was time averaged from 0.02 s to 0.15 s and shown in Table 5.12. Pressure drop data again did not

Max Courant Number	4.0	2.0	% diff.	1.0	% diff.	0.5	% diff.
ΔP, Pa	2614	2630	0.6%	2659	1.1%	2685	1%
ΔT, K	6.31	6.25	1.1%	6.14	1.8%	5.99	2.5%

Table 5.12: Time averaged data of overall cold flow domain quantities.

vary significantly with respect to different simulation time steps whilst more difference can be seen in terms of the overall temperature change. Overall, it was concluded that a maximum Courant number not higher than 0.5 should be used for accurate unsteady simulations. However, it should be noted that lowering Courant number restriction further was not attempted due to significant computational time increase. Simulations using $Co_{max} = 0.5$ were also run further to $t = 0.25$ s to compare the $k-\omega$ SST and laminar flow models (Figure 5.29). Interestingly, no significant differences are observed between the two models when time averaging the results, despite the

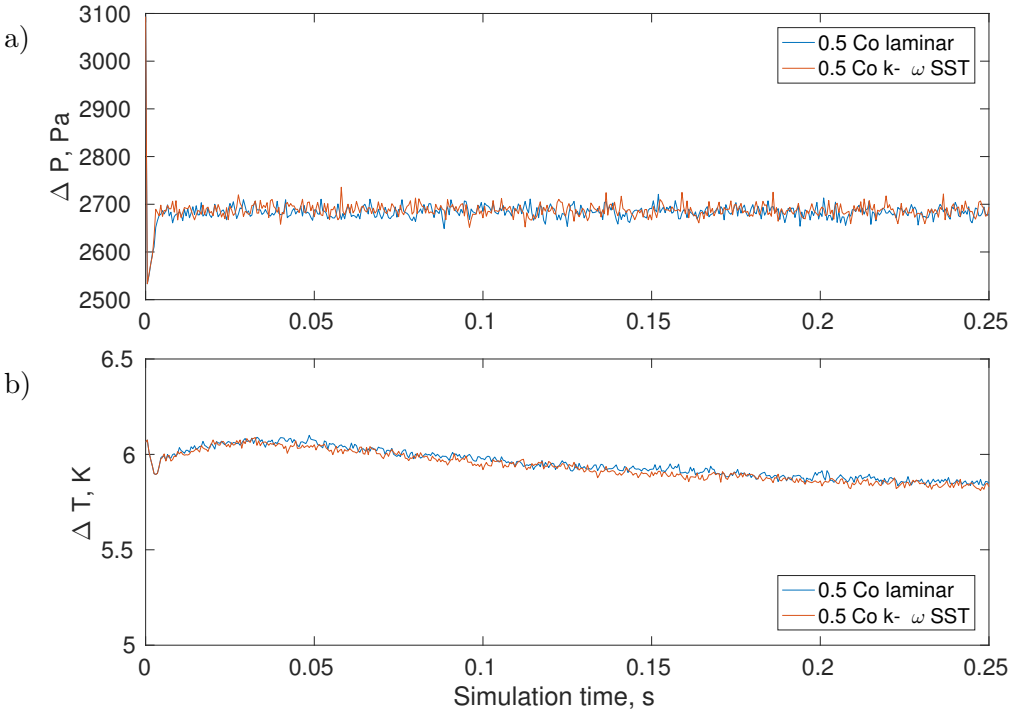

Figure 5.29: Overall a) pressure drop ΔP and b) temperature change ΔT predictions for the cold fluid at $Re_{corrug} = 1213$ with medium mesh resolution and comparing the two flow momentum modelling assumptions.

minor differences visible. This suggests slightly different instability levels between the two models, similar result as in Chapter 4, however, it did not lead to significantly different overall results. Potential reasons for the lack of contrast between the laminar and $k-\omega$ SST models are: inevitably lower grid resolution compared to 2D case resolved in Chapter 4 and overall less disruptive HE corrugation. It should also be noted that the transient solutions required to run the simulations for more than a week on 72 cores of Broadwell E5-2650v4. Thus, it was concluded that the unsteady flow simulations were overly time consuming, eliminating their use due to the low unsteady flow levels observed.

Mesh	No. of Elements	Boundary layer thickness, m
Coarse	7.19×10^5	5×10^{-4}
Medium	2.7×10^6	3.92×10^{-4}
Fine	4.8×10^6	3.18×10^{-4}
Fine1	8.59×10^6	2.07×10^{-4}
Fine2	11.5×10^6	1.71×10^{-4}

Table 5.13: Mesh resolution data of HE unit model.

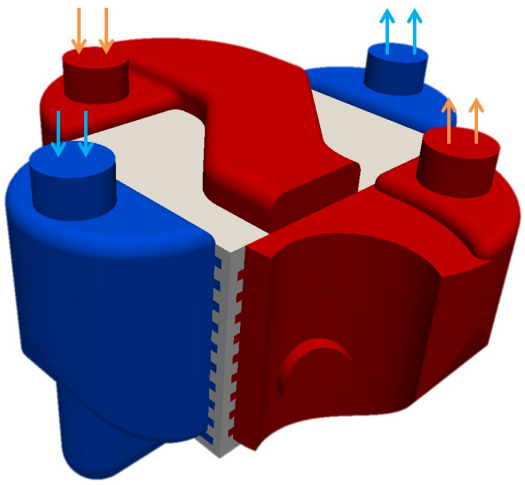

Figure 5.30: HE flow volumes with solid separating them. Refer to Figure 5.2 for the photograph of the assembled HE unit.

5.3.5 HE Unit Modelling

HE unit model considers simplified flow and heat transfer in the HE core and models the HE headers connected to the HE core layers. Firstly, to create the CFD model cold and hot flow HE fluid volumes together with the solid separating them were extracted from an industrial CAD model (Figure 5.30). Then cold HE flow side was meshed as the cross-flow heat transfer effects were taken into account by the HE section model (Section 5.3.1). This allowed to use a single fluid domain `bouyantSimpleFoam` solver

with incompressible assumption and constant fluid properties (Table 5.3). Flow and heat transfer modelling inside the HE core was simplified by adding source terms to the momentum and energy equations (described in detail in Chapter 3). It was undertaken because the flow and heat transfer cannot be modelled in detail due to the computational expense caused by the large surface area of the HE (Section 5.3.2). To account for the pressure drop through HE core, Darcy-Forscheimer (Equation 3.47) and power law (Equation 3.48) models were used. Heat transfer through the HE core is simplified using heat transfer effectiveness model (Equation 3.50) which defines a proportion of maximum possible energy transfer to the fluid under certain conditions [34].

5.3.5.1 HE Unit Model Solution Independence

The HE unit grid modelling was undertaken by generating five meshes (Table 5.13) using the `snappyHexMesh` application and the setup outlined in Section 5.3.5 at $Re_{inlet} = 11121$ at cold domain inlet. Inlet temperatures were set to $T_{\text{cold inlet}} = 302\ K$ and $T_{\text{hot inlet}} = 373\ K$ with corresponding constant fluid properties. The HE core was modelled using Darcy-Forchheimer porous media and effectiveness models for flow and heat transfer. Arbitrary values were used for both friction ($f = 714$, uni-directional) and the effectiveness ($\epsilon = 0.613$ across all the HE layers). However, solution residuals were found to remain reasonably high during the calculations. Thus, all the meshes

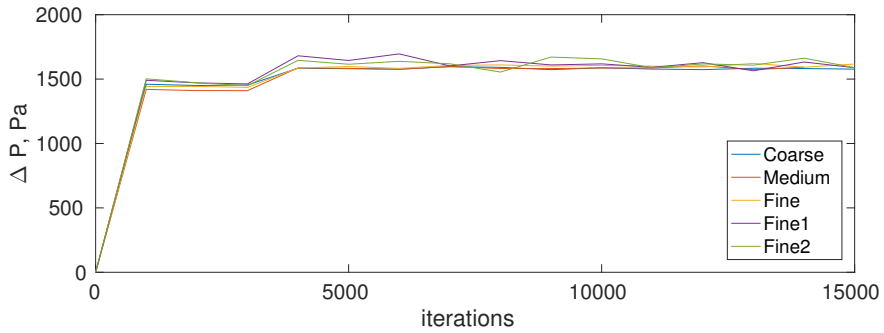

Figure 5.31: Overall ΔP through the cold HE unit domain versus solution iterations.

were initialised by using the low order dominant discretisation (Table 5.5) to iteration 3000. Then the simulations were continued using the second order dominant discretisation (Table 5.5) up to iteration 15000 with the solution results being saved every 1000 iterations (solution visualisation is given in Figure 5.32). High residuals required plotting ΔP versus the solution iterations (Figure 5.31) which showed that the solutions converged to an acceptable stability.

Overall results were summarised in Table 5.14, obtained by averaging the data from iteration 5000 to 15000. In terms of the pressure drop only minor differences were found

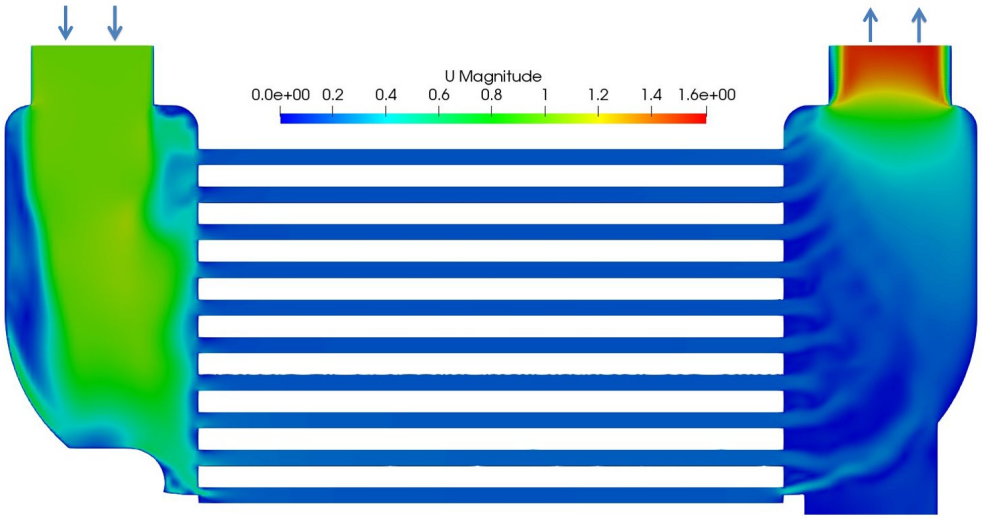

Figure 5.32: Velocity contours through the middle of the cold flow side of the HE unit at medium mesh resolution (inlet at the left) at $Re = 11121$.

between the different meshes. However, again agreeing with the previous results, more differences were observed in terms of the ΔT predictions. Overall, the Fine2 grid resolution mesh produced the most stabilising temperature change compared to the other meshes and was selected for further HE unit simulations.

Mesh	ΔP, Pa	% diff	ΔT, K	% diff
Coarse	1582	-	14.31	-
Medium	1586	0.3%	19.16	33.9%
Fine	1602.7	1.1%	25.99	33.9%
Fine1	1619.8	1.1%	21.95	15.54%
Fine2	1620	0.01%	23.72	8.06%

Table 5.14: Summarised data for running the HE unit flows separately.

5.3.6 Extending the HE Corrugation Domains

5.3.6.1 Single Channel Model

After generating mesh independent domain the single column model was extended to 100% length of the cold HE flow layer ($\approx$ 80 mm), compared to 50% ($\approx$ 40 mm) channel length used prior. Medium mesh resolution was maintained by using identical `snappyHexMesh` settings and simulation setup (Section 5.3.3.1). Development of pressure drop ΔP and temperature change ΔT through the corrugation periods was compared to ensure solution similarity. Data extraction was done using the sampling planes and averaging them every HE corrugation period (Figure 5.18). Results in Figure 5.33 were found to differ only slightly between the two channel models when comparing the flow and heat transfer development in the channel. This was expected

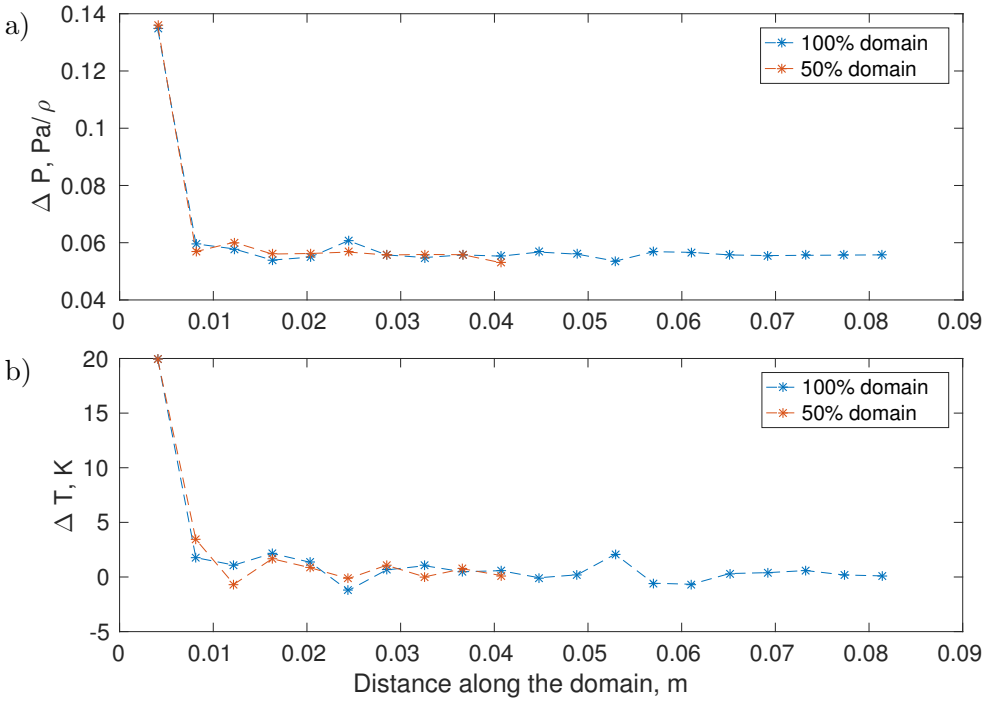

Figure 5.33: Visualisations of a) ΔP, Pa/ρ cold and b) ΔT, K of different length single column domains.

as the shorter channel domain would lead to a slightly different overall development of the flow. Averaging quantities over a single period of the channel (Table 5.15) showed that there was little difference between the two models. This enabled using the full length single channel model for higher Reynolds number calculations where the extended model would be more important for accurate predictions.

Domain	ΔP, Pa/ρ	ΔT, K
50% length	0.0642	2.704
100% length	0.0642	2.704

Table 5.15: Averaged quantities per period of the single channel domain.

5.3.6.2 HE Section Model

The HE section model was extended twice in the cold flow direction, resulting in the $1/8^{th}$ of the layer area model. Selective extension of the domain was undertaken to minimise the increase in grid size and because experimentally only the cold flow rates were varied whilst the hot flow side remained at a constant low Reynolds number ($Re_{\text{corrug, hot}} = 35$, assuming no maldistribution). Flow conditions, setup and mesh resolution between the two simulation domains remained the same as during the mesh independence study (Section 5.3.4). Cold flow data is analysed here which was mainly affected by the extension of the computational domain. Both HE section models are

compared to the two single channel domains to verify the novel modelling approach. The comparison uses the friction factor f, derived from the Equation 3.47 as

$$f = \frac{2|\nabla p_{flow-wise}|}{\rho u_f^2} \tag{5.1}$$

where u_f was taken as an inlet velocity. To compare the results between the models the data was sampled at every corrugation period and shown in Figure 5.34. The

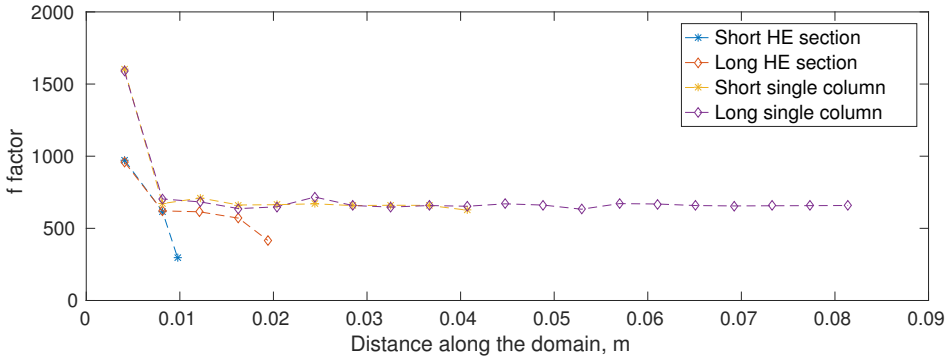

Figure 5.34: f factor comparison between the four simulation domains.

results clearly show that the shorter HE section domain is not sufficient for predictions, especially for the higher Reynolds number flows and is affected by the flow exit effects, caused by not analysing the full HE corrugation period and resulting in drop of flow resistance. More similarities can be seen between the longer HE section model and the single channel domains. However, the longer HE section model still predicts slightly lower overall flow resistance which is thought to relate to the lower grid resolution. Also, the flow exit effects are still observed for the longer HE section domain. These are caused by inherently shorter domain length than in the single channel model and led to reduction in friction factor at the end of the domain. Thus, the data from the last period of the predictions was excluded whilst calculating the overall flow resistance and heat transfer performance in simulations across the experimental Reynolds numbers range, shown in Sections 5.4.2 & 5.4.2.1.

5.4 Validating the CFD Modelling with the Experiments

5.4.1 Single Column Model Results

Results of the full length single column domain for pressure drop experiments ($118 \leq Re_{corrug} \leq 2010$) are presented in this section. Numerical setup remained as in Section 5.3.3 with laminar and steady-state assumptions. The artificial heating source using a constant wall temperature of $T_w = T_{in} + 35\ K$ was also prescribed to establish

thermal performance of the HE corrugation. It should be noted that laminar steady-state predictions above $Re_{corrug} = 2010$ diverged and the highest $Re_{corrug} = 2957$ experimental point was not reached. Interestingly, increase in the solution residuals was observed at $Re_{corrug} \approx 300$, suggesting the unsteady flow onset. This is similar to the result in Chapter 4 where the unsteady flow was detected at $Re_{corrug} \approx 200$ and the fully periodic simulations of this corrugation in Section 5.3.2. Increase of solution residuals also led to slight fluctuations of the results. However, it was previously shown

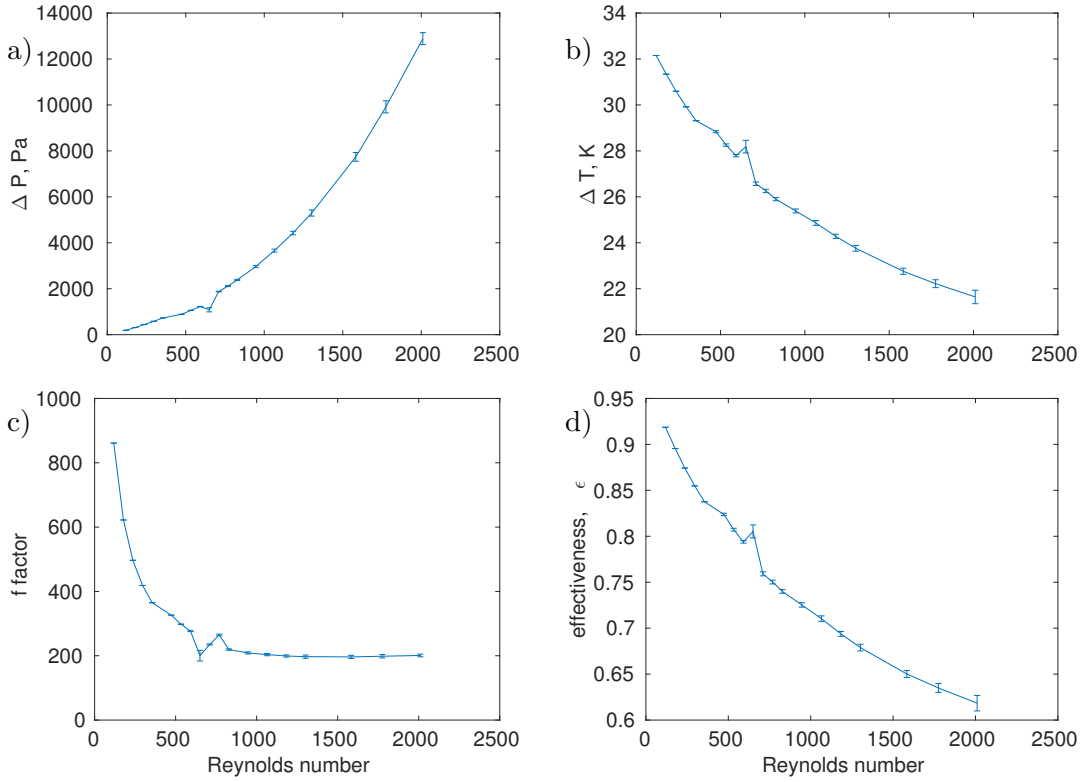

Figure 5.35: Data of a) pressure drop ΔP, Pa and b) temperature change ΔT, K c) f factor and d) effectiveness of the single channel domain across the Reynolds number range.

that the full transient solution was time consuming, thus the steady state assumption was maintained (Section 5.3.3.1). Instead, the solution instability was quantified by averaging the predictions every 100 solution iterations from iteration 2000 to 8000 and using a standard deviation function for error bars. Flow resistance and heat transfer results across the single channel domain length are given in Figure 5.35. The error bars clearly show that the solutions did not fluctuate significantly throughout the test points and suggest low levels of unsteady flow. Interesting fluctuations occurred at the Reynolds numbers 650, 710 and 769 which did not follow the general trends. However, similar discrepancies were also observed during the experimental work and are further investigated later in the chapter (Section 5.4.2).

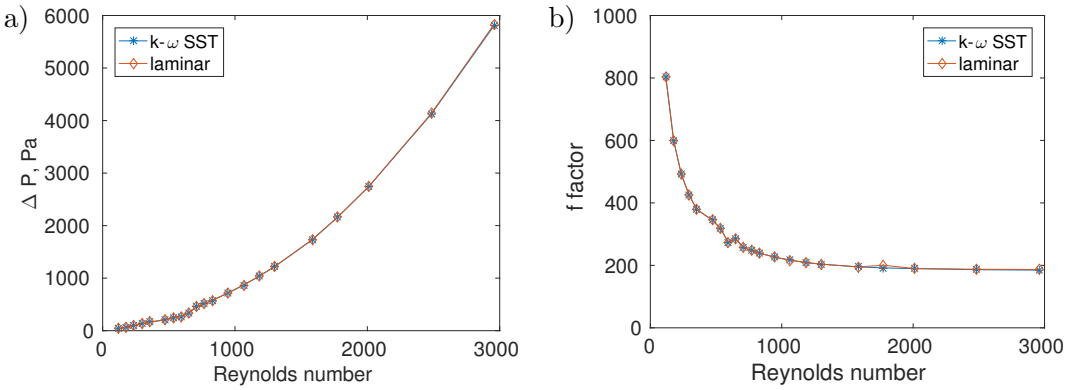

Figure 5.36: HE corrugation data of a) pressure drop and b) f factor of the HE section cold flow domain for the pressure drop experiments across the Reynolds number range.

5.4.2 HE Section Domain Data

In contrast to the single channel domain, the HE section model was used to generate the data for both pressure drop and thermal performance experiments. Laminar and $k-\omega$ SST models were used with the steady-state assumption and numerical setup as in Section 5.3.4. The HE section model fully converged across the Reynolds number range in contrast to the single channel model results afore. Steady-state predictions were even achieved around the Reynolds numbers where it was shown that the unsteady flow solution exists already with the shorter HE section model (Section 5.3.4.3). This is believed to be possible because of the two reasons: firstly, the HE section domain had a coarser near-wall mesh resolution compared to the single column domain. Secondly, the HE section domain is shorter and does not allow the cold flow to develop as far compared to the single channel case, reducing the chances of unsteady flow occurrence. HE section predictions for the pressure drop experiments are presented in Figure 5.36. They were generated by simulating only the cold fluid flow part of the HE section model at isothermal conditions and $118 \leq Re_{corrug} \leq 2957$ was covered. The same fluctuation in the frictional performance at $Re_{corrug} \approx 600-700$ (although to a smaller magnitude) is observed, agreeing to the single column flow domain results (Figure 5.35).

The HE section model results for the thermal performance experiments (Figure 5.37) were generated at $88 \leq Re_{\text{corrug, cold}} \leq 1213$ range. Again, a fluctuation in flow resistance was observed, however, towards the end of the test range. It can be potentially explained by a higher fluid viscosity as the cold side was run at a lower inlet temperature during thermal performance experiments which altered the Reynolds number at which the instability is predicted. Cold flow effectiveness (Figure 5.37d) also revealed an interesting trend. At the lowest Reynolds numbers the HE was predicted to operate with high efficiency which then dropped. In this regime, flow mixing is low and the heat transfer is thought to be driven mostly by the fluid properties. Forced

convection then takes over at $Re_{corrug} \approx 300$ and continually increases its dominance with the Reynolds number, making the heat transfer more efficient. Similar trend was also observed during the physical experiments (Figure 5.10b), reinforcing the trust in the HE section model results.

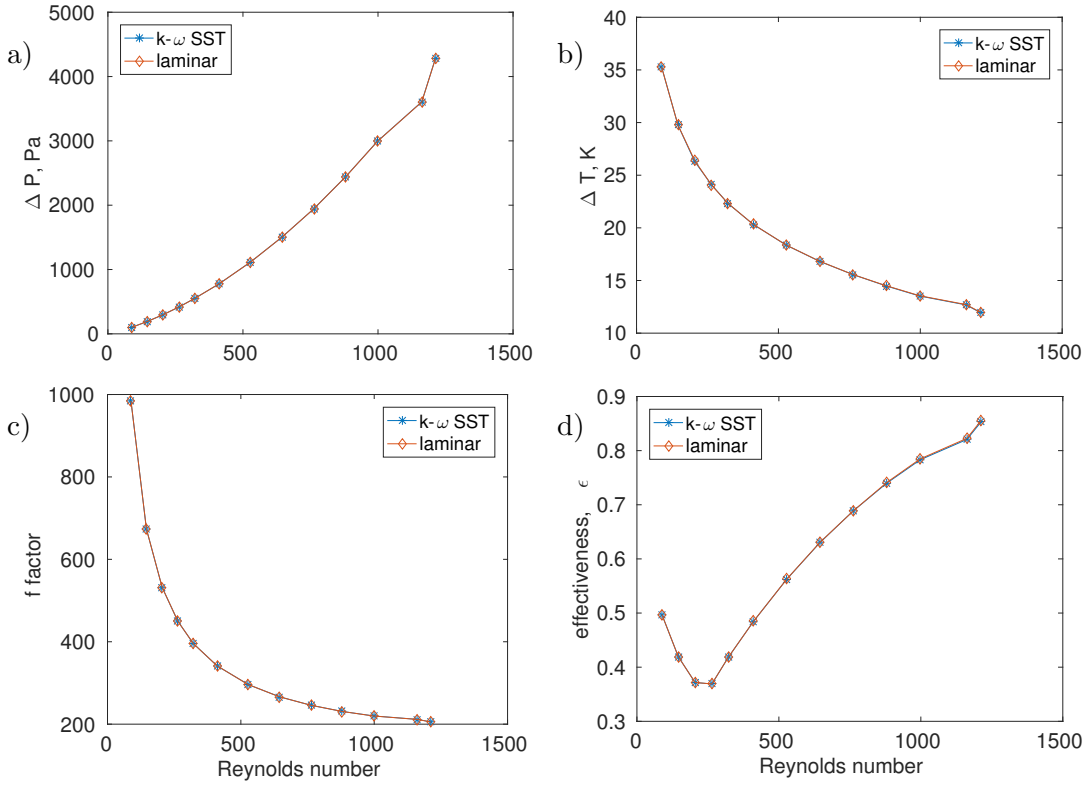

Figure 5.37: Data of a) pressure drop, b) temperature change, c) f factor and d) heat transfer effectiveness of the HE section cold flow domain at thermal performance test experimental points.

No significant differences were observed between laminar and turbulent flow prediction models, contrasting to the findings in Chapter 4. It is thought to relate to the compromises necessary for the mesh resolution to predict the three-dimensional flow and also the less disruptive serrated corrugation compared to the sinusoidal one in Chapter 4. Whilst maintaining the steady state assumption probably caused an inaccuracy in the predictions, it is difficult to quantify the extent of it. It could be only estimated to be up to 10% at the highest Reynolds numbers, based on low unsteady flow levels detected in Section 5.3.4.3. As the error was considered low and the steady-state assumption was the only computationally feasible way to resolve the HE section model, the results were considered valid.

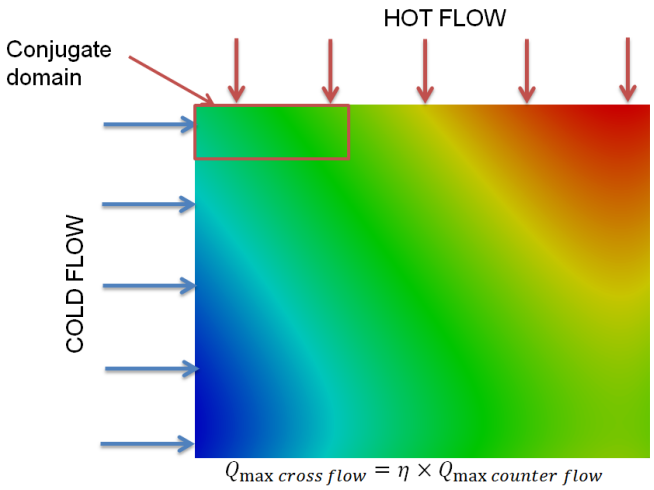

Figure 5.38: Approximate portion of a HE layer simulated shown on the the cross-flow heat transfer result between the two flows separated by a flat plate.

As only a portion of both fluid layers was simulated (Figure 5.38) due to the computational constrains, the cold side HE section model data required interpolation across the HE core layer dimensions. This was necessary in order to implement the HE section data into the HE unit model. Figure 5.39 shows the mean temperature change data along the cold flow direction (flow-wise, left to right in Figure 5.38) of the HE section domain. In this particular application the model predicted that the vast majority of heat transfer occurred in the beginning of the layer, driven by the

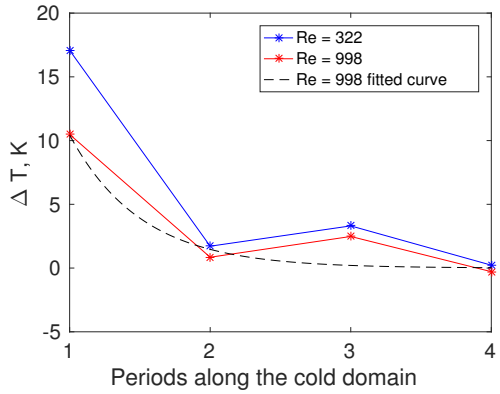

Figure 5.39: ΔT along the cold flow direction at $Re_{\text{corrug, cold}} = 322$ and $Re_{\text{corrug, cold}} = 998$ together with the curve-fitted result for $Re_{\text{corrug, cold}} = 998$ case.

high temperature gradient between the two flows. Curve fitting was undertaken along the flow-wise direction, but did not add a significant increase in overall ΔT (the heat gained to the cold flow) when extrapolated to the full length of the layer for this application.

Measuring the detrimental cross flow heat transfer effects to the efficiency of the HE corrugation proved to be more difficult. It was done by sampling the temperature line data at each HE corrugation period through the middle of the HE section cold flow domain (Figure 5.26). Example of such data extraction after one HE corrugation period is given in Figure 5.40a where the cross flow effects were found strong. This data was then used to estimate the decrease of ΔT along the flow domain by averaging the temperature of the fluid between the solid walls. The extrapolated result for the full HE core layer width is given in Figure 5.40b. This data is then averaged across the layer width to give the mean ΔT through the corrugation periods and enables to calculate the detrimental cross-flow effects. The interpolated results suggested that a significant correction in heat transfer (reduction of $\approx 18 - 30\%$, increasing with the Reynolds number) was required to model the HE core performance accurately. These corrected results (Figure 5.41) were then used for the input to the HE unit model.

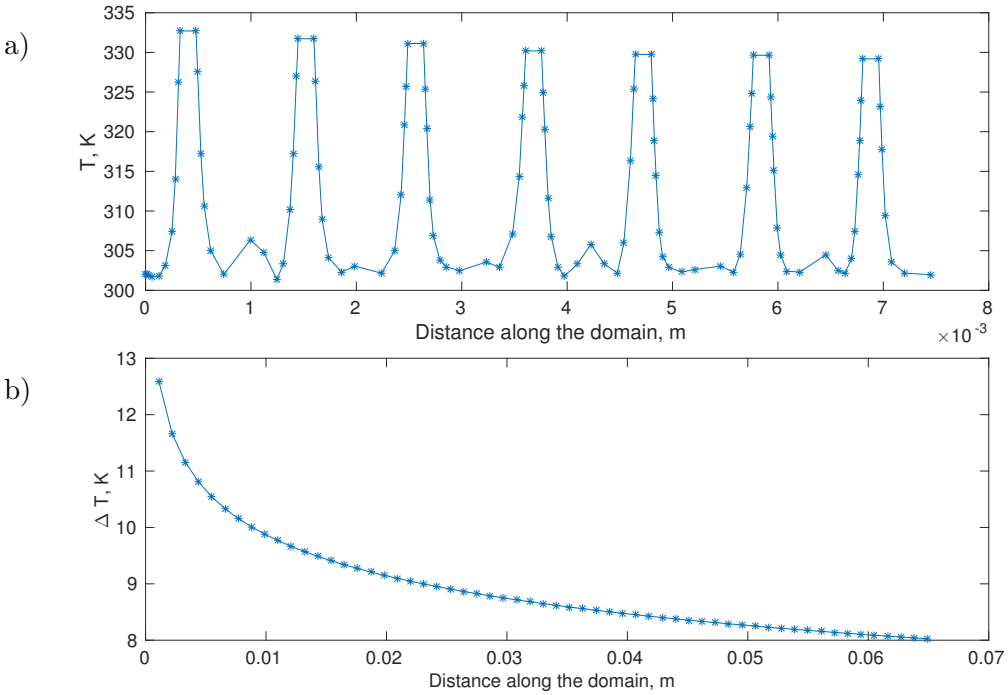

Figure 5.40: Data at $Re = 205$ of a) line data showing the overall temperature decrease after one period of the corrugation b) Curve fitted data of ΔT, K of the first corrugation period extrapolated to the width of the domain.

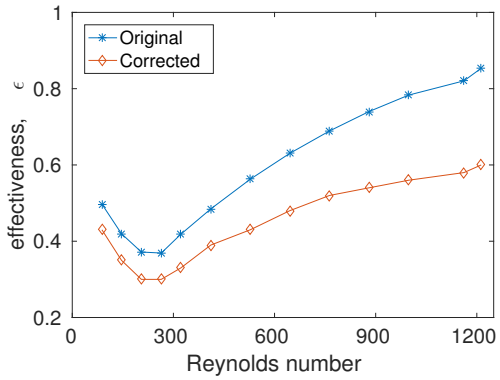

Figure 5.41: Comparing the original HE section effectiveness to the result adjusted for the cross flow heat transfer effects.

5.4.2.1 Contrasting the HE Corrugation Models

A comparison of the results between the single column and HE section corrugation domains was completed using the friction factor f (Equation 5.1). The data in Figure 5.42 shows that the single column domain flow resistance was slightly higher compared to the HE section data, confirming previous results (Figure 5.34). This again is believed to be due to the single column model mesh having a finer resolution. However, the differences were considered insignificant and enabled to verify the HE section model to the single channel simulations.

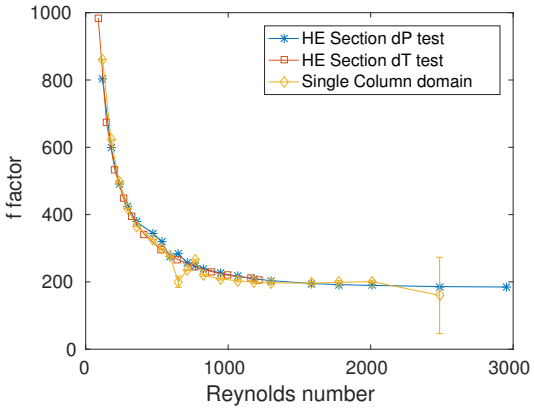

Figure 5.42: Data selection planes for the cold flow domain.

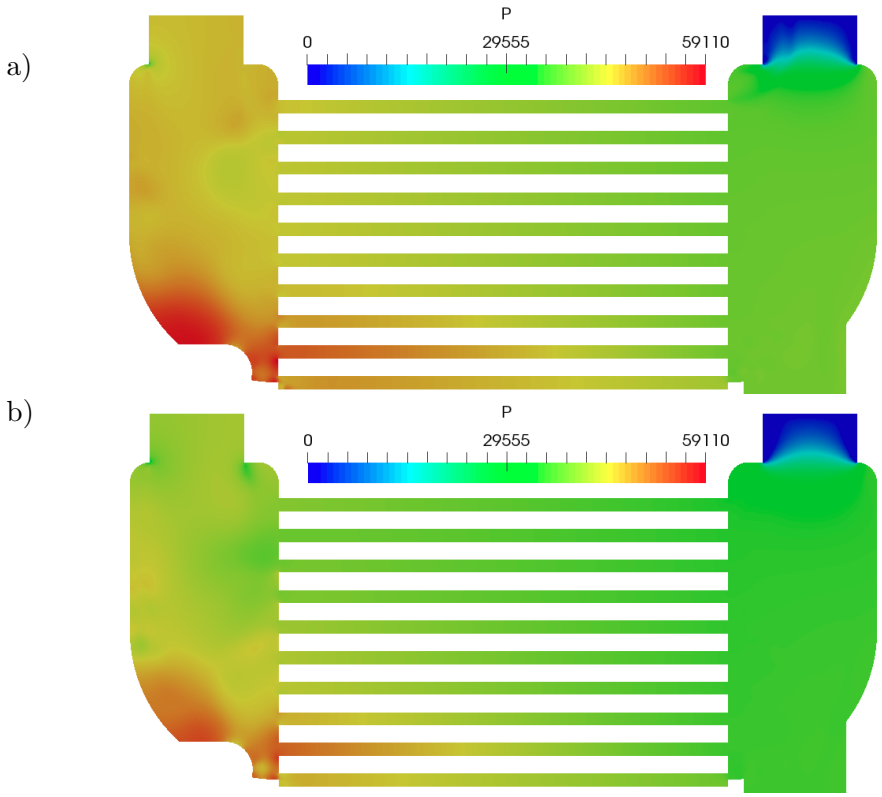

Figure 5.43: Contours of pressure at $Re_{inlet} = 66680$ ($Re_{corrug} = 880$) using a) Power law and b) Darcy-Forschheimer models.

5.5 HE Unit Model Comparison to the Experiments

This section discusses the overall CFD methodology performance against the pressure drop and thermal performance experiments. It was completed using the HE section data implemented in the HE unit model with the setup described in Section 5.3.5. Both Darcy-Forschheimer (Equation 3.47) and power law (Equation 3.48) HE core flow simplifications were evaluated as their implementation in OpenFOAM is different with example pressure drop and temperature change contours shown in Figures 5.44 & 5.43. Darcy-Forchheimer model in each case uses a constant resistance across all layers based on the corresponding HE section result. Power law model, however, automatically selects a resistance based on the mass flow coming into each HE core layer. The difference between the models in turn has an effect on the heat transfer effectiveness source term. The model selects a certain amount of heat transferred based on the mass flow coming to a certain HE core layer across the Reynolds number range and has a visible effect on the HE unit predictions and is further investigated in the following pages.

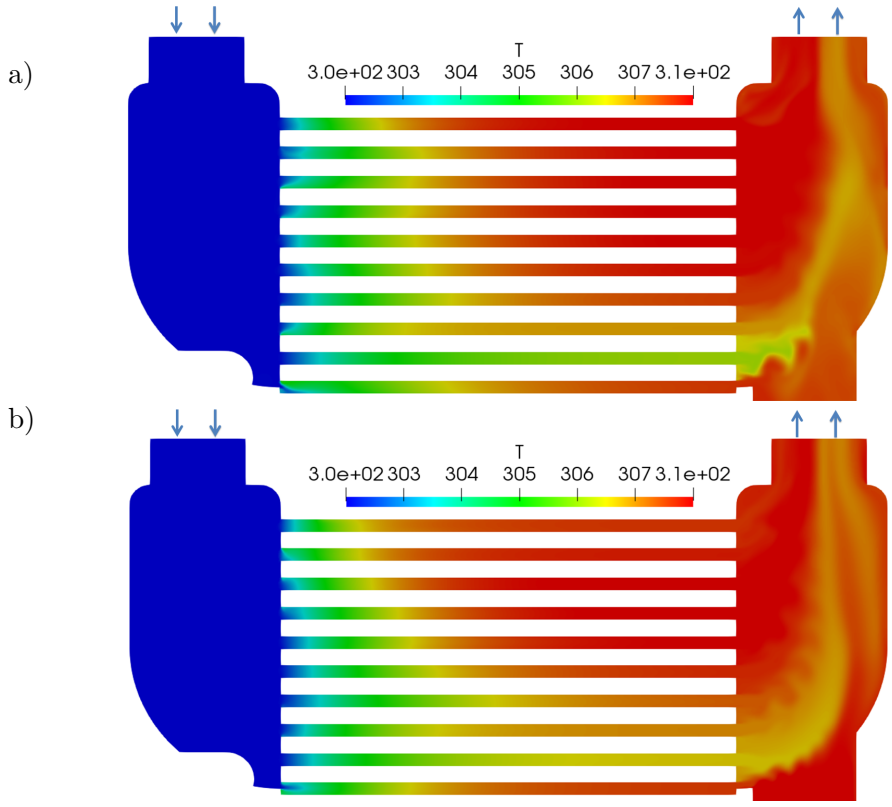

Figure 5.44: Contours of temperature at Re_{inlet} = 66680 (Re_{corrug} = 880) using a) Power law and b) Darcy-Forschheimer models.

In terms of the pressure drop and temperature change only small differences were found between the two HE core models at the HE unit level (Figure 5.45) together with a good agreement of the HE unit model CFD predictions to the experiments. Maximum disagreement of only ≈ 10% in terms pressure drop was found at the highest Reynolds number (Figure 5.45a). It should be noted that the full experimental

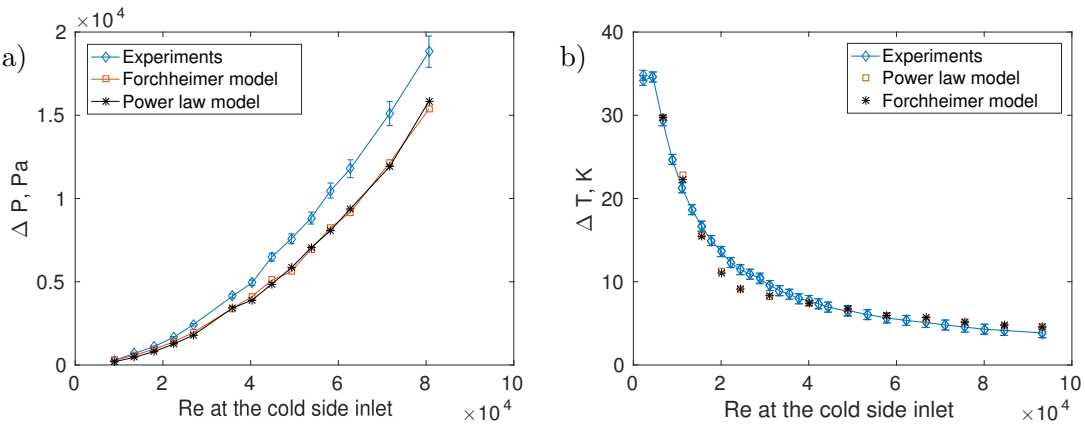

Figure 5.45: Data comparison of: a) pressure drop and b) temperature change through the Reynolds number range (error bars show the experimental error).

Reynolds range for the pressure drop test could not be simulated with CFD due to the convergence problems which occurred because of the extreme pressure gradients inside

the compact HE unit. However, this was not considered critical as this HE unit was experimentally evaluated beyond its typical operation. Increasing disagreement with the experiments is thought to be due to the steady-state assumption used during the HE section predictions, suggested by the previous results in Chapter 4. In Chapter 4 the onset of the unsteady flow was shown at $Re_{corrug} \approx 200$ (sinusoidal geometry), agreeing with the results in this chapter where the unsteady flow is suspected from $Re_{corrug} \approx 300$ onwards.

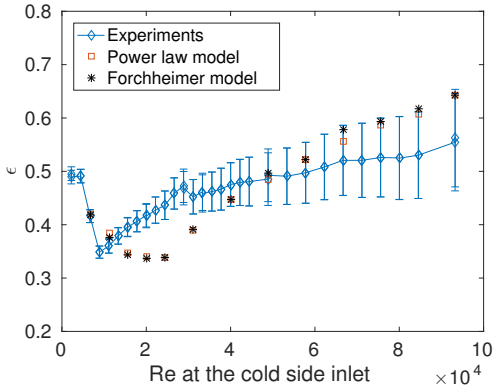

Figure 5.46: Effectiveness comparison (Error bars show the maximum possible experimental error).

Agreement of the HE unit simulations with the thermal performance experiments was also good - the mean difference in terms of ΔT was $\approx 0.94\ K$ whilst the average difference in heat transfer effectiveness (Figure 5.46) was at $\approx 4.8\%$. Again, the steady-state assumption during the HE section model simulations is thought to be the main reason for discrepancy between the HE unit model predictions and the experiments. This helps to explain the lower ΔT and heat transfer effectiveness ϵ around the suspected onset of the transitional regime ($15000 \lesssim Re_{inlet} \lesssim 30000$). However, issues with the experimental work should also be considered. They could have affected the agreement, particularly in terms of ϵ, where even small differences in ΔT are exaggerated (Figures 5.45b vs. 5.46). Firstly, the thermocouples used had a tolerance of ± 0.3 K which partially eliminates some of the disagreement between the simulations and experiments. Secondly heat balance (Q_{hot}/Q_{cold}) was measured during the experiments (Figure 5.10a) and was around $\approx 105\%$. This suggests some loss of heat to the environment which was not simulated numerically and would lead to higher heat transfer predicted by CFD. Thirdly, partial blockages of the physical HE unit caused during manufacturing (Section 5.2.2) could have increased the pressure drop through the HE unit and lowered heat transfer performance (estimated at around $2 - 10\%$).

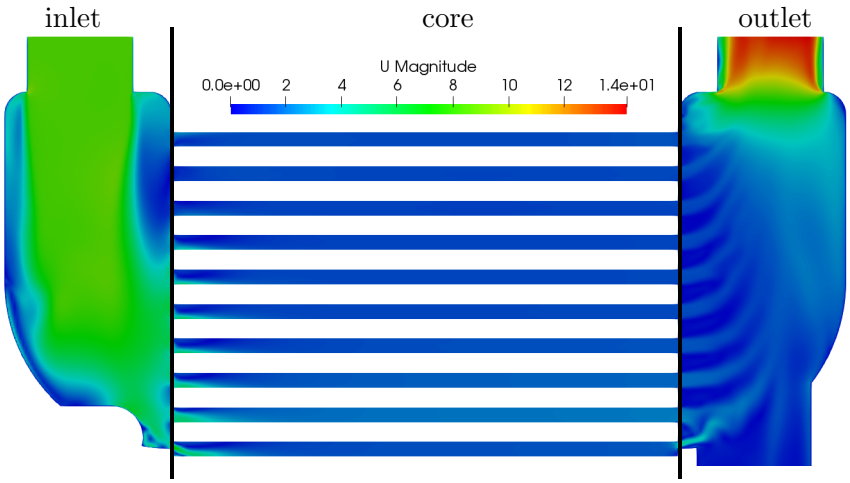

Figure 5.47: Velocity contours through the middle of the cold HE side at $Re_{inlet} = 93240$ $Re_{corrug} = 1213$, showing sectioning of the results for detailed analysis.

5.5.0.1 Detailed Analysis of the HE Unit Model Output

Visible flow maldistribution inside the HE core (Figures 5.43, 5.44 & 5.47) led to the need of a more detailed flow analysis inside the HE unit. To accomplish this, the HE unit domain was firstly split into three sections: inlet/outlet HE headers and the HE core and was analysed in terms of pressure drop and temperature change. Additionally, individual HE core layer performance was analysed to compare the Darcy-Foschheimer and power law HE core simplifications. The data revealed that with increasing Reynolds number the pressure drop becomes increasingly dominant in the outlet HE header compared to the HE core (Figure 5.48). Contrastingly, the flow resistance was found comparably negligible in the inlet HE header. Overall, little

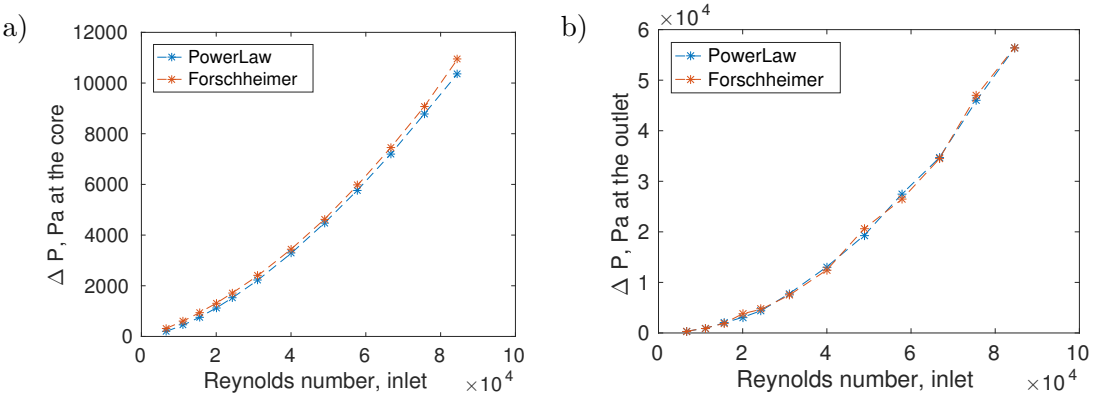

Figure 5.48: Analysis of the separate components of the cold side of the HE: a) average core and b) outlet header pressure drops versus the Reynolds number simulated.

difference was found between the models for the outlet HE header pressure drop prediction whilst the HE core resistance was predicted generally slightly higher by the Darcy-Forschheimer simplification. High pressure drop part at the HE outlet header

was sanity checked using analytical sudden contraction in pipes theory, found in fluid dynamics books, such as White [174]. The head losses in such conditions can be quantified using a common formula:

$$h_f = K\frac{U^2_{outlet}}{2g} \tag{5.2}$$

where g - gravitational constant, U_{outlet} - velocity at the outlet and K - empirical resistance constant. For this case $K = 0.5$ ($A_{core} >> A_{outlet}$) was selected to estimate the pressure drop. Using velocity data extracted from $Re_{corrug} = 1213$ (highest point) ΔP was estimated to $\approx 33000\ Pa$ or $\approx 60\%$ of the predicted value at the outlet HE header. It was expected to obtain a lower ΔP estimate because the flow within the outlet header is more complex than in pipes, however, the estimate helps to further reinforce reliability of the CFD simulations.

b)

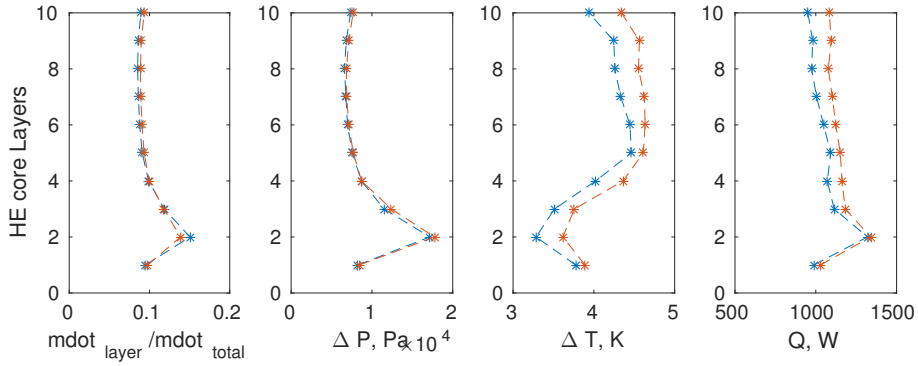

Figure 5.49: Maldistribution, Pressure drop, Temperature change and heat transfer data across the different HE core layers at $Re_{corrug} = 998$. Blue lines indicate power law and red lines - Forscheimer core models. Layer 1 to 10 - indicate bottom to top layers in Figure 5.47.

To better understand the extent of maldistribution in the HE core a more detailed look into the individual HE core layer performance was undertaken (Figure 5.49). Maldistribution across the Reynolds number range was mainly observed within the second and the third layers of the HE core. This in turn led to higher pressure drop and lower overall temperature change through the two HE core layers. It should be noted that first HE core layer was partially blocked during manufacturing which lead low mass flow through during numerical simulations. However, significant maldistribution was found only in those two layers of the HE core whilst the layers above showed rather uniform flow. Moreover, only small differences were found between the power law (blue line) and Darcy-Forschheimer (red line) HE core simplifications which reduced with the increasing Reynolds number. Overall, the Darcy-Forschheimer model predicted marginally smaller maldistribution levels. This in turn led to slightly higher temperature change predictions as the lower mass flow leads to higher ΔT for this

application. However, as shown in Section 5.5, differences between the two HE core simplifications identified become negligible at the HE unit level for this application.

5.6 Conclusions of the Chapter

A compact plate-fin HE with serrated corrugation was evaluated experimentally and numerically. The experiments were carried out at an industrial facility to produce a comprehensive data set which is difficult to find in the literature. A novel HE corrugation domain termed HE section was introduced which takes a slice of a HE core and simulates both the cold and hot flow streams separated by a solid, resolved using conjugate heat transfer methodology. This model eliminates the need for analytical/empirical corrections from books such as Kays and London [6] and was used to generate the data for the HE unit model. The second HE corrugation model used a single corrugation period width channel of the HE cold layer (termed single column). This model was based on similar recent literature studies and was used to verify the novel HE section domain. The HE unit was modelled using two HE core simplifications for the flow and the heat transfer effectiveness model for the heat transfer inside the HE core. Both HE unit models produced similar results in terms of the overall pressure drop and temperature change. In addition, similar levels of flow maldistribution inside the HE core were found despite different implementations of the HE core flow simplifications in OpenFOAM. Results of the HE unit CFD modelling agreed well with the experimental data with the maximum $\approx 10\%$ difference in pressure drop at the highest Reynolds number and an average of $\approx 4.9\%$ difference in heat transfer effectiveness. Small levels of disagreement arose from both experimental inaccuracies and the numerical assumptions employed. The results allowed to validate the novel HE CFD design methodology developed.

Chapter 6

Compact Heat Exchangers and Additive Layer Manufacturing

Contents

6.1 Introduction

In this chapter HE design work which combines Computational Fluid Dynamics (CFD) and Additive Layer Manufacturing (ALM) is presented. Among various ALM tech-

niques Selective Laser Melting (SLM) method is selected as it provides unprecedented design freedom compared to the traditional HE manufacturing methods and can produce surfaces at the lengthscales relevant to the HE (Chapter 2). Concept HE design work is accomplished by splitting the HE unit into two parts: HE corrugation and HE headers. Initially a number of concepts are generated and small representative sections are manufactured to evaluate their feasibility. Findings of the study are then used in designing and manufacturing a full size proof of concept novel HE unit. It is then numerically evaluated using the CFD methodology established in Chapters 4 & 5 and compared to a conventional pin-fin HE unit.

6.2 Generating Novel Heat Exchanger Structures

6.2.1 HE Corrugation Concepts

HE corrugation is crucial in determining the size and efficiency of the HE, however, thermally efficient HE fins often lead to high frictional resistance and ALM has a potential to balance them both. This can be accomplished by either customising current HE corrugation or by proposing a novel heat transfer solution which would eliminate drawbacks of current technology. Thus, generating the HE corrugation was completed in two steps: firstly, current plate-fin HE corrugations were iterated. Then the second part of the design work introduced a new type of corrugation, creating a hybrid HE core structure. Iterative designs of the HE core are shown in Figures 6.1 - 6.3

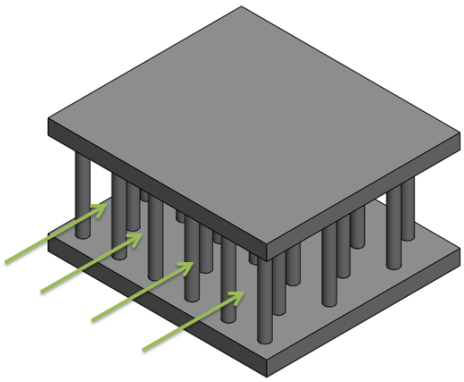

Figure 6.1: Cylindrical HE corrugation section.

with the cylindrical pin-fin corrugation in Figure 6.1 created as a robust baseline design. It is a combination of two conventional types HE: plate-fin and tube-fin. However, in this design the cylinders were designed solid, contrary to the tube-fin HE (Figure 2.10) where the cylinders carry the second HE flow stream. Spacing the cylindrical corrugation evenly enables good structural integrity of the HE core and provides an

alternative to plate-fin HE. The structure is also enabled by the SLM process whilst the manufacture of it using the traditional processes is difficult. Figures 6.2 and 6.3 show

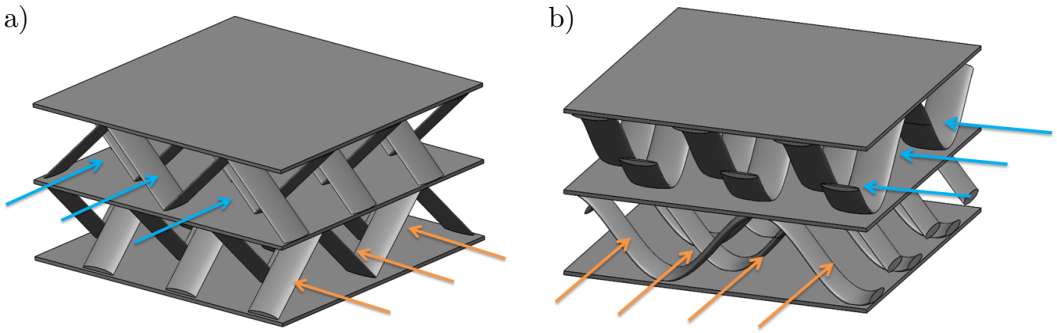

Figure 6.2: a) Triangular and b) Sinusoidal HE corrugation in cross flow configuration.

iterations of the serrated plate-fin HE corrugation (thoroughly analysed in Chapter 5) in cross and counter flow orientations. Out of the two orientations, counter-flow is more efficient [6], however, both were created in order to test structural integrity of them when manufactured with SLM. Both triangular and sinusoidal fins are made of thin

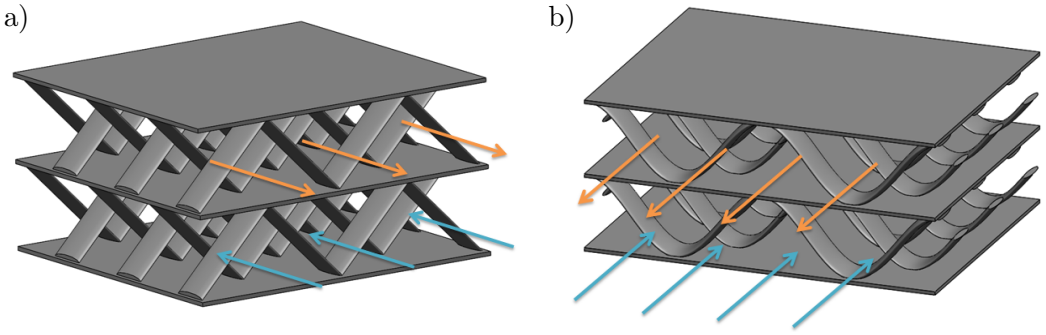

Figure 6.3: a) Triangular and b) Sinusoidal HE corrugation in counter flow configuration.

ellipses (maximum thickness 0.5 mm). This potentially reduces pressure drop through the fins compared to the traditional serrated corrugation which is manufactured by pressing the fins from a flat metal sheet. Additionally, ALM designs have the potential to vary the angle of attack of the serrations which could provide additional mixing to match a certain heat transfer requirement.

Different versions of the novel corrugation are presented in Figures 6.4 and 6.5 in both cross and counter flow arrangements. The novel corrugation is fundamentally different and introduces vertical flow pathways between the same HE core fluid layers, designed to:

- Allow maldistributed flow entering the HE core to adjust itself inside the HE core in order to minimise underutilised HE regions.

- Provide additional fluid-fluid mixing caused by fluid entering through vertical conduits into the neighbouring HE core layers of the same fluid stream. This mixing is achieved with no structural turbulators which are often used in current HE and is expected to result in increased heat transfer performance.

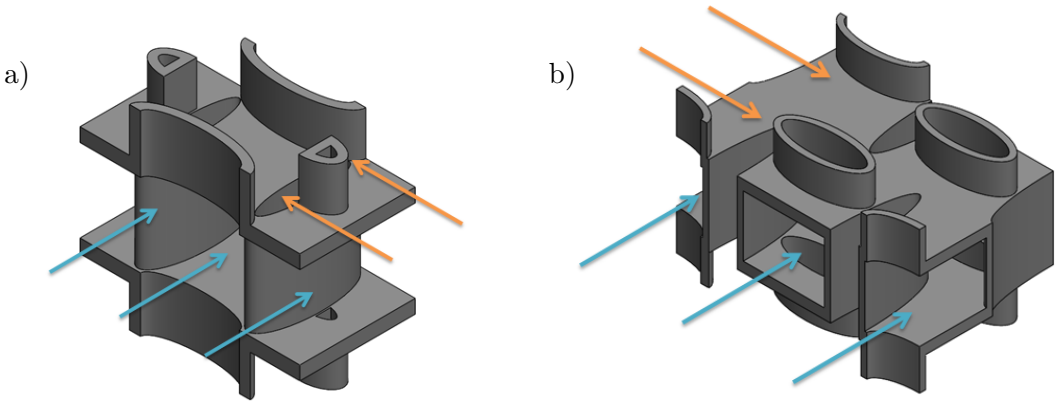

Figure 6.4: Two periodic versions of novel HE geometry in cross-flow orientation.

Figure 6.4 shows two iterations of the novel HE corrugation in cross-flow arrangement. A corrugation version with additional turbulators is shown in Figure 6.4a. It was designed to enhance heat transfer at the lower Reynolds numbers where level of forced convection is lower. Figure 6.4b shows the novel corrugation with different aspect ratios of the vertical conduits for the two fluids in thermal contact. This was designed assuming that they have contrasting thermal properties. Figure 6.5 shows the novel inter-layer corrugation in a more efficient counter-flow orientation. Such alignment of the conduits provides the simplest structure to manufacture as the vertical channels are at the 45^o angle to the parallel HE core layers. This aids the manufacturing process by eliminating the need for support material. A series of these concepts were then manufactured using SLM to evaluate their feasibility (Section 6.2.3).

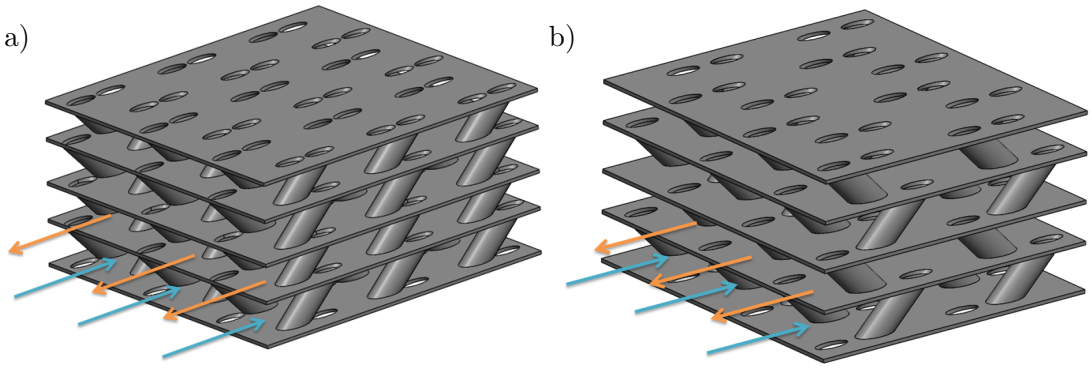

Figure 6.5: Two versions of the novel inter-layer HE corrugation in counter-flow orientation.

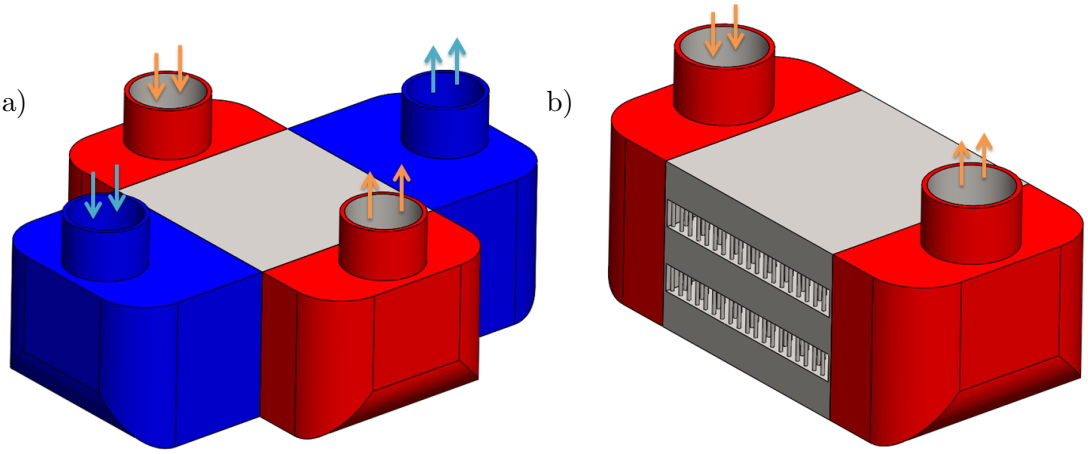

Figure 6.6: a) Cross-flow header arrangement with two flow streams covered with headers. b) Cross-flow header arrangement where one of the flows is subjected to the ambient air. Red and blue colours indicate hot and cold flow streams respectively.

6.2.2 Manifold HE Header Design

Design of the HE headers was focused on next as their design is critical for efficient HE core performance. Current HE headers are manufactured by welding metal sheets onto HE core with two example layouts shown in Figure 6.6. However, this methodology has numerous disadvantages. Firstly, the welding process can lead to flaws inside the HE flow streams, even to blockages of HE core sections (Chapter 5 discusses this in more detail). Secondly, the traditional manufacturing leads to inefficient HE headers requiring a large installation volume. Thirdly, the flow cross-sectional area inside such headers is twice over-expanded compared to the HE core flow path for a specific fluid (Figure 6.6b). This results in an unnecessary pressure drop inside HE unit.

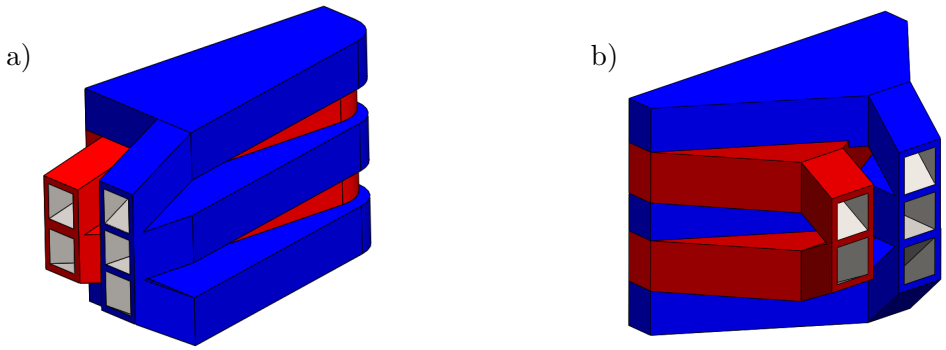

Figure 6.7: Two versions of manifold HE headers designed for counterflow.

Manifold HE headers were proposed as a solution (Figure 6.7). This type of design shows a potential to solve the afore described issues with currently used HE headers. It is not a feasible solution with current manufacturing techniques, however, it can be easily built with SLM (shown in Section 6.2.3). In addition, although the headers in

Figure 6.7 are designed for the counter-flow orientation - the idea could also be applied for cross-flow HE.

6.2.3 Initial Manufacturing

Feasibility of the selected HE concepts was evaluated by manufacturing them using commercially pure titanium with a Renishaw AM250 SLM machine (Figures 6.8 - 6.11). HE corrugation samples (Figures 6.8 & 6.9) were manufactured using a common

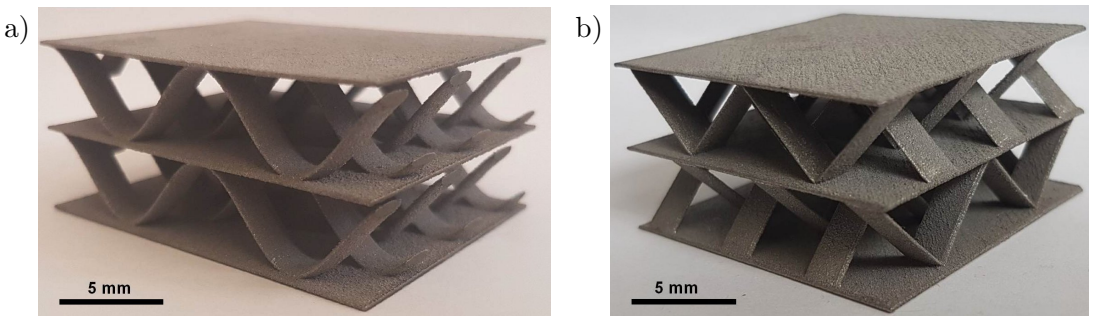

Figure 6.8: a) Sinusoidal and b) Triangular corrugations manufactured using the SLM process.

hydraulic diameter $d_h = 5\ mm$ and uniform 0.5 mm wall thickness. Figure 6.8 shows that the iterated current HE corrugation types were manufactured successfully in both cross and counter-flow orientations. This suggests that extra performance could be gained by adjusting direction of the flow streams for current HE types by utilising ALM. In addition, two complex inter-layer HE corrugation concepts were built without defects (Figure 6.9), confirming feasibility of the novel HE structure with SLM. All the HE corrugation sections have a granular surface finish which is an inherent SLM process feature. Post-manufacturing techniques, such as sand blasting, can be used to obtain a smoother surface finish, however, in this case the thin walled surfaces were not post-processed to avoid potential damage.

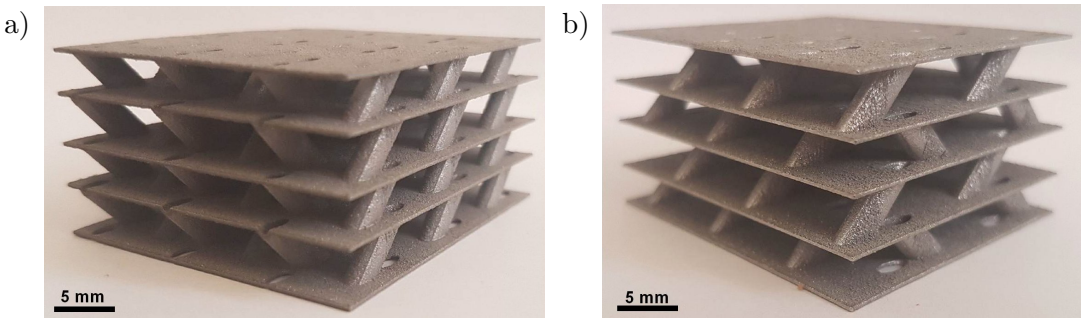

Figure 6.9: Two versions of novel HE corrugation manufactured using the SLM process.

HE header concepts were manufactured (Figure 6.10) with reduced channel height of 2.5 mm to test scalability of SLM. In addition, HE header models were sand blasted

which produced a visually smoother surface finish and confirmed the structural integrity of SLM designs after post-processing. Figure 6.11 shows further scaling down

a) b)

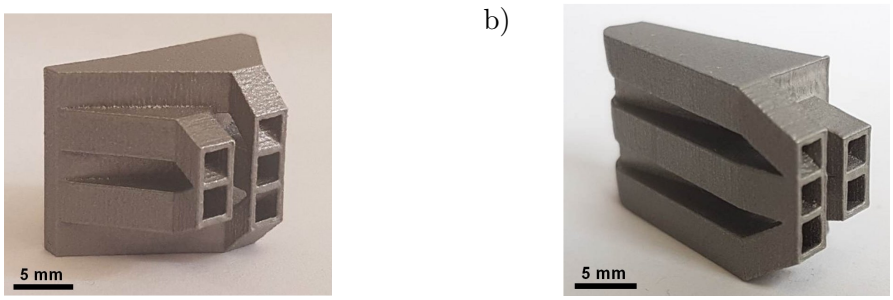

Figure 6.10: Two trial header designs manufactured using the SLM process.

of the HE prototypes. A version of the novel HE corrugation was produced with hydraulic diameter reduced to $d_h = 2.5mm$ and uniform wall thickness of 0.5 mm (Figure 6.11a). The manufactured part was again not affected in terms of both surface quality or structural integrity. Figure 6.11b shows a cylindrical HE corrugation with reduced wall thickness of 0.25 mm. This resulted in thermal stress induced bending of the part and random rough surface of the cylindrical pins. Thus, whilst this rough surface finish in theory could increase mixing and heat transfer, 0.5 mm wall thickness to ensure structural integrity was selected for the prototype HE unit shown in Section 6.3.

a) b)

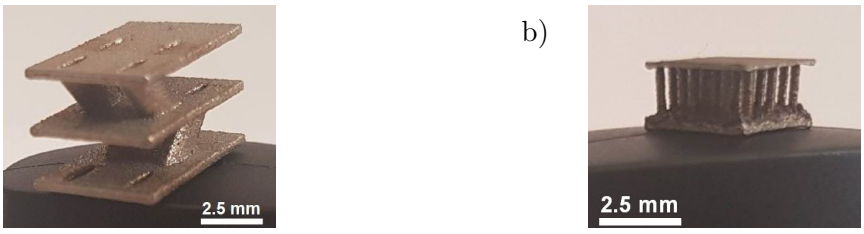

Figure 6.11: Scaled down versions of: a) Inter-layer and b) Cylindrical fins manufactured using the SLM process.

6.3 Design and Manufacture of the Heat Exchanger Demonstrator

A proof of concept HE unit combines the novel inter-layer HE corrugation and manifold HE header ideas (Figure 6.12). It was assembled in a counter-flow HE orientation to highlight SLM capability. ALM HE unit was restricted to be manufactured in a single build volume of the Renishaw AM250 ($250 \times 250 \times 300$ mm), aiming to reduce the cost of manufacture. Thus, a concept HE unit with 4 cold and 3 hot flow pathways was designed with overall dimensions of $78 \times 42.5 \times 262$ mm (Figure 6.13). Identical manifold HE headers were designed for either 3/8" or 1/2" BSP connectors during experimental testing. In addition, the manifold HE headers were designed, thus, manufacture of the

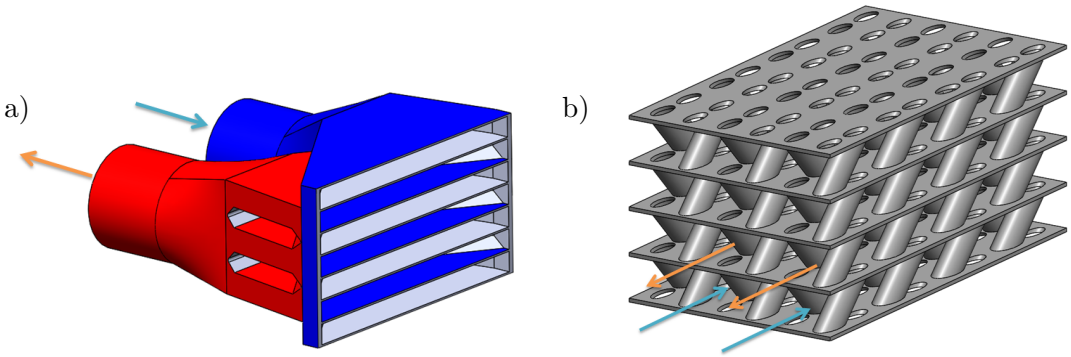

Figure 6.12: Final version of a) HE header and b) corrugation designs used for the proof of concept unit build.

HE would start from the connectors vertically upwards, eliminating the need for any support material and expensive post-processing.

Base corrugation layout shown first in Figure 6.5a was selected because of the ease of manufacture and due to higher potential to be compacted compared to the alternative design in Figure 6.5b. Final corrugation was manufactured with a hydraulic diameter of $d_h = 2.75\ mm$ (Figure 6.12b) and HE compactness β [6] (a widely used design factor) of:

$$\beta = \frac{A_h}{V} = \frac{\text{heat transfer area}}{\text{volume for the flow}} = 818\frac{m^2}{m^3}. \tag{6.1}$$

The two HE unit parameters were inserted into the diagram by Shah [30] (Figure 6.14). It confirmed that the demonstrator HE can be classed as compact for both gases and liquids, a necessity for aerospace HE to save installation space and weight.

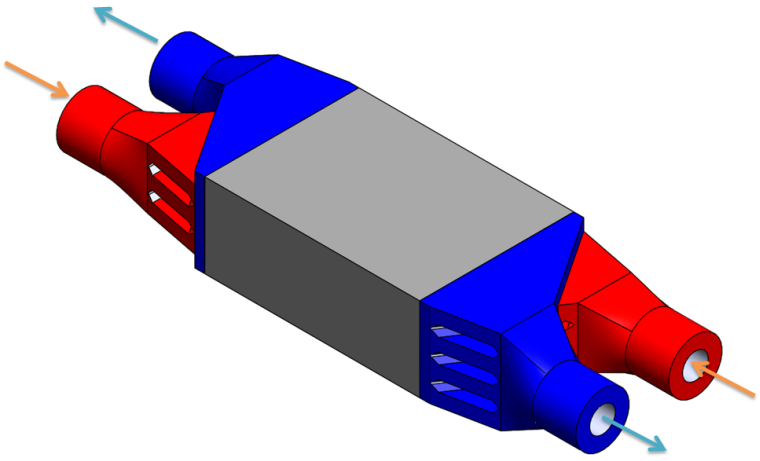

Figure 6.13: Assembled ALM HE unit CAD model.

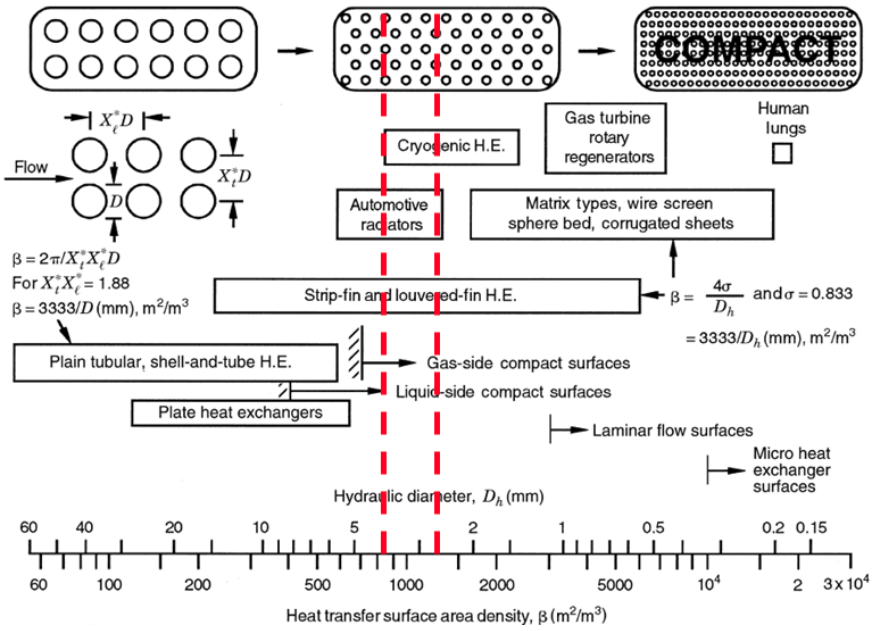

Figure 6.14: Diagram clasifying different types of HE (Shah [30]) with the $d_h = 2.75$ mm and $\beta = 818$ m^2/m^3 of the prototype HE shown by the dotted lines.

Manufactured full size SLM HE unit was made of commercially pure titanium is shown in Figures 6.15 & 6.16. This material was selected as it was preferred by the outsourced SLM manufacturing experts. It should be noted that although it is not a particularly thermally conductive material, it is similar to some high temperature alloys used for HE (e.g. inconel). Uniform wall thickness of 0.5 mm was used inside the HE core to make it comparable to the serrated plate-fin HE unit used in the Chapter 5. Overall, the HE unit manufacture was completed without any quality issues and no post-manufacturing procedures (apart from a clean-up) were applied to preserve the surfaces inside the HE core, resulting in surface finish as shown in Figures 6.15 & 6.16. In addition, successful manufacture allowed evaluation of the novel HE unit using CFD in Section 6.4.

a) 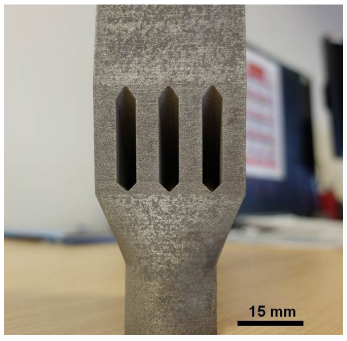

b) 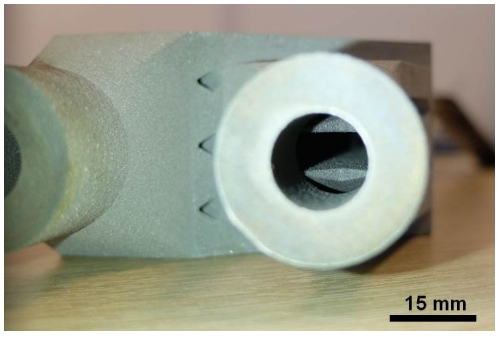

Figure 6.15: Close up views of the manufactured novel ALM HE.

Figure 6.16: SLM manufactured novel HE in printing orientation.

6.4 CFD Modelling of the Novel Heat Exchanger

Numerical ALM HE modelling follows the guidelines established in Chapters 4 & 5 of the thesis and is used to evaluate the novel HE design. The novel HE corrugation is evaluated across the $25 \leq Re_{corrug} \leq 500$ Reynolds number range. For HE unit calculations it is equivalent to $1400 \leq Re_{inlet} \leq 55000$ (assuming even flow expansion in the HE core). HE corrugation predictions are undertaken using laminar flow assumption whilst the HE unit predictions are completed using $k-\omega$ SST model, initialised with 5% turbulence intensity and hydraulic HE corrugation diameter as a mixing lengthscale. All the simulations are completed using a steady-state assumption to save computational time. Mesh independent solutions are obtained for HE corrugation and HE unit models. Both computational domains are approximated using discretisation schemes in Table 6.1. Water was chosen as the working fluid for the simulations with constant fluid properties (Table 6.2). Hot side of the HE was assumed to remain at a constant temperature of $T = 318\ K$ whilst the cold HE side inlet was set to $T_{inlet} = 293\ K$. This was enabled to reduce the computational cost by eliminating hot flow and solid domains. However, it still allowed to characterise the novel HE in terms of heat transfer and flow performance.

	Discretisation scheme
Gradient	Gauss linear
Pressure	Gauss linear corrected
Momentum	bounded Gauss linearUpwind
Energy	bounded Gauss linearUpwind
Time	steady state

Table 6.1: Summary of discretisation schemes used for ALM simulations.

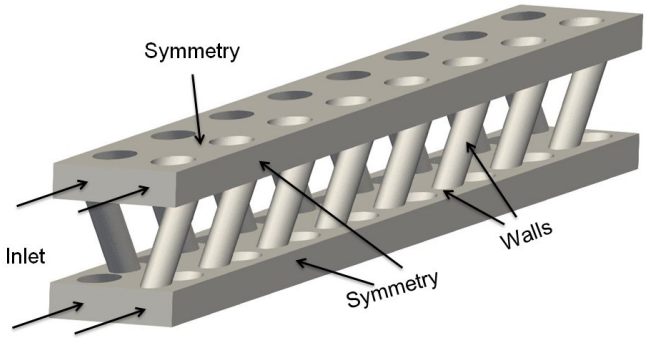

Figure 6.17: HE corrugation domain with the boundary conditions explained.

6.4.1 HE Corrugation Model

Firstly, the HE corrugation model is presented, developed to generate the data for the simplified HE unit model. In this case a fully symmetric cold flow corrugation channel of the ALM HE core was used (Figure 6.17). Its meshing process was completed using `blockmesh` and `snappyHexMesh` tools inbuilt within OpenFOAM. The methodology firstly selects the computational domain of interest inside the `blockmesh` generated (Figure 6.18). The selected domain mesh is then refined and snapped to the surface using control parameters for a certain computational domain set by the `snappyHexMesh` dictionary. A range of meshes were created (Table 6.3) to study grid independence with the numerical settings described in Section 6.4. $Re_{corrug} = 200$ was selected to avoid being close to the unsteady flow region, studied thoroughly in Chapters 4 & 5.

	Cold flow	Units
ρ	994.1	ks/m^3
μ	0.719×10^{-3}	$Pa \cdot s$
C_p	4178	$J/(kgK)$
Pr	4.885	-

Table 6.2: Properties of water used for the numerical ALM HE predictions.

Visualisations are given in Figures 6.19 & 6.20 where the computational domain was clipped across the middle top half of the corrugation domain and through the first inter-layer tube row. Time-averaged vortex shedding resolved behind the elliptical

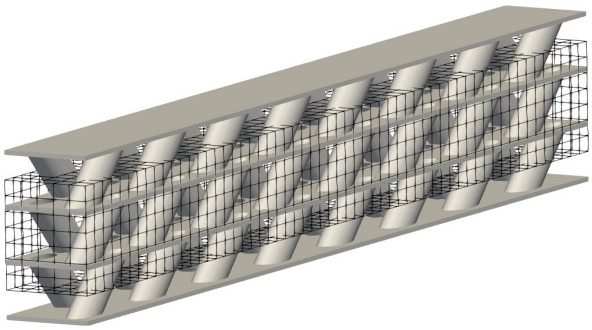

Figure 6.18: HE core section of the ALM HE with blockMesh to show the extracted fluid volume for HE corrugation model.

channels is given in Figure 6.19a, showing flow mixing induced by the elliptical conduit shape. Figure 6.19b shows the vertical velocity component inside the HE corrugation model and a clear occurrence of the inter-layer flow, despite uniform velocity specified at the inlet of the domain. Figure 6.20a shows the constant temperature condition applied onto the computational domain and heat transfer occurring inside the inter-layer conduits. Pressure drop inside the HE corrugation channel is given in Figure 6.20b. It can be seen increasing faster in the first period of the domain and then stabilising for the rest of the corrugation periods.

a)

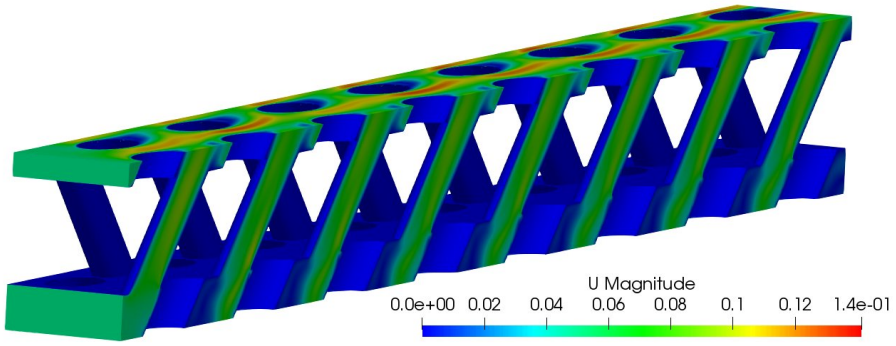

b)

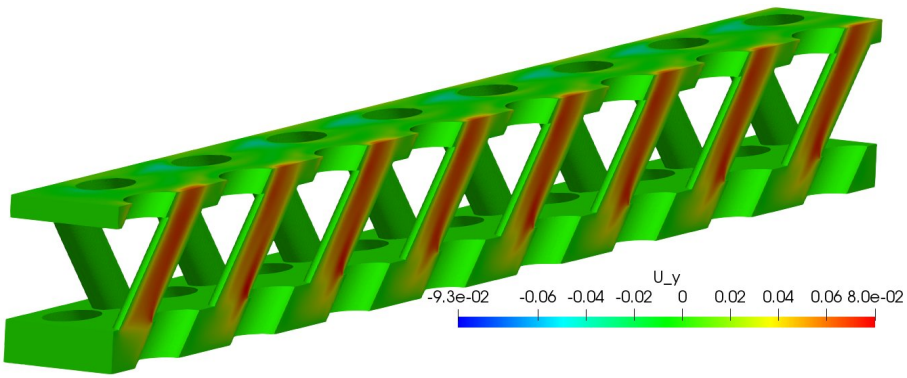

Figure 6.19: Visualisations of the novel ALM HE corrugation model at $Re_{corrug} = 200$ using contour plots of a) velocity magnitude and b) vertical velocity component. Flow direction is left to right.

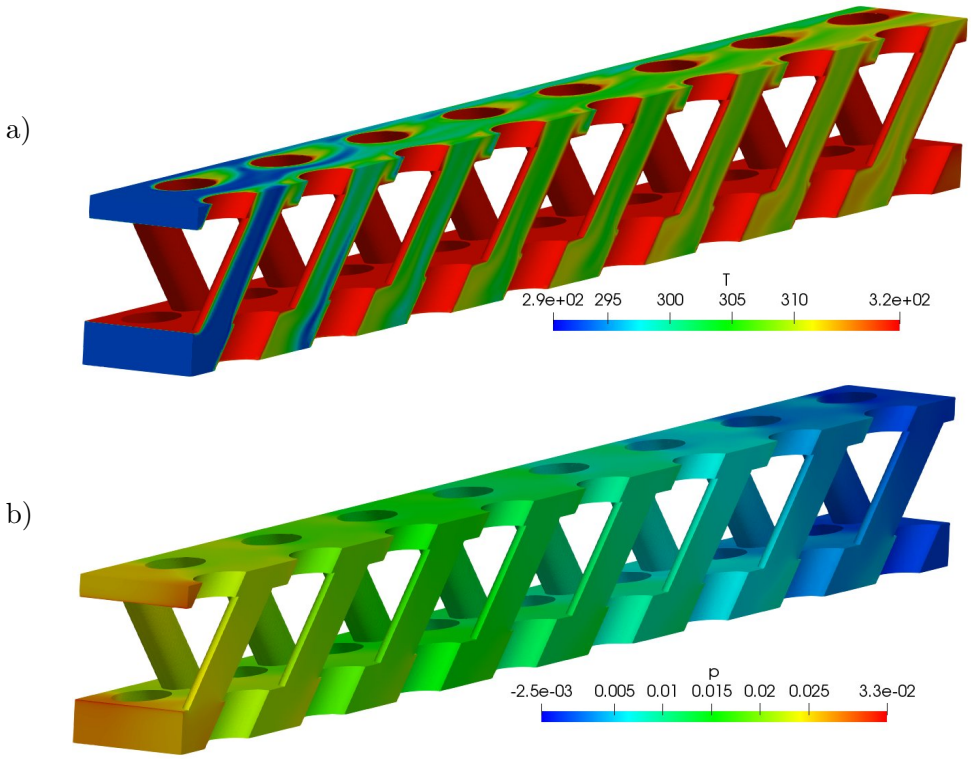

Figure 6.20: Visualisations of the novel ALM HE corrugation model at $Re_{corrug} = 200$ using contour plots of a) temperature and b) pressure. Flow direction is left to right.

The HE corrugation model results were summarised in Table 6.3 to study the overall channel performance as it is the input to the simplified HE unit model. This produced more visible differences between the meshes and allowed choosing the fine mesh for further simulations despite having a high ($\approx 13 \times 10^6$ cells) mesh resolution. This grid was also selected because of the low Reynolds number used for grid independence and considering that higher flow rates will be analysed which in turn normally require higher computational resolution.

Mesh	Mesh size	ΔP, Pa	ΔT, K
Coarse	43951	20.28	16.28
Coarse 2	296930	25.75	18.54
Medium	1.6×10^6	26.44	18.91
Medium 2	2.1×10^6	26.44	18.81
Fine	13.4×10^6	26.24	18.61
Fine 2	20.4×10^6	26.14	18.64

Table 6.3: Mesh resolution data of the ALM HE corrugation showing the overall performance of the channel.

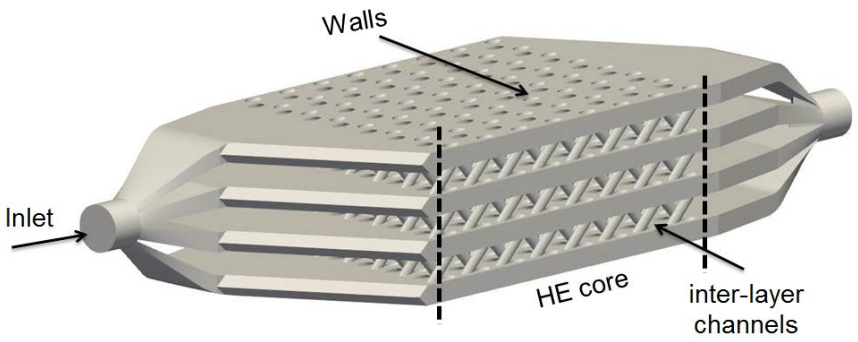

Figure 6.21: Cold flow domain of the ALM HE unit used for CFD predictions.

6.4.2 HE Unit Model

Two models for resolving the novel HE unit mesh were developed: fully resolved inter-layer HE unit (Figure 6.21) and the simplified HE unit domains (Figure 6.22). Compared to the traditional simplified HE core, resolving the novel inter-layer channel HE unit model is advantageous as it allows to study the complex flow in detail, essential in understanding effectiveness of the inter-layer conduits. Both computational domains were meshed using a combination of `blockMesh` and `snappyHexMesh`, identical procedure to the HE corrugation model (Section 6.4.1). Simulations were completed at $Re_{inlet} = 7532$ with numerical setup in Section 6.4. Fully detailed analysis of the ALM HE prototype was computationally feasible due to two reasons: smaller overall HE size and larger hydraulic diameter of the HE corrugation than in Chapter 5. Same as in the HE corrugation model, a constant temperature condition of $T = 318\ K$ for HE unit modelled was applied to the inner HE core walls (Figure 6.21). Heat transfer through the HE header surfaces was not included as it was considered negligible.

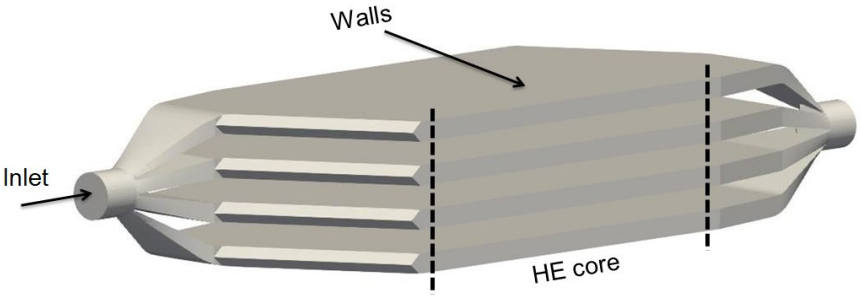

Figure 6.22: The cold flow HE unit domain extracted for the simplfied HE modelling.

Simplified HE model setup developed to use the data from the HE corrugation model for input (Section 6.4.1) was similar to Chapter 5 model as the HE core was reduced to four empty layers (Figure 6.22). This model does not consider the vertical

flow pathways (initial inclusion of them led to solution divergence) and uses Darcy-Forschheimer and heat transfer effectiveness source terms (Equations 3.47 & 3.50) for flow and heat transfer. Arbitrary uni-directional flow resistance of $f = 236$ (with Darcy term $d = 0$) and effectiveness of $\epsilon = 0.4$ values were used as inputs for mesh independence. It should be noted that using constant temperature boundary condition, the effectiveness model simplifies:

$$\epsilon = \frac{T_{\text{out, cold}} - T_{\text{in, cold}}}{T_{\text{in, hot}} - T_{\text{in, cold}}}. \tag{6.2}$$

This enables to calculate the HE outlet temperature which should be predicted by the simplified model ($T_{out} = 303\ K$ or $\Delta T = 10\ K$). A series of meshes were also created to evaluate predictions using both domains (Table 6.4).

Mesh	Inter-layer HE unit mesh size	Simplified HE unit mesh size
Coarse	1.69×10^6	1.69×10^6
Coarse2	8.82×10^6	6.71×10^6
Medium	27.4×10^6	27.71×10^6
Fine	69.58×10^6	44.56×10^6

Table 6.4: Data of the HE unit meshes, cold flow domain only.

Firstly, the detailed inter-layer HE model is visualised using flow and temperature contours which cut through the third and fourth layers of HE in Figures 6.23 & 6.24. Velocity distributions in both layers show clear maldistribution in the inlet HE header.

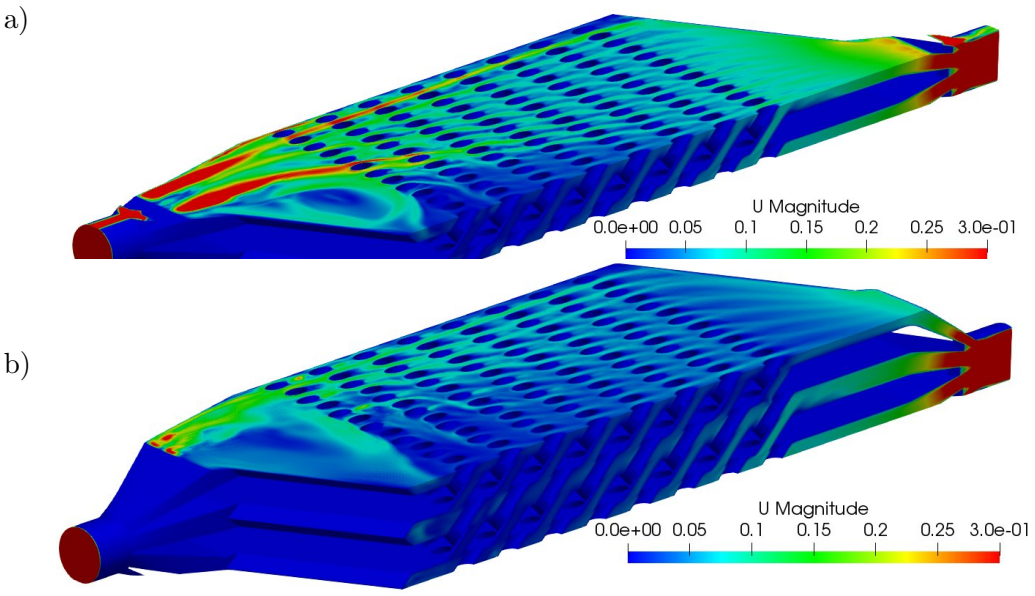

Figure 6.23: Velocity contours through the middle of a) third and b) fourth layers of the novel ALM HE at Coarse2 resolution (counting the layers from the bottom to the top of the inter-layer HE model, Figure 6.21).

It was caused by a non-optimal initial HE header design, driven by the restricted printing volume of the SLM apparatus used to manufacture the prototype. Also, much higher fluid velocities are seen in the third HE layer (Figure 6.23a) compared to the fourth (Figure 6.23b). It suggests maldistribution at the inlet to HE core section, studied further in Section 6.6.1.1. Temperature contours in Figure 6.24 show that the maldistribution leads to uneven fluid heat up inside the HE core. Also, the heat is entrained into the inlet HE header and pre-heats the flow prior the HE core section. However, Figures 6.23 & 6.24 show a clear presence of inter-layer flow and heat transfer. This agrees with HE corrugation model predictions and shows the potential of the novel HE. To evaluate the solution independence the overall HE unit performance

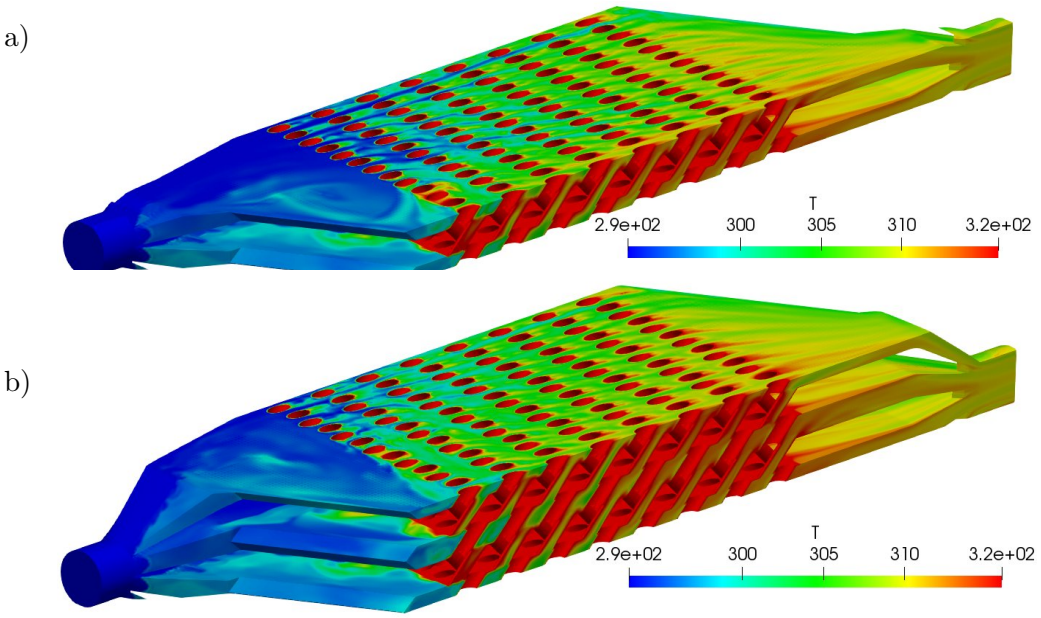

Figure 6.24: Temperature contours through the middle of a) third and b) fourth layers of the novel ALM HE at Coarse2 resolution (counting the layers from the bottom to the top of the inter-layer HE model, Figure 6.21).

Mesh	ΔP, Pa	ΔT, K
Coarse	143.69	15.088
Coarse 2	143.75	16.13
Medium	157.87	16.5
Fine	163.44	17.43

Table 6.5: Mesh resolution data of the ALM HE unit model showing the overall performance.

was summarised in Table 6.5. The data allowed to conclude that medium mesh is of sufficient accuracy as it provided the closest values for both pressure drop and heat

transfer to the fine mesh. It was also much more manageable than the fine mesh with current computational capabilities (27×10^6 versus 70×10^6 cell size meshes).

Simplified HE model (Figure 6.22) was post-processed using the same procedure. However, in this section the two models were not compared directly since arbitrary values were selected to simplify the HE core. Firstly, the flow was visualised in Figure 6.25 to show the effect of assumptions on the flow and heat transfer. Velocity distri-

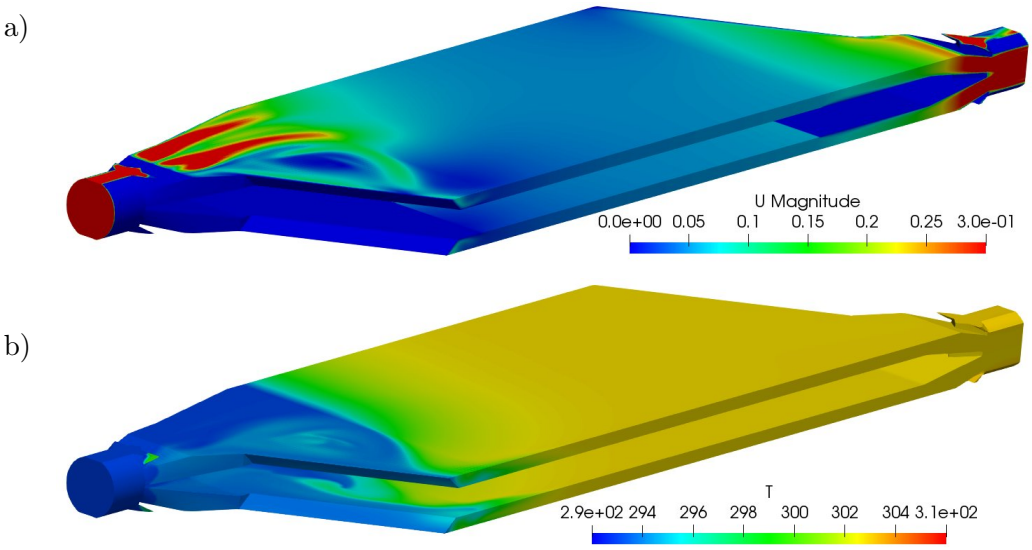

Figure 6.25: a) Velocity and b) Temperature contours of the third layer of the novel ALM HE at Coarse2 resolution (counting layers from the bottom to the top of the porous HE mode, Figure 6.22).

bution (Figure 6.25a) shows that the inlet HE header maldistribution is still resolved. However, overly simplified flow is predicted, compared to the inter-layer HE (Figure 6.23). Because of this the temperature distribution inside the HE model (Figure 6.25b) was resolved to the prescribed value of $T_{out} = 303\ K$ almost directly at the entrance to the porous region, oversimplifying the result. It should be noted that in this case all four layers were prescribed with an identical temperature jump, irrespectively of the mass flow coming to each HE core layer. To understand the overall performance

Mesh	ΔP, Pa	ΔT, K
Coarse	148.88	9.92
Coarse 2	156.77	10.15
Medium	167.17	9.76
Fine	170.63	9.85

Table 6.6: Mesh resolution data of the simplified ALM HE model showing the overall performance of the channel.

differences the results were summarised in Table 6.6. All the meshes produced a close

result to the prescribed temperature jump of $\Delta T = 10\ K$ whilst more differences were observed in ΔP. Medium resolution mesh was selected again for further simulations as it predicted the closest pressure drop to the fine mesh whilst still maintaining a reasonable computational expense.

6.5 Novel HE Corrugation Modelling Across Reynolds Number Range

In this section, mesh independent novel inter-layer HE corrugation model is analysed at $25 \leq Re_{corrug} \leq 500$. It is undertaken to establish a dataset for the simplified HE unit model and to analyse the changing HE corrugation performance. The overall single channel model performance was summarised in Figure 6.26 using friction factor (f) and heat transfer effectiveness (ϵ) data. Additionally, pressure drop (ΔP) and temperature change (ΔT) results are in Table 6.7. Friction factor f data (Equation 3.47, Figure 6.26a) reduces to a steady value at the higher Reynolds numbers, trend-wise agreeing with Chapter 5 results. Heat transfer effectiveness (Equation 3.50, Figure 6.26b) predictions decay with increasing Reynolds number, an expected result with fixed temperature heat transfer condition. The last point ($Re_{corrug} = 500$), however, is an outlier from the overall trends which suggests a possible switch from steady-state to the unsteady flow regime. It is thought to relate to the occurring flow instability which led to the slight fluctuations in the overall pressure at $Re_{corrug} = 500$ in Figure 6.27.

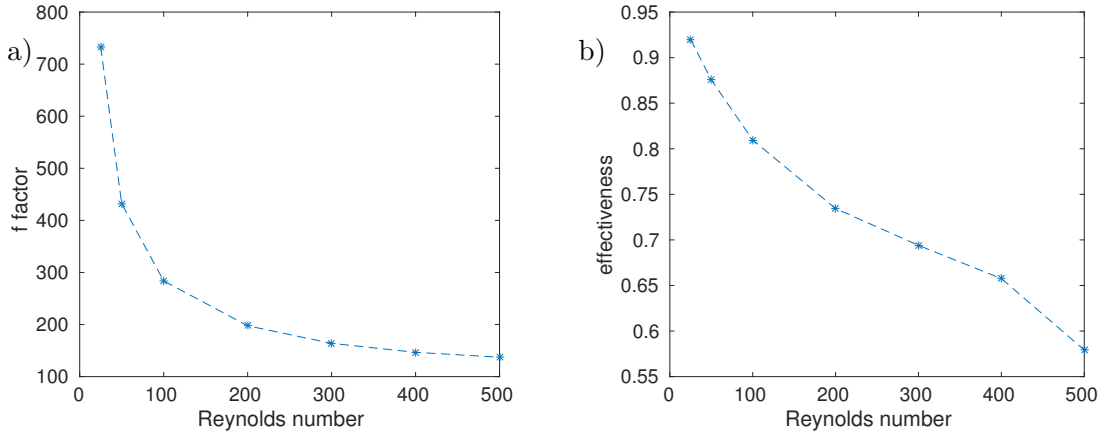

Figure 6.26: Overall single channel characteristics using a) f factor and b) heat transfer effectiveness.

To test the theory, an additional run at $Re_{corrug} = 600$ was completed. It showed that any increase in the Reynolds number leads to solution divergence using the steady-state and laminar assumptions. Thus, numerical assumptions at the higher Reynolds

number flows should be reconsidered by enabling turbulence modelling and potentially utilising the transient flow solver.

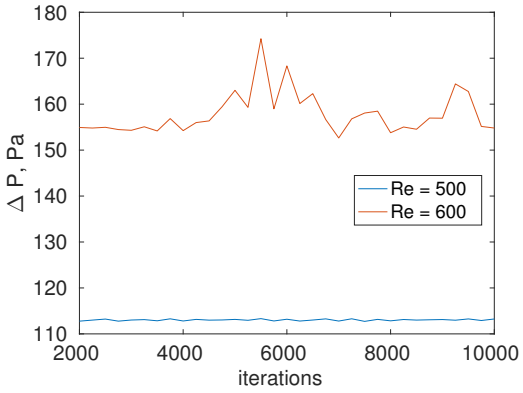

Figure 6.27: Pressure drop to show the occurrence of unsteady flow which leads to the breakdown of the steady assumption at $Re_{corrug} = 600$.

Re	ΔP, Pa	ΔT, K	Re	ΔP, Pa	ΔT, K
25	1.5	23	300	48.56	17.35
50	3.5	21.89	400	77.23	16.44
100	9.34	20.24	500	113	14.48
200	26.028	18.36			

Table 6.7: Averaged data of the detailed ALM HE corrugation model.

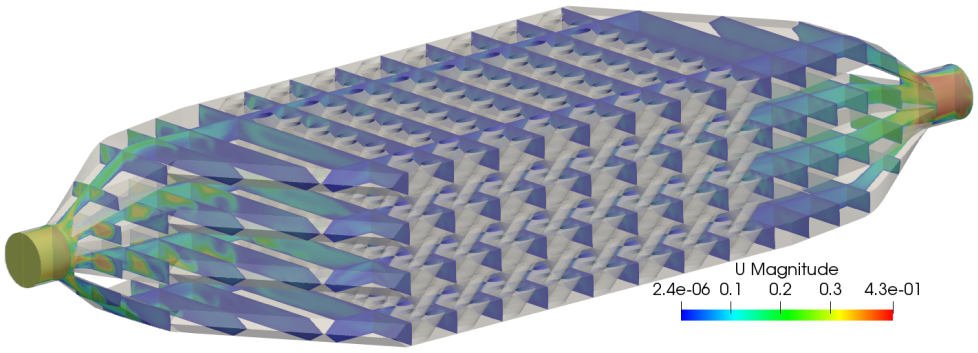

Figure 6.28: Data extraction planes at $Re_{corrug} = 100$ showing velocity contours.

6.6 HE Unit Modelling across the Reynolds Number Range

6.6.1 Inter-layer HE Unit Simulations

In this section, performance of the fully detailed ALM HE unit model is assessed at $25 \leq Re_{corrug} \leq 500$ to understand the change in novel inter-layer HE performance with increasing flow rate. It was undertaken using the sampling planes in Figure 6.28

where the data was averaged across all four HE layers at each location. Example results of pressure and temperature for $Re_{corrug} = 100$ and $Re_{corrug} = 300$ cases along the domain are shown in Figure 6.29. A clear jump in pressure drop is observed at the

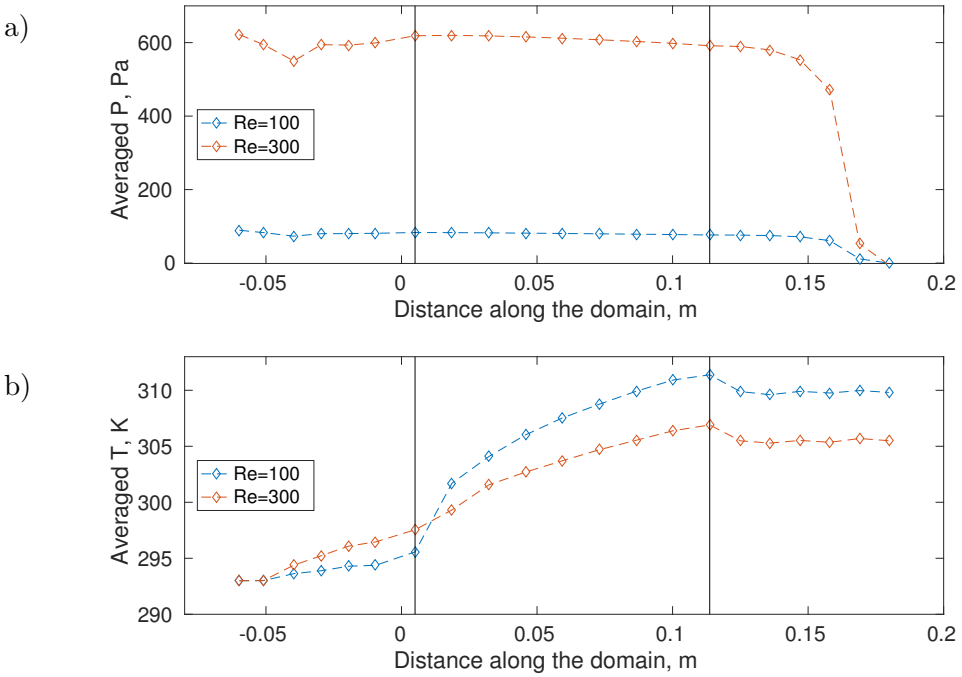

Figure 6.29: Flow-wise averaged a) pressure drop and b) temperature change. Red vertical lines show the limits of the HE core (Locations 7 to 14).

point where the flow from the different manifolds converges at the outlet header (Figure 6.29a) and increases non-linearly with Reynolds number - a similar result to Chapter 5. In addition, it should be noted that in both cases, a small drop in temperature was observed straight after the HE core section (period 15). Location relates to the HE unit section immediately after the HE core and the drop in temperature is caused by a sudden increase in the flow cross-sectional area.

Two flow and heat transfer regimes are shown in Figure 6.29. At $Re_{corrug} = 100$ pressure drop and temperature change are minimal within the inlet HE header and the majority of heat transfer occurs in the first HE core corrugation period. However, at $Re_{corrug} = 300$ the results are different - the fluctuations in pressure drop at the inlet header are apparent and relate to the rapidly increasing flow cross-sectional area. Heat transfer is also predicted to occur within the inlet HE header and relates to heat entrainment in the inlet HE header. This is well shown in Figure 6.30 where temperature contours are compared at $Re_{corrug} = 50$ and $Re_{corrug} = 500$ and illustrate intensifying heat entrainment with increasing Reynolds number. This change in behaviour occurs from $Re_{corrug} > 200$ onwards, suggesting that it could relate to unsteady flow occurrence inside HE core, particularly observed at $300 \leq Re_{corrug} \leq 500$. At these

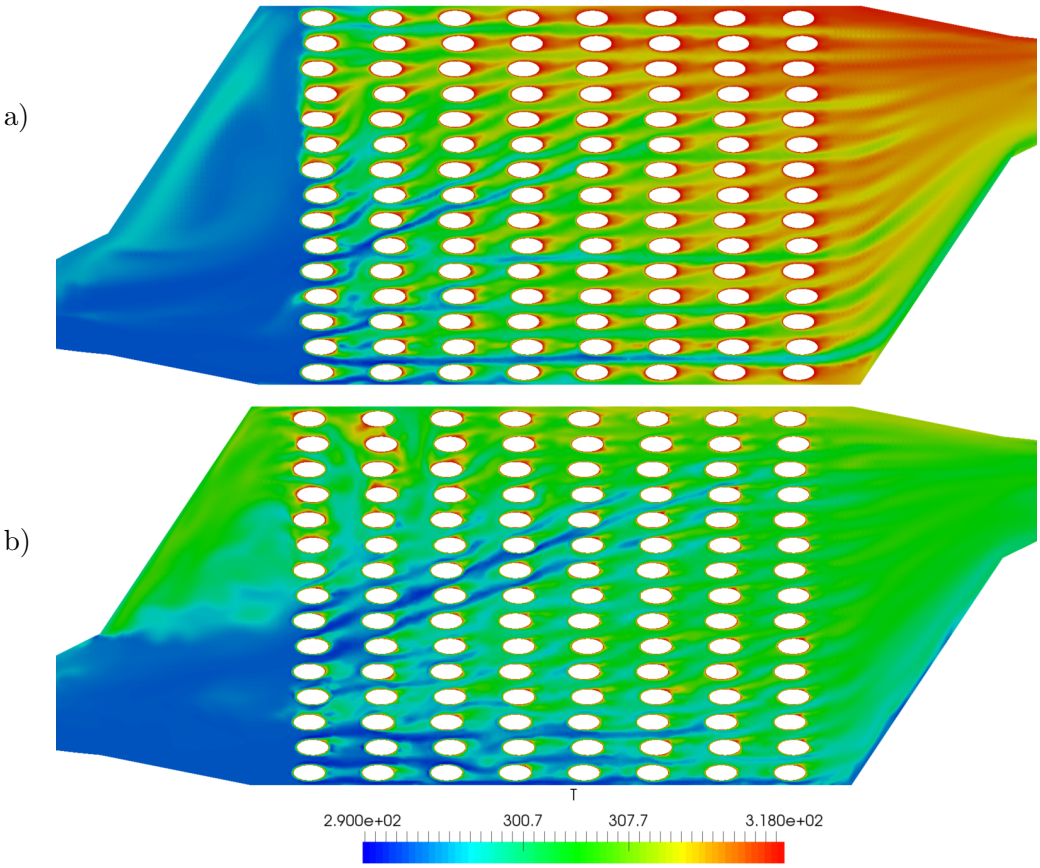

Figure 6.30: Temperature contours at a) $Re_{corrug} = 50$ and b) $Re_{corrug} = 500$ through the third HE core layer.

flow rates small fluctuations in the overall HE predictions were observed, shown using overall ΔP in Figure 6.31. It suggests the onset of the unsteady flow regime which was also indicated by rather high solution residuals, similar result to Chapter 5. To avoid the effects of flow unsteadiness, data at $300 \leq Re_{corrug} \leq 500$ was averaged from iteration 6000 to 10000, producing an averaged quantity for each corrugation period inside the HE core.

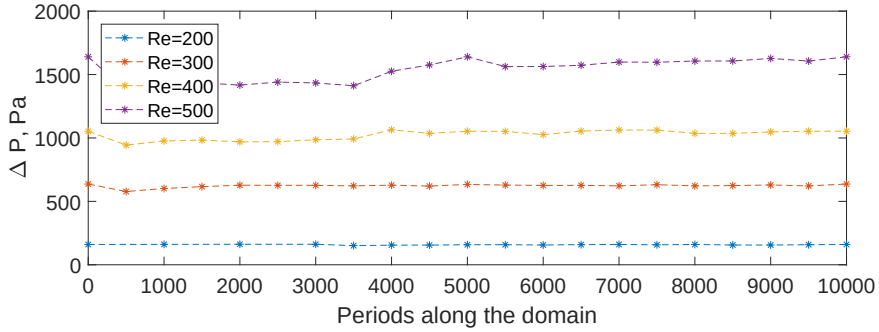

Figure 6.31: Overall pressure drop (ΔP) across the unit versus the solution iterations to show the fluctuation levels.

Overall HE unit performance was summarised in Table 6.8. The standard deviation data shows that the predictions were fluctuating only for the pressure drop. Temperature change remained almost-steady state and suggests that unsteady flow levels are relatively low at these Reynolds numbers, allowing to reassure confidence in predictions. Results were also sanity checked by comparing the inter-layer HE unit

Re	ΔP, Pa	σ, ΔP, Pa	ΔT, K	σ, ΔT, K
25	8.18	–	22.39	0.02
50	26.45	–	19.69	0.04
100	89.58	0.15	16.82	0.02
200	301.7	1.91	16.21	0.03
300	626.64	4.96	12.50	0.03
400	1047.83	12.53	11.34	0.12
500	1602.06	23.72	10.50	0.12

Table 6.8: Overall performance of the inter-layer HE unit.

pressure drop with the head loss formula for sudden flow contraction in pipes (taken from White [174]):

$$h_f = K\frac{U_{outlet}^2}{2g} \tag{6.3}$$

with K=0.5. Example calculation was completed for the highest $Re_{corrug} = 500$ case and provided a $\Delta P \approx 1100\ Pa$, a sizeable proportion of the overall pressure drop through the inter-layer HE unit predicted with CFD ($\Delta P = 1602$, Table 6.8). The result further increases confidence in the CFD results obtained, especially taking into the account that the flow within the header is more complex compared to the pipe flow and higher pressure drop can be expected in the manifold header.

6.6.1.1 Performance of the Individual HE Core Layers

Four layers of the ALM HE core were analysed separately to measure the levels of inter-layer HE mixing and the effect of it to overall HE performance. For this the individual layers were numbered 1 to 4 from the bottom to the top of the HE core (Figure 6.21). The mass flow and pressure drop performance of the individual layers was observed similar trend-wise across $25 \leq Re_{corrug} \leq 500$ with an example in Figure 6.32. The results obtained are encouraging - irrespectively of the Reynolds number the outer layers (Layers 1 and 4) entrained almost twice the mass flow in the middle of the HE core compared to the inlet to the HE core. It is a particularly positive output, taking into account this is not an optimised design. Interestingly, in Figure 6.32a a return of the mass flow to the middle HE layers at the last period of the HE core was observed. This relates to the flow redistributing to the straightest path towards the HE outlet, compared to a more complicated passage through the top and bottom

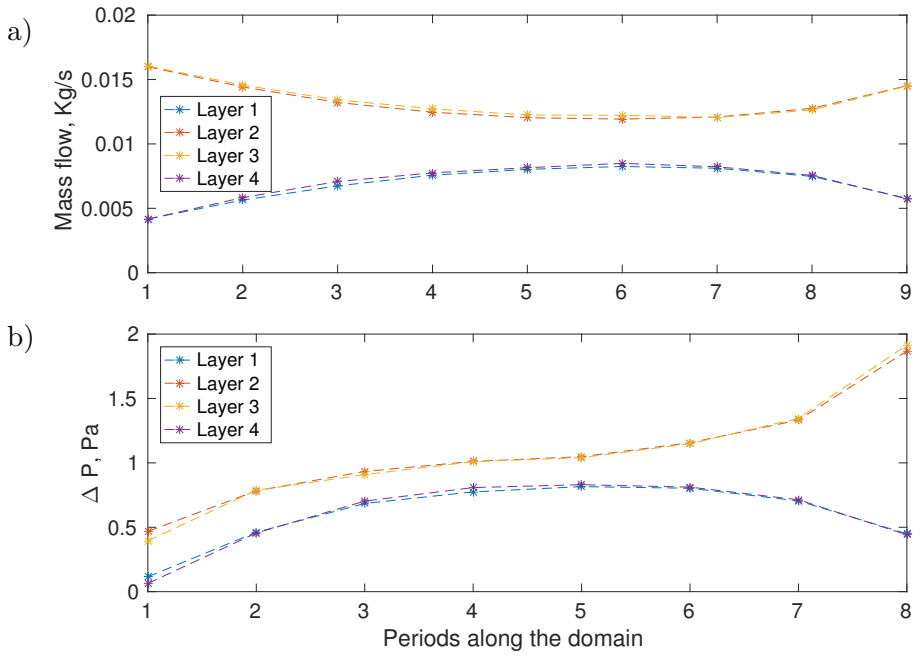

Figure 6.32: a) Mass flow and b) pressure drop data averaged at every period of the HE core corrugation for individual layers at $Re_{corrug} = 100$.

branches of the manifold HE header (Figure 6.21). Pressure drop (Figure 6.32b) was found the lowest at the inlet to the HE core in all cases and increased through the HE core as the flow became further mixed inside the HE core. Exception is the last period of the HE core where the pressure drop increases sharply in the central HE core layers and reduces within the outer layers of the HE core, aligning with the flow redistributing back to the middle HE core layers.

More differences were observed in terms of heat transfer (Figures 6.33 & 6.34). At the lower Reynolds number ($Re_{corrug} = 100$, Figure 6.33) most of the heat transfer was predicted in the first period of the HE corrugation and then dropped sharply. This agrees with the previous result at the HE unit level, shown in Section 6.6.1. At the higher Reynolds numbers ($Re \gtrsim 200$) heat transfer behaviour inside the HE core was changed significantly by heat entrainment in the inlet HE header (Figure 6.30). The destabilising effect of it was also found to be particularly strong at the middle HE layers (2 & 3) where most of the flow enters the HE core. It should be noted that the visible small solution fluctuations have little difference to the overall heat transferred by each HE core layer and the overall solution stability of the HE as shown in the Table 6.8. Here, the temperature change is lower in the first corrugation period than in the outer layers (1 & 4). However, in both figures the heat transfer performance between the layers equalises from the fourth HE corrugation period onwards. It is driven by the mass flow redistribution inside the HE core and confirms that the novel inter-layer HE corrugation is efficient.

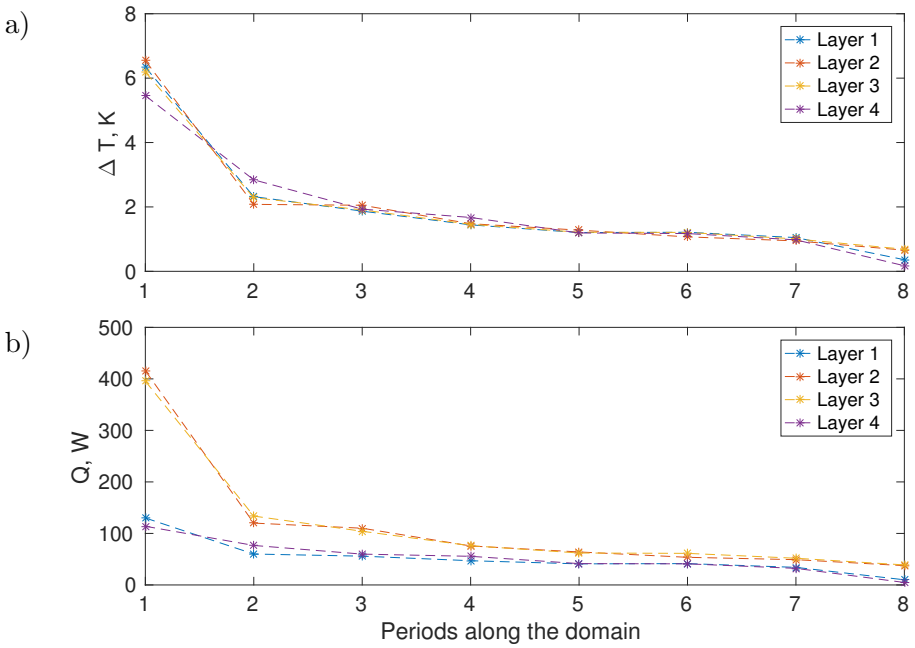

Figure 6.33: a) Temperature change and b) heat transfer data averaged at every period of the HE core corrugation for individual layers at $Re_{corrug} = 100$.

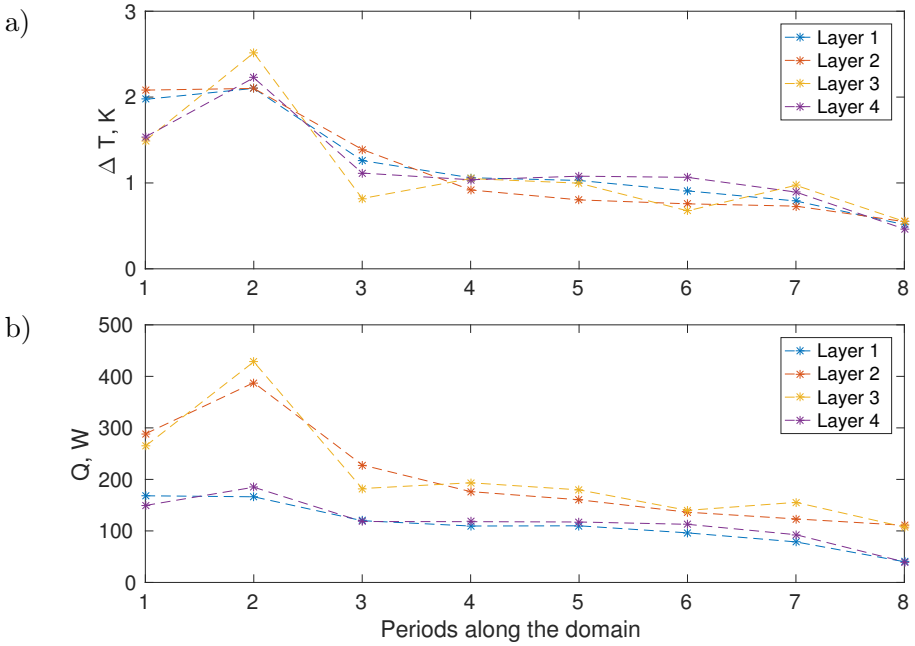

Figure 6.34: a) Temperature change and b) heat transfer data averaged at every period of the HE core corrugation for individual layers at $Re_{corrug} = 300$.

6.6.2 Simulations of the Individual Inter-layer HE Components

After observing high pressure gradients at the outlet HE header with the two HE types (plate-fin HE in Chapter 5 and the inter-layer HE in Chapter 6) and large computational cost, the inter-layer HE computational domain was split into two individual

parts: outlet HE header and superchannel HE core models (Figure 6.35). Superchan-

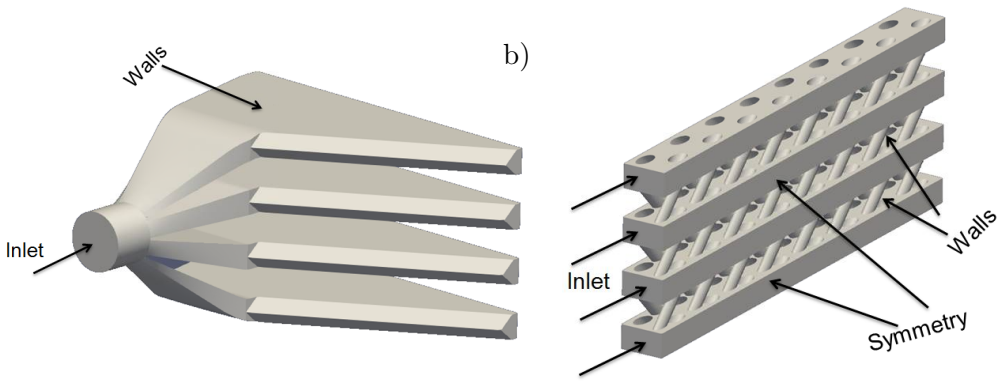

Figure 6.35: a) Inlet/outlet header and b) Superchannel computational domains.

nel model is a novel single corrugation width period HE core model. It represents an idealised scenario within the HE core by uniform, non-maldistributed velocity inlet which enables the highest heat transfer. It should be noted that uniform velocity inlet was also applied for the outlet HE header and the same Reynolds number range ($25 \leq Re_{corrug} \leq 500$) was used for both domains suing the numerical setup of the inter-layer HE (Section 6.4.2). Inter-layer HE unit model mesh resolution was maintained by cropping the HE unit `blockmesh` size and keeping the same `snappyHexMesh` settings.

	Outlet Header		Superchannel	
Re	ΔP, Pa	$\sigma, \Delta P$, Pa	ΔP, Pa	ΔT, K
25	9.05	-	1.48	22.89
50	33.28	-	3.49	21.25
100	133.78	-	9.2	19.06
200	495.85	29.65	26.12	16.48
300	1097.1	6.015	49.78	14.42
400	1616.3	1.5	79.63	13.73
500	2425	8.28	116.15	12.1

Table 6.9: Results obtained by simulating the individual inter-layer HE unit components.

Outlet HE header data is given in Figure 6.36a and Table 6.9. Higher ΔP in the outlet header was predicted than with the overall inter-layer HE (Table 6.8). This is connected to the uniform velocity inlet condition into the outlet HE header which forces more flow through the outer HE header layers than in the HE unit model predictions. However, the data could still be used as a conservative estimate for the HE unit pressure drop. Figure 6.36b compares the ΔP between the two HE corrugation models - the fully symmetric single channel and the idealised HE core (superchannel) models. Little

difference is observed between them with the superchannel model predicting marginally higher ΔP due to the vertical restriction by the HE unit walls with no-slip condition.

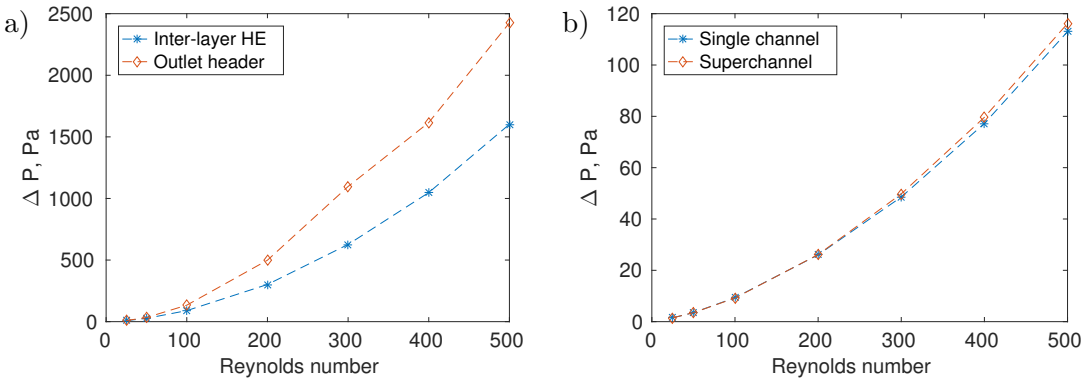

Figure 6.36: Pressure drop comparison between: a) inter-layer HE unit and the outlet header b) single channel and superchannel models.

Thermal results between the three models are compared in Figure 6.37. As expected, the most idealised single channel model produced the highest temperature change. In case of the superchannel model the temperature change was predicted consistently lower compared to the single channel results. The inefficiency arises due to the

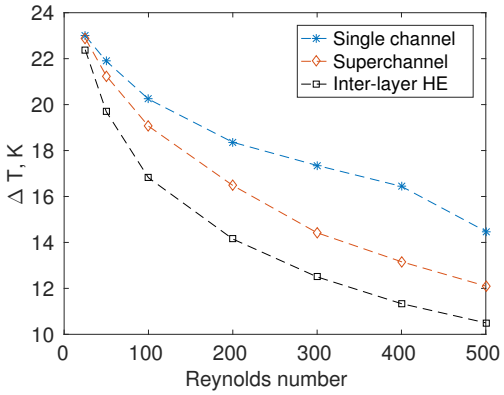

Figure 6.37: Temperature change data between single/super channel and the detailed inter-layer HE unit outputs.

height restriction of the HE unit size in the superchannel model compared to the single channel domain. The inter-layer HE unit results were the lowest and show the detrimental maldistribution effects which increase with the Reynolds number. However, splitting the computational domains proved as a useful alternative design methodology. It reduced the computational cost by 3.5 times allowing cheap and fast estimate of pressure drop and heat transfer.

6.6.3 Simplified Porous Media HE Unit Model Results

The simplified HE unit model was setup as in Section 6.4.2 to evaluate whether a layered porous media modelling assumption is adequate for the complex ALM design. Firstly, the simplified HE unit flow-wise performance was averaged over the four HE layers as previously (Figure 6.28). The obtained results were then compared to the inter-layer HE unit data in Figures 6.38 & 6.39. In both figures the pressure predictions

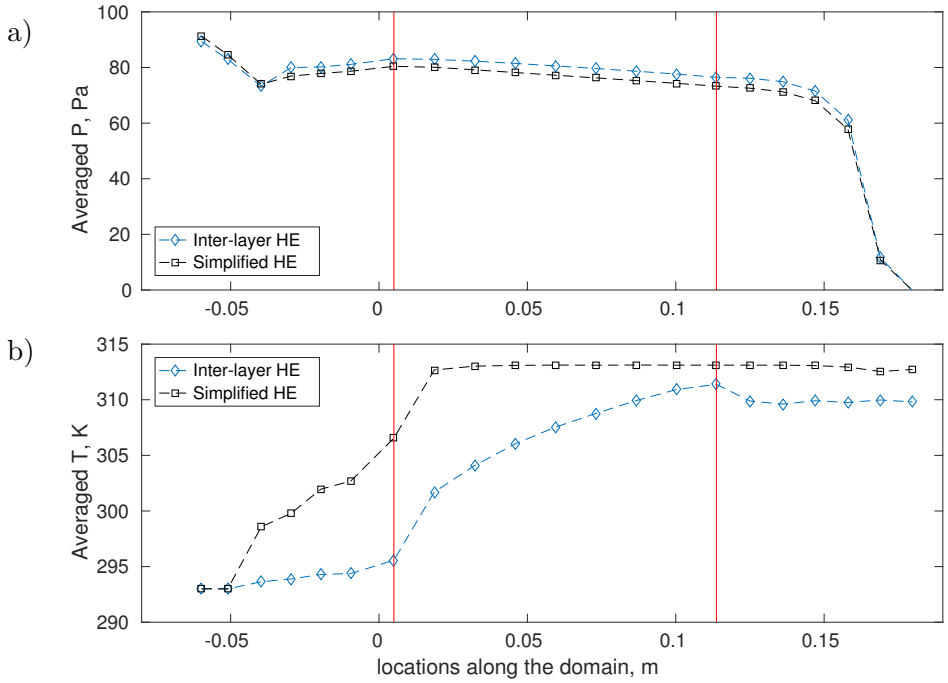

Figure 6.38: Flow-wise averaged a) Pressure and b) Temperature values at $Re_{corrug} = 100$. Red vertical lines show the limits of the HE core (Locations 7 to 14).

were found to be similar between the two models, dominated by the outlet HE header effects. However, a much higher contrast is observed in terms of temperature and the disagreement between the two models increases with the Reynolds number. The main reason identified was the empty layer simplification required for the conventional simplified HE modelling methodology. This uses the idealised heat transfer data from the single channel HE corrugation model selecting an optimistic heat transfer estimate for a layer. In addition, the heat transfer effectiveness model (Equation 3.50) employed to simplify the heat transfer inside HE core releases the heat transfer faster compared to the inter-layer HE unit model results (Figures 6.38b and 6.39b). This in turn makes more heat available close to the inlet HE header (Figure 6.40a), creating conditions for more heat to be entrained inside the inlet HE header. The heat entrainment increases at higher Reynolds numbers (Figure 6.38b vs 6.39b) and results in increasingly over-prediction of ΔT comparing the simplified HE versus the inter-layer HE model (Table

6.8 vs Table 6.10) and further distorts the results. These drawbacks severely limit the usage of the simplified HE unit model for complex ALM HE designs.

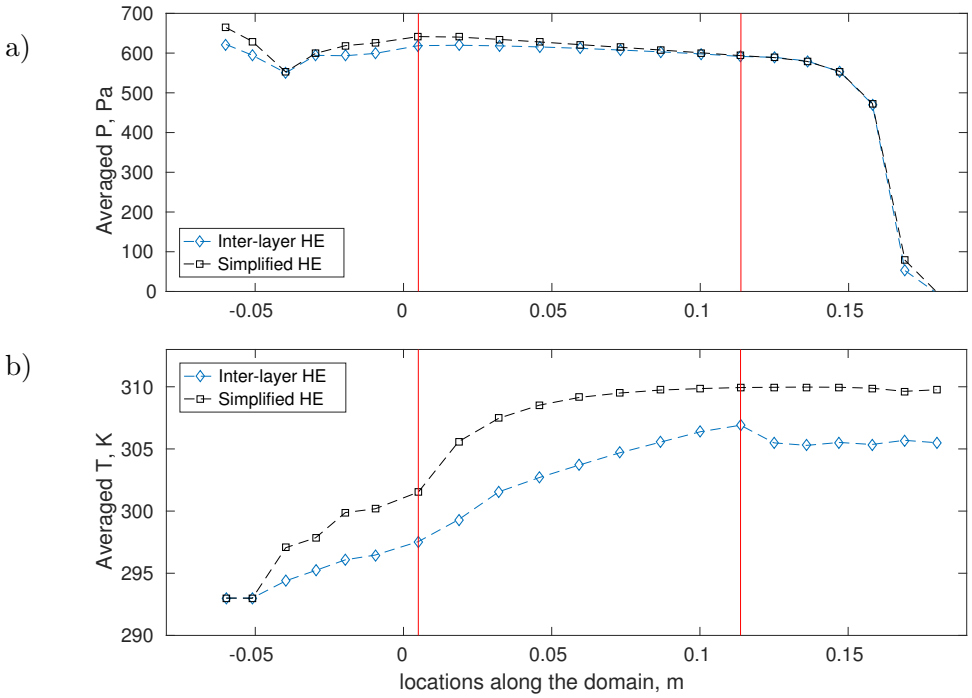

Figure 6.39: Flow-wise averaged a) Pressure and b) Temperature values at $Re_{corrug} = 300$. Red vertical lines show the limits of the HE core (Locations 7 to 14).

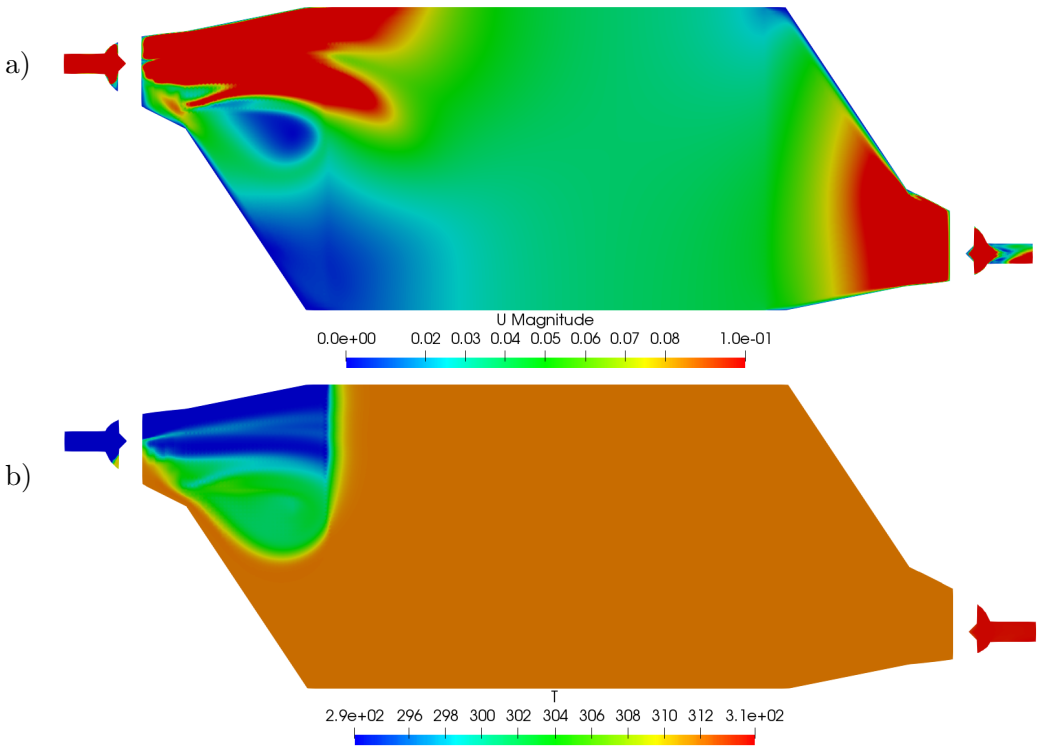

Figure 6.40: Contours at $Re_{corrug} = 100$ through the second porous media HE layer of a) velocity and b) temperature.

Re	ΔP, Pa	σ, ΔP, Pa	ΔT, K	σ, ΔT, K
25	6.34	–	22.08	–
50	26	–	21.19	–
100	91.51	–	19.67	–
200	326.4	–	17.87	–
300	666.4	1.47	16.79	–
400	1144.2	10.89	15.54	0.29
500	1735.1	6.06	15.38	0.26

Table 6.10: Averaged data of the porous ALM HE unit.

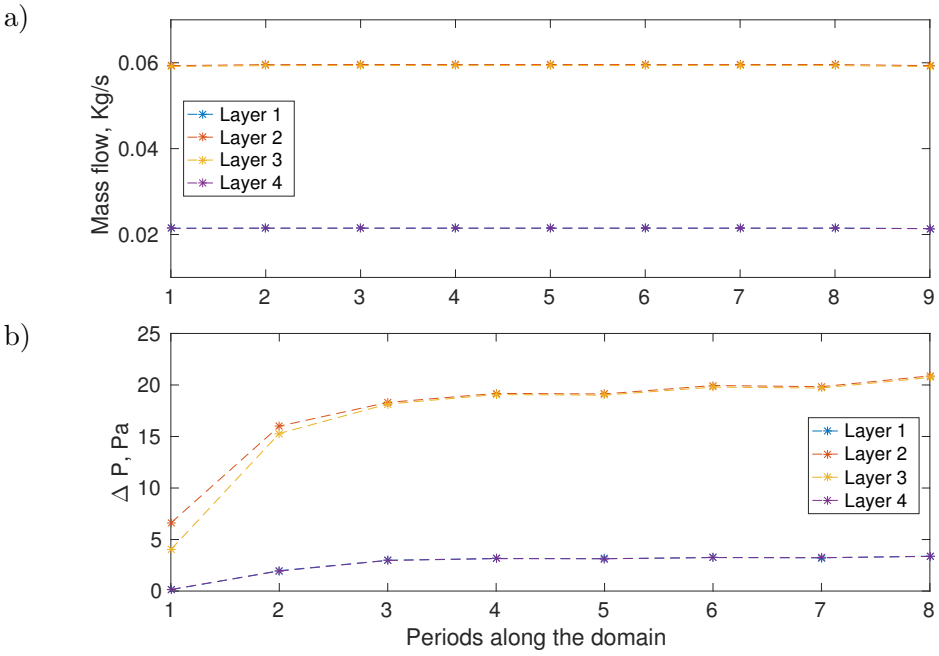

Figure 6.41: a) Mass flow and b) pressure drop data averaged every period of the simplified HE core for individual layers at $Re_{corrug} = 400$.

6.6.3.1 Individual Layer Performance of the Simplified HE Unit Model

Individual layer performance of the simplified HE unit is discussed here. A similar trend-wise behaviour was predicted across the Reynolds number range with the example outputs given in Figures 6.41 & 6.42 ($Re_{corrug} = 400$). The maldistribution at the inlet HE header resulted in three times lower mass flow through the outer (1 & 4) HE layers compared to the middle (2 & 3) HE core layers (Figure 6.41a). In addition, inter-layer connection between the layers was not modelled, thus, maldistribution levels remained the same through the HE core. This creates conditions under which the pressure drop in the middle HE layers is several times higher (Figure 6.41b) compared to the inter-layer HE model (Figure **??**b) where performance across all HE core layers is more uniform. Simplified HE model also led to different thermal predictions between the HE core layers (Figures 6.42) when compared to the inter-layer HE results (Figure

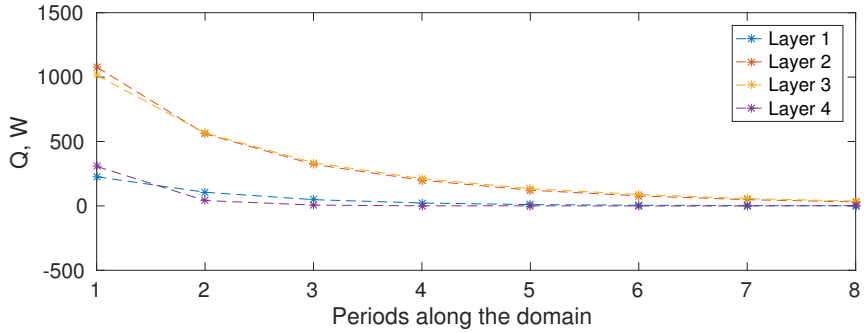

Figure 6.42: Heat transfer data averaged every period of the simplified HE core for individual layers at $Re_{corrug} = 400$.

6.34), again arising from no inter-layer mixing and provides an inaccurate prediction of the inter-layer HE unit.

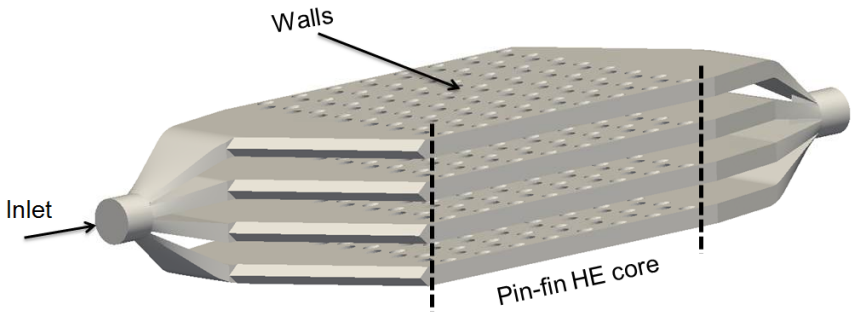

Figure 6.43: The cold flow domain of the HE unit with no vertical flow passages (pin-fin HE).

6.7 Comparing the Novel HE to a Conventional Design

A special HE model was designed to evaluate the performance of the novel inter-layer HE unit. It was accomplished by blocking the vertical inter-layer HE pathways and creating a pin-fin HE with the extracted cold flow domain given in Figure 6.43. The numerical setup was left identical to the inter-layer HE unit setup (Section 6.4) to enable solution similarity between the two CFD models. Firstly, the pin-fin HE performance was compared to the detailed inter-layer HE unit model in Figures 6.44 & 6.45. The data was averaged across the HE layers as previously at the sampling planes shown in Figure 6.28. Pressure predictions were similar between the inter-layer and the pin-fin HE models across the Reynolds number range ($25 \leq Re_{corrug} \leq 500$) (Figures 6.44a & 6.45a). It was dominated again by the outlet header effects, agreeing with the results of the previous inter-layer and simplified HE models. In terms of the temperature as well as the overall thermal HE performance (Tables 6.11 & 6.8), pin-fin and inter-layer HE models agree better compared to the simplified HE model,

especially in terms of heat entrainment into the inlet HE header. However, it can be observed that the temperature change predicted by the pin-fin HE was lower compared to the inter-layer HE results. This is thought to relate to the removal of the inter-layer mixing and is further compared across a Reynolds number range in Section 6.7.2.

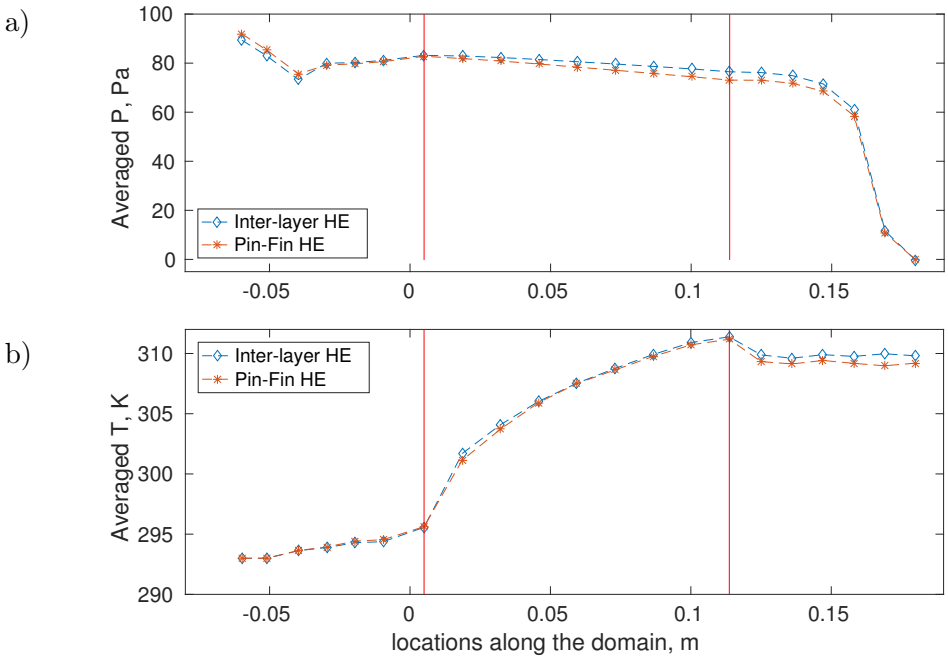

Figure 6.44: Flow-wise averaged a) Pressure and b) Temperature at $Re_{corrug} = 100$. Red vertical lines show the limits of the HE core (Locations 7 to 14).

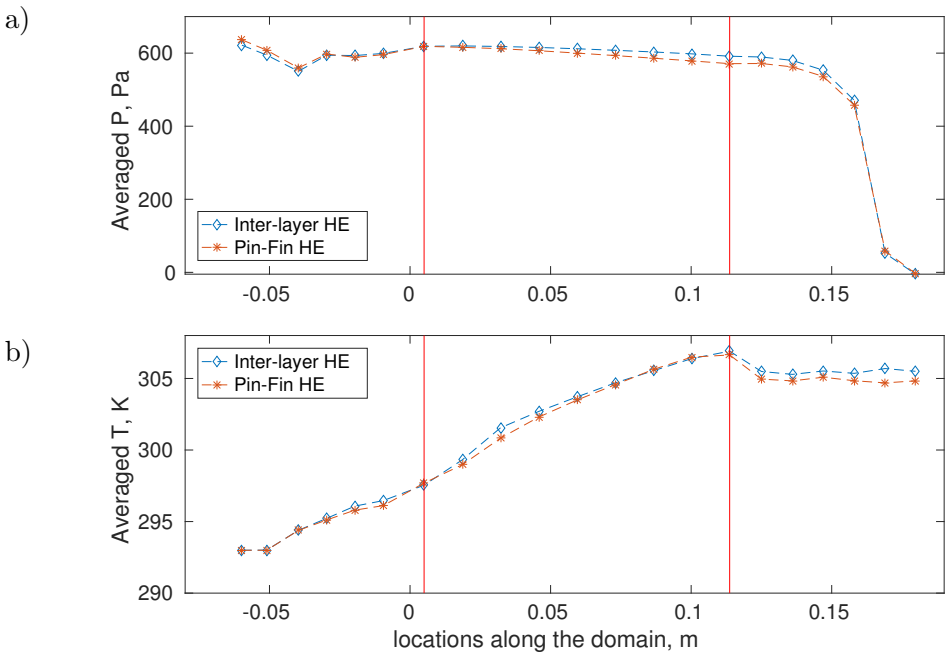

Figure 6.45: Flow-wise averaged a) Pressure and b) Temperature at $Re_{corrug} = 300$. Red vertical lines show the limits of the HE core (Locations 7 to 14).

Re	ΔP, Pa	σ, ΔP, Pa	ΔT, K	σ, ΔT, K
25	8.6	–	21.03	–
50	27.5	–	18.27	–
100	92.2	0.044	15.5	–
200	311	1.73	12.79	–
300	643.4	4.72	11.2	–
400	1071	7.62	10.1	–
500	1602.06	26.32	9.28	–

Table 6.11: Averaged data of the pin-fin HE unit model.

6.7.1 Performance of the Individual Pin-Fin HE Layers

Individual layer performance of the pin-fin HE core is evaluated at $Re_{corrug} = 400$ (Figures 6.46 & 6.47). In terms of trend-wise mass flow and pressure drop performance the pin-fin HE predictions were found similar to the simplified HE model (Figure 6.41, $25 \leq Re_{corrug} \leq 500$). In both numerical models, around 3 times lower mass flow

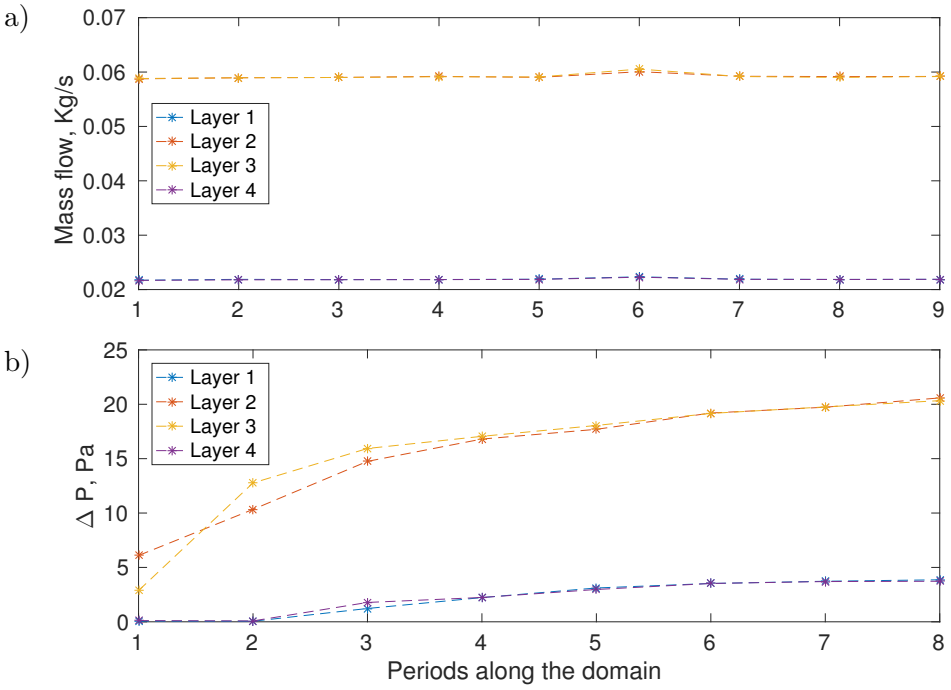

Figure 6.46: a) Mass flow and b) pressure drop data averaged every period of the core corrugation for individual layers at $Re_{corrug} = 400$.

coming into the outer layers (1 & 4) compared to the middle layers (2 & 3) was predicted (Figure 6.46a). It was due to maldistribution in the inlet HE header and no inter-layer mixing inside the HE core. This resulted in a much larger pressure drop in the middle HE core layers (2 & 3) compared to the outer ones (1 & 4) where it was almost negligible. It contrasts again with the inter-layer HE model (Figures 6.32 & **??**) where performance of the individual layers is much more uniform. This illustrates the

advantages of the inter-layer HE corrugation as it creates smaller pressure differentials inside the HE core, potentially prolonging the lifetime of HE.

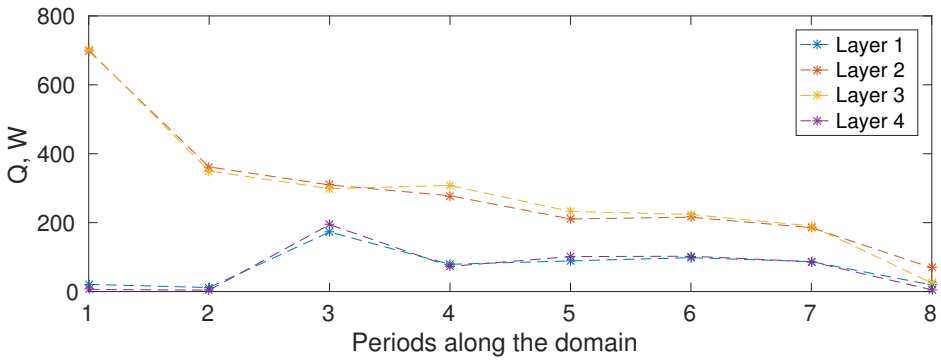

Figure 6.47: Heat transfer data averaged every period of the core corrugation for individual layers at $Re_{corrug} = 400$.

Inlet HE header maldistribution also affected the heat transfer results (Figure 6.47). This is particularly clear for the outer HE core layers (1 & 4) where in the first two periods of the HE core negligible heat transfer is produced. This occurs because of a combination of lower mass flow in the outer HE layers and recirculation inside the inlet HE header which heats up the flow prior to entering HE core (Figure 6.48). After the

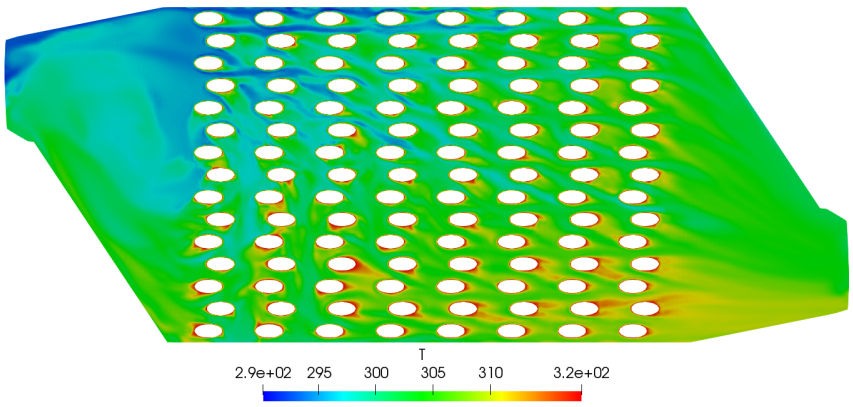

Figure 6.48: Temperature contours of the fourth (top) layer of the HE unit with no vertical flow passages (pin-fin HE) at $Re_{corrug} = 400$.

first two periods of HE corrugation the pre-heating effect is no longer present and heat transfer (Q) between the corrugation periods in the outer HE core layers is observed. However, it is still significantly lower than the heat transfer in the middle HE core layers. This is contrary to the inter-layer HE results (Figures 6.33 & 6.34) where the individual layer performance equalises at around period 3 of the HE core corrugation, reinforcing superiority of the novel inter-layer HE.

6.7.2 Comparing Different HE Model Results

Performance of different HE models using the overall pressure drop ΔP and temperature change ΔT is compared in Figure 6.49. Inter-layer and pin-fin HE unit pressure drops are predicted very similar (Figure 6.49a) and shows that the additional inter-layer mixing does not significantly contribute to the overall pressure drop. Simplified

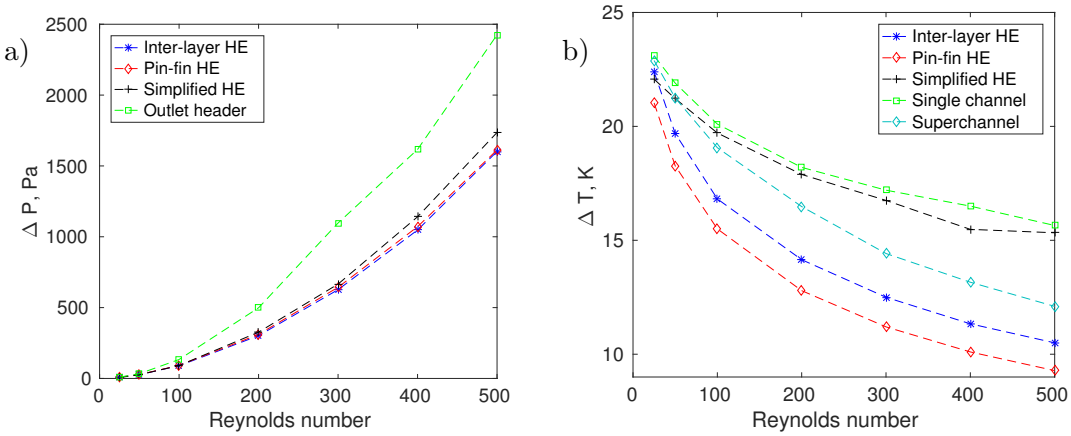

Figure 6.49: a) Pressure drop ΔP, Pa and b) Temperature change ΔT, K data using different modelling assumptions.

HE model, however, produced slightly higher overall pressure drop (within $\approx 10\%$), small differences relating to simplifying the HE core as an empty layer where uniform resistance is predicted throughout. Outlet HE header model produced the highest pressure drop of all the models due to the uniform velocity inlet boundary condition applied to all four channels of the HE header. This results in more flow through the outer header layers than in the inter-layer HE unit model and creates progressively higher flow resistance. However, as the model is significantly computationally cheaper it could be used for a conservative estimate of the overall flow resistance.

Temperature change (ΔT) data (Figure 6.49b) compares the performance of five different HE models. The first two are the HE corrugation only single channel and superchannel models. Here the single channel is the most idealised fully symmetric HE corrugation model (Figure 6.17) and is used to generate the data for the porous media HE model. Superchannel model (Figure 6.35b) is a one channel width HE core model with top and bottom limits and serves as an idealised HE core model with no flow maldistribution. The single channel model produced the highest temperature change between the models as it does not have the vertical restriction, creating an infinite height channel. The superchannel model, however, had the vertical restriction (due to the height of the HE) which in turn limited flow mixing and the heat transfer area in the outer layers of the HE core. This resulted in differences between the two

corrugation models becoming pronounced at $Re_{corrug} \geq 300$, leading to lower heat transfer prediction (16% in terms of ΔT).

The next two models compared are the superchannel and the inter-layer HE. In this case the superchannel model predicts consistently higher ΔT ($2-13\%$), increasing with the Reynolds number. This shows a not perfect mass flow redistribution inside the inter-layer HE despite the vertical conduits and highlights the necessity of an efficient HE header design. Simplified HE unit model in terms of the thermal performance does not even follow the trend-wise behaviour of any other HE unit model, severely limiting its use for complex ALM HE designs. The model progressively over-predicts heat transfer caused by the HE core simplification discussed afore and results in similar ΔT predicted to the single channel model. Comparing the inter-layer to the pin-fin HE models shows that the former predicted constantly higher ΔT (7-13% depending on the Reynolds number). This confirms that the inter-layer flow conduits enhance heat transfer by enabling a more uniform HE core performance.

6.8 Conclusions of the Chapter

A series of novel HE concepts utilising design freedom of SLM process were designed and manufactured using titanium at HE relevant lenghtscales to ensure feasibility of the structures. The most promising HE corrugation utilising novel inter-layer flow channels and manifold HE headers were then implemented in a proof of concept HE in counter-flow orientation. Flow resistance and heat transfer performance of the novel inter-layer HE was then established using CFD. Commonly used simplified HE unit modelling (same as in Chapter 5) and fully detailed inter-layer HE unit simulations were undertaken. A third pin-fin HE model was designed by blocking the inter-layer conduits to evaluate the performance of the novel inter-layer HE corrugation. All HE unit models produced a very similar response in terms of the pressure drop, dominated by the outlet HE header effects, a similar result to Chapter 5. More differences were observed in terms of the overall temperature change between the different CFD models. Porous media HE model increasingly over-predicted thermal performance which was caused by the HE core simplification to empty layers, limiting its use for complex ALM HE designs. Between the inter-layer and pin-fin HE models the former model predicted a $7-13\%$ higher ΔT. The additional performance relates to mass flow redistribution inside the inter-layer HE core, enabled by the novel corrugation as well as increased flow mixing and heat transfer area. Based on the idealised superchannel HE core model performance results up to additional $\approx 10\%$ ΔT could be obtained by optimising the inlet HE header. Nonetheless, the novel inter-layer HE corrugation is a

significant step in heat exchanger industry and has a strong potential to be a popular ALM based solution of the future.

Chapter 7

Summary

Contents

7.1 Conclusions

The driver for this research was to produce a novel thermal management solution, superior to the current devices for the use in future defence aerospace applications. This sector is particularly challenging as it requires combining multiple design objectives: firstly, high performance operation of the aircraft as defence industry requires more intensive cooling than civil aerospace. This arises from the dense installation of powerful electronics such as radars. Other major challenges include the overall thermal signature of an aircraft and limited installation space available. Different thermal tasks within the aircraft are assembled into thermal management systems where heat addition or rejection is undertaken using heat exchangers, playing a vital role in the overall performance of the system. Thus, the project focused on improving the performance of heat exchangers using computational fluid dynamics and additive layer manufacturing with the research undertaken as outlined in the Aims & Objectives (Section 1.4). The main research outcomes (Chapters 4-6) are bullet-pointed and related back to the original project aims below:

Chapter 4: Flow and Heat Transfer Modelling of a Single HE Corrugation Channel

- A two dimensional sinusoidal heat exchanger channel was modelled based on a published numerical study and analysed at $5 \leq Re \leq 1000$ to study the change

in flow and heat transfer characteristics using a range of numerical assumptions for the detailed flow and heat transfer [Objective 1.1].

- It was found that analysing a single period of the HE fins with periodic flow and heat transfer assumptions was not sufficient in the majority of scenarios, especially in order to obtain accurate heat transfer performance estimates. A full length single channel of the HE corrugation layer was found necessary for more reliable predictions [Objective 1.2].

- Transitional Reynolds regime is often observed in gaseous and high velocity heat exchanger applications (for this application it occurred at $Re \approx 200$). However, resolving flow and heat transfer performance in this regime becomes challenging as the numerical methodology is not clear in the literature. It was shown that the $k-\epsilon$ turbulence model completely fails to detect the transitional regime, whilst the laminar assumption produces a chaotic result. However, the $k-\omega$ SST model predictions were found to be the most reliable and should be employed for the solutions in the transitional flow regime [Objective 1.2].

- Importance of accurate discretisation of the flow and heat transfer equations was shown, concluding that the domain should be approximated to second order accuracy to accurately resolve the unsteady flow behaviour. Using lower accuracy discretisation schemes with the $k-\omega$ SST model led to up to 30% lower pressure drop whilst producing similar Nusselt number performance. This suggested that the less accurate output could be used as a close initial guess or in situations where a full transient solution is overly time consuming [Objective 1.2].

Chapter 5: Heat Exchanger Modelling Validation

- In this chapter a compact plate-fin heat exchanger with serrated corrugation was used to develop validated numerical modelling techniques. To accomplish this, the heat exchanger was experimentally tested at a broad Reynolds number range and a comprehensive data set was established [Objective 1.3].

- A novel heat exchanger corrugation modelling domain was proposed utilising the conjugate heat transfer methodology. The method takes a slice of a heat exchanger core and models a portion of both cold and hot flow heat exchanger core layers separated by a solid. It eliminates the need for empirical models (such as Kays and London [6]) to adjust the heat transfer values, enables a better understanding of heat transfer inside the heat exchanger core and provides potential to create more efficient heat exchangers [Objective 1.4].

- The novel heat exchanger corrugation model was used to obtain flow and heat transfer data which was then implemented into the simplified numerical heat exchanger unit model and compared to the experiments. A close agreement was found both in terms of the flow resistance (maximum of $\approx 10\%$ difference in ΔP) and heat transfer (average of $\approx 4.9\%$ difference in HE effectiveness ϵ), resulting in better agreement than reported in industry. This enabled validating the novel heat exchanger design methodology [Objective 1.4].

Chapter 6: Compact Heat Exchangers and Additive Layer Manufacturing

- A number of concept heat exchanger designs were conceived to enhance heat transfer performance, achieved by utilising the design freedom of additive layer manufacturing. To evaluate feasibility of the designs the most promising ones were manufactured using selective laser melting at the heat exchanger relevant lengthscales. All concept ideas were resulted in structurally integral parts, allowing to pursue the subject further [Objective 2.1].

- Using the findings of the feasibility study a proof of concept heat exchanger was designed with the novel inter-layer heat exchanger corrugation in counter-flow orientation combined with the novel manifold header design. It was then manufactured and analysed numerically using the prior developed CFD methodology. Although the simplified heat exchanger unit model proved successful for a standard heat exchanger design it was not as robust for evaluating the more complex heat exchanger, meaning that a fully detailed model of the inter-layer heat exchanger was required. When compared to a conventional pin-fin heat exchanger, the inter-layer heat exchanger unit resulted in up to 13% higher ΔT with no penalty on the pressure drop. This allows the design to be classed as a significant step in heat exchanger design. [Objective 2.2]

7.2 Implications of the Results

This thesis has shown that computational fluid dynamics modelling is a feasible and reliable alternative to traditional analytical/experimental heat exchanger design cycle used in industry. In addition, the novel numerical methodology developed allows a better insight into the heat transfer and pressure drop processes occurring inside the heat exchanger core. This enables a designer to produce more efficient heat transfer solutions.

Modelling the two dimensional sinusoidal heat exchanger channel revealed the critical importance of the right modelling assumptions for accurate heat exchanger corrugation predictions as they determine the input into the HE unit model and strongly affects its performance. It was identified that the $k-\omega$ SST model should be used with second order accuracy discretisation of the momentum and energy equations for accurate predictions across the different Reynolds number regimes. However, this is not undertaken or acknowledged in the majority of current literature studies which becomes a significant issue at transitional Reynolds numbers where the importance of numerical assumptions amplifies.

Using the serrated plate-fin heat exchanger unit enabled to develop a validated, robust and novel numerical prediction methodology. It also pointed out the drawbacks of current HE manufacturing techniques. These can often result in partial HE core layer blockages which in turn lead to significant under-performance of heat exchangers. Overall, additive layer manufacturing was concluded as a more promising solution for future heat management. Applying selective laser melting technique to the sector is a challenging task due to the low wall thickness required for efficient heat transfer surfaces. However, the initial work showed a much better manufacturing repeatability, greater design freedom and a potential for further enhanced and efficient heat transfer.

7.3 Further Work

There is a broad spectrum of research which would further develop both, additive layer manufacturing and future aircraft thermal management. Some of them are bullet-pointed below:

- Validate the computational fluid dynamics predictions of the complex prototype additive layer manufactured heat exchanger as the laboratory experiments were completed beyond the timeline to be included as a part of the PhD thesis. The additional work would allow to further develop the computational fluid dynamics methodology of the complex heat exchanger core predictions.

- Optimise the novel inter-layer heat exchanger corrugation. The study could consider a number of variables to search for a more optimised solution. Alternatively a study could be undertaken in optimising the novel manifold heat exchanger headers proposed.

- Further work on the computer assisted heat exchanger design cycle. An important step is producing the initial guess using well established analytical calculations. Traditionally, this initial guess is taken to build the prototype heat exchanger which is then physically tested. To replace the design cycle afore, the

research would look into combining both analytical and numerical design methods for producing more efficient heat exchangers and minimising costly physical experiments.

References

[1] Andy B Jones, Thomas Childs, Rui Chen, and Angus Murray. Thermal sensitivity analysis of avionic and environmental control subsystems to variations in flight condition. In *54th AIAA Aerospace Sciences Meeting*, pages 1–15, 2016. 1, 3

[2] David Blanding and Boeing Phantom Works. Subsystem design and integration for the more electric aircraft. In *5th International Energy Conversion Engineering Conference and Exhibit (IECEC)*, page 4828, 2007. 1, 3, 6, 19

[3] William D Gerstler and Ronald S Bunker. Aircraft engine thermal management: the impact of aviation electric power demands. *Mechanical Engineering*, 130(12):74, 2008. 1

[4] Ian Moir and Allan Seabridge. *Aircraft systems: mechanical, electrical and avionics subsystems integration*, volume 52. John Wiley & Sons, 2011. 1, 3, 4, 5, 6

[5] Warren M Rohsenow, James P Hartnett, Young I Cho, et al. *Handbook of heat transfer*, volume 3. McGraw-Hill New York, 1998. xv, 2, 6, 7, 13, 14, 15, 17, 18, 27, 32, 33, 54, 57, 60

[6] William Morrow Kays and Alexander L London. *Compact heat exchangers*. McGraw-Hill, 1964. 2, 7, 8, 12, 27, 28, 29, 32, 33, 35, 57, 104, 125, 129, 134, 164

[7] John E Hesselgreaves. *Compact heat exchangers: selection, design and operation*. Gulf Professional Publishing, 2001. xv, 2, 6, 7, 12, 13, 14, 15, 16, 17, 18, 19, 27

[8] Carl R Deckard. Method and apparatus for producing parts by selective sintering, September 5 1989. US Patent 4,863,538. 2

[9] William Morris et al. *American heritage dictionary of the English language, Fifth Edition*. Houghton Mifflin Harcourt Publishing Company, 2015. xv, 3

[10] Jose VC Vargas and Adrian Bejan. Thermodynamic optimization of finned crossflow heat exchangers for aircraft environmental control systems. *International Journal of Heat and Fluid Flow*, 22(6):657–665, 2001. xv, 3, 8, 27, 35, 36

[11] Thomas Childs, Andy B Jones, Rui Chen, and Angus Murray. Thermal sensitivity analysis of avionic and environmental control subsystems to variations in flight condition. In *54th AIAA Aerospace Sciences Meeting*, pages 1–15, 2016. xv, 3, 4

[12] Thomas Childs, Andy B Jones, Rui Chen, and Angus Murray. A study into refrigeration cycle working fluids using an air cycle machine environmental control system. In *54th AIAA Aerospace Sciences Meeting*, pages 1–15, 2016. 3

[13] He Huang, Louis J Spadaccini, and David R Sobel. Fuel-cooled thermal management for advanced aero engines. In *ASME Turbo Expo 2002: Power for Land, Sea, and Air*, pages 367–376. American Society of Mechanical Engineers, 2002. 4

[14] Mike Sinnett. 787 no-bleed systems: saving fuel and enhancing operational efficiencies. *Aero Quarterly*, (07):6–11, 2007. xv, 5

[15] Richard E Quigley Jr. More electric aircraft. In *Applied Power Electronics Conference and Exposition, 1993. APEC'93. Conference Proceedings 1993., Eighth Annual*, pages 906–911. IEEE, 1993. 5

[16] Joseph A Weimer. Electrical power technology for the more electric aircraft. In *Digital Avionics Systems Conference, 1993. 12th DASC., AIAA/IEEE*, pages 445–450. IEEE, 1993. 5

[17] RI Jones. The more electric aircraft: the past and the future? In *Electrical Machines and Systems for the More Electric Aircraft (Ref. No. 1999/180), IEE Colloquium on*, pages 1–1. IET, 1999. 5

[18] Babak Lotfi, Min Zeng, Bengt Sundén, and Qiuwang Wang. 3d numerical investigation of flow and heat transfer characteristics in smooth wavy fin-and-elliptical tube heat exchangers using new type vortex generators. *Energy*, 73:233–257, 2014. xv, 6

[19] R Borrajo-Peláez, J Ortega-Casanova, and JM Cejudo-López. A three-dimensional numerical study and comparison between the air side model and the air/water side model of a plain fin-and-tube heat exchanger. *Applied Thermal Engineering*, 30(13):1608–1615, 2010. 6, 49

[20] Li Li, Xiaoze Du, Yuwen Zhang, Lijun Yang, and Yongping Yang. Numerical simulation on flow and heat transfer of fin-and-tube heat exchanger with longitudinal vortex generators. *International Journal of Thermal Sciences*, 92:85–96, 2015. 6

[21] K Kritikos, C Albanakis, D Missirlis, Z Vlahostergios, A Goulas, and P Storm. Investigation of the thermal efficiency of a staggered elliptic-tube heat exchanger for aeroengine applications. *Applied Thermal Engineering*, 30(2):134–142, 2010. 6

[22] Resat Selbaş, Önder Kızılkan, and Marcus Reppich. A new design approach for shell-and-tube heat exchangers using genetic algorithms from economic point of view. *Chemical Engineering and Processing: Process Intensification*, 45(4):268–275, 2006. xv, 6

[23] Hamidreza Najafi and Behzad Najafi. Multi-objective optimization of a plate and frame heat exchanger via genetic algorithm. *Heat and Mass Transfer*, 46(6):639–647, 2010. xv, 7

[24] Ramesh K Shah and Dusan P Sekulic. *Fundamentals of heat exchanger design*. John Wiley & Sons, 2003. xv, 7, 14, 15, 16, 18, 19, 27, 32, 33

[25] Teresa J Leo and Isabel Pérez-Grande. A thermoeconomic analysis of a commercial aircraft environmental control system. *Applied Thermal Engineering*, 25(2):309–325, 2005. 8, 27, 35

[26] Muhammad Mahmood Aslam Bhutta, Nasir Hayat, Muhammad Hassan Bashir, Ahmer Rais Khan, Kanwar Naveed Ahmad, and Sarfaraz Khan. Cfd applications in various heat exchangers design: A review. *Applied Thermal Engineering*, 32:1–12, 2012. 8, 45

[27] Zhe Zhang and YanZhong Li. Cfd simulation on inlet configuration of plate-fin heat exchangers. *Cryogenics*, 43(12):673–678, 2003. 8, 29, 57

[28] L Sheik Ismail, Ch Ranganayakulu, and Ramesh K Shah. Numerical study of flow patterns of compact plate-fin heat exchangers and generation of design data for offset and wavy fins. *International journal of heat and mass transfer*, 52(17):3972–3983, 2009. xvi, 8, 39, 56

[29] Li-Zhi Zhang. Flow maldistribution and thermal performance deterioration in a cross-flow air to air heat exchanger with plate-fin cores. *International journal of heat and mass transfer*, 52(19):4500–4509, 2009. 8, 29

[30] R. K. Shah. Classification of heat exchangers. In S. Kakac, A. E. Bergles, and F. Mayinger, editors, *Heat Exchangers: Thermal-Hydraulic Fundamentals and Design*, chapter 10, page 946. Hemisphere Publishing, Washington, DC, 1981. xv, xxii, 12, 134, 135

[31] Osborne Reynolds. An experimental investigation of the circumstances which determine whether the motion of water shall be direct or sinuous, and of the law of resistance in parallel channels. *Proceedings of the royal society of London*, 35(224-226):84–99, 1883. 13, 48, 52

[32] R.K Shah. In Attilio Bisio and Sharon Boots, editors, *Encyclopedia of energy technology and the environment*, pages 1651–1670. John Wiley & Sons, 1994. xv, 13

[33] MR Jafari Nasr and A Shafeghat. Fluid flow analysis and extension of rapid design algorithm for helical baffle heat exchangers. *Applied Thermal Engineering*, 28(11):1324–1332, 2008. xv, 14, 46

[34] John H Lienhard IV and John H Lienhard V. *A heat transfer textbook*. Courier Corporation, 2015. xv, 14, 110

[35] Frank P Incropera, Adrienne S Lavine, Theodore L Bergman, and David P DeWitt. *Principles of heat and mass transfer*. Wiley, 2013. 14, 32

[36] RK Shah and WW Focke. Plate heat exchangers and their design theory. *Heat Transfer Equipment Design*, 227:254, 1988. xv, 14, 15

[37] John H Lienhard. *A heat transfer textbook*. Courier Corporation, 2013. xv, 16

[38] Tim Cowell and Nacer Achaichia. Compact heat exchangers in the automobile industry. *Compact Heat Exchangers for the process industries*, pages 11–28, 1997. 17

[39] Toshiharu Shinmura. Heat exchanger having a radiator and a condenser, March 19 1991. US Patent 5,000,257. xv, 17

[40] James Klett, Rommie Hardy, Ernie Romine, Claudia Walls, and Tim Burchell. High-thermal-conductivity, mesophase-pitch-derived carbon foams: effect of precursor on structure and properties. *Carbon*, 38(7):953–973, 2000. xv, 19, 20

[41] SY Kim, JW Paek, and BH Kang. Flow and heat transfer correlations for porous fin in a plate-fin heat exchanger. *Journal of heat transfer*, 122(3):572–578, 2000. 20

[42] Sven De Schampheleire, Peter De Jaeger, Henk Huisseune, Bernd Ameel, Christophe T'Joen, Kathleen De Kerpel, and Michel De Paepe. Thermal hydraulic performance of 10 ppi aluminium foam as alternative for louvered fins in an hvac heat exchanger. *Applied Thermal Engineering*, 51(1):371–382, 2013. 20, 32

[43] LP Pang, XM Dang, and J Cheng. Study on heat transfer performance of skin heat exchanger. *Experimental Heat Transfer*, 28(4):317–327, 2015. xvi, 20

[44] Elizabeth Dyson, Ab Hashemi. Performance characterization of high-power electronic equipment onboard an aircraft. *Heat transfer engineering*, 21(1):15–24, 2000. 20

[45] Henry Wong and Robert E Peck. Experimental evaluation of air-cooling electronics at high altitudes. *Journal of Electronic Packaging*, 123(4):356–365, 2001. 20

[46] E Reginald Von Driest. *The problem of aerodynamic heating.* Institute of the Aeronautical Sciences, 1956. 20

[47] J-P Kruth, Ming-Chuan Leu, and Terunaga Nakagawa. Progress in additive manufacturing and rapid prototyping. *Cirp Annals*, 47(2):525–540, 1998. 21, 23

[48] TS Srivatsan and TS Sudarshan. *Additive manufacturing: innovations, advances, and applications.* CRC Press, 2015. xvi, 21, 22, 23, 24

[49] Yuwei Zhai, Diana A Lados, and Jane L LaGoy. Additive manufacturing: making imagination the major limitation. *Jom*, 66(5):808–816, 2014. xvi, 21

[50] Jean-Pierre Kruth. Material incress manufacturing by rapid prototyping techniques. *CIRP Annals-Manufacturing Technology*, 40(2):603–614, 1991. xvi, 22

[51] Charles W Hull. Apparatus for production of three-dimensional objects by stereolithography, March 11 1986. US Patent 4,575,330. 22

[52] Kaufui V Wong and Aldo Hernandez. A review of additive manufacturing. *ISRN Mechanical Engineering*, 2012, 2012. xvi, 22, 23

[53] Kenneth G Cooper. *Rapid prototyping technology*, volume 200. Marcel Dekker New York, 2001. 22

[54] Rafiq Noorani. *Rapid prototyping: principles and applications.* John Wiley & Sons Incorporated, 2006. 22

[55] S Scott Crump. Apparatus and method for creating three-dimensional objects, June 9 1992. US Patent 5,121,329. 23

[56] Duc Truong Pham and Rosemary S Gault. A comparison of rapid prototyping technologies. *International Journal of machine tools and manufacture*, 38(10-11):1257–1287, 1998. 23

[57] Michael Feygin. Apparatus and method for forming an integral object from laminations, June 21 1988. US Patent 4,752,352. 23

[58] Joon Park, Michael J Tari, and H Thomas Hahn. Characterization of the laminated object manufacturing (lom) process. *Rapid Prototyping Journal*, 6(1):36–50, 2000. xvi, 23, 24

[59] D Klosterman. Affordable, rapid composite tooling via laminated object manufacturing. *Materials and Process Challenges: Aging Systems, Affordability, Alternative Applications.*, 41:220–229, 1996. 23

[60] Lawrence E Murr and Lawrence E Murr. Additive manufacturing: Changing the rules of manufacturing. *Handbook of Materials Structures, Properties, Processing and Performance*, pages 1–10, 2016. 24

[61] R Ippolito, Luca Iuliano, and A Gatto. Benchmarking of rapid prototyping techniques in terms of dimensional accuracy and surface finish. *CIRP Annals-Manufacturing Technology*, 44(1):157–160, 1995. 24

[62] R. Baker. Method of making decorative articles, 21 1925. US Patent 1533,300. 24

[63] Fude Wang, Stewart Williams, and Matthew Rush. Morphology investigation on direct current pulsed gas tungsten arc welded additive layer manufactured ti6al4v alloy. *The international journal of advanced manufacturing technology*, 57(5-8):597–603, 2011. 24

[64] JD Spencer, PM Dickens, and CM Wykes. Rapid prototyping of metal parts by three-dimensional welding. *Proceedings of the Institution of Mechanical Engineers, Part B: Journal of Engineering Manufacture*, 212(3):175–182, 1998. 24

[65] Daniel Clark, MR Bache, and Mark T Whittaker. Shaped metal deposition of a nickel alloy for aero engine applications. *journal of materials processing technology*, 203(1-3):439–448, 2008. 24

[66] Bernd Baufeld, Omer Van der Biest, and Rosemary Gault. Additive manufacturing of ti–6al–4v components by shaped metal deposition: microstructure and mechanical properties. *Materials & Design*, 31:S106–S111, 2010. 24

[67] PS Almeida and S Williams. Innovative process model of ti–6al–4v additive layer manufacturing using cold metal transfer (cmt). In *Proceedings of the twenty-first annual international solid freeform fabrication symposium, University of Texas at Austin, Austin, TX, USA*, 2010. 24

[68] Linkan Bian, Nima Shamsaei, and John Usher. *Laser-based Additive Manufacturing of Metal Parts: Modeling, Optimization, and Control of Mechanical Properties*. CRC Press, 2017. xvi, 24, 25

[69] Donghong Ding, Zengxi Pan, Dominic Cuiuri, and Huijun Li. A multi-bead overlapping model for robotic wire and arc additive manufacturing (waam). *Robotics and Computer-Integrated Manufacturing*, 31:101–110, 2015. xvi, 24, 25

[70] Ahmadreza Jahadakbar. *The Additively Manufactured Porous NiTi and Ti-6Al-4V in Mandibular Reconstruction: Introducing the Stiffness-Matched and the Variable Stiffness Options for the Reconstruction Plates.* PhD thesis, University of Toledo, 2016. 25

[71] Ahmadreza Jahadakbar, Narges Shayesteh Moghaddam, Amirhesam Amerinatanzi, David Dean, Haluk E Karaca, and Mohammad Elahinia. Finite element simulation and additive manufacturing of stiffness-matched niti fixation hardware for mandibular reconstruction surgery. *Bioengineering*, 3(4):36, 2016. 25

[72] Amirhesam Amerinatanzi, Narges Shayesteh Moghaddam, Ahmadreza Jahadakbar, David Dean, and Mohammad Elahinia. On the effect of screw preload on the stress distribution of mandibles during segmental defect treatment using an additively manufactured hardware. In *ASME 2016 11th international manufacturing science and engineering conference*, pages V002T03A015–V002T03A015. American Society of Mechanical Engineers, 2016. 25

[73] Ian Gibson, David W Rosen, and Brent Stucker. *Additive Manufacturing Technologies*. Springer, 2010. xvi, 25

[74] Jean-Pierre Kruth, X Wang, Tahar Laoui, and Ludo Froyen. Lasers and materials in selective laser sintering. *Assembly Automation*, 23(4):357–371, 2003. xvi, 25, 26

[75] Sanjay Kumar. Selective laser sintering: a qualitative and objective approach. *Jom*, 55(10):43–47, 2003. 26

[76] Nikolay Tolochko, Sregei Mozzharov, Tahar Laoui, and Ludo Froyen. Selective laser sintering of single-and two-component metal powders. *Rapid Prototyping Journal*, 9(2):68–78, 2003. 26

[77] Serguei Kolossov, Eric Boillat, Rémy Glardon, P Fischer, and M Locher. 3d fe simulation for temperature evolution in the selective laser sintering process.

International Journal of Machine Tools and Manufacture, 44(2-3):117–123, 2004. 26

[78] Jean-Pierre Kruth, Peter Mercelis, J Van Vaerenbergh, Ludo Froyen, and Marleen Rombouts. Binding mechanisms in selective laser sintering and selective laser melting. *Rapid prototyping journal*, 11(1):26–36, 2005. 26

[79] Udo Behrendt and Mike Shellabear. The eos rapid prototyping concept. *Computers in industry*, 28(1):57–61, 1995. 26

[80] Uday Hejmadi and Kevin McAlea. Selective laser sintering of metal molds: the rapidtooltm process. In *Proceedings of the Solid Freeform Fabrication Symposium*, pages 97–104. Citeseer, 1996. 26

[81] Ronald Knight, Joe Wright, Joseph Beaman, and Douglas Freitag. Metal processing using selective laser sintering and hot isostatic pressing (sls/hip). In *Solid Freeform Fabrication Symposium*, pages 1996–349, 1996. 26

[82] NK Tolochko, SE Mozzharov, NV Sobolenko, YUV Khlopkov, and I Yadroitsev. Main relationships governing laser sintering of loose single-component metallic powders. *Journal of Advanced Materials(UK/Russia)(UK)*, 2:151–157, 1995. 26

[83] Jean-Pierre Kruth, Ludo Froyen, Marleen Rombouts, Jonas Van Vaerenbergh, and P Mercells. New ferro powder for selective laser sintering of dense parts. *CIRP Annals-Manufacturing Technology*, 52(1):139–142, 2003. 26

[84] Peter Mercelis and Jean-Pierre Kruth. Residual stresses in selective laser sintering and selective laser melting. *Rapid prototyping journal*, 12(5):254–265, 2006. 26

[85] Philip J Withers and HKDH Bhadeshia. Residual stress. part 1–measurement techniques. *Materials science and Technology*, 17(4):355–365, 2001. 26

[86] Da Buchbinder, HB Schleifenbaum, S Heidrich, W Meiners, and J Bültmann. High power selective laser melting (hp slm) of aluminum parts. *Physics Procedia*, 12:271–278, 2011. 26

[87] Lore Thijs, Frederik Verhaeghe, Tom Craeghs, Jan Van Humbeeck, and Jean-Pierre Kruth. A study of the microstructural evolution during selective laser melting of ti–6al–4v. *Acta materialia*, 58(9):3303–3312, 2010. 26

[88] Marleen Rombouts, Jean-Pierre Kruth, Ludo Froyen, and Peter Mercelis. Fundamentals of selective laser melting of alloyed steel powders. *CIRP Annals-Manufacturing Technology*, 55(1):187–192, 2006. 26

[89] KN Amato, SM Gaytan, LE Murr, E Martinez, PW Shindo, J Hernandez, S Collins, and F Medina. Microstructures and mechanical behavior of inconel 718 fabricated by selective laser melting. *Acta Materialia*, 60(5):2229–2239, 2012. 26

[90] I Yadroitsev, Ph Bertrand, and I Smurov. Parametric analysis of the selective laser melting process. *Applied surface science*, 253(19):8064–8069, 2007. 26

[91] RK Shah and AL London. Thermal boundary conditions and some solutions for laminar duct flow forced convection. *Journal of Heat Transfer*, 96(2):159–165, 1974. 28, 47

[92] RK Shah. bmindf flow forced convection heat transfer and flow friction in straight and curved ducts a summary of analytical solutions. 1971. 28

[93] WM Kays and AL London. Heat transfer and flow friction characteristics of some compact heat exchanger surfaces. *Trans. AsME*, 72:1075–1097, 1950. 28

[94] AL London and CK Ferguson. Test results of high-performance heat exchanger surfaces used in aircraft intercoolers and their significance for gas-turbine regenerator design. *Trans. ASME*, 71:17–26, 1949. 28

[95] Anjun Jiao, Rui Zhang, and Sangkwon Jeong. Experimental investigation of header configuration on flow maldistribution in plate-fin heat exchanger. *Applied Thermal Engineering*, 23(10):1235–1246, 2003. xvi, 29, 30

[96] Jian Wen, Yanzhong Li, Aimin Zhou, and Ke Zhang. An experimental and numerical investigation of flow patterns in the entrance of plate-fin heat exchanger. *International Journal of Heat and Mass Transfer*, 49(9):1667–1678, 2006. xvi, xvii, 29, 32, 56, 57

[97] Jian Wen and Yanzhong Li. Study of flow distribution and its improvement on the header of plate-fin heat exchanger. *Cryogenics*, 44(11):823–831, 2004. 29, 57

[98] Young-Chull Ahn, Jae-Min Cho, Hee-Soo Shin, Yu-Jin Hwang, Chang-Gun Lee, Jae-Keun Lee, Hyun-Uk Lee, and Tae-Wook Kang. An experimental study of the air-side particulate fouling in fin-and-tube heat exchangers of air conditioners. *Korean Journal of Chemical Engineering*, 20(5):873–877, 2003. 30

[99] Ho Joon Lee, Duk Gyu Han, Sung Ho Lee, Jin Woong Yoo, Sung Heum Baek, and Eun Kyu Lee. On-line monitoring and quantitative analysis of biofouling in low-velocity cooling water system. *Korean Journal of Chemical Engineering*, 15(1):71–77, 1998. 30

[100] Hong-Joo Lee, Jin-Soo Park, and Seung-Hyeon Moon. A study on fouling mitigation using pulsing electric fields in electrodialysis of lactate containing bsa. *Korean Journal of Chemical Engineering*, 19(5):880–887, 2002. 30

[101] Mark S Breuker and James E Braun. Common faults and their impacts for rooftop air conditioners. *HVAC&R Research*, 4(3):303–318, 1998. 30

[102] BC Krafthefer and U Bonne. Energy use implications of methods to maintain heat exchanger coil cleanliness. *ASHRAE Trans.;(United States)*, 92(CONF-860106-), 1986. 30

[103] Ian H Bell and Eckhard A Groll. Air-side particulate fouling of microchannel heat exchangers: experimental comparison of air-side pressure drop and heat transfer with plate-fin heat exchanger. *Applied Thermal Engineering*, 31(5):742–749, 2011. xvi, 31

[104] Raija Lankinen, Juhani Suihkonen, and Pertti Sarkomaa. The effect of air side fouling on thermal-hydraulic characteristics of a compact heat exchanger. *International Journal of Energy Research*, 27(4):349–361, 2003. 31

[105] R Haghighi-Khoshkhoo and FMJ McCluskey. Air-side fouling of compact heat exchangers for discrete particle size ranges. *Heat Transfer Engineering*, 28(1):58–64, 2007. 31

[106] Bock Choon Pak, Eckhard A Groll, and James E Braun. Impact of fouling and cleaning on plate fin and spine fin heat exchanger performance. *ASHRAE Transactions*, 111(1), 2005. 31

[107] S Freund and S Kabelac. Investigation of local heat transfer coefficients in plate heat exchangers with temperature oscillation ir thermography and cfd. *International Journal of Heat and Mass Transfer*, 53(19):3764–3781, 2010. xvi, 31, 32

[108] Herchang Ay, JiinYuh Jang, and Jer-Nan Yeh. Local heat transfer measurements of plate finned-tube heat exchangers by infrared thermography. *International Journal of Heat and Mass Transfer*, 45(20):4069–4078, 2002. 32

[109] Jin-Sheng Leu, Ying-Hao Wu, and Jiin-Yuh Jang. Heat transfer and fluid flow analysis in plate-fin and tube heat exchangers with a pair of block shape vortex generators. *International Journal of Heat and Mass Transfer*, 47(19-20):4327–4338, 2004. 32

[110] R Boukhanouf, A Haddad, MT North, and C Buffone. Experimental investigation of a flat plate heat pipe performance using ir thermal imaging camera. *Applied Thermal Engineering*, 26(17-18):2148–2156, 2006. 32

[111] Yang Wen-Jai. *Computer-Assisted Flow Visualization*. Begell House, New York, 1994. 32

[112] Besir Sahin, Nurhan Adil Ozturk, and Cahit Gurlek. Horseshoe vortex studies in the passage of a model plate-fin-and-tube heat exchanger. *International Journal of Heat and Fluid Flow*, 29(1):340–351, 2008. xvi, 32

[113] JV Simo Tala, S Russeil, D Bougeard, and J-L Harion. Investigation of the flow characteristics in a multirow finned-tube heat exchanger model by means of piv measurements. *Experimental Thermal and Fluid Science*, 50:45–53, 2013. 32

[114] Zhenhui Dai, David F Fletcher, and Brian S Haynes. Impact of tortuous geometry on laminar flow heat transfer in microchannels. *International Journal of Heat and Mass Transfer*, 83:382–398, 2015. xvi, 32, 51, 58, 98

[115] ANSYS Inc. *ANSYS Fluent Theory Guide*. Ansys Inc., 2013. 35, 38, 54, 55, 58

[116] Michael J Moran. Availability analysis: a guide to efficient energy use. 1982. 35

[117] MJ Moran and E Sciubba. Exergy analysis: principles and practice. *Journal of Engineering for Gas Turbines and Power*, 116(2):285–290, 1994. 35

[118] Adrian Bejan. *Entropy generation through heat and fluid flow*. Wiley, 1982. 35

[119] Adrian Bejan. Entropy generation minimization: The new thermodynamics of finite-size devices and finite-time processes. *Journal of Applied Physics*, 79(3):1191–1218, 1996. 35

[120] Michel Feidt. *Thermodynamics and optimization energe systemic and proce*. 1996. 35

[121] Robert Eymard, Thierry Gallouët, and Raphaèle Herbin. Finite volume methods. *Handbook of numerical analysis*, 7:713–1018, 2000. 38

[122] Christopher J Greenshields. Openfoam user guide. *OpenFOAM Foundation Ltd, version*, 3(1), 2015. 38

[123] Joel H Ferziger and Milovan Peric. *Computational methods for fluid dynamics*. Springer Science & Business Media, 2012. 38, 42, 43, 44

[124] Nam-Trung Nguyen, Steven T Wereley, and Steven T Wereley. *Fundamentals and applications of microfluidics*. Artech house, 2002. 38

[125] Subrahmanyan Chandrasekhar. *Hydrodynamic and hydromagnetic stability.* Courier Corporation, 2013. 38

[126] Arun K Saha and Sumanta Acharya. Unsteady rans simulation of turbulent flow and heat transfer in ribbed coolant passages of different aspect ratios. *International Journal of Heat and Mass Transfer*, 48(23-24):4704–4725, 2005. 39

[127] Richard Wood. *Experimental and Theoretical Studies of Contaminant Transport Due to Human Movement in a Hospital Corridor.* PhD Thesis, University of Leeds, 2016. xvi, 39, 41, 42, 52, 76

[128] Joseph Boussinesq. *Essai sur la théorie des eaux courantes.* Impr. nationale, 1877. 40

[129] Ludwig Prandtl. Bericht uber untersuchungen zur ausgebildeten turbulenz. *Zs. angew. Math. Mech.*, 5:136–139, 1925. 40

[130] Brian Edward Launder and Dudley Brian Spalding. The numerical computation of turbulent flows. In *Numerical Prediction of Flow, Heat Transfer, Turbulence and Combustion*, pages 96–116. Elsevier, 1983. 40, 41

[131] Florian R Menter. Zonal two equation kw turbulence models for aerodynamic flows. In *23rd fluid dynamics, plasmadynamics, and lasers conference*, page 2906, 1993. 41

[132] David C Wilcox. Reassessment of the scale-determining equation for advanced turbulence models. *AIAA journal*, 26(11):1299–1310, 1988. 41

[133] Florian R Menter, Martin Kuntz, and Robin Langtry. Ten years of industrial experience with the sst turbulence model. *Turbulence, heat and mass transfer*, 4(1):625–632, 2003. 41

[134] Florian R Menter. Two-equation eddy-viscosity turbulence models for engineering applications. *AIAA journal*, 32(8):1598–1605, 1994. 41

[135] Frank M.White. *Chapter 6 Viscous Flow in Ducts, Fluid Dynamics fifth edition.* WCB McGraw Hill, PO Box 182605, Columbus OH 43218-2605 USA, 2003. 44

[136] Malcolm J Andrews and Bashir I Master. 3-d modeling of the abb lummus heat transfer helixchanger using cfd. In *International Conference on Compact Heat Exchangers, Banff, Canada*, 1999. 46

[137] Xiang-hui Tan, Dong-sheng Zhu, Guo-yan Zhou, and Liu Yang. 3d numerical simulation on the shell side heat transfer and pressure drop performances of twisted oval tube heat exchanger. *International Journal of Heat and Mass Transfer*, 65:244–253, 2013. xvi, 46

[138] Athanasios G Kanaris, Aikaterini A Mouza, and Spiros V Paras. Flow and heat transfer prediction in a corrugated plate heat exchanger using a cfd code. *Chemical engineering & technology*, 29(8):923–930, 2006. 46, 50, 52

[139] AG Kanaris, AA Mouza, and SV Paras. Optimal design of a plate heat exchanger with undulated surfaces. *International Journal of Thermal Sciences*, 48(6):1184–1195, 2009. xvi, 46, 50, 52

[140] Ying-Chi Tsai, Fung-Bao Liu, and Po-Tsun Shen. Investigations of the pressure drop and flow distribution in a chevron-type plate heat exchanger. *International communications in heat and mass transfer*, 36(6):574–578, 2009. 46, 50, 52

[141] M Ferrero, Alessandro Scattina, Eliodoro Chiavazzo, F Carena, D Perocchio, M Roberti, G Toscano Rivalta, and Pietro Asinari. Louver finned heat exchangers for automotive sector: Numerical simulations of heat transfer and flow resistance coping with industrial constraints. *Journal of Heat Transfer*, 135(12):121801, 2013. xvi, 46, 50, 51

[142] Man-Hoe Kim and Clark W Bullard. Air-side thermal hydraulic performance of multi-louvered fin aluminum heat exchangers. *International Journal of Refrigeration*, 25(3):390–400, 2002. 46

[143] Thomas Perrotin and Denis Clodic. Thermal-hydraulic cfd study in louvered fin-and-flat-tube heat exchangers. *International Journal of Refrigeration*, 27(4):422–432, 2004. 46, 50, 52

[144] Raj M Manglik, Jiehai Zhang, and Arun Muley. Low reynolds number forced convection in three-dimensional wavy-plate-fin compact channels: fin density effects. *International Journal of Heat and Mass Transfer*, 48(8):1439–1449, 2005. 46, 48, 53

[145] Nathan R Rosaguti, David F Fletcher, and Brian S Haynes. Low-reynolds number heat transfer enhancement in sinusoidal channels. *Chemical engineering science*, 62(3):694–702, 2007. 46, 48, 53

[146] Jiehai Zhang, Jaydeep Kundu, and Raj M Manglik. Effect of fin waviness and spacing on the lateral vortex structure and laminar heat transfer in wavy-plate-fin cores. *International Journal of Heat and Mass Transfer*, 47(8):1719–1730, 2004. xvii, xxv, 46, 48, 53, 60, 61, 62, 69, 70, 71

[147] SV Patankar, CH Liu, and EM Sparrow. Fully developed flow and heat transfer in ducts having streamwise-periodic variations of cross-sectional area. *Journal of Heat Transfer*, 99(2):180–186, 1977. 46, 47, 48, 52, 57, 60, 61, 62, 69, 71, 72

[148] KM Kelkar and SV Patankar. Numerical prediction of flow and heat transfer in a parallel plate channel with staggered fins. *Journal of heat transfer*, 109(1):25–30, 1987. 48

[149] HM Metwally and Raj M Manglik. Enhanced heat transfer due to curvature-induced lateral vortices in laminar flows in sinusoidal corrugated-plate channels. *International Journal of Heat and Mass Transfer*, 47(10):2283–2292, 2004. 48

[150] Y-Q Wang, Qi-Wu Dong, Min-Shan Liu, and Dan Wang. Numerical study on plate-fin heat exchangers with plain fins and serrated fins at low reynolds number. *Chemical engineering & technology*, 32(8):1219–1226, 2009. 48

[151] Arafat A Bhuiyan, M Ruhul Amin, and AKM Sadrul Islam. Three-dimensional performance analysis of plain fin tube heat exchangers in transitional regime. *Applied Thermal Engineering*, 50(1):445–454, 2013. xvi, 49, 52

[152] Hacı Mehmet Şahin, Ali Rıza Dal, and Eşref Baysal. 3-d numerical study on the correlation between variable inclined fin angles and thermal behavior in plate fin-tube heat exchanger. *Applied Thermal Engineering*, 27(11):1806–1816, 2007. 49

[153] Yong-Gang Lei, Ya-Ling He, Li-Ting Tian, Pan Chu, and Wen-Quan Tao. Hydrodynamics and heat transfer characteristics of a novel heat exchanger with delta-winglet vortex generators. *Chemical Engineering Science*, 65(5):1551–1562, 2010. xvi, 49

[154] NK Mitra, M Fiebig, et al. Comparison of wing-type vortex generators for heat transfer enhancement in channel flows. *Journal of heat transfer*, 116(4):880–885, 1994. 49

[155] Henk Huisseune, C Tā, Peter De Jaeger, Bernd Ameel, Joachim Demuynck, Michel De Paepe, et al. Numerical study of flow deflection and horseshoe vortices in a louvered fin round tube heat exchanger. *Journal of Heat Transfer*, 134(9):091801, 2012. xvi, 51

[156] R Bala Sundar Rao, G Ranganath, and C Ranganayakulu. Development of colburn jfactor and fanning friction factor fcorrelations for compact heat exchanger plain fins by using cfd. *Heat and Mass Transfer*, 49(7):991–1000, 2013. 51, 52

[157] Zhanying Zheng, David F Fletcher, and Brian S Haynes. Transient laminar heat transfer simulations in periodic zigzag channels. *International Journal of Heat and Mass Transfer*, 71:758–768, 2014. xvi, 51, 52, 53, 58, 60, 63, 98

[158] TA Rush, TA Newell, and AM Jacobi. An experimental study of flow and heat transfer in sinusoidal wavy passages. *International Journal of Heat and Mass Transfer*, 42(9):1541–1553, 1999. xvi, 52, 53, 74, 75

[159] Michio Hiramatsu, Tsuneo Ishimaru, and Takaki Ohkouchi. Numerical analysis of innerfins for intercoolers. *JSME international journal. Series 2, Fluids engineering, heat transfer, power, combustion, thermophysical properties*, 35(3):406–412, 1992. 52, 53, 74, 75

[160] Tatsuo Nishimura, Koji Yano, Tadashi Yoshino, and Yuji Kawamura. Occurrence and structure of taylor-goertler vortices induced in two-dimensional wavy channels for steady flow. *Journal of chemical engineering of Japan*, 23(6):697–703, 1990. 54

[161] Henry Darcy. *Les fontaines publiques de la ville de Dijon: exposition et application...* Victor Dalmont, 1856. 54

[162] Yehuda Bachmat and Jacob Bear. Macroscopic modelling of transport phenomena in porous media. 1: The continuum approach. *Transport in porous media*, 1(3):213–240, 1986. 54

[163] Rainer Helmig et al. *Multiphase flow and transport processes in the subsurface: a contribution to the modeling of hydrosystems.* Springer-Verlag, 1997. 54

[164] P. Forchheimer. Wasserbewegung durch boden. *Zeitschrift des Vereines deutscher Ingenieure*, (45):1782–1788., 1901. 54

[165] Morris Muskat, Ralph Dewey Wyckoff, et al. Flow of homogeneous fluids through porous media. 1937. 54

[166] David Cornell and Donald L Katz. Flow of gases through consolidated porous media. *Industrial & Engineering Chemistry*, 45(10):2145–2152, 1953. 54

[167] Leon Green Jr and Pol Duwez. Fluid flow through porous metals. *J. Applied Mech.*, 18, 1951. 54

[168] E Carluccio, G Starace, A Ficarella, and D Laforgia. Numerical analysis of a cross-flow compact heat exchanger for vehicle applications. *Applied Thermal Engineering*, 25(13):1995–2013, 2005. 56, 95

[169] Andrew M Hayes, Jamil A Khan, Aly H Shaaban, and Ian G Spearing. The thermal modeling of a matrix heat exchanger using a porous medium and the thermal non-equilibrium model. *International Journal of Thermal Sciences*, 47(10):1306–1315, 2008. 56

[170] S Lalot, P Florent, SK Lang, and AE Bergles. Flow maldistribution in heat exchangers. *Applied thermal engineering*, 19(8):847–863, 1999. 57

[171] Turbo oil 2380 product data. `https://msdspds.bp.com/bpglis/FusionPDS.nsf/Files/802577040037FB4B80257AD800035A64/$File/BPXE-92RGEV.pdf`, May 2019. xxv, 91, 104

[172] Ender Ozden and Ilker Tari. Shell side cfd analysis of a small shell-and-tube heat exchanger. *Energy Conversion and Management*, 51(5):1004–1014, 2010. 95

[173] Richard Courant, Kurt Friedrichs, and Hans Lewy. Über die partiellen differenzengleichungen der mathematischen physik. *Mathematische Annalen*, 100(1):32–74, 1928. 102, 108

[174] Frank M. White. *Fluid Mechanics*. Mcgraw-Hill, 2011. 124, 148

Appendix A

Experimental Data

A.1 Pressure drop test points

Test point	1	2	3	4	5	6	7
Fuel $\dot{m}$, kg/s	0.0378	0.0756	0.1134	0.1512	0.0757	0.1135	0.1513
Fuel ρ, kg/m^3	786.7	786.7	786.7	786.7	742.7	742.7	742.7
Fuel μ_{fuel}, $Pa \cdot s$	0.0014	0.0014	0.0014	0.0014	0.0006	0.0006	0.0006
T_{in}, K	294	294	294	294	353	353	353
Re_{inlet}	962	1924	2886	3848	4481	8962	11202
Test point	8	9	10	11	12	13	14
Fuel $\dot{m}$, kg/s	0.1891	0.2270	0.2648	0.3026	0.3404	0.3782	0.4161
Fuel ρ, kg/m^3	742.7	742.7	742.7	742.7	742.7	742.7	742.7
Fuel μ_{fuel}, $Pa \cdot s$	0.0006	0.0006	0.0006	0.0006	0.0006	0.0006	0.0006
T_{in}, K	353	353	353	353	353	353	353
Re_{inlet}	11202	13443	15682	17922	20162	22403	24643
Test point	15	16	17	18	19	20	21
Fuel $\dot{m}$, kg/s	0.4539	0.4917	0.5296	0.6052	0.6809	0.7565	0.8321
Fuel ρ, kg/m^3	742.7	742.7	742.7	742.7	742.7	742.7	742.7
Fuel μ_{fuel}, $Pa \cdot s$	0.0006	0.0006	0.0006	0.0006	0.0006	0.0006	0.0006
T_{in}, K	353	353	353	353	353	353	353
Re_{inlet}	26883	29123	31367	35848	40329	44805	49286
Test point	22	23	24	25	26	27	28
Fuel $\dot{m}$, kg/s	0.9077	0.9834	1.059	1.1345	1.21	1.2855	1.4367
Fuel ρ, kg/m^3	742.7	742.7	742.7	742.7	742.7	742.7	742.7
Fuel μ_{fuel}, $Pa \cdot s$	0.0006	0.0006	0.0006	0.0006	0.0006	0.0006	0.0006
T_{in}, K	353	353	353	353	353	353	353
Re_{inlet}	53766	5847	62727	67194	71667	76138	85096
Test point	29	30	31				
Fuel, $\dot{m}$, kg/s	1.5879	1.7392	1.8904				
Fuel ρ, kg/m^3	742.7	742.7	742.7				
Fuel μ_{fuel}, $Pa \cdot s$	0.0006	0.0006	0.0006				
T_{in}, K	353	353	353				
Re_{inlet}	92666	107351	126587				

Table A.1: Pressure drop test data

A.2 Thermal performance test

Test point	1	2	3	4	5	6	7
Fuel $\dot{m}$, kg/s	0.0757	0.1135	0.1514	0.1893	0.2271	0.2649	0.3027
Fuel ρ, kg/m^3	781	780	781	781	781	781	780
Fuel μ_{fuel}, $Pa \cdot s$	0.012	0.012	0.012	0.012	0.012	0.0012	0.0012
Fuel T_{in}, K	302	302	302	302	302	302	302
Fuel Re_{inlet}	2241	3342	4475	5607	6672	7782	7892
Test point	8	9	10	11	12	13	14
Fuel $\dot{m}$, kg/s	0.3405	0.3777	0.4155	0.4531	0.4911	0.53	0.5672
Fuel ρ, kg/m^3	780	779	779	779	779	781	780
Fuel μ_{fuel}, $Pa \cdot s$	0.0012	0.0012	0.0012	0.0012	0.0012	0.0012	0.0012
Fuel T_{in}, K	302	304	304	305	304	302	303
Fuel Re_{inlet}	10002	11095	12205	13308	14424	15568	16661
Test point	15	16	17	18	19	20	21
Fuel $\dot{m}$, kg/s	0.6054	0.6427	0.681	0.7185	0.7560	0.8321	0.9082
Fuel ρ, kg/m^3	780	780	780	780	780	780	781
Fuel μ_{fuel}, $Pa \cdot s$	0.0012	0.0012	0.0012	0.0012	0.0012	0.0012	0.0012
Fuel T_{in}, K	302	303	302	303	303	303	302
Fuel Re_{inlet}	17782	18879	20005	21106	22207	24443	26678
Test point	22	23	24	25	26	27	28
Fuel $\dot{m}$, kg/s	0.9839	1.0595	1.135	1.211	1.2864	1.3623	1.4388
Fuel ρ, kg/m^3	781	781	780	781	780	781	781
Fuel μ_{fuel}, $Pa \cdot s$	0.0012	0.0012	0.0012	0.0012	0.0012	0.0012	0.0012
Fuel T_{in}, K	302	302	303	302	303	302	302
Fuel Re_{inlet}	28902	31122	33340	35573	37787	40018	42265
Test point	29						
Fuel $\dot{m}$, kg/s	1.5871						
Fuel ρ, kg/m^3	780						
Fuel μ_{fuel}, $Pa \cdot s$	0.0012						
Fuel T_{in}, K	304						
Fuel Re_{inlet}	46620						

Table A.2: Fuel data of the thermal performance test.

Test point	1	2	3	4	5	6	7
Oil $\dot{m}$, kg/s	0.1513	0.1513	0.1513	0.1513	0.1513	0.1513	0.1513
Oil ρ, kg/m^3	926	926	926	926	926	926	926
Oil μ_{fuel}, $Pa \cdot s$	0.0031	0.0031	0.0031	0.0031	0.0031	0.0031	0.0031
Oil T_{in}, K	372	373	373	373	373	373	373
Oil Re_{inlet}	1792	1791	1792	1792	1792	1792	1792
Test point	8	9	10	11	12	13	14
Oil $\dot{m}$, kg/s	0.1513	0.1513	0.1513	0.1513	0.1513	0.1513	0.1513
Oil ρ, kg/m^3	926	926	926	926	926	926	926
Oil μ_{fuel}, $Pa \cdot s$	0.0031	0.0031	0.0031	0.0031	0.0031	0.0031	0.0031
Oil T_{in}, K	372	373	373	373	373	372	372
Oil Re_{inlet}	1792	1791	1791	1792	1792	1792	1792
Test point	15	16	17	18	19	20	21
Oil $\dot{m}$, kg/s	0.1513	0.1513	0.1513	0.1513	0.1513	0.1513	0.1513
Oil ρ, kg/m^3	926	926	926	926	926	926	926
Oil μ_{fuel}, $Pa \cdot s$	0.0031	0.0031	0.0031	0.0031	0.0031	0.0031	0.0031
Oil T_{in}, K	373	373	372	372	372	372	373
Oil Re_{inlet}	1792	1792	1792	1792	1792	1792	1792
Test point	22	23	24	25	26	27	28
Oil $\dot{m}$, kg/s	0.1513	0.1513	0.1513	0.1513	0.1513	0.1513	0.1513
Oil ρ, kg/m^3	926	926	926	926	926	926	926
Oil μ_{fuel}, $Pa \cdot s$	0.0031	0.0031	0.0031	0.0031	0.0031	0.0031	0.0031
Oil T_{in}, K	373	373	373	373	373	373	373
Oil Re_{inlet}	1792	1792	1792	1792	1792	1792	1792
Test point	29						
Oil $\dot{m}$, kg/s	0.1513						
Oil ρ, kg/m^3	926						
Oil μ_{fuel}, $Pa \cdot s$	0.0031						
Oil T_{in}, K	373						
Oil Re_{inlet}	1791						

Table A.3: Oil data of the thermal performance test